Electrical Properties of Graphite Nanoparticles in Silicone Flexible Oscillators and Electromechanical Sensing

Littlejohn, Samuel

Award date:
2013

Awarding institution:
University of Bath

Electrical Properties of Graphite Nanoparticles in Silicone: Flexible Oscillators and Electromechanical Sensing

submitted by

Samuel David Littlejohn

for the degree of Doctor of Philosophy

of the

University of Bath

Department of Physics

November 2012

Signature of Author .....

Samuel David Littlejohn

Abstract

This thesis reports the discovery of a wide negative differential resistance (NDR) region in a graphite-silicone composite that was utilized to create a strain-tuned flexible oscillator. Encoding the strain into frequency mimics the behavior of mechanoreceptor neurons in the skin and demonstrates a flexible and electronically active material suitable for state of the art bio-electronic applications.

The NDR was investigated over a range of composite filling fractions and temperatures; alongside theoretical modelling to calculate the tunneling current through a graphite-silicone barrier. This led to the understanding that the NDR is the result of a semi-metal to insulator transition of embedded graphene bilayers within the graphite nanoparticles. The transition, brought about by a transverse bias across specifically orientated particles, opens a partial band-gap at the Fermi level of the bilayer. NDR in a flexible material has not been observed before and has potential for creating a flexible active device.

The electromechanical properties of the composite were considered through a bend induced bilayer strain. The piezoresistance was found to be dominated by transient resistance spiking from the breaking of conduction lines, which then reform according to the viscoelasticity of the polymer matrix. The resistance spiking was embraced as a novel method for sensitive differential pressure detection, used in the development of two applications. Firstly, it was employed for the detection of ultrasound waves and found to have an acoustic pressure detection threshold as low as 48 Pa. A commensurability was observed between the composite width and ultrasound wavelength which was shown to be consistent with the formation of standing waves, described by Bragg's law. Secondly, a differential pressure array of 64 composite pixels was fabricated and demonstrated to image pressures under 3.8 kPa at a resolution of 10 dpi.

The NDR active region was incorporated into an LC circuit where it was demonstrated to sustain oscillations of up to 12.5 kHz. The composite was then strained and an intrinsic frequency was observed which had a linear dependence on the strain with a frequency shift of 84 Hz / % strain. Lastly the composite was used in a strain-tuned amplifier circuit and shown to provide a gain of up to 4.5. This thesis provided the groundwork for a completely flexible electronically active device for futuristic bio-electronic skins with resolutions and sensitivities rivalling those of human tactile sensing.

Contents

Acknowledgments

I would like to express my wholehearted gratitude to Dr Alain Nogaret for his unfailing guidance and support over the past three years. I have enjoyed working under his supervision and been guided to this point by his unwavering enthusiasm for the work.

Thanks are also due to:

Ashok Chauhan for his help with building various electronic circuits, the use of his furnace and assistance with the ultrasound experiments.

The technical staff whose expertise is so valuable, especially Wendy for all my chemical needs; Paul for building so many various pieces of equipment; and Harry for the X-Ray diffraction measurements.

Dr Simon Crampin from the University of Bath for theoretical modelling and calculations regarding graphite.

Dr Dan Pantos and Giles Prentice from the University of Bath Chemistry department for fabricating and supplying the NDI molecules.

The EPSRC for providing the financial support necessary to the completion of this research, through the award of a DTA Studentship.

Chapter 1

Introduction

There is a demonstrable and pressing commercial demand for the development of flexible electronic materials. Consumers will soon expect to be able to roll up their electronic newspapers and neatly fold away their computers [1]. Further, advances are also sought in humanoid robotics where there is a need for bio-electronic materials that are capable of fitting curved surfaces, to enable tactile sensing and interaction with the surrounding environment [2], and demonstrate sensitivities and resolutions which exceed those of the human skin [3].

Developing flexible electronic circuits and sensors presents many new challenges, as it is extends beyond the capabilities of current silicon technology. The solutions will need to come about by the development and realisation of novel composite materials with properties that move away from conventional thinking. Conductive composites will certainly be part of this, with their intrinsic soft skin-like texture, tailored conductivity and piezoresistance they meet many of the requirements.

Whilst studying the properties of a graphite-silicon conductive composite we made an unexpected discovery: At low temperatures, above a threshold voltage, the current begins to decrease sharply with increasing voltage, an effect known as negative differential resistance (NDR). The presence of an NDR region is particularly exciting because it can be utilized in creating active devices such as oscillators and amplifiers. This discovery opened up three key questions that this thesis intends to address.

1. Where does the NDR mechanism originate from?

2. How can we utilize the flexibility of the composite?

3. Is the NDR region capable of sustaining oscillations?

In addressing these questions we pursue the development of a flexible active composite material capable of meeting the demands for a high resolution and sensitive bio-electronic skin.

We gain an understanding of the origins of the NDR through a comprehensive experimental study of the various parameters involved, including: The composite temperature, filling fraction, particle type and probe separation distances. We support the experimental results with theoretical modelling of the local density of states (LDOS) in graphite[1] and the tunneling current. This leads us to conclude that the NDR has its origins in an induced partial breaking of the conduction band of an embedded bilayer graphene [4].

This is particularly topical with the recent discovery of graphene [5] and the intensive debate and research surrounding exploitation of graphene's unique electronic properties for transistor devices [6]. One such route is through the application of an electric field across bilayer graphene to tune a band-gap [7, 8]; this is closely related to the embedded bilayer effect we observe in our composite material.

In answering the second question, we explore the electrical properties of our graphite silicone composite (GSC) under bend induced strain, an important property when fitting these flexible skins onto curved surfaces. We find a complex response due to the tunneling nature of the conduction network and the viscoelasticity of the silicone rubber matrix. We observe resistance spikes that occur on the immediate application of bend. While these spikes have been previously reported [9, 10], the focus is normally on how to minimise their presence as they detract from the piezoresistive response. However, we embrace the resistance spiking due to its high sensitivity to perturbations and are able to utilize it for differential pressure sensing. We demonstrate a novel use for this effect, using the composite to detect underwater acoustic pressure waves from a low power ultrasound transducer.[2] We also fabricate an array of 64 composite pixels to create an imaging device sensitive to the resistance spiking.

Conducting composites are widely used in state of the art development of flexible skins [11]. Numerous research groups are competing to create flexible transistors using materials such as carbon nanotubes [12], nanowires [13] and organic molecules [14]. They then demonstrate their flexible transistors by combining them with conductive rubbers that act as passive piezoresistive materials in order to make flexible pressure sensitive skins, which have a sensitivity of 30 kPa

[1] Calculations by Dr. Simon Crampin, University of Bath

[2] Experiment completed in collaboration with Ashok Chauhan, University of Bath

on a resolution of 10 dpi. [15, 16]. The resistance spiking method we develop offers a higher sensitivity of < 3.8 kPa. We also demonstrate new techniques for fabrication of composite devices that are clean room compatible and allow pixel feature sizes of 50 μm which could be used to attain resolutions of 250 dpi. This rivals the most senstive tactile sensor, human skin, which can detect a surface roughness of 100 μm and pressures of 10 kPa [17, 18].

We answer question three by including the composite in an LC oscillator circuit and apply a steady bias to demonstrate that the composite is capable of sustaining oscillations. We then take this a step further by bending the composite, to induce a bilayer strain, and measuring the response. We discover the composite has an intrinsic frequency, independent of the LC frequency, with a linear dependence on the strain. In this way we demonstrate that it is possible to encode the composite strain in frequency, mimicking the behaviour of mechanoreceptor neurons in the human skin. We are even able to build a flexible amplifier circuit, using the composite's active region and intrinsic frequency, with a tunable gain.

This thesis presents an account of the NDR effect and explores the potential of the GSC in new devices and applications based on its active and flexible properties.

Chapter 2

Background Theory

The aim of this chapter is to describe the underlying physics of carbon based structures and percolation conduction in composite materials. This will be done through first presenting carbon and its fascinating allotropic family. The tight binding model will be used to consider the origins of graphite's electronic properties arising from its stacked structure. This will then be put into context and explained in relation to the properties of graphene and bilayer graphene.

The second part of this chapter will be focused on conduction in composites. We will discuss how the incorporation of conductive particles into an insulating matrix enables conduction above the percolation threshold. We consider the significance of tunneling between particles in conduction lines and go on to derive the tunneling current through a single barrier system.

2.1 Carbon

2.1.1 Hybridization of s and p orbitals

Carbon is the sixth element in the periodic table, the fourth most abundant element in the universe and the basic building block for all life. The majority of objects we encounter in our daily lives contain carbon; the air we breathe; the food we eat; the fuel in our cars; the plastic in our pens; and the paper we write on, all contain carbon compounds and molecules. The reason why carbon is found in such a diverse number of forms is because it can form many different types of bonds due to its unique electronic structure. Its six electrons are arranged around the nucleus with two electrons in the innermost tightly bound shell and four electrons in the outer valence shell. Carbon's minimum energy ground state has two valence electrons in the 2s subshell and two in the 2p subshell. What

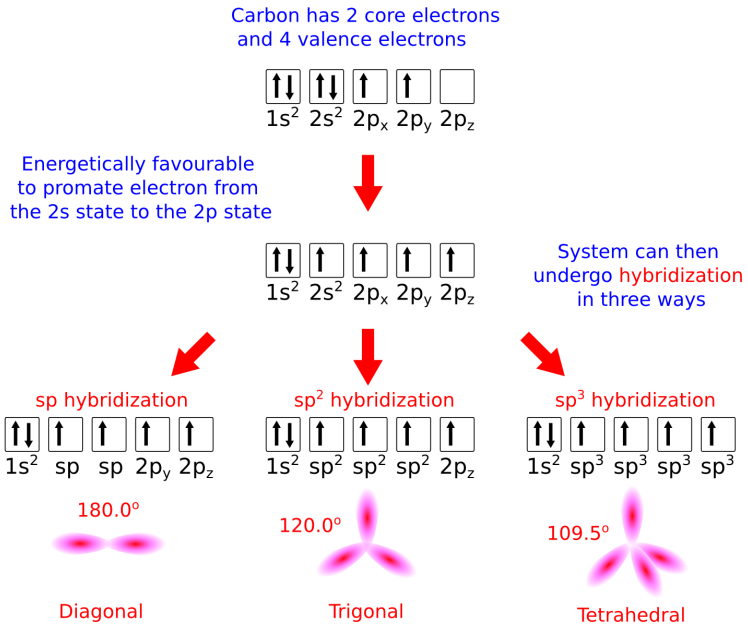

Figure 2-1: Carbon can undergo three types of hybridization allowing it to form a vast array of different types of molecules and compounds.

makes carbon special is that through just a small excitation an electron in the 2s subshell can be promoted into the 2p subshell. This is energetically favourable as all four orbitals become exactly half full and can be used to form strong covalent bonds, which therefore reduces the overall energy.

The valence orbitals are able to hybridize in three different ways either by, sp hybridization, sp^3 hybridization, or sp^2 hybridization, as shown in figure 2-1. Firstly, in sp hybridization a 2s orbital and one of the 2p orbitals hybridize to form two sp orbitals. The carbon forms two covalent sigma, σ, bonds which gives a bond angle of 180° with diagonal symmetry. The two remaining electrons in the $2p_y$ and $2p_z$ orbital form pi, π, orbitals perpendicular to the σ bonds. When two sp hybridized carbons are brought together the π orbitals surround the σ bond and form a triple bond. This occurs in the alkyne family of hydrocarbons.

Next, in sp^3 hybridization all four orbitals can hybridize to form four new orbitals which are all equivalent. This occurs in diamond where each carbon forms four identical covalent bonds to neighbouring carbons. As each bond is equivalent a tetrahedral structure is formed with a bond angle of 109.5°. The four covalent σ bonds give rise to diamonds strong and rigid structure. As each valence electron is in a σ orbital it is tightly bound within the bond, forcing all the electrons to be localized to an atom, and thus making diamond electrically insulating. The antibonding state $\sigma^\star$ is at such a high energy above σ that

electrons are not readily excited into it and so it is not possible for photons to be absorbed and is why diamond is transparent. Any colouring that does occur in diamond is due to presence of impurities absorbed as the diamond was formed.

Lastly, in sp^2 hybridization the 2s and two 2p orbitals hybridize to form three sp^2 orbitals. This enables the carbon to form three covalent σ bonds, separated by a bond angle of 120° with a trigonal symmetry. The fourth electron in the p_z orbital does not take part in the sp^2 hybridization. Instead it forms a delocalized π bond that has a figure of eight-like orbital in the plane perpendicular to that of the three σ bonds. Graphene, graphite and carbon nanotubes are all sp^2 hybridized. The delocalized π electron is responsible for giving these materials many of their interesting characteristics. The ability for the π electron to move freely between carbon atoms gives rise to a high electrical conductivity. The antibonding $\pi^\star$ state is at an energy very close to that of the π state which means the π electrons can readily absorb photons, making graphite black. The exact nature of the π bands formed in graphite will be covered in detail in the next section.

2.1.2 Allotropes of Carbon

Carbon is unique in its ability to form a complete range of dimensionally different allotropes. Due to carbons ability to hybridize it is possible to form nano-sized balls (0D), long thin tubes (1D), single layers (2D) and crystals (3D), all of which are stable structures, figure 2-2. A short description of each of these is now given:

0D Buckyballs Buckminster fullerenes are spherical particles formed of 60 carbon atoms, C60, arranged in a truncated icosahedral structure, like a football, of twenty hexagons and twelve pentagons with a diameter of 0.7 nm [20]. They were discovered in 1985 by Robert Curl, Harold Kroto and Richard Smalley who were awarded the Nobel Prize in Chemistry in 1996. The Buckyball is sp^2 hybridized however due to the curvature of the surface the bond angles are not exactly 120° and it is actually $sp^{2.3}$ hybridized [21]. Buckyballs caused much initial excitement and interest immediately after their discovery with many ideas for potential applications in electronics, chemistry and medicine. The development for applications has been held back by the cost of production. However the recent reduction of this cost, to around £150/g, has led to the use of fullerenes gaining momentum in the medical industry as a drug delivery system [22].

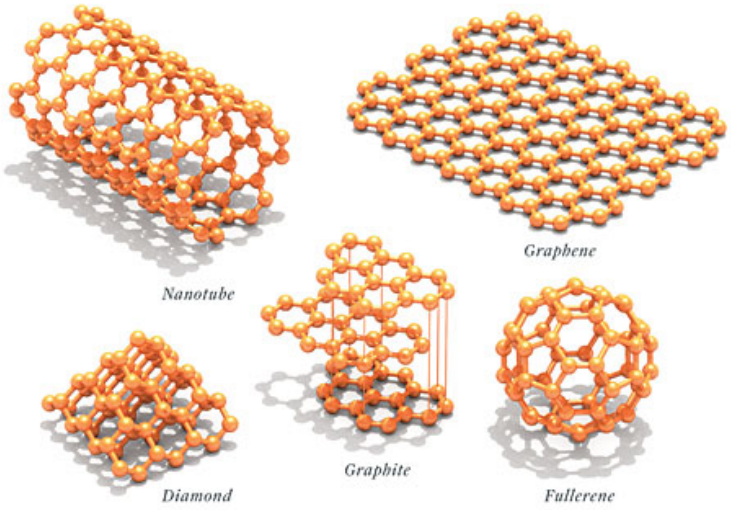

Figure 2-2: Five of carbons allotropes. The 0D fullerene, 1D nanotube, 2D graphene and 3D graphite are all sp^2 hybridized while diamond is sp^3 hybridized. Figure reproduced from [19].

1D Nanotubes Carbon Nanotubes can be thought of as a tightly rolled up graphene sheet that forms a hollow tube. Typically a nanotube will have a diameter of around 1 nm, and can have lengths of up to 18 cm [23] (although more common lengths are of the order 100 μm). The chirality of the nanotube, conceptually the angle at which a graphene sheet has been rolled, determines the nanotubes electronic properties such as whether it is semiconducting or metallic. Nanotubes can be either just one carbon layer thick, single wall nanotubes (SWNTs), or have multiple concentric layers, multi-wall nanotubes (MWNTs). Undoubtedly nanotubes have made a huge impact to the nanoscience world with demonstrated applications in transistors [24], oscillators [25] and super tough fibres [26] to name but a few. It is interesting that no Nobel prize has yet been awarded for the discovery of nanotubes but this could be due to the contention over who actually discovered them. However, Sumio Iijima is generally given the credit for bringing nanotubes to the scientific communities attention with his paper in 1991 [27], in which he observed and imaged MWNTs and then two years later he also synthesized SWNTs [28]. Nanotubes cost vary from just £60/g for an assortment of nanotubes[1] to £410,000/g for purely semiconducting or metallic SWNTs.[2]

[1]Quote from www.nanoamor.com
[2]Quote from www.sigmaaldrich.com

2D Graphene Graphene is single layer, one atom thick, two dimensional array of carbon hexagons. In 2004 Andre Geim and Konstantin Novoselov were able to successfully isolate single graphene flakes on an SiO_2 substrate using just a simple mechanical cleavage technique involving scotch tape [5]; remarkable considering graphene had been predicted to be thermodynamically unstable and therefore unattainable [29]. Their discovery led to a 'graphene explosion' as its unrivalled mechanical, electrical and thermal properties emerged, all of which originate from its sp^2 hybridization. They were awarded the Nobel Prize just six years later in 2010 for 'groundbreaking experiments regarding the two-dimensional material graphene'. Graphene has been touted as the new silicon, however two key hurdles stand in the way namely, large scale production and the lack of a band-gap to allow the graphene to be turned off [6]. These are two very different problems; large scale production requires the ability to have a bottom up approach of growing defect free graphene which is technically extremely difficult, although some headway has been made with companies like IBM recently achieving wafer sized epitaxial graphene on SiC [30]. The other problem of switching graphene on and off, so as to make high gain transistors, is an intrinsic problem arising from the lack of a band-gap in graphene's band structure. However this could be solved through bilayer graphene which is discussed in the following sections [31]. Currently purchasing a single gram of free standing graphene would cost in the region of £2.5 billion, although this would be enough to cover an area equivalent to ten tennis courts.

3D Diamond Diamond has been known to humans for thousands of years, as far back as Ancient India where it was used for religious icons and jewellery. Diamonds form at high temperature and pressures deep underground where the carbon is able to sp^3 hybridize. As already mentioned the sp^3 hybridization leads to exceptional hardness and thermal conductivity but low electrical conductivity [32]. A naturally occurring 5 carat (1 gram) diamond costs in the region of £100,000.

3D Graphite Graphite has also been known to humans for thousands of years with the Ancient Greeks having used it in pencils just like we do today. Graphite is built up from many stacked layers of graphene planes each slightly offset from the plane below. This is called a lamellar structure and the most simple stacking scheme is the Bernal AB stacking. The layers are loosely bound together through Van der Waals interactions from the p_z

electron in the π orbital [33]. This is why layers of graphite can be easily sheared off. Graphite is also highly valued in industry applications as a dry lubricant for the same reasons [32]. Other uses of graphite include conductive fillers [34], battery electrodes [35] and in nuclear fission reactors [36]. The lamellar structure means that graphite is highly anisotropic with very different properties across its planes than perpendicular to them, for instance the electrical conductivity is 3000 thousand times greater in the plane than across the plane [35]. The anisotropy will be a central feature to our explanation of the sharp NDR we observe in graphite-silicone composites. Solid blocks of highly ordered pyrolytic graphite (HOPG) graphite cost around £1,000/g.[3].

So why is it that the discovery of each new carbon allotrope, the buckyball, 1985, nanotubes, 1991 and graphene, 2004, has generated such huge excitement in the scientific community; opening up whole new areas and applications in physics?

The answer all lies with carbons ability to sp^2 hybridize forming a strongly bound lattice whilst leaving one free electron per carbon atom in the p_z orbital that can become delocalized. Collectively the delocalized electrons form the valence and conduction energy bands where they have high mobility and give rise to the unique and fascinating properties seen in these carbon structures.

2.2 Band Structure: Graphite to Graphene

A band structure arises when a large number of atoms, each with its own discrete energy levels, are brought close together. The outer electrons interfere with surrounding atoms which causes the discrete energy levels to broaden into a continuum, forming bands. Thus the band structure describes the range of energies that an electron may have and the forbidden energies, band-gaps, it cannot have.

The band structure tells us the relationship between the valence band, the highest filled energy band, and the conduction band, the lowest unfilled available energy band. When electrons move into the conduction band they are not bound to a specific atom and as a result are mobile and responsible for conduction. Therefore in metals, where the valence band overlaps the conduction band, electrons are readily able to conduct, which is why metals have high conductivities. Conversely, for an insulator there is a large a band-gap leading to very low

[3]Quote from www.2spi.com

electrical conductivities.

Semiconductors have a small band-gap, typically < 4 eV. Electrons can be excited through the band gap allowing the semiconductor to conduct under certain conditions. The Fermi energy, ε_f, gives the energy up to which the highest electron state is likely to be occupied. The Fermi energy can be shifted through applying electric potentials and when it is raised up into the conduction band, the semiconductor can readily conduct.

The next thing to consider is that for a crystalline solid the band structure will depend on the spatial distribution of the atoms in the crystalline lattice. To describe this dependence we use the Brillouin zone which is the primitive cell in reciprocal space. The Brillouin zone has points of high symmetry and it is around these points that all the interesting physics takes place [37].

Clearly the exact crystalline structure is very important in determining the band structure. One method that can be used to calculate the band structure in a crystal lattice is the tight binding model. It combines the solution for a single electron system and maps this onto a crystalline structure found from the unit cell and the corresponding lattice transformations from the translation symmetry. The solution for the total energy is a matrix of terms, the Hamiltonian, which can be used to find the band structure around the Brillouin zone. Using the tight binding model we will show that: graphite is a semi-metal with a 150 meV overlap between the conduction and valence bands [33]; graphene is a zero band-gap semiconductor and has charge carriers that mimic relativistic particles with zero rest mass [38]; and bilayer graphene can be influenced through a transverse electric field to have a finite band-gap [7].

2.2.1 3D Model of Graphite

The most widely used model for calculating the band structure of 3D graphite is the Slonczewski-Weiss-McClure (SWMC) model developed in 1957-1958 [39, 40]. It uses the tight-binding model from a 2D graphite approximation, developed by Wallace [41] in 1947, and adds a perturbation calculation to take into account the interactions between layers. The solutions can be then be found from a parametrized fourth order equation using various techniques or experimental values. This makes the model popular amongst experimentalists as the parameters have physical origins and can be validated experimentally. The model has been shown to work well in calculating the band structure around the edges of the Brillouin zone, H-K, close to the Fermi level, which is where the interesting physics

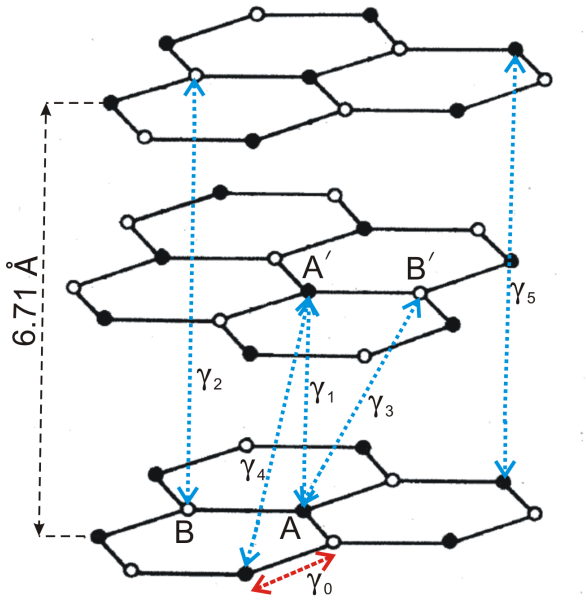

Figure 2-3: Graphite with an AB stacking structure has four atoms per unit cell. The atoms A and A′ have neighbours directly above and below. Atoms B and B′ are directly above and below the centers of a hexagon. The atoms that lie directly above or below are 6.71 Å, two layers, away. The parameters $\gamma_0, \gamma_1, \gamma_2, \gamma_3, \gamma_4, \gamma_5$ for the SWMC model are shown. Figure adapted from [42].

occurs. The presence of many interacting layers alters the band structure so that the conduction and valence band overlap making graphite a semi-metal. Other methods can be used to describe the band structure right across the Brillouin zone however these tend not to be so accurate.

As discussed previously, graphite is built up from stacking layers of hexagonal graphene on top of each other in an AB stacking structure. This gives graphite a hexagonal unit cell that contains four atoms. We label these atoms A, A′ and B, B′ as they are inequivalent, labelled in figure 2-3. Atoms A and A′ have neighbours directly above and below them, 3.35 Å away. Whereas B and B′ lie directly above and below centers of the hexagons in neighbouring layers. The next atoms directly above or below B and B′ are 6.71 Å, two layers, away. The non-equivalence of atoms A and B is important as it leads to some interesting features in the Fermi surface.

The difference between the carbon atoms A and B has a subtle effect on the band structure and properties of graphite. The coupling between these atoms lowers the symmetry of the system so that it has a three fold symmetry which leads to a trigonal warping of the Fermi surface.

The first Brillouin zone of graphite is shown in figure 2-4(a). It is a hexagonal

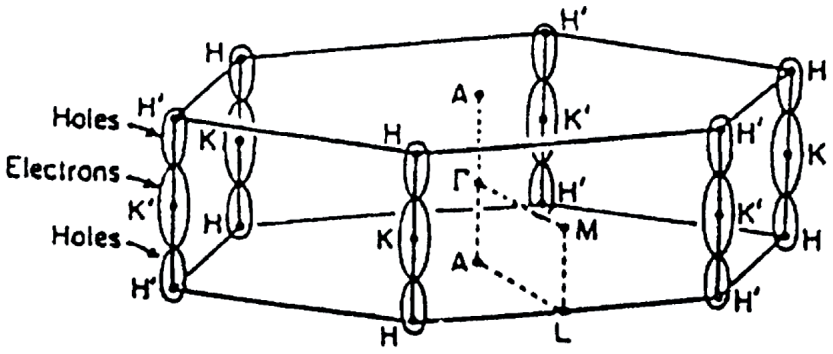

Figure 2-4: The first Brillouin zone for graphite is a hexagonal prism with height $\frac{2\pi}{c}$. The points of high symmetry are the center Γ, corners H and H$'$, centers of the top and bottom faces A, centers of the side faces M, centers of the of sides edges K and K$'$ and the centers of edges of the top and bottom faces L. Figure reproduced from [43].

prism with height $\frac{2\pi}{c}$. This is not the true Brillouin zone, which should have a height of $\frac{4\pi}{c}$, however it is the one originally adopted by McClure and has become the conventional Brillouin zone to use. The points of high symmetry are the center Γ, corners H and H$'$, centers of the top and bottom faces A, centers of the side faces M, centers of the of sides edges K and K$'$ and the centers of edges of the top and bottom faces L [40].

Slonczewski, Weiss and McClure used perturbation theory to calculate the band structure of graphite taking into account the effects of interactions between the layers [39]. The SWMC model calculates the band structure and Fermi surface in the region of the H-K-H axis. The seven independent band parameters it uses are $\gamma_0, \gamma_1, \gamma_2, \gamma_3, \gamma_4, \gamma_5, \Delta$. The first six define the interaction energies, in eV, between the atoms in the unit cell, as shown in figure 2-3. While Δ gives the energy shift between atoms A and B arising from the offset stacking. If the exact values of these seven parameters are known, it is possible to calculate the energy bands near the H-K-H axis and completely determine the Fermi surface.

γ_0	γ_1	γ_2	γ_3	γ_4	γ_5	Δ	ε_F
3.16	0.39	-0.02	0.315	0.044	0.038	0.008	-0.024
3.12	0.377	-0.020	0.29	0.120	0.0125	0.004	-0.0206

Table 2.1: Parameter values for the SWMC model. Top row from Brandt *et al.* [44] and bottom row from a more recent review by Chung [33].

The calculation can be expressed in the form of the following Hamiltonian,[4]

$$\hat{H} = \begin{pmatrix} E_1 & 0 & H_{13} & H_{13}^* \\ 0 & E_2 & H_{23} & -H_{23}^* \\ H_{13}^* & H_{23}^* & E_3 & H_{33} \\ H_{13} & -H_{23} & H_{33}^* & E_3 \end{pmatrix}, \tag{2.1}$$

where,

$$\begin{aligned} E_1 &= \Delta + \gamma_1\Gamma + \frac{1}{2}\gamma_5\Gamma^2 & H_{13} &= \frac{-\gamma_0(1-\upsilon)\sigma e^{i\alpha}}{\sqrt{2}} \\ E_2 &= \Delta - \gamma_1\Gamma + \frac{1}{2}\gamma_5\Gamma^2 & H_{23} &= \frac{\gamma_0(1+\upsilon)\sigma e^{i\alpha}}{\sqrt{2}} \\ E_3 &= \frac{1}{2}\gamma_2\Gamma^2 & H_{33} &= \gamma_3\Gamma\sigma e^{i\alpha} \\ \Gamma &= 2\cos\pi\xi & \upsilon &= \frac{\gamma_4\Gamma}{\gamma_0} \end{aligned} \tag{2.2}$$

The accepted values of the parameters have been found through a mixture of experiment and theory and have been revised many times over the years as experimental techniques have become more accurate with terms such as γ_2 even changing sign during the 1970's [44]. The most recent accepted values are shown in the bottom row of table 2.1. The physical meaning of each SWMC parameter and what effect it has on determining the band structure is as follows.

γ_0 The interaction between nearest neighbours, atom A to atom B. This is the only band parameter that describes an interaction in the plane and also has the largest magnitude of 3.12 eV as the interactions are much greater in the plane. All the other parameters are out of the plane and of lesser energy.

γ_1 Nearest neighbour interaction between atoms of type A. These are in neighbouring layers placed one under the other, i.e A to A′. This parameter determines the width of the π bands at the K points on the Brillouin zone, equal to $4\gamma_1$ [44].

[4]For the complete derivation refer to Brandt *et al.*;[44] or Charlier and Charlier [45]

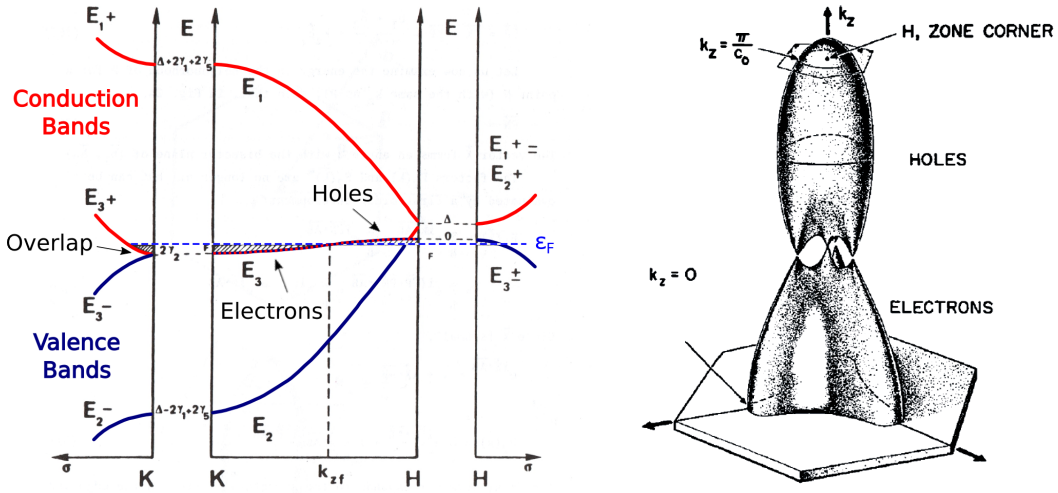

(a) (b)

Figure 2-5: (a) The band structure of graphite from K to H. The bands overlap around the Fermi level by 0.03 eV. Carrier pockets are created along the H-K-H axis where the doubly degenerate E_3 states lie close to ε_F, which creates a complex Fermi surface [45]. (b) The Fermi surface for graphite at the corners of the Brillouin zone centered around the H-K-H axis. All the free carriers are located along the zone edges, giving rise to slender Fermi surfaces. The γ_3 parameter leads to a trigonal anisotropy which is exaggerated here for clarity. Figures adapted from [45] and [33].

γ_2 Nearest neighbour interaction between atoms of type B, i.e B to B′. This is one of the most significant parameters as it determines the coupling between the π and σ bands and the magnitude of the overlap between π bands, which is equal to $2|\gamma_2|$ [44].

γ_3 The interaction between A and B′. The presence of such coupling lowers the symmetry of the interaction Hamiltonian. This leads to trigonal warping in the Fermi surface around K.

γ_4 The interaction between like atoms not directly above one another. This interaction gives rise to non-mirror like characteristics of the valence and conduction bands [46].

γ_5 The interaction between two A atoms separated by a layer.

Δ This is the energy shift due to the non equivalence of A and B. It is the direct measure of the potential energy difference between atom sites A and B [33].

There are four valence electrons in each carbon atom in graphite and four atoms per unit cell. Therefore the band structure will have sixteen bands, with

twelve σ bands and four π bands. Of the twelve σ bands six are bonding and the other six are antibonding with a higher energy. The separation between the bonding and antibonding groups is large, approximately 5 eV and therefore does not interest us here.

The π bands can be found between these two groups. Likewise there are two bonding π bands and two antibonding $\pi^\star$ bands which are strongly coupled. There are four electrons to fill the bands but not more than two electrons can sit in each band due to the Pauli exclusion principle. The Fermi level will thus lie in the middle of the four π bands.

The Hamiltonian in equation 2.1 can be solved to find the band structure close to the H-K-H axis of the Brillouin zone and can be seen in figure 2-5(a). The two bonding π bands are labelled as E_2^- and E_3^- and the antibonding $\pi^\star$ bands as E_1^+ and E_3^+. At the K points the E_3^- and E_3^+ bands overlap making a doubly degenerate band, E_3^0 which contains four states. The overlap is by 0.03 eV making graphite a semi-metal. The importance of the parameters Δ, γ_1 and γ_2 can be easily seen by examining the solution for the Hamiltonian only around K and around H using the equations in 2.2:

K	H
$k_z = 0 \implies \xi = k_z c_0/2\pi = 0$	$k_z = \pi/c \implies \xi = k_z c_0/2\pi = 1/2$
$\Gamma = 2\cos\pi\xi = 2$	$\Gamma = 2\cos\pi\xi = 0$
$E_1 = \Delta + 2\gamma_1 + 2\gamma_5$	$E_1 = \Delta$
$E_2 = \Delta - 2\gamma_1 + 2\gamma_5$	$E_2 = \Delta$
$E_3 = 2\gamma_2$	$E_3 = 0$

It can be seen that the width of the π bands at K, between E_2^- and E_1^+, is $4\gamma_1$. The Δ parameter at H stops all the bands becoming degenerate. The energy at the overlap of the doubly degenerate state E_3 is $2\gamma_2$. Referring back to table 2.1 we can see that the $2\gamma_2$ = -0.04 eV while $\varepsilon_F = -0.0206$ eV so at K E_3 lies below the Fermi energy by 0.02 eV. At H we find $E_3 = 0$ which is 0.02 eV above ε_F.

Therefore the degenerate band, E_3^0, moves from being below the Fermi energy at K to above the Fermi energy at H. The point where the change of sign occurs is labelled k_{zf}. Between K and k_{zf} all the E_3^0 states are filled with electrons while between k_{zf} and H the states are occupied by holes. The means that the charge carriers are localized in electron and hole pockets. However this is only a 2D cross section and if we then consider the third axis we can construct a Fermi surface as shown in figure 2-5(b). The Fermi surface clearly shows the electron and hole

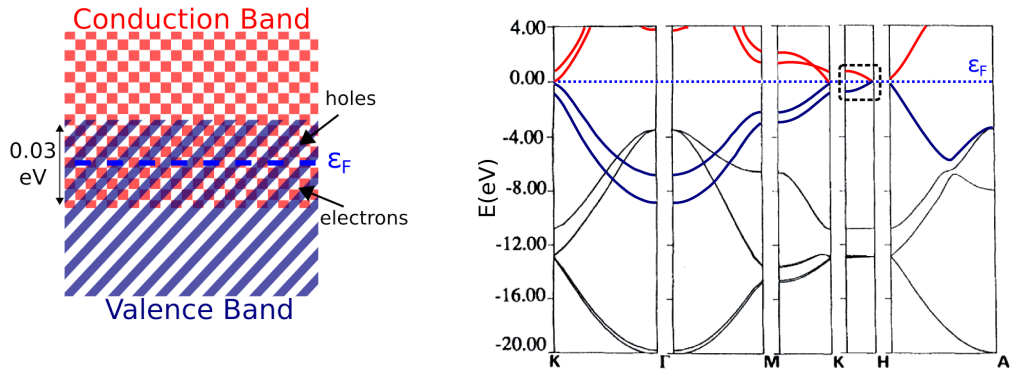

(a) (b)

Figure 2-6: (a) A schematic of the band structure of graphite to show that the valence and conduction band overlap by 0.03 eV around the Fermi level making graphite a semi-metal. (b) The complete band structure of graphite around the Brillouin zone. The red lines show the conduction bands and the blue lines are the valence bands. The black box indicates the section of the band structure found using the SWMC model. Figure adapted from [43].

pockets as we move from K to H, up the k_z axis. The Fermi surface is slender as it extends less than 1% of the distance from K, the zone edge, to Γ, the zone centre [33].

In the construction of the Fermi surface there is a $\gamma_3 \cos\alpha$ term, where α describes an angle on the plane that is perpendicular to k_z [45]. This leads to an interesting feature on the Fermi surface around K whereby the electron pockets have a trigonal warping, unlike the holes which remain cylindrical near H. Furthermore the pockets are connected by four legs, three legs lie off the H-K-H axis and one leg which lies along the H-K-H axis [33]. The legs connect at k_{zf} and at the Fermi energy.

To summarize, graphite is a semi-metal due to the overlap of the conduction and valence bands , shown in figure 2-6(a), of 0.03 eV. For reference the complete band structure is shown in figure 2-6(b). The box indicates the K-H region, found using the SWMC model. The significance of the parameters in the model has been shown such as; the band overlap due to γ_2; the on-site energy term Δ which stops the valence and conduction bands becoming entirely degenerate at H; and γ_3 which leads to trigonal warping in the Fermi surface for the electron pockets. The importance of these parameters will become apparent when we next consider the band structure of graphene and bilayer graphene.

2.2.2 Graphene's Band Structure

When Wallace in 1947 worked on calculating the band structure of graphite he started by first considering a single 2D graphite layer, graphene [41]. This was a sensible approach as graphite layers are only weakly bound together through Van der Waals interactions. Wallace was able to demonstrate, with the use of a nearest neighbour tight binding model, an analytical expression for the band structure of the π bands of graphene [41, 47].

Amazingly Wallace's analytical expression predicted that graphene would be a zero band-gap semiconductor with the valence and conduction bands exactly touching at the Fermi energy at the corners, K and K' of the hexagonal Brillouin zone. With most importantly, a linear dispersion between the energy and wave vector $\mathbf{k}$.

The significance of the linear dispersion with regard to massless Dirac fermions was only understood some 40 years later by Semenoff in 1984 [48]. Graphene became a toy model for theoreticians interested in (2+1) dimensional quantum electronics to play with [6]. However theoreticians also predicted that 2D crystals were an impossibility as they would be thermodynamically unstable [29, 49]. Thus despite some attempts to isolate graphene through different physical and chemical methods, including intercalation, it was generally expected that graphene would just remain a theoreticians toy model [47, 50, 51].

Therefore in 2004 the discovery of single layer graphene flakes by Konstantin Novoselov and Andre Geim, in their own words, "flaunted common wisdom by experimental discovery". They used scotch tape to mechanically exfoliate thin layers of graphite from a HOPG block and repeated the process on the exfoliated layers over and over until they were left with just single layer graphene flakes. The flakes were then transferred to a SiO_2 substrate. Part of the success of their discovery lies in their realization that single layers were visible under an optical microscope if the SiO_2 substrate had a thickness of 300 nm. Successive papers in 2004, 2005 and 2007 showed that graphene did indeed have the properties of a material with massless Dirac fermions arising from the linear E-$\mathbf{k}$ dispersion [5, 6, 38].

The complete band structure for graphene around the Brillouin zone can be seen in figure 2-7(a). Methods for calculating this can be found in either the original Wallace and Slonczewski papers or Castro's more recent review [39, 41, 52].

The valence and conduction band exactly touch at the Fermi level, the Dirac

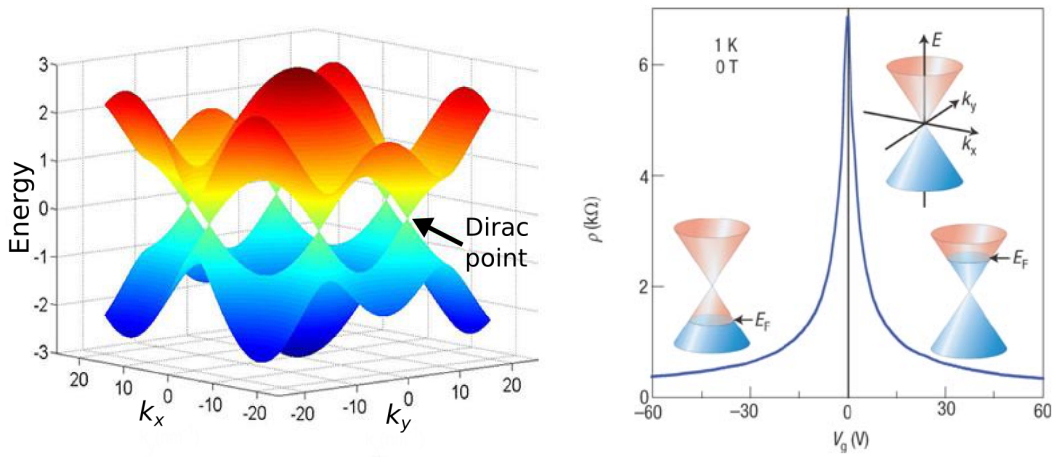

(a) (b)

Figure 2-7: (a) The valence and conduction bands around the Brillouin zone for graphene. The bands exactly meet at the Dirac point. Close to the Dirac points the bands have a linear dependence between E and **k**. (b) Ambipolar electric field effect in graphene. The Fermi energy is shifted using a gate voltage, V_G, leading to a symmetrical resistivity around $V_G = 0$. The resistivity, ρ, has a maximum of 6.4532 kΩ that occurs when the Fermi energy is at the Dirac point. Figure reproduced from [6].

point. This makes graphene a zero band-gap semiconductor. If we now examine the band structure more closely around the Fermi energy, at low energies we see that there is a linear dispersion between E and **k**, figure 2-7(b) center-inset, with:

$$E_k = v_F|\mathbf{k}|, \tag{2.3}$$

where **k** is the wave-number and v_F is the Fermi velocity. The linear dispersion between E and **k** is characteristic of massless particles and implies that graphene has charge carriers that have an effective rest mass of zero. This means that the charge carriers mimic relativistic particles and thus the Dirac equation can be employed to describe them.

The electrons are not moving at relativistic speeds, but the way in which they interact with the periodic potential of graphene's honeycomb lattice gives rise to quasi particles that are best described by the relativistic Dirac equation where $v_F = 10^6$ ms^{-1} is substituted for c [6].

The valence and conduction bands exactly touch at the critical Dirac point. The Fermi level intrinsically sits at this point. However in fabricating devices a gate voltage, V_G, can be used to apply a potential that shifts the Fermi level up or down. Due to the symmetry of the system graphene exhibits an ambipolar

electric field effect, figure 2-7(b). This means that shifting the gate voltage to a negative or positive value gives the same change in resistivity. The charge carriers can be tuned continuously between electrons and holes in concentration as high as 10^{13} cm^2 and with mobilities in excess of 150,000 cm^{2}Vs^{-1} at room temperature [6].

Another fascinating feature of graphene is that when $V_G = 0$ the Fermi energy is at the Dirac point but the conductivity does not tend to zero, as it would in a semiconductor, instead its tends to a minimum conductivity value that is the same for all samples, regardless of size. It tends to multiple of a conductivity quantum, $4e^2/h$, which gives a maximum resistance, or resistivity as it is size independent, of 6.4532 kΩ. Further it is is temperature independent from 100 K to 10 K. The maximum resistivity can be seen in 2-7(b) when $V_G = 0$.

The minimum conductivity is a double edge sword. On the one hand it is fascinating and exciting for physics as it is a direct consequence of the massless Dirac fermions which leads to many other interesting physics including graphene's room temperature integer quantum hall effect [53].

However for those wishing to utilize graphene's high mobility for use in devices such as transistors it becomes a major obstacle. The minimum conductivity means that graphene's electrical conduction cannot be turned off. Thus in making graphene transistors the on-off ratio will always low, with ratios only of the order 30 [5].

For bilayer graphene the presence of the additional layer enables a change in the band structure such that instead of a Dirac point and a minimum conductivity, it is possible to induce a band-gap through the use of a transverse electric field across the layers. This then allows for significantly higher on-off ratios.

2.2.3 Bilayer Graphene

Graphite posses an overlap between its valence and conduction bands around the K-H axis, making it a semi-metal. While graphene has valence and conduction bands that are exactly degenerate at the K point and linear at low energies close to the K point, thus making graphene a zero band-gap semiconductor.

Clearly the interactions between many stacked graphene layers leads to a dramatic change in the band structure from just a single layer. What happens when there is just one additional layer, bilayer graphene, has been a topic of intense research for the last five years [7].

It has been shown that bilayer graphene is a zero band-gap semiconductor,

without the linear dispersion of graphene, and in the presence of an electric field across the layers a band-gap is opened up [54]. Thus making bilayer graphene a tunable band-gap semiconductor with a band-gap that is approximately proportional to the difference in potential across the layers.

Edward McCann can be considered the pioneering theoretician with regard to bilayer graphene. He predicted that it would be able to exhibit a *tunable band-gap* between the conduction and valence bands in 2006 [54]. He described the use of a parametrized tight binding model, similar to the one used earlier for graphite, to describe the band structure of bilayer graphene as the gap is opened up [55, 31]. This will be summarized next before going on to briefly summarise some of the impressive experimental work undertaken to fabricate bilayer graphene devices and measure this tunable band-gap.

In a similar way to the structure of graphite shown in figure 2-3, bilayer graphene has two coupled hexagonal lattices arranged according to Bernal stacking AB. The unit cell contains 4 atoms on inequivalent sites A, B, A$'$, B$'$ with A and B on the lower layer and A$'$, B$'$ on the top layer. The A, A$'$ atoms lie directly on top of one another while A$'$ lies below the center of a hexagon of the upper layer and B$'$ lies above the centre of a hexagon from the lower layer.

The tight binding model is used to calculate the band structure using a SWMC parametrization, as before for graphite. Clearly not all seven parameters will be required as there are only two layers, with less interaction, therefore for bilayer graphene we can define [55]:

γ_0 The in-plane nearest neighbour interaction.

γ_1 The strongest inter-layer interaction between A and A$'$, atoms that lie directly above and below one another.

γ_3 The weak inter-layer coupling between A and B$'$ (or B and A$'$). This term gives rise to trigonal warping however it does not have a major significance in the opening of the band-gap and therefore for a first approximation it is often set to zero.

Δ The on-site energy difference between the lower and upper layer, which we define as ε_1 and ε_2 with $\Delta = \varepsilon_2 - \varepsilon_1$ where $\varepsilon_2 = \frac{1}{2}\Delta$ and $\varepsilon_1 = -\frac{1}{2}\Delta$.

The Hamiltonian that describes the four π bands is as follows [55]:

$$\hat{H} = K_v \begin{pmatrix} -\frac{1}{2}\Delta & H_3 & 0 & H_0^\dagger \\ H_3^\dagger & \frac{1}{2}\Delta & H_0 & 0 \\ 0 & H_0^\dagger & \frac{1}{2}\Delta & H_1 \\ H_0 & 0 & H_1 & -\frac{1}{2}\Delta \end{pmatrix} \tag{2.4}$$

with,

$$\begin{aligned} H_0 &= \sqrt{3/2}\frac{a\gamma_0}{\hbar}(p_x + ip_y), \\ H_1 &= K_v\gamma_1, \\ H_3 &= \sqrt{3/2}\frac{a\gamma_3}{\hbar}(p_x + ip_y), \end{aligned} \tag{2.5}$$

where $H^\dagger$ denotes the Hermitian conjugate of H, $p = (p_x, p_y) = \hbar|\mathbf{k}|$ is the momentum with respect to the K point and $K_v = +1(-1)$ labels valley K ($\tilde{K}$). To simplify, we take $\gamma_3 = 0$ as this term has little effect on the size of the band-gap opened up. This allows us to write the equation that describes all four π bands as,

$$E_\alpha^\pm \approx \sqrt{\frac{\gamma_1^2}{2} + \frac{\Delta^2}{4} + v^2p^2 + (-1)^\alpha\sqrt{\frac{\gamma_1^4}{4} + v^2p^2(\gamma_1^2 + \Delta^2)}}, \tag{2.6}$$

where $\alpha = 1, 2$ and $v = \sqrt{3/2}\frac{a\gamma_0}{\hbar}$. Exactly at the K point $p = 0$ and so we can further simplify,

$$E_1^\pm = \pm\frac{|\Delta|}{2}, \tag{2.7}$$

and,

$$E_2^\pm = \pm\sqrt{\gamma_1^2 + \frac{\Delta^2}{4}}. \tag{2.8}$$

The band structure of equation 2.6 is shown in figure 2-8(a) for $\Delta = 0$. As can be seen from equations 2.7 and 2.8, the $E_1^\pm$ bands are degenerate at the K point, where they exactly touch, $\Delta = 0$. The $E_2^\pm$ bands do not touch at the K point and instead are separated by an energy γ_1, the split due to the inter layer coupling. The band dispersions are not linear and thus the effective mass, unlike graphene, is non zero. The effective mass is light with $m^\star = \frac{\gamma_1}{2v^2} \approx 0.054m_e$ [55].

When we apply a potential across the layers such that $\Delta \neq 0$. The $E_1^\pm$ bands no longer touch at the K point, instead they are separated by an energy gap, Δ, thus Δ is not just the difference in on-site energies it is also equal to the size of

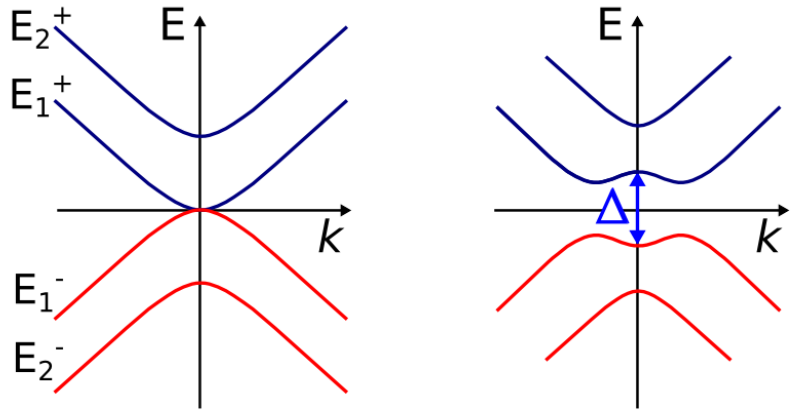

(a) (b)

Figure 2-8: (a) The band structure of bilayer graphene close to the K point for $\Delta = 0$. The $E_1^{\pm}$ bands are degenerate at the K point, while $E_2^{\pm}$ are separated by γ_1. (b) The band structure for bilayer graphene when a potential has been applied across the layer and $\Delta \neq 0$. The $E_1^{\pm}$ bands are now separated by Δ at the K point.

the *induced band-gap*. The higher bands $E_2^{\pm}$ will still be separated predominately by γ_1 with just a small contribution from Δ. This is plotted figure 2-8(b). At large values of Δ, when $\Delta \approx \gamma_1$, a 'Mexican hat' structure begins to form in the $E_1^{\pm}$ bands. The band-gap becomes indirect and puts a maximum on the induced band-gap value of about 400 meV.

Theoretically, it is possible to induce a *band-gap* in bilayer graphene up to a value of 400 meV [55]. When the Fermi level is shifted into the band-gap there is an induced *semi-metal to insulator* transition. Experimentally this can be achieved by using electric fields to break the symmetry between the layers and cause a substantial change in conductivity.

In 2006 Ohta *et al.* used angle-resolved photoemission spectroscopy (ARPES) to demonstrate that through potassium doping of the upper layer of a bilayer graphene it is possible to directly manipulate the size of the band-gap between the valence and conduction band [56]. The use of potassium doping is crude and the size of the field applied through the doping across the layers is of the same order of magnitude as an electric field that could be applied between a top and bottom gate and was the next obvious development.

In 2007 Oostinga *et al.* achieved the formidable task of placing a top gate onto bilayer graphene [57]. They mounted bilayer graphene samples onto a 285 nm SiO_2 layer with p-doped silicon underneath to form the bottom gate. A 15 nm

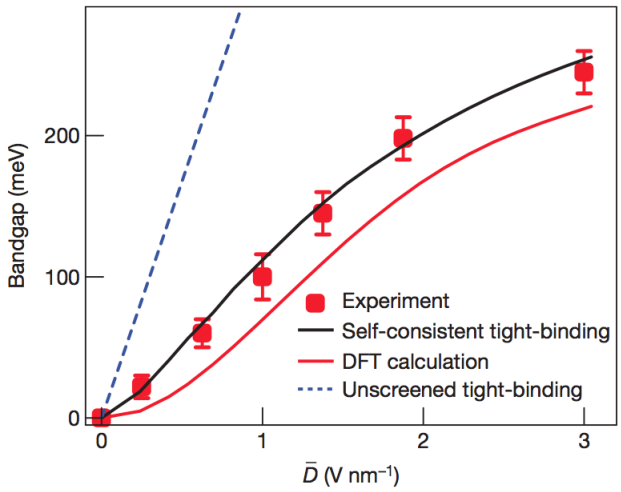

Figure 2-9: Zhang *et al.* were able to use electrical gating to tune a band gap in bilayer graphene up to 250 meV that follows closely the predicted band-gap from the tight-binding model when screening is included. $\bar{D}$ is the electric field across the bilayer. Figure reproduced from [8].

SiO_2 layer, followed by titanium and gold, was patterned on top of the graphene bilayer to form a top gate. The double gated structure allows simultaneous and independent control of the charge density in the system, the effective Fermi level, and the electric field perpendicular to the graphene layers.

Oostinga *et al.* demonstrated that through the use of two gates, a band-gap in bilayer graphene could be induced while at the same time the charge neutrality point (CNP) could be shifted to lie within the band gap, causing the resistance to increase. However the size of band-gap induced was only of the order 10 meV. Which due to thermal activation necessitates temperatures of the order of just a few Kelvin to experimentally measure the induced band-gap.

In 2009, Zhang *et al.* extended the work of Oostinga *et al.* [8]. Zhang *et al.* also used a top and bottom gate to control independently the electronic band-gap and the carrier doping concentrations, the effective Fermi level. The difference is that Zhang *et al.* used infrared spectroscopy to directly measure the band-gap, using optical transitions from the π to the $\pi^\star$ bands. The optical determination of the band-gap is less affected by defects and any external doping effects, than the electrical measurement of the band-gap. They succeeded in measuring a clear band-gap in the bilayer graphene of up to 250 meV induced through an electric field applied across the layers. They further demonstrated that through fine adjustment of the top and bottom gates the band-gap could be tuned between 0 and 250 meV at room temperature [8]. A plot of the band-gap induced as a

function of the applied electrical field $\bar{D}$ is shown in figure 2-9. The tight binding model, derived previously, gives a linear dependence between the field across the bilayer and the size of the induced band-gap and can be seen to be a good first approximation.

2.2.4 Summary

We have seen that bilayer graphene, intrinsically a zero-band semiconductor, can have an induced band-gap that is tunable in the presence of an electric potential *perpendicular* to the layers. There has been a lot of interest regarding bilayer transistors and Zhang *et al.* was able to demonstrate a two atomic layer thick switch. However the interactions between the two layers means that some of the special electrical properties of graphene due to the, massless Dirac fermions, are lost for bilayer graphene where the dispersion is not linear. Thus the exceptionally high mobility seen for a suspend single layer graphene, up to 200,000 $\mathrm{cm^2V^{-1}s^{-1}}$ is an order of magnitude smaller, $\simeq 15,000$ $\mathrm{cm^2V^{-1}s^{-1}}$ in bilayer graphene [58]. The technical challenges involved in creating the double gated structures required are certainly not trivial. However the idea of having a electrically tunable band-gap is still very exciting and may have some applications for novel nanophotonic devices for infrared light generation, amplification and detection [8].

2.3 Graphite Nanoparticles

In the previous section we have considered graphite as a perfect crystalline form of AB stacked graphene planes. In the real world graphite does not always come as this perfectly stacked structure. There are in fact many different forms of graphite and in the literature there is a huge range of terminology that depends on the exact degree of graphitisation and the original source of the graphite, i.e whether it is synthetic or natural. There is also a substantial grey area between the different types and with graphite used in such a huge range of industrial applications it is natural that for different industries to each have their own definitions and terminology. Graphite's industrial uses include: conductive coatings, glass manufacturing, lubricant formation, metallic alloys, nuclear reactors, powder metallurgy, structural materials, steel making, brake linings, zinc-carbon batteries, electric motor brushes and this is to name but a few [32, 34, 35, 36, 37].

For the purposes of simplification all the different types of graphite can be generally split into three categories of increasing levels of crystallinity, amorphous

carbon (AC), pyrolytic carbon (PC) and HOPG.

AC Amorphous carbon does not have any crystalline structure. There is no long range order such as stacking although there may be small clumps of carbon joining together to form small hexagonal segments and thus it is possible to observe some short range order. There will be a range of sp^2 and sp^3 bonding, the ratio of which can be used to characterise the amorphous carbon. Carbon black is a good example of a processed amorphous carbon and it is used extensively as a filler in rubber and in printing [59].

PC Pyrolytic carbon has a good degree of crystalline structure with groups of graphite layers but that have completely random orientations about the layer. This is probably the most broad group as the degree of crystallinity can vary so much. PC can be either: grown through chemical vapor deposition; formed through annealing AC at temperatures between 1,000°C and 2,500°C that restores some long range order; or mined as natural graphite [32].

HOPG Highly oriented pyrolytic graphite has the strictest definition of the three types as it lies close to the ideal graphite crystal with an angular spread between the C-axis of crystallites of less than 1°. It is usually formed through an annealing process of pyrolytic graphite through heating at over 2,700°C whilst under pressures of several atmospheres. This induces further ordering between the planes and stress relieving within each plane. It can also be mined naturally where similar high temperature and high pressure processes have occurred naturally deep underground [32].

Lastly there has recently, with the advent of graphene, become another form available referred to as graphene nano-platelets (GNP). These are normally some form of expanded graphite where a chemical method has been used to break apart the HOPG into small particles that have just 5-20 layers of stacked graphene sheets. In some ways these could still be considered graphite nanoparticles but what sets them aside is their aspect ratio with widths of up to 20 μm but thickness of just 2-10 nm. Providing that the particles do not aggregate they are able to provided unprecedented surface to volume ratios and are being rapidly developed for use in a new generation of supercapacitors for electric cars. The high surface area means that the GNP based supercapacitor can be rapidly charged whilst having a high energy density [60, 61].

2.4 Percolation in Composites

Composites combine two or more materials of differing desirable characteristics to engineer the resulting composite properties for specific applications. Often this involves incorporating a reinforcement filler into a binding matrix. The filler may have the desirable strength, electrical or colour characteristics, while the matrix enables the composite to have the desired shape, flexibility or viscosity to support or bind the filler.

Carbon black, an amorphous carbon, can be used to form many interesting types of composites as it has a range of particle sizes and structures that readily disperses into polymers, resins, plastics and rubbers. Carbon black is a by-product of combustion and being easily available has found applications in a wide variety of industries. For instance carbon black is added to natural rubber to form tyres with better wear characteristics, it is dispersed in printing inks for its dark colour and it is incorporated in high concentrations into polymers to form anti-static coating materials [59].

Due to carbon black being widely used in industry there is a vast amount of literature regarding its composite forms. This enables a detailed discussion of its percolation behaviour and we will use carbon black as an example. Furthermore carbon black composites share many similarities with the composite used in this thesis and therefore it is a good starting point to discussing the expected electrical characteristics. As our interest is in the electrical conduction behaviour of composites when the filler is highly conductive and the matrix is a completely insulating medium that binds the filler. These highly conductive composites are explained with the use of percolation theory.

2.4.1 Percolation Theory

Percolation is a critical concept for the understanding of transport systems in disordered systems [62]. Percolation theory deals with the process of fluid flow in a random media, where the fluid could be water, electrons, or microbes and the media could be coffee granules, atomic structures or human populations. It has been used to successfully describe physical phenomena such as: how a solvent percolates through a solute; electron transport in an atomic lattice; or a disease infecting a community [63]. The pioneers for the mathematical description of percolation processes were Broadbent and Hammersley in the late 1950's [64].

The simplest way to picture a percolation network is to take a regular square lattice and randomly occupy sites with a probability, p. At a critical threshold,

p_c, the first long range connection will occur called the *percolation threshold*. Now, imagine that each occupied sites is a wire with a resistance R and there are two contact points on each side of the lattice, A and B. Below the percolation threshold the total resistance, R_T, will be infinitely large as no current can flow, figure 2-10(a). At the percolation threshold current can first start to flow and the resistance will be at a finite maximum, some multiple of R, figure 2-10(b). As further sites are occupied more paths will be created that are in parallel to each other and therefore lowering R_T, figure 2-10(c). This continues up to a maximum filling fraction, $p = 1$, where R_T will now be less than R.

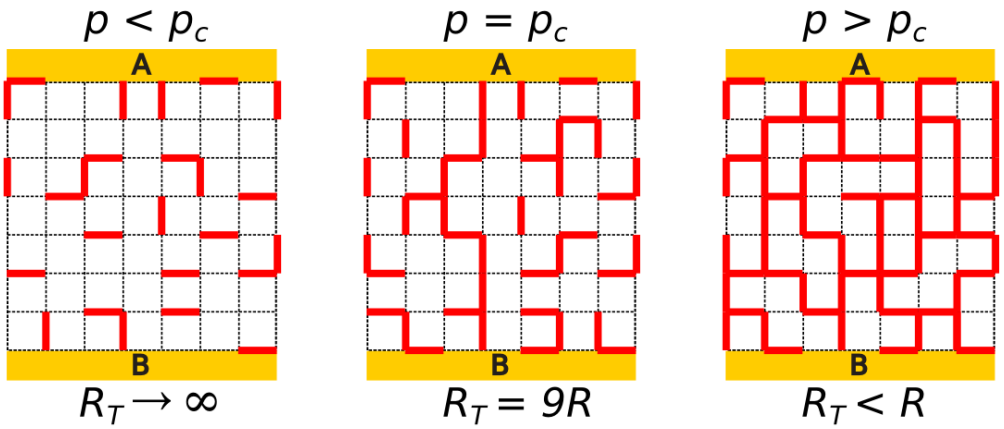

Figure 2-10: As the probability, p, that a site is occupied increases, the total resistance, R_T, decrease from an infinite value for (a) with $p < p_c$; to a finite but large value at (b) with $p = p_c$; and then tends to a value less than R at (c) with $p > p_c$, as parallel conduction paths occur.

2.4.2 Electrical Percolation

It was Kirkpatrick who first formally took the percolation theorems of Broadbent and Hammersley and applied them specifically to the problem of conductive particles in an insulating matrix [65]. In composites we can readily apply percolation theory as the conductive particles have conductances which are many orders of magnitude greater than the insulating matrix. At low filling fractions of filler, p, there are no current paths through the material and the resistance is high, if not infinite. As the conductive particles are added to the matrix at some critical volume filling fraction, which we also call p_c, the material makes a transition from being an insulator to conductor. As further particles are added the resistance quickly decreases. Eventually the matrix is saturated with particles

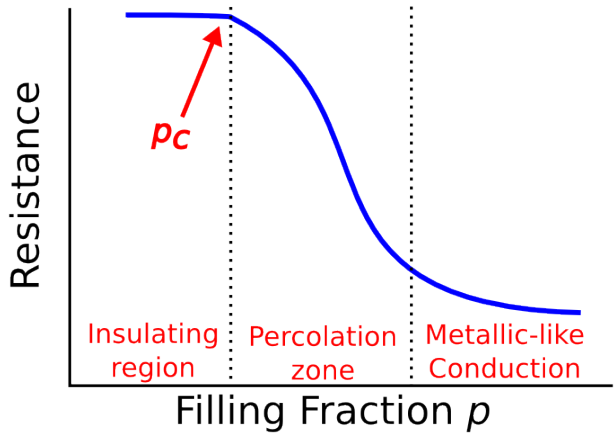

Figure 2-11: As the filling fraction of particles in the composite is increased there is a transition at the critical volume (percolation threshold), p_c, from insulator to conductor. The resistance decreases many orders of magnitude through the percolation zone.

and no more can be added.The conduction becomes almost metallic-like as the resistance tends to a minimum. This evolution is shown in figure 2-11.

Kirkpatrick was specifically interested in the conductance of 2D and 3D resistor networks and at what critical volume fraction they crossed the percolation threshold [65]. His work led to a simple power law dependence that could describe the DC electrical conductivity close to and above the percolation threshold,

$$\sigma \propto (p - p_c)^t, \tag{2.9}$$

where σ is the bulk composite conductivity, p the volume filling fraction of filler to insulating matrix, p_c the critical filling fraction and t the conduction coefficient.

Computational modelling of the process described above yields the universal percolation theory predictions that in a 3D systems $p_c = 0.16$ and $t = 2.0$ [59, 63, 66]. The universal percolation theory is a 'touching' model that assumes that particles have to be in contact to conduct but that when they do there is zero contact resistance between them.

The power law can be tested for real composites by fabricating samples of different amounts of filler into the same amount of matrix and measuring the resistance. It can be shown that t is a function of the system geometry and p_c is a function of particle geometry, dispersion and the nature of the conduction between particles. Thus finding the values of p_c and t enables conclusions to be drawn regarding the nature of the particle dispersions and the percolation processes.

2.4.3 Carbon Black Example

In studying different carbon black composites with varying sizes and geometries of filler incorporated into different insulating mediums it was found, by Balberg, Carmona and many others, that often the expected values of p_c and t did not conform with the calculated values from universal percolation theory [59, 62, 66, 67, 68, 69]. Much work has gone into understanding where the discrepancy arises and interpreting the values of t and p_c with respect to the conduction mechanisms in the composite and the nature of the particle dispersion.

To enable easy comparisons between different carbon black types they are categorised according to their structure. With a *low structure* corresponding to spherical well dispersed isolated particles and a *high structure* meaning either geometrically highly anisotropic particles that are long and thin, or particles with a tendency to agglomerate in large anisotropic clumps, figure 2-12.

It is found that generally the high structure particles have p_c and t values close to that of 0.16 and 2.0, following universal percolation theory. However the low structure particles tend to have t values as high as 6.4 [68], many times greater than predicted [63].

This is counter intuitive as the low structure particles should conform most closely to the universal percolation theory as they most closely resemble the theoretical ideal of an even dispersion. However, the universal percolation theory makes a central assumption that the conduction between particles is either on, touching, or off, not touching. This binary approach is not valid as electrons are able to tunnel, and hop, between particles that are not actually in physical contact.

If we examine our composites more closely we find that the particles dispersed in the insulating medium are likely to be encased in a thin layer of insulating medium. Experimental evidence shows that providing the medium is capable of a high degree of wetting and the particles have a tendency to disperse, then a surrounding insulating layer will *encapsulate* the particles [67]. Therefore true particle-particle contact will not occur due to the insulating buffer, unless p_c approaches 0.7 which is the maximum packing fraction of spheres. However, composites with the insulating buffer present around the filler are still able to conduct at much lower filling fractions than this. This means our mechanism for conduction, that underpins the percolation theory, is not 'touching'. We must take into account the ability of the electrons to *tunnel* between particles to form conduction lines.

Thus the central assumption of the universal percolation theory of particle - particle touching must be adapted to include the effects of tunneling. At first the inclusion of tunneling might appear to completely undermine the idea of percolation. Instead of a system where particles are only electrically connected when they touch we now have the entire system of particles that are theoretically electronically connected to every other particle via tunneling. How these two apparently conflicting ideas are reconciled is that the probability of tunneling *exponentially decays* with separation distance. Therefore the tunneling is only likely to happen between particles that are closely separated. Typically tunneling distances are of the order 5-50 nm depending on the nature of the barrier and the materials that form it.

Percolation theory is still effective as only nearest neighbours are assumed to be able to tunnel but with an adjustment required to take into account tunneling which is a function of the distribution of distances between the particles. If we consider the resistance of a conduction line in the composite we must now sum the resistance of all the particles in the conduction path, R and sum the resistance of all the tunneling barriers between the particles:

$$R_T = \sum_{i=0}^{n} R + \sum_{i=0}^{n} R_c, \tag{2.10}$$

where R_c is a function describing the resistance encountered to tunneling. Simply put we can expect the universal percolation theory to hold when the sum of R_c is negligible compared to R, while for percolation systems where the resistance is dominated by R_c then we can expect non-universal percolation and $t > 2.0$.

In low structure systems, where the particles are small and well dispersed, we can expect that percolation will start at low filling fractions as tunneling will enable particles to connect without physically touching. However the resistance will only decrease slowly as with the addition of more particles the tunneling distances only decrease by a small amount and the medium surrounding the particles forces tunneling to always take place. Due to there being many particles in a percolation path there will always be many contacts, R_c, to include. Thus t will be tend to a larger value as the conductivity only increases slowly but starts increasing at a lower threshold p_c, figure 2-12.

On the other hand for the high structure particles such as large agglomerates or highly anisotropic particles, the first percolation path will not occur until a higher critical volume fraction as there is a greater distance between the particles. However above the percolation threshold, as the particles are large, there are less

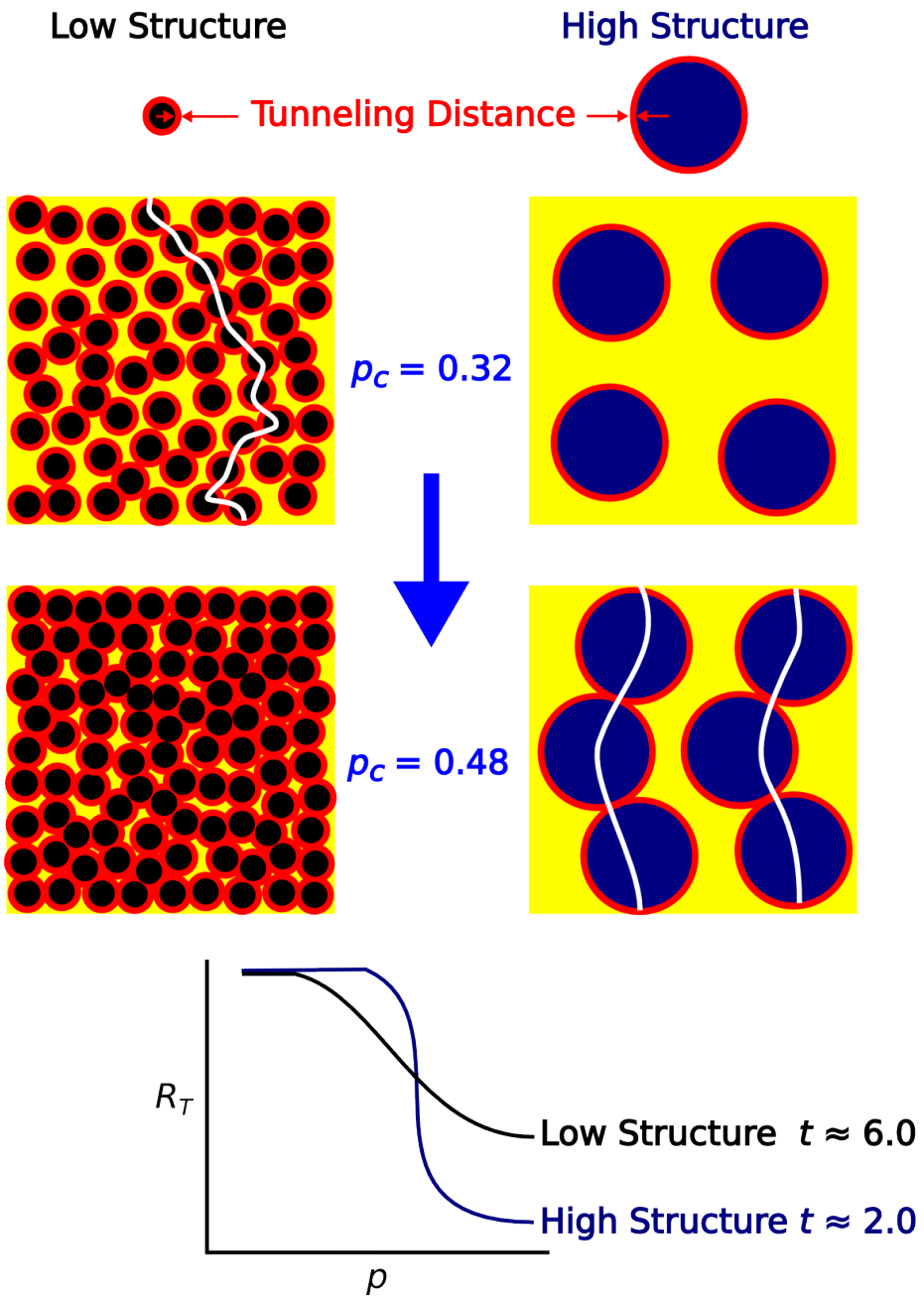

Figure 2-12: A schematic to show the difference between low and high structure fillers in a composite. At two representative filling fractions, the low and high structure fillers clearly show very different behaviours. The low structure is able to reach the percolation threshold for a lower p however the high structure once it reaches the percolation threshold decreases in resistance at a much sharper rate. This is due to the resistance being less dependant on the tunneling between particles.

tunneling barriers to be overcome in a percolation path and so the total resistance is not so dependant on tunneling. Thus t will tend towards values of 2.0, as for the universal percolation theory.

This situation is shown in figure 2-12, comparing equal filling fractions of large (high structure) and small (low structure) particles. The high structure has a much sharper percolation region, that onsets at a higher p_c and reaches a lower resistance. While the low structure reaches the percolation threshold sooner but cannot reach such a low resistance due to more numerous resistance critical tunneling barriers. The simple schematic in figure 2-12 has actually been confirmed experimentally by Hong through comparing like composites but with nano-sized fillers and micron sized filler [70]. Hong found that the percolation threshold of the nano-sized filler was 14% and 30% for the micron sized particles. The onset of percolation is also shown to occur at the same average inter-particle distance, $\bar{b} = 45$ nm, calculated from:

$$\bar{b} = l\left[\left(\frac{\pi}{6p}\right)^{1/3} - 1\right], \tag{2.11}$$

where l is the length of the particle and p is the filling fraction [70]. This gives a typical tunneling distance in these types of composites of 45 nm.

In summary the power law dependence from percolation theory is shown to be a good starting point for describing the conductivity in composites. However the impact of tunneling yields greater values of t in low structure composites If the tunneling distance is large compared to the particle size then universal percolation theory doesn't apply; if the particle size is much greater than the tunneling distance then universal percolation theory does apply. We now consider the tunneling processes between the particles more closely.

2.5 Tunneling

Tunneling is a quantum mechanical process by which a particle can penetrate through a classically forbidden region. In considering electrons of energy, E, incident on a one dimensional rectangular barrier of height, ϕ, and width, b, classical mechanics dictates that when $E < \phi$ electrons will be unable to pass through the barrier. However in quantum mechanics while most electrons incident on the barrier are reflected, some are in fact transmitted through the barrier. The probabilty of electron tranmssion is given by $|T|^2$. The transmission probability for a one dimensional rectangular barrier when $E_z < \phi$ is,

$$|T|^2 = \frac{16E(\phi - E)}{\phi^2} \exp\left(-2bk_z\right) \tag{2.12}$$

where k_z is the value of the wave-vector through the barrier,

$$k_z = \sqrt{\frac{2m(\phi - E_z)}{\hbar^2}}. \tag{2.13}$$

The tunneling probability decays exponentially with barrier width, b. The importance of this has been discussed in the previous section where the average distance between particles in a composite strongly effects the overall resistance. Further the tunneling probability is also a function of the effective barrier height and the temperature, T.

We wish to calculate the overall current density through a single barrier system when the barrier is biased between the emitter and collector contacts by a potential, eV. The bias causes the barrier to be become trapezoidal, shown in figure 2-13, and become increasingly *transparent* as electrons are able to more readily cross the barrier via thermionic emission.

We proceed by first finding an expression for the tunneling current through a metal-insulator-metal (M-I-M) barrier as a function of the available electronic states and the tunneling probability. The Wentzel-Kramers-Brillouin (WKB) approximation is utilized to obtain the transmission coefficient of the biased barrier and we eventually arrive at the generic Tsu-Esaki tunneling equation. We apply this in chapter 4 to derive the current - voltage ($I-V$) characteristics for a single graphite-silicone-graphite barrier.

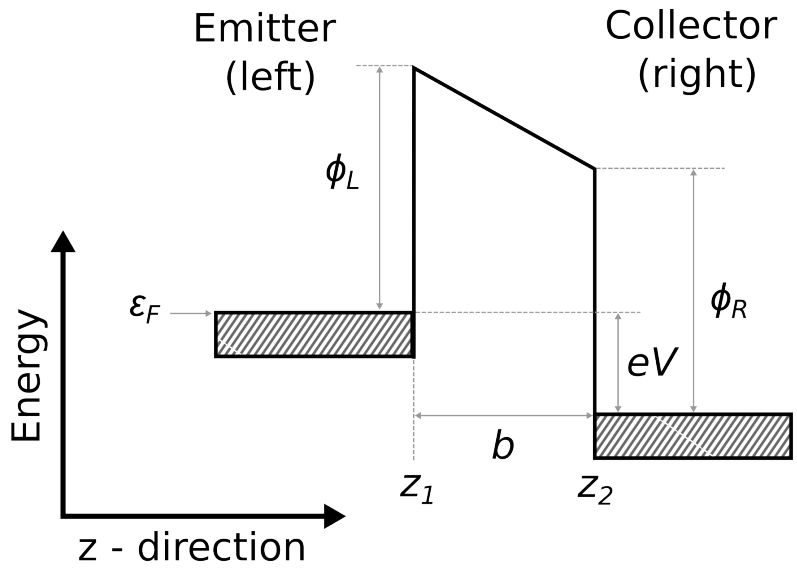

Figure 2-13: A one dimensional M-I-M barrier. Electrons are able to tunnel through the barrier of height, ϕ, and width, b, with probability $Z(E_z)$. The barrier is sloped due to the applied potential eV.

2.5.1 Current Density Through a Barrier

Current density, J, is defined as the product of the number of electrons per unit volume, n, the electronic charge, e, and the electron velocity, v, with,

$$J = nev. \tag{2.14}$$

Applying this for the tunneling barrier, shown in figure 2-13, the number of electrons per unit volume is given through summing over all the allowed electron states in k-space with a certain probability that each state is occupied, $f_L(E)$, given by the Fermi-Dirac distribution. The electron is only able to cross the insulator if there is a corresponding unfilled allowed state on the the other side and so we multiply by $1 - f_R(E)$. For tunneling to occur we also need to account for the tunneling probability which we define as $Z(E_z) = |T|^2$. Thus our current density from left to right, emitter to collector, is given by,

$$J_{L\to R} = e \sum_k f_L(E)(1 - f_R(E))Z(E_z)v_z \,, \tag{2.15}$$

where v_z is the electron velocity in the z-direction over the barrier. Rather than taking the sum of all k-states, instead we integrate over the volume element of k-space using the three dimensional density of electron states per unit volume,

$\frac{\mathrm{d}^3k}{8\pi^3}$. We also take account of the two possible spin states of the electrons by multiplying by 2. Thus,

$$J_{L\to R} = 2e \int \frac{\mathrm{d}^3k}{8\pi^3} f_L(E)(1 - f_R(E))Z(E_z)v_z \,. \tag{2.16}$$

Substituting in the electron velocity in the z-direction,

$$v_z = \frac{1}{\hbar}\frac{\mathrm{d}E_z}{\mathrm{d}k_z} \,, \tag{2.17}$$

and splitting k into its three elemental components $d^3k = \mathrm{d}k_x\mathrm{d}k_y\mathrm{d}k_z$,

$$J_{L\to R} = \frac{2e}{8\pi^3} \int\int\int \mathrm{d}k_x\mathrm{d}k_y\mathrm{d}k_z f_L(E)(1 - f_R(E))Z(E_z)\frac{1}{\hbar}\frac{\mathrm{d}E_z}{\mathrm{d}k_z} \,. \tag{2.18}$$

As the k_x and k_y states are symmetric and equivalent integrating over $\mathrm{d}k_x$ and $\mathrm{d}k_y$ is equivalent to integrating over a cross-section of the Fermi sphere, $k_\parallel 2\pi \mathrm{d}k_\parallel$. Then by cancelling the $\mathrm{d}k_z$ terms gives,

$$J_{L\to R} = \frac{2e}{8\pi^3\hbar} \int\int k_\parallel 2\pi \,\mathrm{d}k_\parallel \, f_L(E)(1 - f_R(E))Z(E_z) \,\mathrm{d}E_z \,. \tag{2.19}$$

From the kinetic energy relation for $k_\parallel$ we find,

$$\frac{\mathrm{d}E_\parallel}{\mathrm{d}k_\parallel} = \frac{\hbar^2 k_\parallel}{m} \,, \tag{2.20}$$

which leads to,

$$J_{L\to R} = \frac{em}{4\pi^2\hbar^3} \int\int f_L(E)(1 - f_R(E))Z(E_z) \,\mathrm{d}E_\parallel \,\mathrm{d}E_z \,. \tag{2.21}$$

Next, we find the total current density over the barrier by subtracting the current going right to left, $J_T = J_{L\to R} - J_{R\to L}$. We assume that any directional dependence of $Z(E_z)$ is negligible to find:

$$J_T = \frac{2em}{(2\pi)^2\hbar^3} \int\int (f_L(E) - f_R(E))Z(E_z) \,\mathrm{d}E_\parallel \,\mathrm{d}E_z. \tag{2.22}$$

The total current density over the barrier has a double integral both over the energy in the z-direction, over the barrier, and the energy perpendicular to the barrier. The total energy of the system is given by the sum of these, $E_T = E_z + E_\parallel$. To evaluate J_T we first integrate the Fermi-Dirac functions for $E_\parallel$.

2.5.2 Supply Function

The Fermi-Dirac equation describes the probability that a state of energy E_T is occupied,

$$f = \frac{1}{1 + \exp(\beta(E_T - \epsilon_F))}\,, \tag{2.23}$$

where $\beta = \dfrac{1}{k_B T}$ and ϵ_F is the Fermi-energy. To evaluate the integrals of f_L and f_R over $E_\parallel$ we take the limits from the minimum energy to infinity,

$$F_L = \int f_L \mathrm{d}E_\parallel = \int_{\epsilon_F}^{\infty} \frac{1}{1 + \exp(\beta(E_\parallel + E_z - \epsilon_F))}\,\mathrm{d}E_\parallel \tag{2.24}$$

$$F_R = \int f_R \mathrm{d}E_\parallel = \int_{\epsilon_F + eV}^{\infty} \frac{1}{1 + \exp(\beta(E_\parallel + E_z - \epsilon_F))}\,\mathrm{d}E_\parallel\,. \tag{2.25}$$

Using the identity,

$$\int \frac{1}{1 + \exp(x)}\,\mathrm{d}x = \ln\left(\frac{1}{1 + \exp(-x)}\right)\,, \tag{2.26}$$

we can integrate f_L over $E_\parallel$,

$$\begin{aligned} F_L &= \frac{1}{\beta}\left[\ln\left(\frac{1}{1 + \exp(-\beta(E_\parallel + E_z - \epsilon_F))}\right)\right]_{\epsilon_F}^{\infty} \\ &= 0 - \frac{1}{\beta}\ln\left(\frac{1}{1 + \exp(-\beta E_z)}\right)\,. \end{aligned} \tag{2.27}$$

We do a similar operation for f_R,

$$\begin{aligned} F_R &= \frac{1}{\beta}\left[\ln\left(\frac{1}{1 + exp(-\beta(E_\parallel + E_z - \epsilon_F))}\right)\right]_{\epsilon_F + eV}^{\infty} \\ &= 0 - \frac{1}{\beta}\ln\left(\frac{1}{1 + \exp(-\beta(E_z + eV)}\right)\,. \end{aligned} \tag{2.28}$$

We then subtract left from right as from equation 2.22,

$$F_L - F_R = \frac{1}{\beta}\ln\left(\frac{1}{1 + \exp(-\beta(E_z + eV)}\right) - \frac{1}{\beta}\ln\left(\frac{1}{1 + \exp(-\beta E_z)}\right) \tag{2.29}$$

$$= \ln\left(\frac{1 + \exp(-\beta E_z)}{1 + \exp(-\beta(E_z + eV))}\right)\,. \tag{2.30}$$

We have integrated the distribution of states in the emitter, minus the states in the collector, that are perpendicular to the barrier to arrive at the *supply function*.

The supply function describes the number of electrons in energy interval, E_z to $E_z + \mathrm{d}E_z$ that are available to tunnel.

2.5.3 Tunneling Probability

Now we turn our attention to finding the tunneling probability, $Z(E_z)$, for which we utilize the WKB approximation. This is a semi classical approximation for the wave function through the barrier which provides a good solution provided that the potential varies slowly with z and that the barrier is not too thin [71]. For the sloped barrier in figure 2-13 the potential is a linear function of z and thus the WKB approximation states,

$$Z(E_z) \simeq \exp\left(-2\int_{z_L}^{z_R} |k_z|\,\mathrm{d}z\right)\,, \tag{2.31}$$

where k_z is the value of the wave vector in the barrier from z_L to z_R. If barrier was rectangular we would easily find,

$$Z(E_z) \simeq \exp\left(-2bk_z\right)\,, \tag{2.32}$$

where $b = z_R - z_L$, the barrier width. This is the same result as given in equation 2.12. However the applied potential eV means the barrier becomes sloped. We define $U(z)$ as the linear dependence of potential variation through the barrier with,

$$U(z) = \phi - \gamma(z - z_L)\,. \tag{2.33}$$

Which makes the tunneling probability,

$$Z(E_z) \simeq \exp\left(\frac{-2\sqrt{2m}}{\hbar}\int_{z_L}^{z_R} (U(z) - E_z)^{1/2}\,\mathrm{d}z\right)\,. \tag{2.34}$$

If we now make a substitution with X where

$$X = \frac{2m(\phi - \gamma(z - z_L) - E_z}{\hbar^2}\,, \tag{2.35}$$

and

$$\frac{\mathrm{d}X}{\mathrm{d}z} = \frac{-2m\gamma}{\hbar^2}\,, \tag{2.36}$$

we arrive at a single integral of,

$$Z(X) = \exp\left(\frac{\hbar^2}{m\gamma}\int_{X_1}^{X_2} X^{1/2}\,\mathrm{d}X\right). \tag{2.37}$$

Integrating and replace X from the substitution yields,

$$Z(E_z) = \exp\left(\frac{2\hbar^2}{3m\gamma}\left[X^{3/2}\right]_{X_1}^{X_2}\right), \tag{2.38}$$

$$\begin{aligned} Z(E_z) = \exp\Bigg(\frac{2\hbar^2}{3m\gamma}\Bigg(&\left[\frac{2m(\phi-\gamma(z_2-z_1)-E_z)}{\hbar^2}\right]^{3/2} \\ -\quad&\left[\frac{2m(\phi-\gamma(z_1-z_1)-E_z)}{\hbar^2}\right]^{3/2}\Bigg)\Bigg). \end{aligned} \tag{2.39}$$

As the slope of the barrier is linear $\gamma = eV/b$ and $\gamma(z_2 - z_1) = eV$ and so we find,

$$Z = \exp\left(\frac{-4(2m)^{1/2}b}{3eV\hbar}\left[(\phi-E_z)^{3/2}-(\phi-E_z-eV)^{3/2}\right]\right), \tag{2.40}$$

the *tunneling probability* in a linearly *sloped* barrier.

2.5.4 Tsu-Esaki Equation

Combining the Fermi-Dirac distributions integrated over $E_\parallel$ and the tunneling probability in the sloped barrier we arrive at,

$$J = \frac{2emk_BT}{(2\pi)^2\hbar^3}\int_{\epsilon_F}^{\infty} Z(E_z)F(E_z)\,\mathrm{d}E_z\,, \tag{2.41}$$

where

$$F(E_z) = \ln\left(\frac{1+\exp(-\beta E_z)}{1+\exp(-\beta(E_z+eV))}\,,\right) \tag{2.42}$$

and

$$Z(E_z) = \exp\left(\frac{-4(2m)^{1/2}b}{3eV\hbar}\left[(\phi-E_z)^{3/2}-(\phi-E_z-eV)^{3/2}\right]\right). \tag{2.43}$$

This is a very general result that can be readily applied to many tunneling situations such as M-I-M systems and super-lattices with multiple barriers [72]. It is possible to find exact analytical solutions for certain situations through either assuming; low temperatures, $T \to 0$; a low applied potential; or a very high applied potential. In the instance of a high potential we have a triangular barrier and

we arrive at the Fowler-Nordheim tunneling equation [71]. In the chapter 4.3 we solve equation 2.41 numerically for a graphite-silicone-graphite barrier in order to model the theoretical $I-V$ curves for a single barrier system and in the process extract the height of the silicone barrier.

2.6 Summary

The aim of this chapter was to discuss some of the underlying physics behind carbon and the nature of conduction in carbon-based composites.

Graphite was shown to be a semi-metal and graphene a zero band-gap semiconductor with the significance of its linear $E-\mathbf{k}$ dispersion briefly explained. The tight binding model was applied to bilayer graphene to show that is has an electric field *tunable band-gap*. This will certainly be of interest in the next chapter where we discuss the origins of the NDR mechanism.

Next we considered percolation theory in relation to conductive composites. The concept of electrons 'percolating' through a network of conductive particles, forming conduction lines, will be of particular interest in chapter 5.4, where conduction line destruction through perturbations will be used in differential pressure detection.

Experimental work with carbon black composites was used to show that the universal percolation theory is not always correct. Instead a non-universal percolation theory is required that includes the ability of electrons to *tunnel* between particles due to *encapsulation* of the insulation matrix. This highlights the importance of tunneling between particles in the conduction lines.

A general tunneling equation was derived, based on a M-I-M barrier, to describe the current through the barrier. We have included the effect of a potential that causes the barrier to become increasingly *transparent* for higher biases. We use this in chapter 4.3 to model the $I-V$ characteristics of single graphite-silicone-graphite barrier.

Chapter 3

Fabrication and Measurement

This chapter describes the processes involved for the fabrication and measurement of GSCs. Many of the processes are novel, having been developed at the University of Bath, and are explained in detail. Firstly the composite mixing and curing methods are given. Then the mounts that hold and enable electrical contact to the composite are described. This includes a description of the imprint lithography method, which holds much promise for future development of flexible GSC devices. Next we discuss our development of naphthalene centered molecules that increase the miscibility of graphite in silicone. The measurement processes are all given, with special attention paid to the different bend-strain systems developed. The method for calculation of the bend induced strain is derived. Finally the design and measurement process for a differential pressure array (DPA) is given in detail.

3.1 Sample Fabrication

3.1.1 Chemical Properties of Pristine Silicone Rubber

Before describing the fabrication of GSCs it is worthwhile considering pristine silicone rubber itself. The silicone rubber (Alchemie, RTV139) is a room temperature vulcanization (RTV) silicone that cures on addition of a platinum based catalyst (Alchemie, C149). A RTV silicone was selected because of its ease of mixing, curing and physical properties. RTV139 is commonly used in mould making, producing replicas and prototyping; it has a low viscosity (before cure), exceptionally high tear strength and good elongation [73]. A piece of cured pristine silicone rubber is shown in figure 3-1(a).

In general silicone rubber consists of polymer chains of siloxanes, which consist

(a)

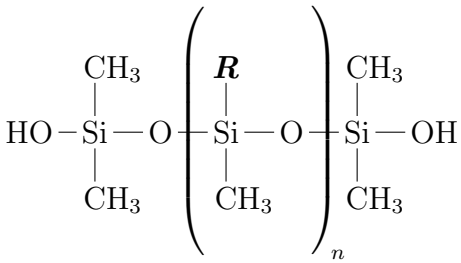

(b)

Figure 3-1: (a) Pristine silicone rubber with a 20:1 mix of RTV139:C149 after curing for 24 hours. (b) The molecular structure of silicone rubber where $\boldsymbol{R}$ is either a methyl group, vinyl group, phenyl group or hydrogen atom, depending on the desired properties of the silicone rubber.

of silicon - oxygen chains with two organic side groups attached to each silicon. The siloxane backbone is common to sand, glass and quartz; it is the organic side groups on the silicon that give silicone rubber its elastomer properties. In general the side groups can be any of the following:

- Methyl Group $Si-CH_3$ $\Rightarrow$ Most commonly found group
- Vinyl group $Si-CH=CH_2$ $\Rightarrow$ Gives cross linking via double bond
- Phenyl Group  $\Rightarrow$ Enables flexibility by reduced packing
- Hydrogen $Si-H$ $\Rightarrow$ Provides cross linking site

It is the proportions of these four groups contained in the silicone rubber that defines its physical properties such as its flexibility or tear strength. The molecular structure of the silicone polymer is shown in figure 3-1(b), where $\boldsymbol{R}$ represents the location of either a methyl group, vinyl group, phenyl group or hydrogen atom.

The curing process, that solidifies the rubber, is by the formation of a complex 3D network of polymer chains achieved through cross linking between the chains. The cross linking reaction occurs via a platinum catalyst. The platinum has one free coordination site which interacts with the double bond in a vinyl group. The double bond is broken and a single bond is formed instead to a nearby $Si-H$ group, leaving the two chains cross linked. The platinum is then released and available to continue further cross linking. This is known as a platinum-catalyzed hydrosilylation reaction [74].

To make pristine silicone rubber catalyst is admixed to the liquid rubber in a 1:20 ratio by mass. The mixture can then be poured into a template and left to cure for 24 hours. If a detailed mould is being used the rubber can be degassed which ensures it is bubble free. Once cured the rubber is both very flexible and durable and can be elastically stretched a great deal, with a maximum elongation of 400% [73]. For low temperatures when the rubber is cooled below 200K it goes through a glass transition, T_g and becomes rigid and glass-like. On warming back again, above T_g, the rubber fully regains its elastomer properties.

The ability to combine the flexible, electrically insulating, silicone rubber with highly conductive graphite nanoparticles allows for the fabrication of a flexible conductive composites.

3.1.2 Composite Mixing

The process for the fabrication of GSCs was developed at the University of Bath. Others have combined silicone rubber and various forms of graphite particles, such as carbon black [75, 76]. What is unique for our composite is both the high conductivity of the HOPG particles and the high volume fraction of graphite in the silicone matrix that we achieve. This combines to form a composite with a much lower resistivity. The GSC compromises of three main elements, silicone rubber (Alchemie, RTV139), catalyst (Alchemie C149) and 450 nm HOPG nanoparticles (NanoAmor, 1246HT)[1].

The mixing process is relatively basic but requires user skill and patience to accurately produce the precisely desired concentrations of composite. The main difficulty arises in mixing the thick viscous paste enough, so that all the nanoparticles are homogeneously dispersed. The fabrication process is shown in the flow chart in figure 3-2. It includes typical quantities that would provide a surface coverage of 15 cm^2 at a height of 100 μm. The concentration of graphite nanoparticles in the composite is given by the volume fraction, p_g,

$$p_g = \frac{\dfrac{m_g}{\rho_g}}{\dfrac{m_s}{\rho_s} + \dfrac{m_c}{\rho_c} + \dfrac{m_g}{\rho_g}}, \tag{3.1}$$

where m_g, m_s and m_c are the mass of the graphite, silicone rubber and catalyst mixed into the composite and ρ_g, ρ_c and ρ_s are the densities of graphite, catalyst and pristine silicone rubber. Using the masses given in figure 3-2 and the den-

[1] 1246HT is no longer available and replaced by 400 nm HOPG nanoparticles, 1250HT

Property	Units	Silicone RTV 139	Catalyst C149	Graphite1246HT
Appearance	-	white liquid	clear liquid	black fine powder
Density	gcm^{-3}	1.11-1.15 [73]	1.12-1.17 [73]	2.25 [77]
Viscosity	mPaS	25,000 [73]	10 [73]	N/A
Resistivity	$\mu\Omega$m	∞	∞	0.4[78]

Table 3.1: The density, viscosity and resistivity of the silicone rubber, catalyst and graphite used in GSCs.

sities, given in table 3.1, the volume fraction is p_g=35.4%. This is close to the maximum volume fraction attainable before the composite becomes too viscous to mix homogeneously.

To overcome the greatest difficulty of fabrication, the high viscosity of the wet mixture, various techniques were attempted including incorporating, hexane, silicone oil, acetone or additional catalyst into the mix. However all of these were unsuccessful, either they inhibited the cure processes; caused a significant degradation to the rubber properties; or simply had no impact on the viscosity at all.

Ideally the fabrication process would be scaled up to enable larger batches of composite to be produced. This would improve the accuracy in achieving the desired concentrations through reduction of errors in weighing out. An automated mixing process would be an obvious improvement and might allow for even greater concentrations of graphite in the silicone. Possibly the use of a mechanical stirrer and some form of sonification, to minimise aggregation, would be successful. Others have reported improved dispersions through the addition of large quantities of hexane and then using mechanical stirring and ultrasonic vibration whilst the hexane is slowly allowed to evaporate off [75].

3.2 Composite Mounts

Predominantly there are two mounts used in making the samples, a PCB board, which provides a rigid surface and easy electrical contacting; and an acetate sheet, which allows the composites flexible properties to be investigated. The acetate mount required some imaginative solutions for bonding wires to enable ohmic contacts.

As well as the two main mounts a third mount was developed which used pristine silicone rubber as the mount substrate. Using imprint lithography composite Hall bars were made in a silicon template and transferred onto the pristine

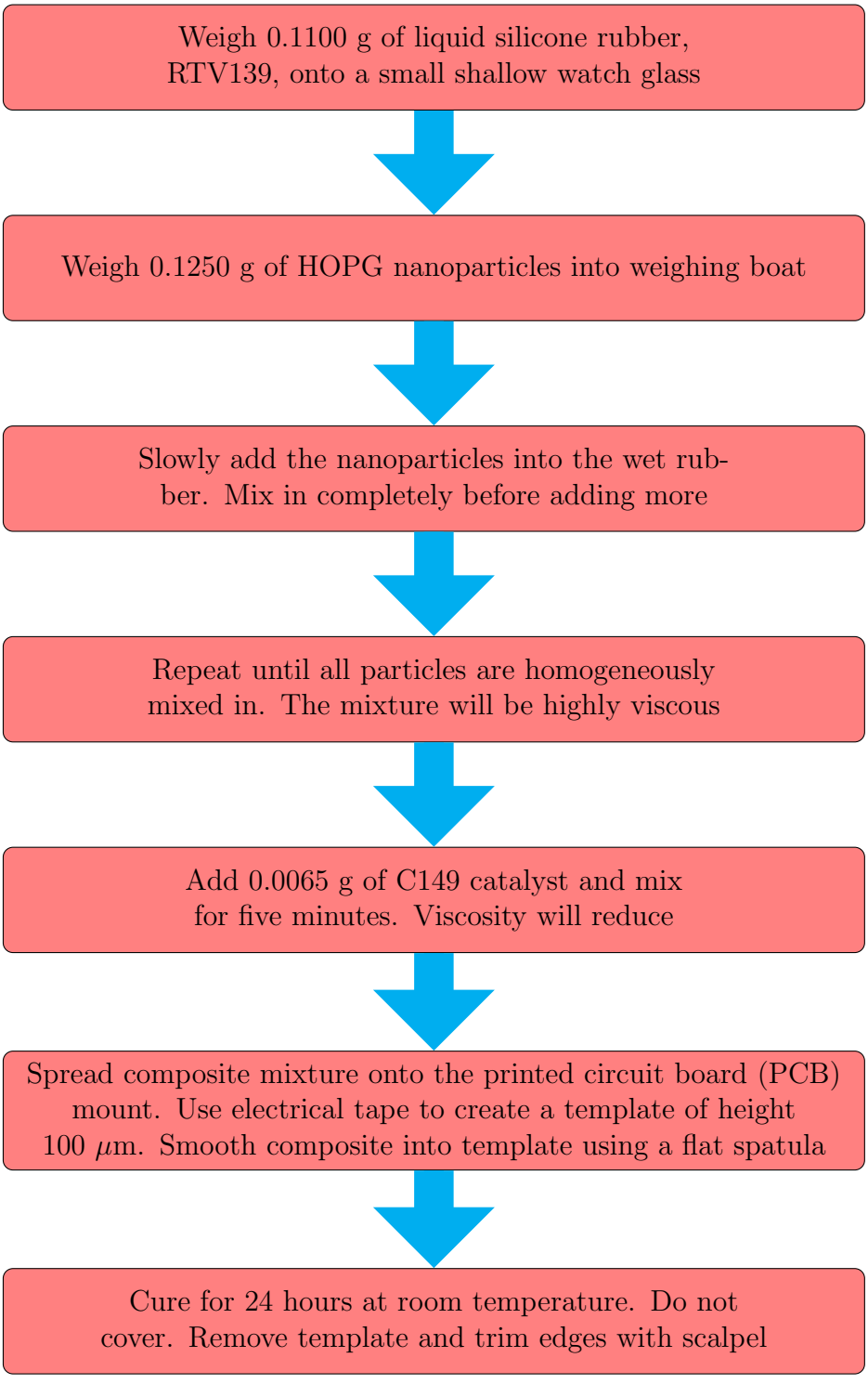

Figure 3-2: Flow chart outlining the steps in fabrication of GSCs for a sample of p_g=35.4%. The mixing of the graphite nanoparticles as a homogeneous dispersion in the silicone requires user skill and patience as the mixture becomes highly viscous.

silicone with feature sizes of 25 μm. Very few results for this are included, however the processes have still been described as imprint lithography with silicone rubber is a completely novel method and holds the best opportunities for future development of flexible GSC devices.

3.2.1 Rigid PCB Mount

The greatest advantage of the PCB mount is its ease of use for prototyping and quick development of GSC devices. It is a simple case of designing a template in software and then following a standard PCB fabrication procedure to produce a custom PCB board in under an hour.

The geometric layout of the PCB is critical as it must allow four-terminal (4T) measurements over small separation distances, whilst allowing the composite to adhere well for good electrical contact. Contact pads must be greater than 1 mm^2 to minimise contact resistance. However the composite was also found to adhere best to the PCB insulating surface, a rough surface of woven glass fibre and resin, than the smooth copper contact pads. Therefore hollow contact pads were used so that the composite adhered strongly to the PCB and was forced down onto the contact pads which allowed good electrical contact. For the 4T measurement, discussed in section 3.4.1, very thin copper voltage probes were required. A tight restriction on the total length of the sample between the contact pads, to enable voltages under 50 V, and the requirement of more than two probes meant that the probes had to be less than 100 μm wide. Usually PCB manufacture, in the above way, is limited to line widths of no less than 150 μm. However an optimised process was derived to enable 80 μm probes that involved a controlled over etching of the probes.

The PCB mount is relatively easy and simple to fabricate as it follows well used and documented processes. For the acetate mount and silicone rubber imprint lithography method this is not the case. Similar issues still had to be considered such as contact pads, contact resistance, and minimum feature size. However, for these novel processes there is little or no documented techniques, and advancement was through a process of trial and error with much experimentation of different materials and methods.

3.2.2 Flexible Acetate Mount

An important aspect of the research was to explore how the composite properties respond to bend induced strain. This required a flexible mount which would

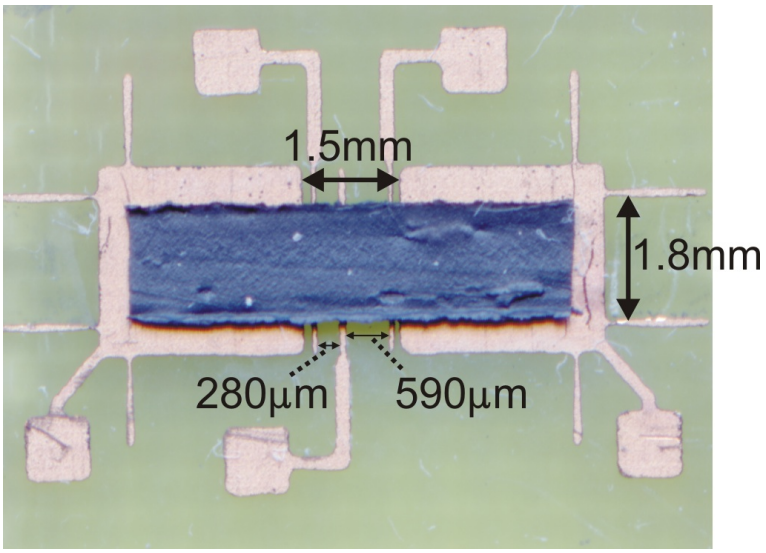

Figure 3-3: A 100 μm thick GSC on a PCB mount. Contact probes are 80 μm wide. This set-up allows a 4T measurement for different probe separation distances. The contact pads are large and are hollow in the centre creating better adhesion of the composite.

allow the composite to adhere well to the surface and then readily deform as the composite was bent. Further the mount would have to be able to provide adequate contact to the composite and allow electrical connections to an external circuit. It was found that 100 μm thick acetate sheet was best suited to the task.

Contacts were fabricated onto the acetate through a thermal deposition process using a specially designed card mask. The card was cut using a laser cutter[2] with a feature size of 100 μm. A simple cross shaped mask was found to be effective. The mask was fixed to the acetate sheet, and secured to a metal plate in a thermal evaporator ready for deposition.

Firstly 80 nm of chromium was deposited as it was found to form a better layer on to the acetate than gold. Then 80 nm of gold was deposited on top of the chromium. The composite adheres more readily to the gold surface and creates the lowest resistance contacts.

Templates using electrical tape were formed across the acetate to enable 100 um high strips of composite to be cured across the gold contacts. The composite was mixed, using the method in figure 3-2 and cured for 24 hours. The templates were removed and a further deposition of gold was done over the contact areas to minimise the contact resistance, $< 100\ \Omega$. Either two-terminal (2T) or 4T samples could be made through a simple alteration of the mask. An

[2]A Epilog 45W laser cutter was used courtesy of the University of Bath Engineering Department. Settings: Speed = 100% Frequency = 450 Hz Power = 45%

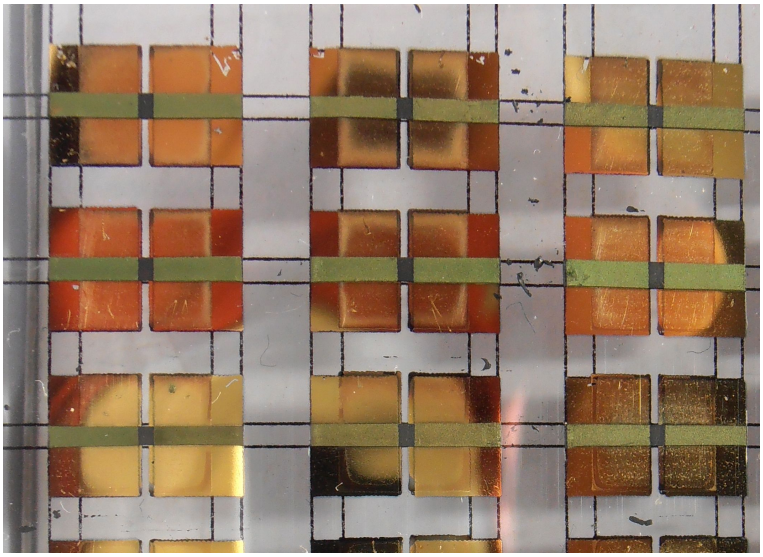

Figure 3-4: An array of nine composite samples on an acetate sheet. Deposition of chromium and gold was used to create low resistance contacts. A cross shape template allows a 4T measurement to be made.

array of nine samples is shown in figure 3-4.

To contact the composite samples to an external circuit thin electrical wires were attached to the acetate. A 50 SWG unshielded copper wire was used as it is very thin, 110 μm, and light. Therefore the wires do not significantly impact on the acetate or interfere with bending. To secure the wire in place it was threaded through a tiny hole punched in the acetate in a region covered by the deposited gold, and fastened by twisting the end back on itself. A small drop of silver epoxy was then applied to secure the wire and cured at 80°C for 15 minutes. The acetate samples were cut into 11 mm by 5 mm strips ready for testing.

This is an effective and scalable way to fabricate the samples. A more detailed mask could be made through using a better mask material than card, such as acrylic, glass or thin metal. A laser cutter could potentially be used to cut feature sizes as small as 25 μm and allow a pixel resolution of 50 μm. This would enable a device of comparable resolution to the human finger, which can detect surface roughness down to 100 μm [17] and is one of the most sensitive tactile sensors known [18]. Therefore this method has potential for helping create suitable bio-mechanical skin devices. Another way in which to approach these feature sizes is through using an imprint lithography method.

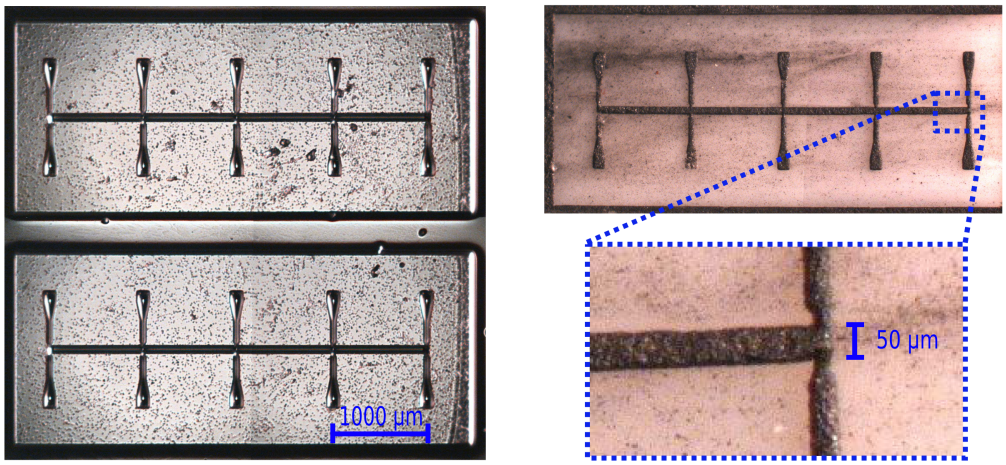

(a) (b)

Figure 3-5: (a) A Hall bar shape is etched, 110 μm deep, into silicon to make a stamp. (b) The composite is then cured in the stamp and released through a pristine silicone substrate. Composite Hall bars of 50 μm wide and 110 μm high were successfully fabricated.

3.2.3 Imprint Lithography

The aim of this work was to adapt traditional clean room nanofabrication techniques to create a silicon wafer stamp that could be used to mould the composite in a way that is scalable for creating large numbers of samples. The stamps were made in Hall bar shapes, 1,000 μm long and 50 μm wide and 110 μm deep so that the composite could be spread into the etched out Hall bar, figure 3-5(a). The technique allows for arrays of small composites to be fabricated reproducibly however, the difficulty lies in extracting the composite from the silicon stamp after the composite has cured.

The first stage was to produce a silicon stamp with a *deep etch* of 110 μm and smooth sides without any undercutting to allow the composite to be retrieved. The detailed procedure for this is given in appendix B and the recipe developed for inductively coupled plasma reactive ion etching (ICP-RIE) deep etching without undercutting is given in appendix C. The stamps are shown in figure 3-5(a).

Having fabricated the stamps the next stage was to mix a composite batch and spread it into the hollow Hall bar stamps through compressing it down onto the surface of the stamp. In order to retrieve complete composite Hall bars from the stamp, pristine silicone rubber was chosen as the mount for the GSC. The silicone rubber can polymerise with the GSC directly to create a strong chemical bond between the conductive composite and insulating mount.

An initial trial found that the silicone rubber created a good bond to the composite. However the composite itself had a tendency to tear as it was released from the stamp. A release agent of a 1:20 mix of Vaseline to white spirit painted over the stamp before applying the composite was found to reduce the tearing.

The fabrication of the stamps and transfer of the composite to the pristine silicone rubber was successful. The composite can be seen having been removed from the stamp in a complete Hall bar shape with a width of 50 μm and a depth of around 110 μm in figure 3-5(b).

The next difficulty came in making ohmic contacts to the samples. Various techniques were explored such as threading thin wires into the contact pads and through the rubber and using silver epoxy to hold them in place. However this caused strain and movement in the contact pads and damaged the Hall bars.

With a more suitably designed Hall bar mask with sufficient sized contact pads to allow wires to be attached with silver epoxy this problem could be overcome. Further, the use of cryogenic etching or further optimisation of the ICP-RIE etching needs exploring. Focus should be put on creating semi-circular trenches that would allow better release of the composite, which could be achieved through greater passivation of the side walls during the etching process.

3.3 Naphthalene Molecules for Absorption onto Graphite

We were interested in the effects of the addition of functionalized naphthalene based molecules to the composite. The naphthalene molecule is an organic aromatic hydrocarbon, consisting of two benzene rings joined together to form the center of the slightly larger naphthalene diimide (NDI) molecule. The NDI molecule's benzene core has the same hexagonal structure as graphite and readily lies flat on a HOPG surface via $\pi - \pi$ interactions [79]. These molecules can be functionalized with a range of different appendages. Including: Si — OH groups that are able to polymerise with silicone rubber; benzene groups that are large and form a barrier between the nanoparticles; and groups that alter the electron cloud of the naphthalene through providing additional delocalized electrons.

Four different molecules were prepared following the procedure given in appendix D.[3] These four molecules NDI-Si, NDI-Hex, NDI-Ph, which have NDI

[3]The molecules were prepared by Giles Prentice and Dr Dan Pantos from the Chemistry Department at the University of Bath.

centers, and DN-Silanol, which has a naphthalene center, are shown in figure 3-6. The molecules are in powdered form and were each ground into the HOPG powder for five minutes at a ratio of 1 : 100 by mass. The composites were then fabricated in the usual way following the method in figure 3-2. During the mixing process it was found that the graphite powder with the NDI-Si and DN-Silanol were more readily mixed and produced a lower viscosity mixture. No change in the miscibility was observed for the NDI-Hex or NDI-Ph.

The resistivity of the composite for each of the four molecules and a control sample of equal volume fraction is shown in figure 3-7. The molecules that contain the silicone appendages reduce the resistivity of the composite, in comparison to the control, while the NDI-Hex and NDI-Ph both increase the resistance by up to 200%.

The NDI-Si and DN-Silanol are able to anchor the graphite nanoparticles in the silicone rubber matrix. The naphthalene centers are able to cover the surfaces of the graphite and the appendages directly polymerise with the silicone matrix. This improves the miscibility of the composite, observed during the mixing process and allows for a better dispersion of particles through the composite. A better dispersion lowers the overall composite resistance.

The NDI-Hex and NDI-Ph molecules increase the resistance as they are not able to polymerise into the composite to aid dispersion. Instead they add an additional barrier to tunneling between graphite particles. The effect is most pronounced for NDI-Ph as this has the large benzene appendages.

The NDI molecules are able to lie flat on the graphite surface. Assuming there is no stacking of the molecules the surface coverage of the NDI-Si on the graphite nanoparticles can be calculated to be 58%, for a 1% mix by mass of NDI-Si to graphite, from,

$$SA = \frac{\sqrt{3}}{60} \frac{\rho_g A_g l a^2}{M} \,, \tag{3.2}$$

where ρ_g is the density of graphite, A_g is Avogadros constant, l is the nanoparticle size , $a = 140\ nm$ is the bond length in benzene and M is the molar mass of NDI-Si.

The addition of the NDI molecules is significant. Including NDI-Si increased the maximum volume fraction of graphite from $p = 36\%$ to $p = 39.5\%$ through the greater miscibility. This enabled lower resistance samples to be fabricated, which is in addition to the lowering of the resistance of the composite for the same filling fraction which occurs from the NDI anchoring the graphite nanoparticles into the matrix.

Name	Structure	Molar Mass	Comment
NDI-Si[1]	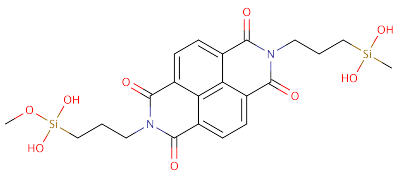	518.62	The naphthalene center readily sticks to the graphite surface while the Si appendages are able to polymerize directly with silicone rubber and provide anchoring into the rubber for the nanoparticle
NDI-Hex	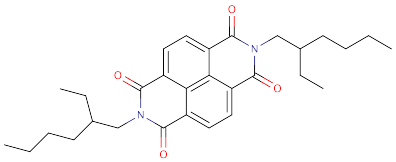	490.63	This molecule has been imaged on a graphite surface and shown to form an ordered arrangement [79].
NDI-Ph	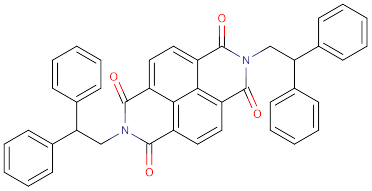	626.70	A large flat structure that lies flat on a graphite surface
DN-Silanol	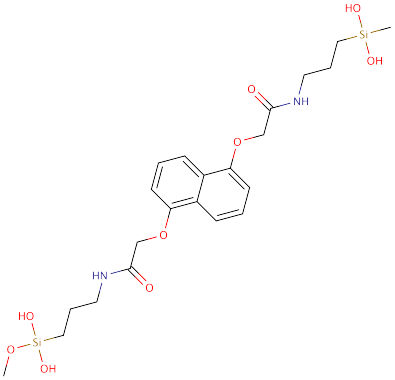	526.68	Si appendages polymerize directly with the silicone rubber. The oxygen atom causes the Naphthalene center to become electron rich which reduces stacking.

[1] Names are short representative forms. NDI stands for naphthalene diimide, Si for silicone, Hex for hexane, Ph for benzene and DN for naphthalene.

Figure 3-6: Table showing the names and structures of the different naphthalene based molecules incorporated into the composite, to altered the graphite properties or provide direct polymerization into the silicone rubber.

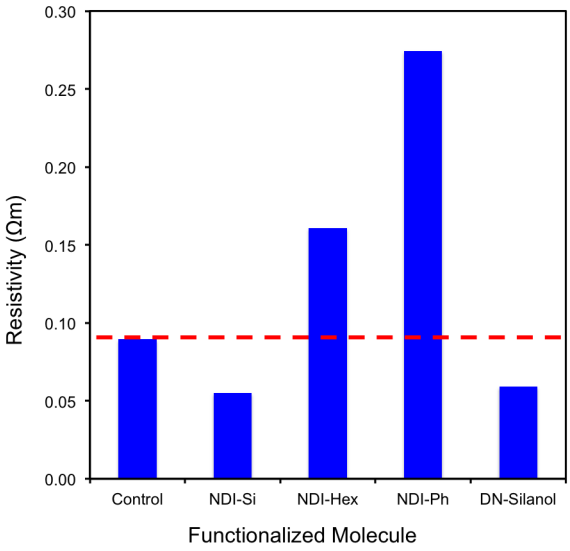

Figure 3-7: The difference in resistivity from the addition of different NDI based molecules for the same filling fractions of composite. NDI-Si and DN-Silanol reduced the resistance in comparison to the control by 38% and 34%, as they improve the particle dispersions through polymerization with the matrix . NDI-Hex and NDI-Ph both increase the resistance by 80% and 200%. These do not have the silicone appendages and do not aid dispersion. The resistance increases as they cover the graphite nanoparticles and create an increased barrier to tunneling.

3.4 Measurement

3.4.1 Four Terminal Measurement

To measure the electrical characteristics of the GSC a 4T set-up was used. The current was injected into the sample and voltage probes were then used to measure the potential drop across a section of the composite. The advantage of a 4T measurement is that only the voltage drop of the sample is measured and not the potential drop due to the contact resistance, R_c, or any wire resistance, R_w. The arrangement for a 4T measurement is shown in figure 3-8(a). The voltmeter used to measure V_{4T} can be considered to have an almost infinitely high resistance and so no current is able to flow through the voltage probes. Therefore, as $V = IR$, there is no voltage drop across R_p and hence only the true voltage drop across the sample is measured, allowing for a precise measurement of sample resistance, R_s. The 4T measurement was particularly important in measuring the properties of GSCs because the insulating nature of silicone rubber meant that ohmic contacts were particularly difficult to fabricate with contact resistances of the order 100 Ω.

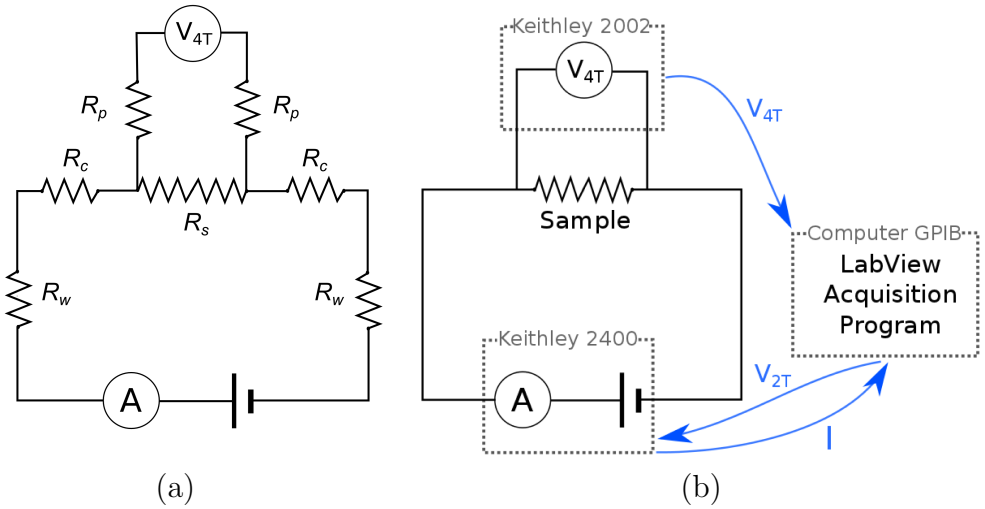

Figure 3-8: (a) A 4T set-up was used to measure the electrical characteristics of GSCs. (b) The measurement of the $I - V$ characteristics was automated by a LabView acquisition program.

3.4.2 Current - Voltage Measurement

The most common form of measurement throughout this work is the $I - V$ characteristics of the composite. LabView acquisition software was used to collect the current and voltage measurements and control the source meters directly through a computer via a GPIB connection. A program was written that swept the applied voltage, through a Keithley 2400 high precision source-meter, from zero to a desired value and back again. The ramp rate was set to 500 mV per second in 100 mV steps. The Keithley 2400 source-meter also measured the current. A current limit of 80 mA was set to protect both the sample and equipment in case of shorting. The 4T voltage was simultaneously measured by a Keithley 2002 multi-meter for each increment in the applied bias. The schematic for the measurement process is shown in figure 3-8(b).

3.4.3 Low Temperature Measurement

Some of the most interesting characteristics of the composite occur at low temperature; below its glass transition temperature 200 K. The ability to quickly measure $I - V$ curves was paramount to the success of the work as it enabled rapid development, prototyping and many repeat measurements. The use of a sealed cryostat was often unnecessary. Instead a simple custom probe was designed. Samples were attached to the probe and the probe was then directly lowered into a flask of liquid nitrogen. A polystyrene lid covered the top to

minimize evaporation losses.

For helium temperature experiments, 4 K - 250 K, a variable temperature cyrostat (VTC) from Cryogenic Ltd was used. The temperature of the sample space was controlled through a Lakeshore 340 Temperature Controller as the helium was gently pumped on. The desired temperature was set on the temperature controller, which automatically controlled heating elements in the cryostat using a feedback system. Typically it took around 30 minutes to stabilize at a desired temperature.

3.4.4 Oscillation Frequency Measurement

For measurement of the oscillation frequencies of the composite in an LC circuit an Agilent DS06014A oscilloscope with a USB connection to a LabView program was used. Due to the nonlinearities in the frequency response of the composite, the low single/noise ratio and the presence of two or more resonant frequencies it was necessary to perform a fast fourier transform (FFT) to identify the position of the key oscillation frequencies. The pseudo-code for the LabView program responsible for the data analysis is as follows:

- Read in 100, 0.2 ms frames of time series data
- For each frame
  - Perform a second order Savitzky-Gorlay averaging
  - Apply a Butterworth bandpass filter between 150 Hz to 20 kHz
  - Compute the FFT to find the power spectral density
- Average over the 100 frames
- Detect the main peak and perform a second order polynomial fit to find the central frequency to a 5 Hz resolution.

The program was adapted for different measurements depending on the frequency range or the accuracy desired. It could also be used in conjunction with the $I-V$ program to calculate the FFT for each voltage increment. To minimize the effect of noise; coaxial cables were used to shield the signal; grounded metal boxes were used to contain the key components; and the entire experimental set-up was contained within a closed Faraday cage. The overall effect of the noise reduction measures was to shift the base noise level down from -80 dB to -120 dB (100 μV to 1 μV).

3.5 Bend Induced Bilayer Strain

3.5.1 Room Temperature Bend

To explore the effect of *bend induced strain* on the composite, at room temperature, a precisely controlled stepper motor was employed, shown in figure 3-9. The stepper motor was used as a linear actuator with a shaft screw pitch of 0.5 mm, with each single step corresponding to a 1.25 μm horizontal displacement. The horizontal displacement is achieved by a sliding vernier calibre jaw along the main guide bar such that two supports, that hold the sample in place, move relative to each other. The supports have machined 70° grooves that pin the sample in place, restricting any horizontal or vertical movement at the sample ends, whilst allowing it to rotate freely in a vertically upwards motion. The horizontal displacement was measured by the attached dial gauge to an accuracy of ± 1 μm. The electrical resistance of the sample is continuously measured in a 4T configuration.

The stepper motor was controlled by a trigger that could be selected to produce either a 20 μm or 200 μm horizontal displacement. This was achieved through, a series of logic gates, pulse generators and an 80 Hz oscillator, in order to signal a Samtronic-101 drive motor. The trigger could be either through a manual switch or via remote operation. The remote operation was controlled by a LabView program so that the process of measuring the resistance whilst the composite strain was incremented was completely automated.

3.5.2 Low Temperature Bend

Ideally a similar set-up to the one described above would be used to control the bend at low temperatures, 77 K. However this was not possible because the composite bend must be altered above the glass transition temperature with the composite then cooled down again to 77 K. Therefore the set-up was required to cope with regular thermal cycling by having a low thermal mass without any electronic components, while still being able to provide an actuate and calibrated *horizontal displacement* of the sample.

The solution was to use a lead screw actuator, in a similar way to the stepper motor for the room temperature set-up, to control the horizontal displacement between two aluminium plates, shown in figure 3-10(a). PTFE blocks were attached to the plates and had grooves cut into them to hold the sample in place. The set-up could be inverted and placed on a long probe so that it could be fully

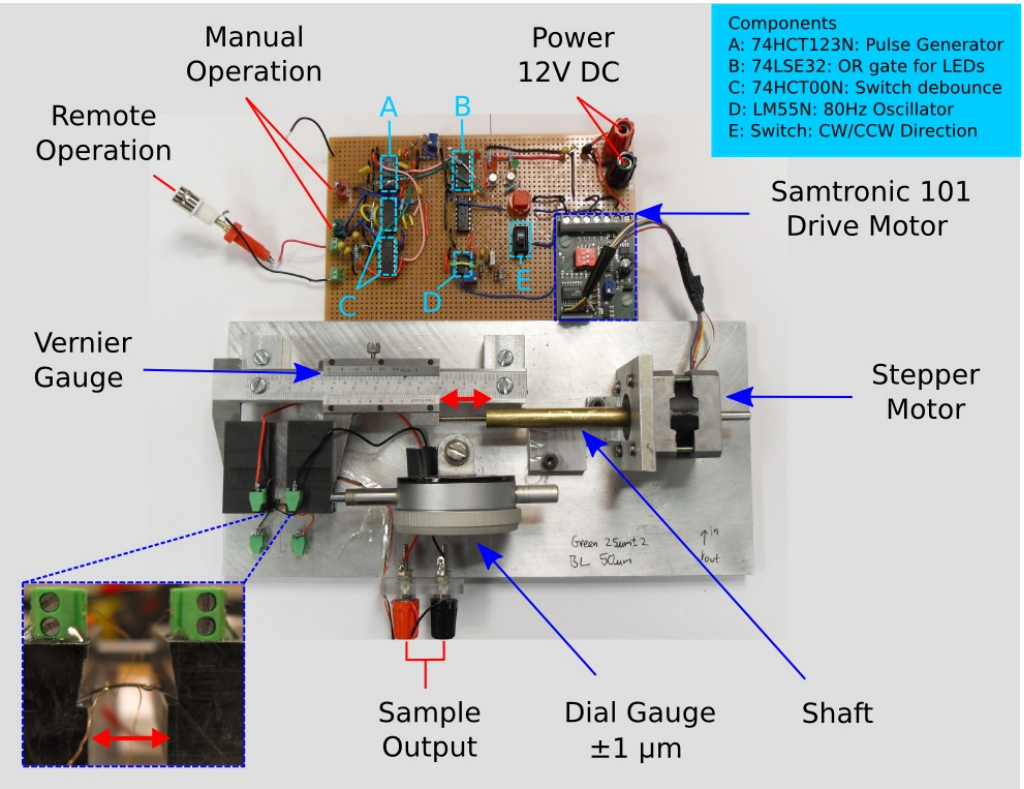

Figure 3-9: The bend in the composite at room temperature was precisely controlled through a stepper motor functioning as a linear actuator. Step sizes of 25 μm were triggered from mechanical switching or through remote operation with a 5 V pulse.

(a) (b) (c)

Figure 3-10: (a) The low temperature lead screw linear actuator is placed on a probe so that it can be lowered into a flask of liquid nitrogen. (b) Photos of the sample flat and in compressive strain. (c) Schematic showing the calculation of bend radius, ρ, as a function of the horizontal displacement.

immersed into liquid nitrogen.

The lead screw has a 1/4 inch Whitworth thread with a pitch of 0.05 inch (20 threads per inch). Such that for each 45° turn of the screw the horizontal displacement is 160 μm. This is clearly not as accurate as the 25 μm step size for the room temperature experiment however the screw could be turned 1.5 turns times, whilst bending the composite elastically, corresponding to 12 steps. The greatest error comes from human error of lining up the guiding lines to ensure that the screw is turned exactly through 45°. Other problems were that the screw thread was not perfectly homogeneous with some rust build up over time. In reversing the direction of movement it was difficult to consistently compensate for the backlash. With experience it was found that a 90° counter turn was required.

Although there are many ways in which this crude set-up could be improved with careful user handling it was able to provide consistent and repeatable bends in the sample. To calibrate and confirm that the set-up was producing the desired bend radius a camera was used to photo the bend for each 45° turn, an example for two bends are shown in figure 3-10(b). By fitting an arc to the photos, it was possible to calculate the exact bend radius. This was in good agreement with the bend radius calculated from the number of screw turns and the length of sample. The method used to calculate the bend radius, and the resulting bend induced bilayer strain in the sample is now given.

3.5.3 Calculation of Bilayer Strain

To find the *bend induced bilayer strain* of the composite the bend radius, ρ, must first be calculated. Through knowledge of either the number of steps, of the stepper motor, or the number of screw turns, in the low temperature system, and the initial length of the sample, l_0, the horizontal distance, l, between the two supports can be found. Using the schematic in figure 3-10(c) we use trigonometric functions to find the relationship between l and ρ as:

$$\left.\begin{aligned} l_0 &= \theta\rho \\ l &= 2\rho\sin(\theta/2) \end{aligned}\right\} \quad l = 2\rho\sin\left(\frac{l_0}{2\rho}\right), \tag{3.3}$$

taking θ as the angle in radians of the circular sector, with arc length, l_0, chord l and radius ρ. Equation 3.3 then be put in terms of the horizontal compression, η such that:

$$\eta = \frac{l_0 - l}{l_0} = 1 - \frac{\sin\left(\frac{l_0}{2\rho}\right)}{\left(\frac{l_0}{2\rho}\right)} = 1 - \mathrm{sinc}\left(\frac{l_0}{2\rho}\right). \tag{3.4}$$

Expanding this as a Talyor series and taking the first order terms we find that:

$$\eta = \frac{1}{24}\left(\frac{l_0}{\rho}\right)^2 \quad \Rightarrow \quad \frac{1}{\rho} = \frac{\sqrt{24\eta}}{l_0}, \tag{3.5}$$

gives the bend radius, ρ as a function of the horizontal compression, η.

Next to find the induced strain in the composite we must consider the acetate and the composite as a bilayer system. The radius of curvature can be related to the strain, ε, thickness, a and Young's modulus, E, of each layer where the composite layer is denoted by the subscript 1 and the acetate by subscript 2, through Timoshenko's equation for bend in bilayer systems [80],

$$\frac{1}{\rho} = \frac{6(\varepsilon_2 - \varepsilon_1)(m+1)^2}{h\big(3(1+m)^2) + (1+mn)(m^2 + 1/mn)\big)}\,, \tag{3.6}$$

where,

$$m = \frac{a_1}{a_2} \quad ; \quad n = \frac{E_1}{E_2} \quad ; \quad h = a_1 + a_2\,.$$

The composite and the acetate have approximately the same thickness: $a_1 = a_2 = 100\ \mu$m which allows equation 3.6 to be simplified, using $m = 1$ and $h = a_1 + a_2$,

and rearranged to find an expression for the differential strain, $\Delta\varepsilon$,

$$\Delta\varepsilon = \varepsilon_2 - \varepsilon_1 = \frac{h(14 + n + 1/n)}{24\rho}\,, \tag{3.7}$$

Combining equation 3.7 with equation 3.5 we find the *bilayer strain* as,

$$\varepsilon(\eta) = \frac{h}{l_0}\left(14 + \frac{E_1}{E_2} + \frac{E_2}{E_1}\right)\sqrt{\frac{\eta}{24}}\,, \tag{3.8}$$

where $E_1 \approx 4$ MPa and $E_2 \approx 400$ MPa are the Young's moduli of the composite and acetate respectively; and $h = 200$ μm is the combined thickness of the composite and acetate. Equation 3.8 allows the *bilayer strain* to be found as a function of only the change in horizontal compression. When the composite is placed in compressive strain ε is negative and for a tensile strain ε is positive. Bilayer strains of up to $\pm 20\%$ can be used to elastically deform the composite. Straining the composite-acetate system to $|\epsilon| > 20\%$ leads to a permanent deformation.

3.6 Differential Pressure Array

3.6.1 Concept

The DPA was built to demonstrate that the piezoresistive spiking properties of GSCs can be utilized in an imaging device. To achieve this an 8 by 8 array of 64 individual composite samples, *pixels*, were formed on a PCB board. Each composite pixel can be *individually addressed* using a control circuit. The control electronics were constructed such that each pixel resistance could be measured four times a second. This enables the detection of sharp resistance spikes caused by the destruction of conduction lines from a pressure perturbation, a differential pressure. The control circuit was specifically designed to be electronically isolated from the sample signal through an optocoupler and transistor components to allow the composite to be biased into the NDR region.

3.6.2 Design

To individually measure the resistance of each composite without requiring the use of separate contacts for each pixel, row-column (read -write) lines were used. In order to only measure the resistance of the addressed composite a transistor in series with each composite was required that switches on the current path only

for the addressed composite. The in situ transistor is switched by column (write) lines that apply a 5 V gate voltage.

The sample signal is then measured between the row (read) line and the ground of the transistor, having passed through the composite and the drain-source of the transistor. In total $8 + 8 + 1 = 17$ (row+column+ground) contacts are required to address every individual composite in the array rather than the $8^2 + 1 = 65$ required if the in situ transistors were not used.

To enable a pixel resolution of 10 dpi an array with 2.54 mm (0.1 inch) spacing between each composite center was used. Each composite forms a 2 mm by 2 mm square so that there is a 0.54 mm space between composite pixels. The total array has sides of 19.8 mm.

The row and column lines were fabricated on separate PCB boards, forming upper and lower layers, shown in figure 3-11(a) and (b). A middle layer was used to combine the upper and lower layers and lock the structure together.

Holes were drilled through the three layers to allow the composite to form the connection between the row-column lines. An automated drilling system was used to drill the required 64 holes in each layer with a 0.8 mm diameter and an accuracy of ± 5 μm.[4] The layered construction is shown in figure 3-11(a).

The composite is contacted on the top layer through circular copper tracks, figure 3-11(b). The composite then extends 300 μm into the drilled hole where it contacts to a metal pin. The pin, held in place by the middle layer, passes through to the bottom layer where it is soldered to the drain of the transistor. The circular copper track has a width of 0.4 mm and total diameter 1.8 mm giving the drilled hole a clearance of 0.1 mm. The track has a surface area of 1.76 mm^2 to contact to the composite. The contact area with the pin below is 0.5 mm^2.

3.6.3 Electronics

The electronics was designed to sense the resistance of each individual composite pixel in the array through a *raster scan*. A raster scan being where each a row of pixels is addressed and every pixel in that row is then addressed individually, before progressing to the next row. The aim was to enable a resistance image of the 8 by 8 pressure array to be continually updated at a raster scan rate of 4 Hz, i.e the whole array being addressed four times every second.

[4]The drilling was done by Paul Reddish, technician for the Physics Department at the University of Bath

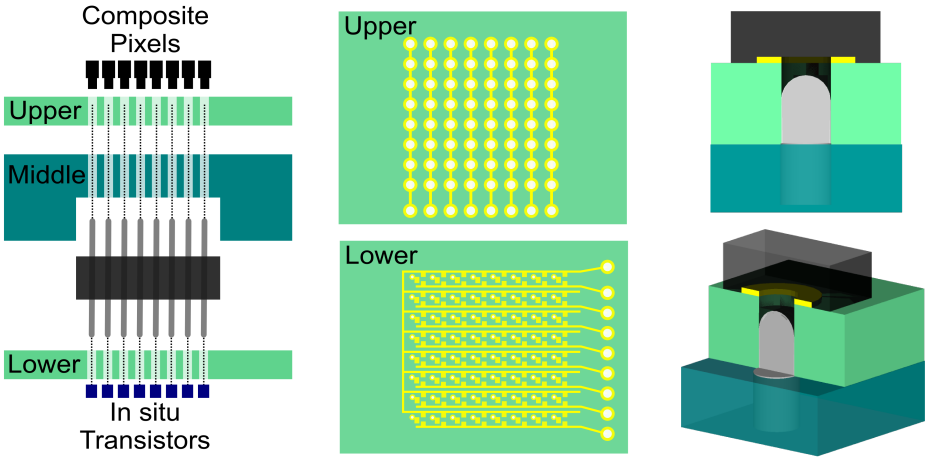

(a) (b) (c)

Figure 3-11: (a) The upper, middle and lower layers of the device. The composite pixels are formed on the upper layer and the transistors soldered to the lower layer. Metallic pins extend through the middle section that lock the device together. (b) The PCB designs of the upper and lower layers. The upper layer holds the row (read) lines and the lower layer the columns (write) lines which run perpendicular to one another. (c) A cross sectional schematic showing the pin, the bottom contact, coming out of the middle layer and part way into the upper layer. The composite is formed on the circular upper track and extends down onto the pin creating the electrical contact between the row and column.

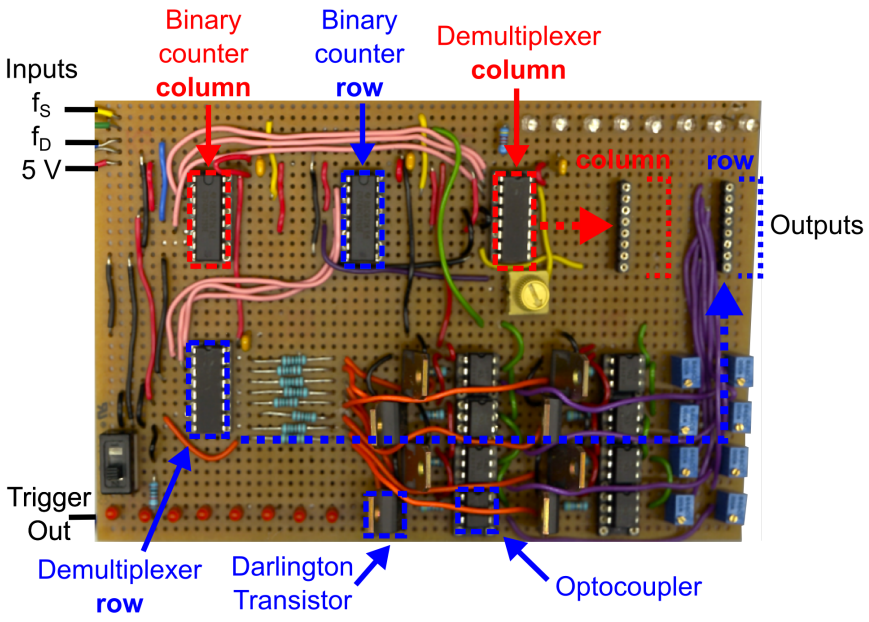

Figure 3-12: The switching circuit that automates the addressing of each composite pixel of the DPA in turn. The row and column counters control which composite pixel is addressed while the Darlington transistor - optocoupler system decouples the switching circuit from the input signal to the composite.

The in situ transistors for switching each composite pixel were N-channel MOSFET's in a SC-75 package. They are suited to this application as they are small, have fast switching times, < 20 ns and low on-resistance of $< 1\ \Omega$.

The composite address system worked by addressing one row and and then each column in turn before addressing the next row. The timing was controlled via the switching circuit in figure 3-12. The role of the key components is as follows.

Binary Counter The binary counters signal the demultiplexer which row or column to address. As the array is 8 by 8 the 4th bit is not required therefore they are used as 3-bit counters that count from 0 to 7. To enable synchronisation between addressing rows and columns (sweeping the column for each row) the row counter is driven at a frequency set by the output of the first column. Each time a column sweep is completed the next row is then addressed.

Demultiplexer The demultiplexer converts the 3-bit binary count to eight individual outputs. The column demultiplexer switches the in situ transistors off and on (0 or 5 V). The row demultiplexer switches the Darlington transistors off and on (0 or 5 V).

Darlington Transistor The NPN Darlington transistors switch a current of 50 mA, off or on, into the optocoupler. The Darlington transistors, which are two bipolar transistors in series, have a high current gain and allow large currents to be switched.

Optocoupler The optocoupler is an integrated GaAs LED and silicone NPN phototransistor. When the current is applied, switched by the Darlington transistors, the internal infrared LED lights and emits photons that incident on the internal phototransistor allowing a current to flow to the composite. The optocoupler allows the control circuit and composite signal to be completely electronically isolated.

3.6.4 Composite Pixels

The GSC were formed on the device through using a template of 64, 2 mm sized squares with a spacing of 0.54 mm. The template was aligned and secured over the drilled holes and circular tracks. A composite of $p = 34.8$ %, that included 2% NDI-Si, was firmly spread into the template to push the composite into the 0.8 mm diameter holes and enable contact with the metal pin. The composite was allowed to cure for 48 hours. A removal template was used to hold the composite squares in position while the template was lifted away to ensure the contacts of the composite pixels to the device were not damaged. The 64 composite array can be seen in figure 3-13. The resistance of each individual composite was measured to be 6 ± 2 kΩ. Its difficult to calculate the exact resistivity, ρ, of the composite due to geometry of the pixel, however we can estimate that the composite conducts through a cylinder of radius 0.4 mm and length 0.4 mm to find $\rho = 7.5$ Ωm. This is higher than would be expected for this filling fraction of composite and is due to contact resistance which mainly arises from the small contact area of the metallic pin.

3.6.5 Data Collection

The overall circuit to control the DPA is shown in figure 3-14. To enable continuous and fast acquisition for the resistance of each array element an Agilent DSO6014A oscilloscope was used that interfaces directly with LabView via USB for quick data transfer.

Two frequency generators are required. One to produce the measurement signal at the sample frequency of $f_S = 10$ kHz. The second frequency generator

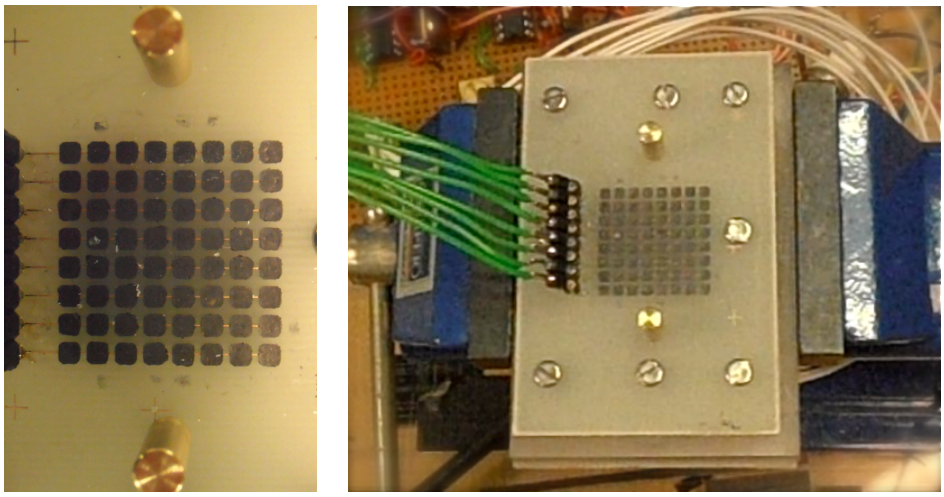

(a) (b)

Figure 3-13: (a) The 64 composite pixels are 2 mm by 2 mm. The circular pillars seen at the top and bottom are guides for sliding the stamp into position. (b) The compete device is held in a vice for stability. The green wires address the eight rows and the white wires seen in the background are for addressing the eight columns.

drives the switching speed of the composite address system. The drive frequency was set to $f_D = 1$ kHz.

The oscilloscope then measures the amplitude of the measurement signal, that passes through the addressed composite pixel and into a resistor to ground, to find the resistance of the pixels. The oscilloscope records a continuous waveform of 10 kHz. As the addressing of the composites is being switched at a drive frequency ten times slower than the sample frequency, ten oscillations are recorded per composite, before the next composite is addressed. The switching is almost instantaneous.

To determine which signal portion is attributable for which composite a trigger signal is used to indicate when the first composite of the raster scan is addressed. Knowing the start location, the waveform can then be split into 64 segments of ten oscillations each. The mean amplitude for each segment is measured to determine the resistance of each of the 64 composite pixels in the array. This process of switching, data acquisition and analysis for all the pixels in the array is repeated four times a second, yielding a raster scan frequency of 4 Hz.

The device is designed for the detection of perturbations that cause the resistance to spike. Therefore for each composite, i, we compute the rolling point by point mean of the resistance using the previous twenty measurements, $\bar{R}_i$, and

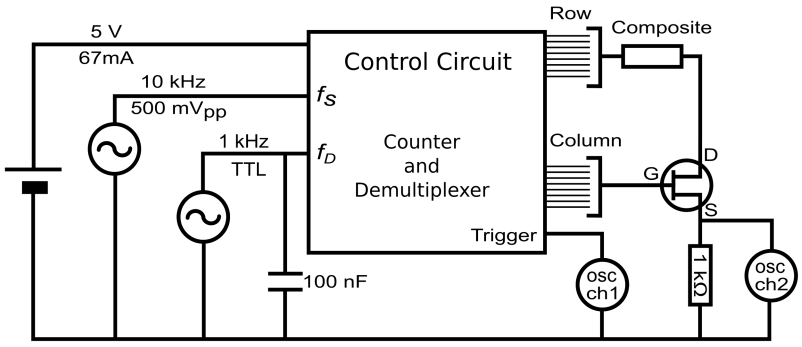

Figure 3-14: The control circuit for the DPA. Two function generators are required: One to generate the signal applied to the composite, f_S, and the other to drive the switching between composite pixels at frequency, f_D. The output of the composite pixel is measured via a potential divider circuit with a 1 kΩ resistor in series. The oscilloscope is triggered by a trigger led from the output of row one that enables the signal to be matched and divided up for each composite pixel.

compare this to the current R_i such that,

$$\frac{\bar{R}_i - R_i}{R_i} = \Delta R_i \,. \tag{3.9}$$

When there is a large change in ΔR_i the composite has been triggered. A sensitivity, S, sets the minimum required change in ΔR_i to say that the pixel has been triggered. A graphical representation of a grid of 64 black or white squares is used, with each pixel corresponding to a different square. If $\Delta R_i > S$ the square corresponding to pixel i changes colour from black to white.

As the resistance changes quickly a forced timeout for a triggered element is then used; this enables the user to identify which composite pixels have been triggered; allows the resistance to decay back to a lower value; and for $\bar{R}_i$ to settle. Typically a sensitivity of $S = 0.15$ was used with a timeout of ten seconds.

3.7 Summary

This chapter has given details for the preparation a GSC fabricated at the University of Bath. The experimental difficulties of incorporating high filling fractions of graphite nanoparticles into the matrix have been explained and the methods used to overcome them. Clearly more automated methods for mixing large batches would be desirable however for the small quantities required it was found manual mixing was most successful. The different mounts used for the composite were described in detail. The imprint lithography technique developed is very exciting and original. Although no results from these samples have been included in this thesis the technique described here offers a lot of potential for future fabrication of composite devices.

The influence on the composite miscibility and resistivity due to incorporation of functionalized naphthalene centered molecules is given. Of the four different molecules tested NDI-Si caused the greatest decrease in resistance of the composite, as the NDI core sticks to the graphite surfaces through $\pi - \pi$ interaction and the silicone appendages polymerize with the surrounding matrix. This anchors the particles into the polymer to provide better particle dispersions, leading to increased miscibility and lower resistivity of the composite.

The methods for inducing strain in the composite are also shown. Although the method utilized at low temperatures appears crude with accurate and careful operation it does provide consistent results, with bending being a well controlled way to induce bilayer strain. There is clearly still a lot of potential for this set-up to be improved upon though. The method for calculating the bilayer strain based on the Timoshenko equation has been derived.

Finally a detailed account of the construction and measurement for the DPA system has been given. This device is novel in that it is designed not to measure the piezoresistive response of the composite per se but instead to detect the resistive spike caused through conduction destruction, due to a perturbation such as the application of pressure. The array of 64 individual composite pixels is designed to demonstrate basic imaging of shapes with a raster scan frequency of 4 Hz.

Chapter 4

Tunneling Negative Differential Resistance in a GSC

This chapter describes the discovery of a wide NDR region in a GSC at low temperatures. Experimental and theoretical evidence is used to demonstrate that the NDR originates from a *semi-metal to insulator* transition of embedded bilayers in specifically orientated graphite nanoparticles. NDR has not been observed before in a GSCs and could be exploited to create flexible oscillators and amplifiers, realizing flexible *active* electronic devices.

4.1 Introduction

This chapter concerns the NDR observed during measurement of the $I-V$ characteristics of a GSC at 77 K. [1] The composite undergoes a transition from being ohmic, with the current increasing linearly with voltage, to above a peak voltage, the current then steadily *decreasing* with further increasing voltage. This is negative *differential* resistance. It is not a negative resistance, which is a physical impossibility but rather NDR refers to the slope of the $I-V$ curves being negative, i.e. $\frac{\mathrm{d}V}{\mathrm{d}I} < 0$. The presence of a wide NDR region, to the best of our knowledge, has not been previously reported in a GSC. The presence of a NDR region enables the composite to be utilized as a flexible active device.

NDR is most commonly associated with inorganic semiconductor structures that have specially engineered band-structure properties, such as tunneling diodes (TD). In these devices the NDR occurs through combining highly doped p and n regions to create a narrow depletion region, < 5 nm. Electrons can readily

[1] First recorded in 2009 with lab partner James Stretton at the University of Bath

tunnel, under forward bias, from the conduction band of the n region into like energy states in the valence band of the p region. Increasing the bias across the junction eventually causes a misalignment between the energy of available states and that of the carriers. This means the electrons are no longer so easily able to tunnel, hence the current decreases as the voltage is further increased. The $I - V$ characteristics are decribed as N shaped, as at a high bias the current again increases due to the barrier having become transparent, and thermal and indirect tunneling currents dominating.

In TD the NDR only takes places due to the carefully engineered narrow depletion region which is a high cost, clean room specific process. The same is true for resonant tunneling diodes (RTD) where, although the tunneling mechanism is different, a very particular double tunneling barrier structure is also required. Whereas, the NDR we observe in our composite comes about in a low cost, bench-top chemistry fabricated, material of randomly dispersed graphite nanoparticles in a silicone matrix. The composite does not have a specifically engineered barrier structure and the NDR occurs through a very different process.

It should also be mentioned that NDR has been observed in some organic molecules and composites. For example in polymer tunnel diodes where the origins of the NDR again relates to narrow tunneling regions [81]. NDR has also been reported for metallic nanoparticles in organic semiconductor composites. The shape of the NDR in this scenario is very different with the current dropping sharply, almost to zero, above a certain voltage threshold and exhibiting a substantial hysteresis. The NDR is caused through a charge trapping mechanism that makes these devices bistable [82, 83]. This is useful for electronic switching devices but with no stable NDR region they cannot be used as oscillators or amplifiers [84].

Here we present NDR in a GSC that is wide and exhibits little hysteresis. We study the effects of volume fraction, voltage probe separation, particle type and temperature dependence on the NDR. We then support the experimental evidence with theoretical calculations, including calculation of the LDOS in graphite and the tunneling current through a single barrier to find that the NDR occurs due to a *semi-metal* to *insulator* transition of embedded bilayers in specifically *orientated* graphite nanoparticles.

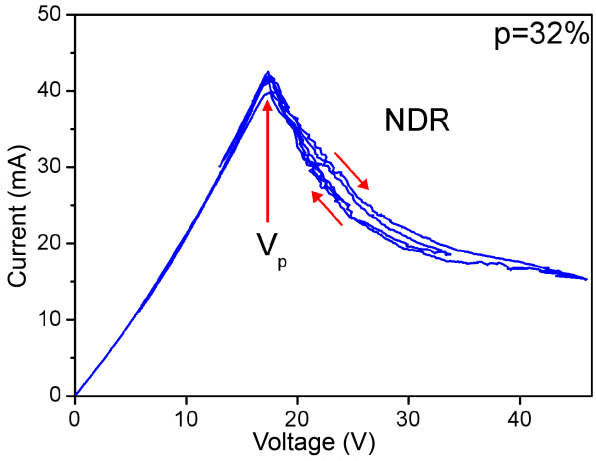

Figure 4-1: The typical $I-V$ characteristics of a GSC. Below V_P the sample is ohmic. At V_P a sharp transition occurs after which the current decreases with increasing voltage, creating the NDR region. Repeated sweeping of the voltage shows little hysteresis and the transition remains sharp even after many hundreds of cycles.

4.2 Results

4.2.1 Negative Differential Resistance

In measuring the $I-V$ characteristics of a GSC a sharp transition is observed at a voltage, V_P, figure 4-1. Before V_P the sample is approximately ohmic with the current almost increasing linearly with voltage. Above V_P the current sharply decreases and continues to do so while V increases. This leads to a wide NDR region which has four outstanding features:

1. The transition around V_P is sharp and distinct.

2. The NDR extends indefinitely with increasing V with the current continually decreasing.

3. The transition is robust surviving hundreds of cycles of bias voltage with little hysteresis.

4. The $I-V$ curves are completely symmetric under a negative bias.

NDR with these features has not been seen before in composites. The sharp, distinct transition that is robust and remains over many cycles, indicates that the NDR cannot be thermally induced or be caused by a dielectric breakdown.

The presence of little hysteresis rules out any exotic charge trapping mechanism such as those seen in granular metallic composite while the symmetry under the reversed bias direction means the NDR is of a completely different nature to that of a tunneling diode.

Above V_P there are current fluctuations that we interpret as the rerouting of conduction lines. The NDR can be described as wide as it extends indefinitely up to voltages as high as 120 V. The current peak to valley ratio in figure 4-1 is around 2.5. This is significant as a peak to valley ratio of 5 is considered high for some RTD devices [85].

4.2.2 Volume Fraction Dependence

The dependence of the $I-V$ characteristics on the graphite particle filling fraction, p, was investigated, figure 4-2. As expected from percolation theory, explained in section 2.4, the low field conductivity varies significantly with p, dropping from $\sigma_0 = 8$ mS at $p = 34.2\%$ to just $\sigma_0 = 0.06$ mS at $p = 25.5\%$. A fit of equation 2.9, figure 4-2(inset), yields a critical threshold of $p = 24\%$ and power law exponent of $t = 4$ such that:

$$\sigma = \sigma_0 (p - 0.24)^4 \,. \tag{4.1}$$

This is characteristic of percolation through a network of conductive nanoparticles. As t is significantly greater than that of the universal percolation model value of $t = 2$ we can infer that a significant amount of tunneling is taking place between particles. While a value of $p_c = 24\%$ is expected for a homogeneous dispersion of particles.

The maximum filling fraction is close to $p = 35\%$, above this value it is not possible to homogeneously disperse any more graphite particles into the silicone as the silicone is saturated.

The current peak shows a systematic shift in peak position from 12 V at 34.2% to 115 V at 25.6%. All the composites exhibit a sharp transition as well as current instabilities in the NDR region. The peak current decreases from 94 mA at 34.2% to 7 mA at 25.6%. The shift in peak is due to the higher filling fractions of graphite producing a narrower tunneling barrier that becomes transparent for a lower bias.

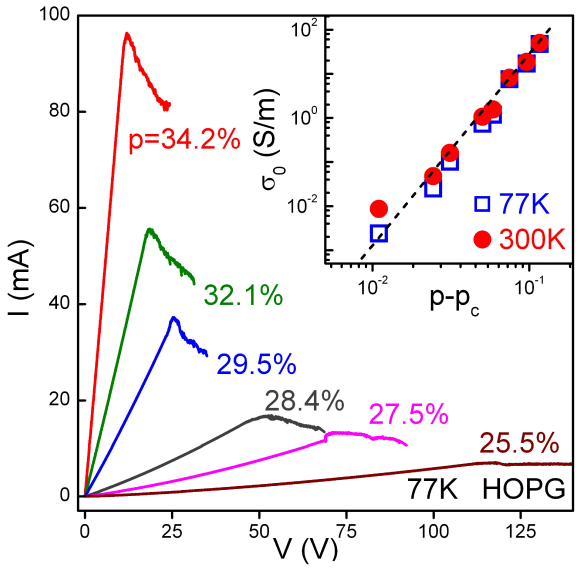

Figure 4-2: Decreasing the filling fraction, p, from 34.2% to 25.5% causes the zero field conductivity, σ_0, to decrease and the onset voltage, V_P, to increase. (inset) A log-log plot of σ_0 against $p - p_c$ yields a linear slope with gradient 4 and $p_c = 24\%$ which indicates non-universal percolation behaviour due to *tunneling* between particles

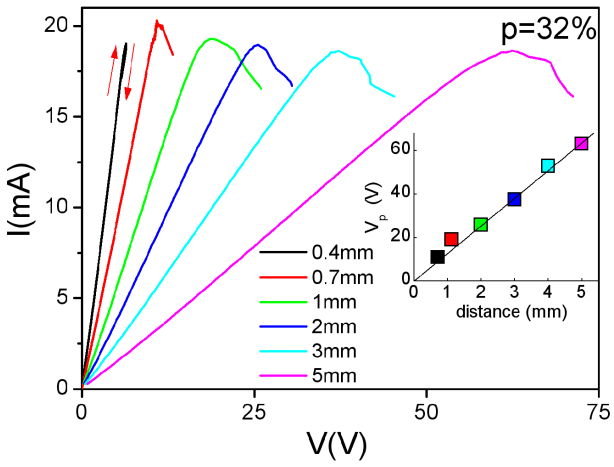

Figure 4-3: $I - V$ characteristics for different voltage probe separations. For the smallest probe separations we often see a local potential decrease even as the external voltage is being increased. This is due to the formation of highly resistive domain boundaries. (inset) A plot of V_P with probe separation distance yields a linear slope through the origin showing the onset of NDR is at a constant field, $E_P = 12$ kVm^{-1}

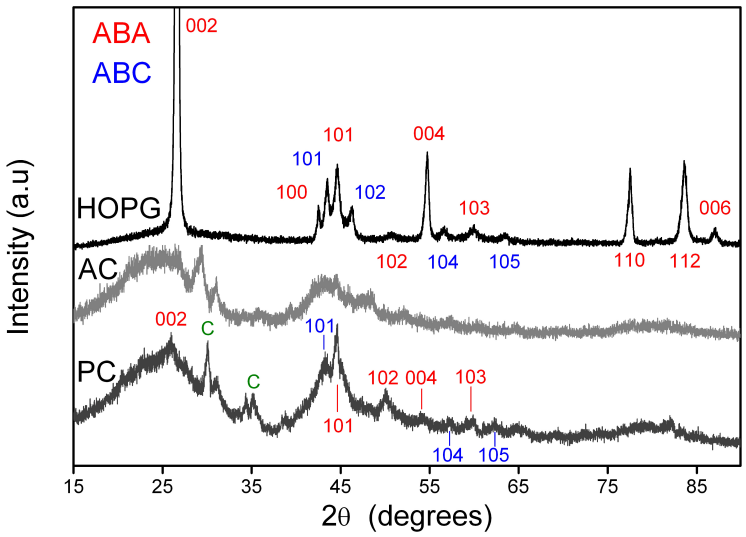

Figure 4-4: Powder XRD data for the three types of nanoparticles. The HOPG has a high degree of crystalline structure evidenced by sharp diffraction peaks. The AC is entirely amorphous with no crystalline structure. Annealing the AC particles restores some crystalline structure in the PC particles. Development of sp^2 structure is evidenced by the resurgence of the (101) peaks.

4.2.3 Electric Field Domains

The $I-V$ curves were next measured over different lengths of composite for the 4T set-up shown in section 3.4. The peak voltage increases linearly with the voltage probe separation, figure 4-3(inset). This demonstrates that the electric field is spatially homogeneous up to the peak where it reaches the maximum field, E_P. Where E_P can be found from the gradient of the linear fit of distance with potential from figure 4-3(inset) equal to $E_P = 12$ kVm^{-1}. Beyond V_P the NDR is present for ribbons of length greater than 0.6 mm. Over shorter distances the current increases up to a peak value E_P but then decreases retracing the same $I-V$ curve while the 2T bias voltage across the current contacts is still increasing.

This behaviour can only be explained by the sample fragmenting into electric field domains at the peak. The domains develop highly resistive boundaries that sustain the extra voltage seen in the NDR region and account for the drop in current.

4.2.4 Crystalline Structure of Conductive Particles

Three allotropic forms of carbon were used to study the effect of the filler crystallographic structure on the $I-V$ curves of the composite. The first was highly ordered pyrolytic graphite (HOPG) nanoparticles, 450 nm in size. The second

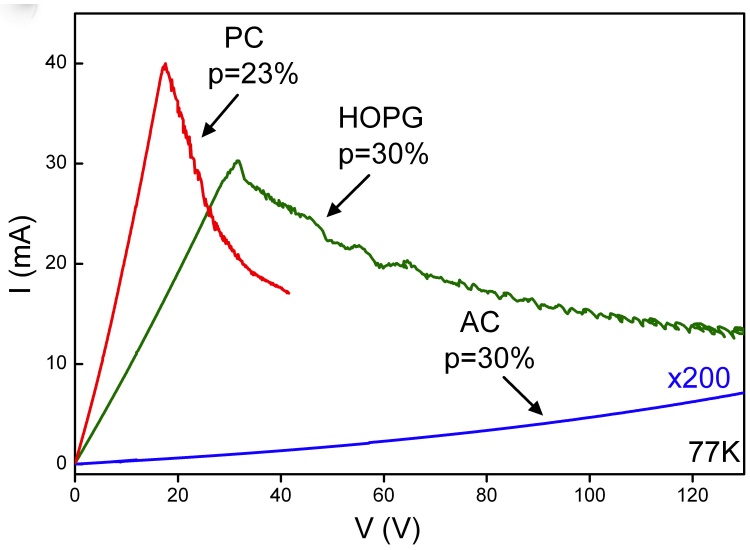

Figure 4-5: $I - V$ curves for the three types of filler particle. Sharp NDR is observed for both HOPG and PC particles, which has crystalline structure, and AC have a low conductivity and no NDR even up to 130 V.

allotrope was an amorphous carbon (AC) nanoparticle of diameter 50 nm (Sigma-Aldrich, 63100) and the third a pyrolytic carbon (PC) nanoparticle also of 50 nm. We obtained the PC through annealing the AC at $1,100°$C for 1 hour in hydrogen.[2]

Powder XRD[3] was used to analyse the extent of crystallisation for each allotropic particle type. The HOPG particles have a high degree of crystalline structure made evident by sharp distinct peaks in figure 4-4. Close inspection reveals a quadruplet of peaks around the (101) and (102) lines which shows the HOPG has planes stacked in two structures AB and ABC. The ABC form is not uncommon is HOPG and is often referred to as rhombohedral graphite, due to the shape of its unit cell.

The AC nanoparticles are amorphous with no stacking or hexagonal structure at all. While the PC nanoparticles developed hexagonal sp^2 structure indicated by the resurgence of the (101) peaks. The graphite layers however have random orientations as evident by the faint main diffraction peak. Covalent bonds between the graphene planes give rise to peaks C.

The $I - V$ characteristics for the three allotropic forms of composites of concentrations, HOPG : $p = 30\%$, PC : $p = 23\%$ and AC : $p = 30\%$ are shown in figure 4-5. The presence of NDR in both HOPG and PC composites but not the AC composites links the NDR to a property associated with conduction through

[2]Annealed using Ashok Chauhan's tube furnace at the University of Bath
[3]XRD data measured by Harry Bone, technician at the University of Bath

graphitic planes. The onset of the NDR at a lower potential and lower filling fraction in PC composites is due to a different structure of the particles with the smaller particles offering a greater number of conduction paths.

4.2.5 Temperature Dependence

The $I - V$ curves were recorded for the composite in a temperature controlled cryostat. Increasing the temperature causes the onset of NDR to occur at a lower V_P, decreasing from 32 V at 90 K to 13 V at 200 K, as shown in figure 4-6. This is due to the thermally activated currents leading to a lower effective barrier height of the silicone rubber. This is discussed in more detail when the barrier height is considered in section 4.3.2.

The low field conductivity is roughly constant between 90 K and 200 K with only a slight decrease in resistance for lower temperatures, but at 210 K the resistance increases dramatically by a factor of three. This is because the composite passes through its glass transition temperature, $T_g \approx 200\ K$. This causes an expansion of the matrix and increase in distance between the particles, leading to the resistance increase. Above the glass transition temperature NDR is no longer observed as the tunneling barriers expand under Joule heating [76, 86]. Below the glass transition temperature the matrix is frozen and there is no thermal expansion of the matrix.

4.2.6 Particle Orientations

The presence of a NDR region in both the HOPG and PC composites, but not the AC composites, links the NDR to conduction through graphitic planes. Combine this with the evidence for formation of electric field domains with highly resistive domain boundaries and the knowledge that percolation behaviour cannot by itself be responsible for the NDR and we naturally look for the cause being intrinsic to the graphite nanoparticles. Therefore we turn our attention to consideration of the graphite nanoparticles and their orientations within the matrix to the electric field.

In a composite the nanoparticles are homogeneously and randomly dispersed with random orientations relative to each other. The highly anisotropic nature of graphite means the conductivity of graphite is 3000 times greater across the plane than perpendicular to the plane [35]. By considering the percolation path through the composite we demonstrate that for the majority of HOPG nanoparticles the current flows inside just one graphite plane. In the remaining nanoparticles,

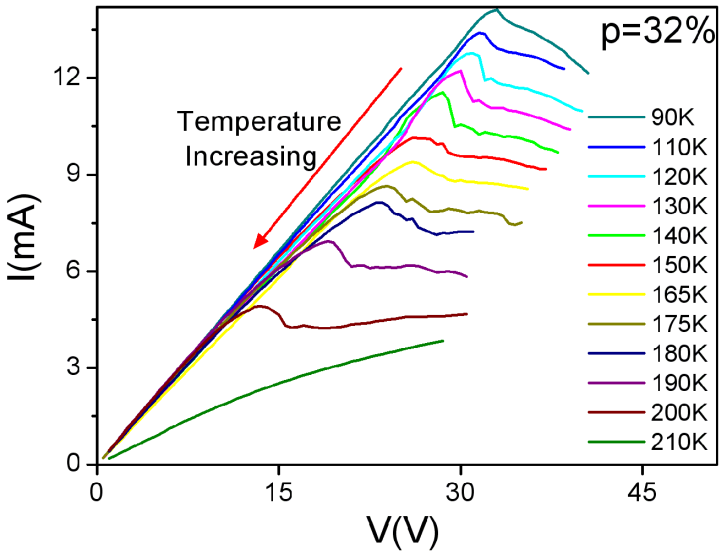

Figure 4-6: Increasing the composite temperature causes V_P to decrease due to thermally activated currents. No NDR region is observed when the composite passes above its glass transition temperature and the low field resistance increases by a factor of three.

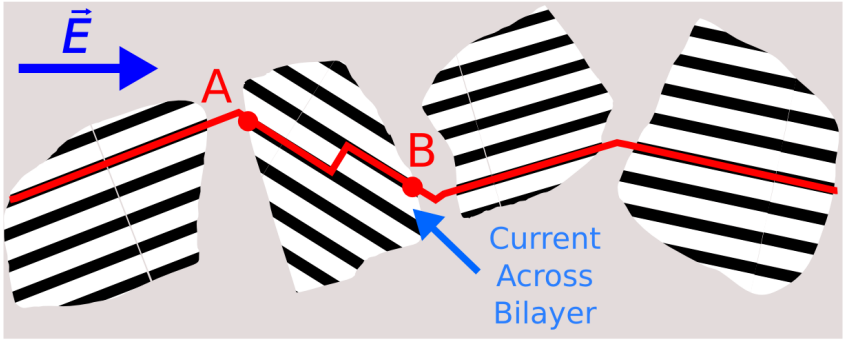

Figure 4-7: A schematic of a conduction line though randomly orientated particles. The black lines indicate a plane of carbon atoms while the particles are intentionally shown as random shapes and sizes (however for 450 nm particles each particle is likely to be around a thousand layers thick). If a particle is angled between 63° and 78° to the electric field the current will cross a bilayer.

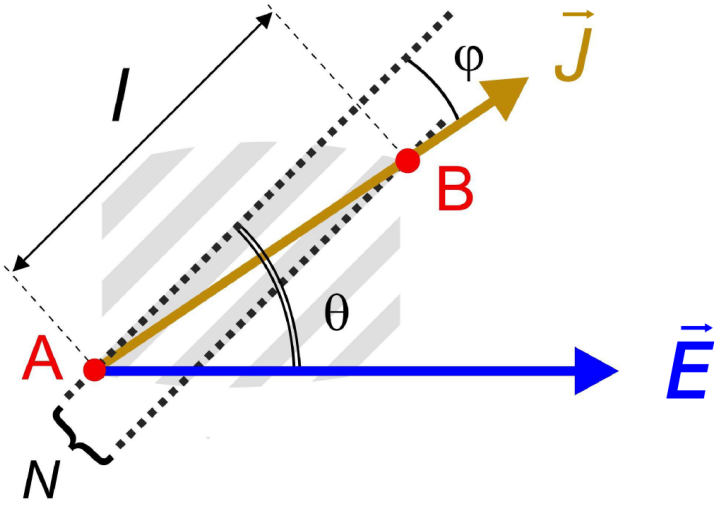

Figure 4-8: The number of layers the current crosses, N, is dependent on the angle, θ, between the graphite planes and the electric field, E. The current will crosses across a bilayer if $63° < \theta < 78°$.

the current jumps one interlayer spacing and rarely more, schematically shown in figure 4-7. Whether a nanoparticle conducts through a graphite monolayer, bilayer or trilayer depends upon the angle θ between its planes and the electric field, $\vec{E}$. Using Ohms law $\vec{J} = \sigma\vec{E}$ we determine the angle ψ between the current density, $\vec{J}$, and the graphite planes. The number of graphite inter-layers, N, between the current entry point A and exit point B of the nanoparticle is then found in terms of the ratio of the in-plane to perpendicular conductivity of graphite, $\frac{\sigma_{\|}}{\sigma_{\perp}} = 3,000$, the distance between graphite planes, $c = 0.335$ nm, and the average length of an HOPG nanoparticle, $l = 450$ nm. Using the construction in figure 4-8(a), we obtain:

$$\tan\varphi = \frac{J_{\perp}}{J_{\|}} = \frac{N\,c}{l}\,, \tag{4.2}$$

rearranging and applying Ohms law,

$$N = \frac{l}{c}\frac{\sigma_{\perp}}{\sigma_{\|}}\tan\theta \simeq 0.448\tan\theta\,. \tag{4.3}$$

Therefore, equation 4.3 tells us that when θ is between 0 and 66°, HOPG nanoparticles will conduct through a single graphite monolayer ($N = 1$). Between 66° and 78° the conduction is through a graphite bilayer ($N = 2$), between 78° and 82° a graphite trilayer (N = 3), and so on.

4.2.7 Embedded Bilayer

The HOPG particles have random orientations in the matrix. If we assume this is with a 3D isotropic distribution, then 93.5% of the particles will be orientated to preferentially conduct across a single plane. For the remaining 6.5%, the current flows into the nanoparticle through one graphite layer (point A), then crosses one interlayer before exiting through the adjacent graphite layer (point B). This means that in a conduction line of fifteen particles it is likely that one will be orientated between 66° and 78° for conduction across a graphene bilayer. For instance in a sample of length 1.5 mm a single conduction line will contain around 220 of these bilayer orientated particles.

At high fields the current crossing one interlayer causes an electric field across a bilayer embedded within the nanoparticle. The potential causes a partial breaking in the conduction band and the particle undergoes a *semi-metal to insulator* transition.

This is because the mostly transverse bias V_{AB} opens a *partial energy gap* at the Fermi level in graphite. This gap is shown in the local density of states plots of figure 4-9. Unlike the gap of the free-standing graphene bilayer, figure 4-10, the gap of the embedded bilayer opens above a threshold $V_{AB} > 2\gamma_2$ corresponding to the energy overlap of the π-band ($2\gamma_2 = 40$ meV). The gap is partial. Nevertheless, it is sufficiently well defined to induce a semi-metal to insulator transition since the density of states at the Fermi level drops from 100% at 0 V to just 3% at 0.6 V. We conclude that nanoparticles tilted at an angle between 66° and 78° develop a high resistance that breaks the composite into domains of constant electric field, E_P.

4.2.8 NDR Mechanism in a Graphite-Silicone Composite

The composite has a three dimensional percolation network with many interlinked conduction lines. Preferentially the electrons take the paths of least resistance as they tunnel between graphite particles. Due to the length of the particles, one in fifteen of these particles are orientated to the electric field such that conduction takes place across a bilayer embedded in the nanoparticle. At low fields this makes little difference to the conduction as most of the resistance arises from the tunneling barrier. However, when the barrier becomes significantly biased, so that it becomes transparent, an electric field is applied across the bilayer. This leads to a partial breaking of the conduction band, in a similar way to that of a double gated bilayer graphene discussed in section 2.2.3. The particle undergoes

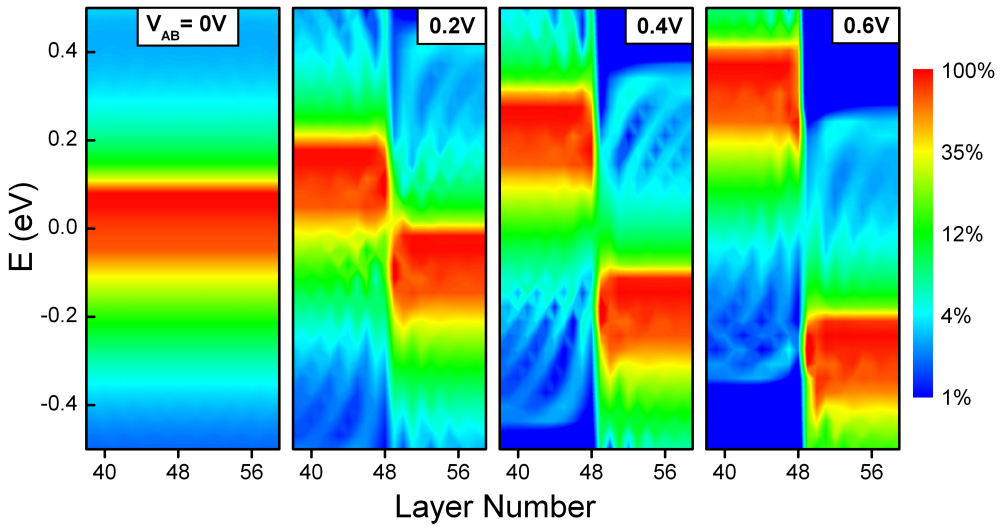

Figure 4-9: Pseudo-continuous representation of the calculated layer-resolved LDOS of the π-band associated with c-axis transport in graphite, indicating the relative availability of electron states at different energies. A potential with the indicated value has been applied across the central layers, 49-50, resulting in a partial breaking of the π-band. Note the data has been normalised and a logarithmic color-scale used. (Calculation by Dr Simon Crampin, Physics Department, University of Bath)

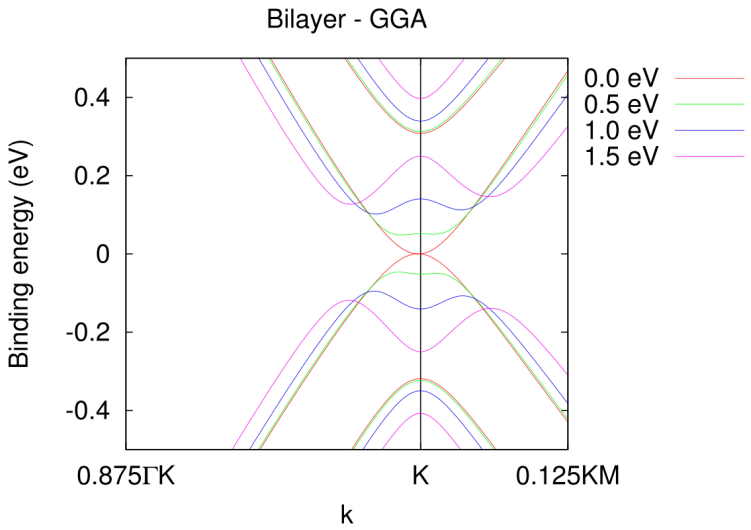

Figure 4-10: Band structure of free standing bilayer graphene showing the classic Mexican hat structure, around the K point, as a potential is applied across the layers [4]. (Calculation and figure by Dr Simon Crampin, Physics Department, University of Bath)

a semi-metal to insulator transition and the current decreases.

It is likely that the current will try to reroute through different conduction lines to avoid the high resistance particle, but which ever path it takes it will most likely encounter another bilayer particle in the conduction line. Either by passing through the bilayer particle, with the broken conduction band; or by rerouting along a longer conduction line; or through having to tunnel greater distances to avoid the higher resistance particles; the resistance increases significantly. This causes the bulk current to drop sharply and as the field is further increased the breaking of the conduction band becomes greater causing the current to decrease further. This causes the observed wide NDR region of figure 4-1. The rerouting process explains the current fluctuations seen in the NDR region. Once the highly resistive domains are established the potential dropped elsewhere in the composite will decrease, even as the external potential is increased. Thus in measuring the potential outside of the resistive domain a potential decrease is observed as seen in figure 4-3.

4.3 Modelling the Current Across a Graphite-Silicone-Graphite Domain

We model the $I-V$ curves of a single graphite-silicone-graphite system to understand the NDR and its dependence on the barrier width and height. The graphite particle is assumed to be orientated such that conduction is through a bilayer. We employ the tunneling current equation derived in section 2.5 but with a modification to allow for bias to be dropped across both the barrier V_{BC} and the graphite V_{AB}, of figure 4-11. The effective mass of electrons in the emitter, $m^* = \gamma_1/(2v_F^2)$, where γ_1 is the coupling between nearest neighbour graphite atoms in the plane and v_F is the electron velocity at the Dirac point with $v_F \approx 10^6$ ms^{-1}. The angle between the current density and the graphite planes is ψ, shown in figure 4-8. Thus equation 2.41 becomes,

$$J = \frac{e\gamma_1 k_B T}{(2\pi)^2 \hbar^3 v_F^2} \int_{\epsilon_F}^{\infty} Z(E_z) F(E_z)\, \mathrm{d}E_z \tag{4.4}$$

where

$$F(E_Z, T, V_{BC}, V_{AB}) = \ln\left(\frac{1+\exp\left(-\beta(E_z + eV_{AB}/2)\right)}{1+\exp\left(-\beta\left(E_z + (eV_{AB}\sin\psi)/2 + eV_{BC}\right)\right)}\right) \tag{4.5}$$

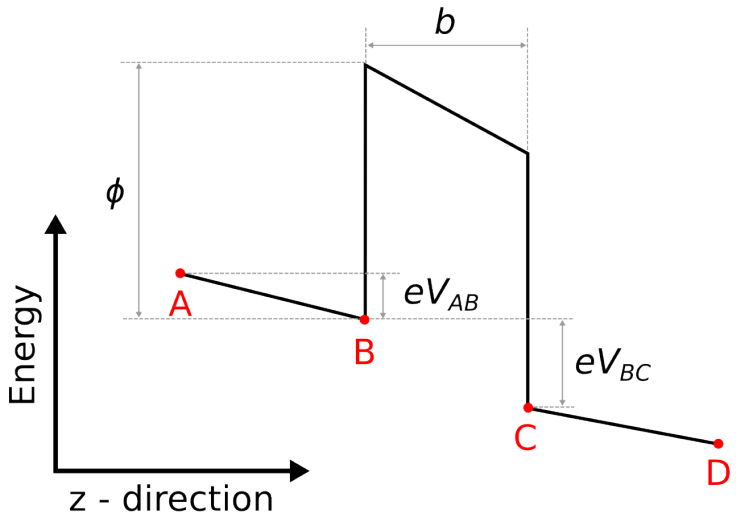

Figure 4-11: Model of a single graphite-silicone-graphite barrier. Extended from the barrier model, shown in section 2.5, by including the bias dropped across the graphite layer V_{AB}.

and

$$Z(E_z, V_{BC}) = exp\left(\frac{-4(2m)^{1/2}b}{3eV\hbar}\left[(\phi - E_z)^{3/2} - (\phi - E_z - eV_{BC})^{3/2}\right]\right) \quad (4.6)$$

Equation 4.4 incorporates both the thermally activated and the tunneling currents. The supply function, $F(E_Z, T, V_{BC}, V_{AB})$ accounts for the thermo-activated current (T dependence), the blockade of tunneling by occupied collector states (V_{BC} dependence) and the opening of an energy gap in the graphite emitter induced by the electric field (V_{AB} dependence). Coherent tunneling is assumed.

Next we find the current density through the graphite emitter. We assume that the emitter is a graphite particle orientated between 66° and 78° to the electric field, such that the bias is dropped across a bilayer, as shown in equation 4.3. The current density in the bilayer graphene is then given by [52],

$$J = \frac{e^2}{h}\frac{\gamma_1 k_B T}{u_0^2}\frac{V_{AB}\cos\psi}{l}\frac{\mu(T)}{\mu(0)}\int_0^\infty dx \frac{1}{1+\exp(\beta(x+(eV_{AB}\sin\psi)/2))} \quad (4.7)$$

where u_0 is the strength of the scattering potential. A value of $u_0 \approx 1$ meV for the interaction potential with impurities is obtained from the conductivity of graphene at 4 K [53]. Increasing the temperature reduces the density of thermal carriers across the gap. At higher temperatures, electron-phonon scattering reduces the mobility in the graphite planes according to $\mu \propto T^{1.2}$ [35, 87]. We have

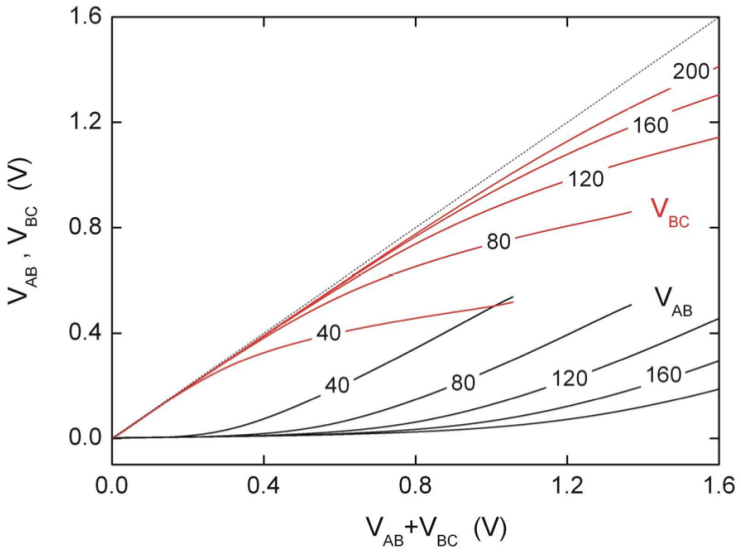

Figure 4-12: At a low bias V (dashed line) the potential is all dropped over the barrier V_{BC} (red curve) and not the graphite emitter V_{AB} (black curve) ≈ 0. As the bias is increased the barrier becomes transparent and the bias starts to be dropped across the graphite emitter. This is seen for all barrier widths, 40 nm to 200 nm.

included the prefactor, $\dfrac{\mu(T)}{\mu(0)} = \dfrac{150^{1.2}}{T^{1.2} + 150^{1.2}}$ which is found from an experimental fit of the mobility data of Sugihara *et al.* [87].

We apply the current conservation law across the graphite-silicone-graphite system by equating equation 4.4 and 4.7, to find the relationship between the potential dropped across the tunneling barrier V_{BC} and the potential dropped across the graphite emitter V_{AB}. The equation is solved numerically. V_{AB} and V_{BC} are plotted as a function of $V = V_{AB} + V_{BC}$ in figure 4-12 for a range of tunneling barrier widths from 40 nm to 200 nm.

At a low bias the graphite is semi-metallic and the silicone is an insulator. The applied bias is all dropped across the silicone layer giving V_{BC}(red curve) $\approx V$ (dashed line) and $V_{AB} \approx 0$ (black curve), where the dashed line is the total bias applied to the system ($V = V_{AB} + V_{BC}$). As the total bias is increased, the silicone tunneling barrier becomes increasingly transparent, curving downwards. When its resistance becomes comparable to that of the graphite emitter, V_{AB} starts to increase and V_{BC} saturates. The increase in V_{AB} is a self-consistent process. As V_{AB} opens a gap in the embedded graphene bilayer, it causes the emitter resistance to increase, which further increases V_{AB}.

Relating the total bias across the graphite-silicone-graphite barrier and the current density, the $I - V$ characteristics can be modelled. The ability to simply

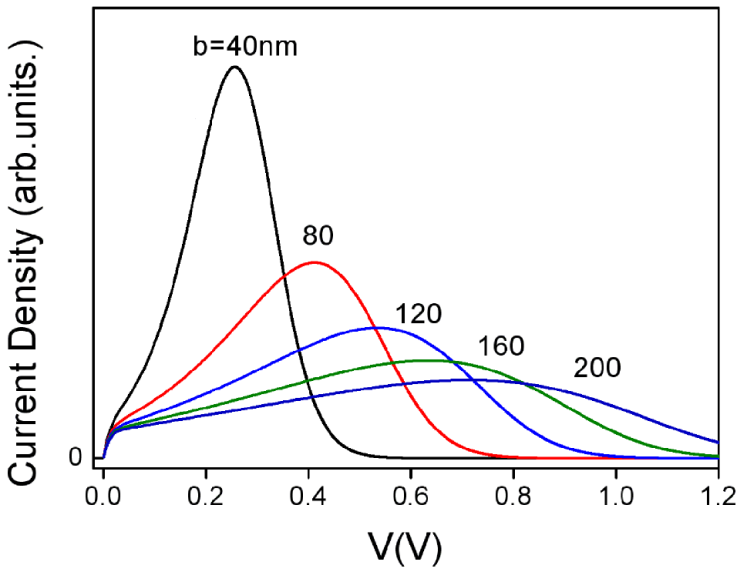

Figure 4-13: The theoretical calculation of $I-V$ curves for barrier widths 40 nm to 200 nm. The model shows a remarkable similarity to the filling fraction dependence of figure 4-2. In the theoretical calculation the current density drops to zero however in the bulk 3D composite rerouting of conduction maintain a finite current.

vary the barrier width, b, and height, ϕ, in the model allows comparisons to be made to the experimental results, which are shown in the next two sections.

4.3.1 Barrier Width

We model the $I-V$ characteristics of graphite-silicone-graphite system with the graphite emitter assumed to be orientated for bilayer favoured conduction. The calculation for barrier widths 40 nm to 200 nm is shown in figure 4-13. The $I-V$ curves show a remarkable resemblance to that for the experimental $I-V$ curves for decreasing filling fraction, figure 4-2, with a clear NDR region above a threshold voltage that increases for increasing barrier width. We explain this as follows:

At a small bias the emitter particle is semi-metallic and the silicone barrier is insulating. Increasing V increases the tunneling current, which gives rise to the Ohmic region of the $I-V$ curves. Near the peak, the resistance of the tunneling barrier drops to the level of the resistance of the emitter. The potential is now dropped across the bilayer particle. The opening of the partial band gap causes the resistance to increase sharply, and the current decreases leading to the NDR that can be seen from any of the curves in figure 4-13.

Increasing the tunneling barrier width, b, causes the peak current to shift to a higher V_p for the simple reason that a wider barrier requires a larger bias to match the resistance to that of the emitter.

We compare this directly to the experimental results of figure 4-2. Decreasing the HOPG filling fraction causes the mean barrier width to increase. We estimate the barrier width, using equation 2.11, through a simple geometrical consideration of the particle and assuming that the particles do not form agglomerates as,

$$b = l\left[\left(\frac{\pi}{6p}\right)^{1/3} - 1\right], \tag{4.8}$$

where $l = 450\ nm$ is the HOPG particle length. Thus b increases from 67 nm at $p = 34.5\%$ to 139 nm at $p = 21\%$. This is in good agreement with the theoretical calculation's from a single nucleation site, shown in figure 4-13. The correlation between the experimental results of figure 4-2 and theoretical results of figure 4-13 support the hypothesis that the NDR originates from a field induced semi-metal to insulator transition of embedded graphene bilayers.

4.3.2 Barrier Height

We now consider the calculated $I - V$ curves of the single graphite-silicone-graphite system for a constant barrier width of $b = 100$ nm and barrier height $\phi = 165$ meV for temperatures 30 K to 210 K, figure 4-14. The onset of NDR follows a similar trend to that seen for the experimental results in figure 4-6, with V_P decreasing significantly for increasing temperature. The main effect of temperature is to activate a thermal current above the silicone tunnel barrier, lowering its resistance and thus causing the barrier to become transparent for a lower bias. Naturally the current through the barrier decreases with decreasing temperature due to the loss of the thermo-activated component. This is hidden for the experimental results where the current arises from the bulk of the composite and not just a single barrier system.

It is possible to calculate the temperature dependence of the peak position using the silicone barrier height, ϕ, as the adjustment parameter and equating equations 4.4 and 4.7 to include both the effects of phonon scattering on the mobility of graphite [35] and the thermal activation of carriers [72]. The theoretical peak positions for barrier heights ranging from 50 meV to 250 meV are plotted in figure 4-15. The experimental results for two different samples are included. The black squares show the variation in V_P for a temperature range 4 K to 200 K

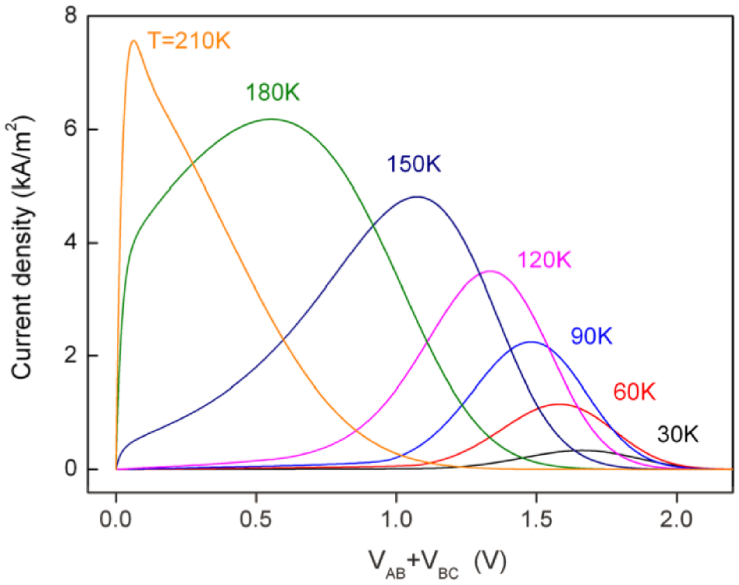

Figure 4-14: The temperature dependence of the modelled graphite-silicone-graphite barrier. The onset of NDR occurs as a lower bias for a greater temperature which is the same dependence we observe in the experimental results show in figure 4-6.

and the blue circles for 90 K to 170 K.

We then use the knee of the theoretical curve, normalising the voltage V_P to extract a best fit for $\phi = 165$ meV. This is an estimate of the *barrier height* in the GSC. This is close to the values of similar composites, for instance carbon black-polyethylene composite has a barrier height of 50 meV and a graphite-polyethylene composite, with the work function of graphite equal to 4.5 eV [88], has a potential barrier height of 180 meV [89].

We can also use figure 4-15 to find the barrier height that would be required for room temperature NDR as 250 meV through extrapolating the fit to 300 K. This is the minimum barrier height required to ensure a finite peak position for an NDR region. Increasing the barrier height would require chemical modification of the polymer matrix.

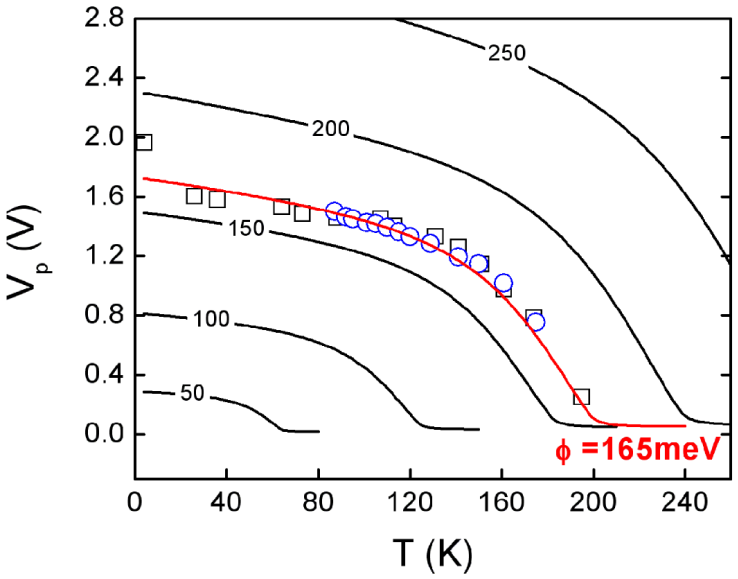

Figure 4-15: Temperature dependence of the peak position for $p = 32\%$ (squares) and $p = 28\%$ (circles) compared to the theoretical temperature dependence's calculated for different heights of the tunneling barrier (full lines). The best fit to the data is for a barrier height $\phi = 165$ meV (red line).

4.4 Discussion

4.4.1 Joule Heating

The possibility that the NDR observed is caused through a Joule heating mechanism was extensively considered because this has been known to cause non-linear behaviour in the $I-V$ of some soft conductive composites [90, 91, 92]. The argument follows that high electric fields cause a large current to flow through the composite and the power, $P = I^2R$, is dissipated as heat energy in the composite. The heat generated would cause the composite to heat up due to the low thermal conductivity of the matrix. If the Joule heating, or self-heating, was significant it could then cause the silicone rubber composite to pass above its glass transition temperature, $T_g \approx 200K$. This in turn would lead to an expansion of the matrix and increase in the tunneling barrier between particles and hence cause the current to decrease.

To directly measure the extent of Joule heating in the GSC the in situ temperature of the composite was recorded whilst measuring the $I-V$ characteristics. A platinum temperature sensor was embedded in the centre of the composite. The sensor was calibrated to within ± 1 K and has an area of 1.2×1.6 mm^2. We immersed the sample in liquid nitrogen and recorded the internal sample temperature while measuring the four terminal $I-V$ curves. The results for a PC and HOPG composite are shown in figure 4-16 (a) and (b) where both the $I-V$ curves and internal composite temperature are recorded for a range of voltage ramp speed.

Some Joule heating was indeed observed but by an increase of just 1 K at V_P in the PC composite and 15 K in the HOPG composite. This is far below the 120 K increase required to reach the composites glass transition temperature. Further heating takes place once the sample is in the NDR region with a 4 K increase in the PC composite and a 65 K increase for the HOPG composite. Both remain below T_g.

To ensure the measured temperature was at thermal equilibrium the ramp rate of the voltage sweep was varied over two orders of magnitude from 20 mVs^{-1} to 2 Vs^{-1}. It can be seen in figure 4-16 that while shape of the NDR does indeed change with ramp rate; the measured temperature increase does not. Confirming that we are indeed measuring the temperature at thermal equilibrium and that the measured temperature increase is small.

If the NDR were due to Joule heating it would be expected that the onset would be at a similar power for both samples, however the power dissipated at

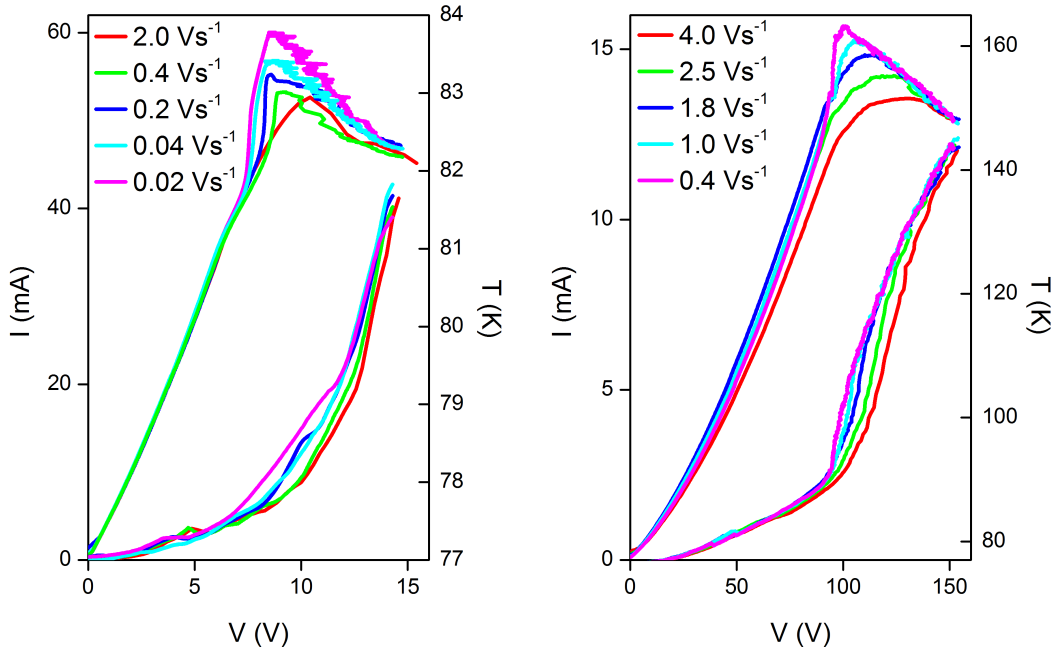

(a) (b)

Figure 4-16: The in situ temperature of the PC (a) and HOPG (b) composites during measurement of the $I-V$ curves over a range of voltage ramp rates. Joule heating is observed however it is not substantial enough to take the composite above its glass transition temperature, $T_g = 200$ K with only a 4 K increase for PC at V_P and a 65 K rise in the HOPG composite.

V_P for PC is 540 mW while for the HOPG it is 1500 mW. This is three times more power for similar sized samples. All these arguments combine to clearly and unequivocally show that the NDR region is not caused through a heating mechanism.

We can further make qualitative arguments that if the NDR were caused through self-heating then a significant hysteresis in sweeping back and forwards over V_P would be expected. The composite melting and refreezing would cause substantial changes in the conduction network as well as the transition having a certain heat latency. Also, we later demonstrate the composite ability to oscillate, due to the NDR region, up to frequencies as high as 12.5 kHz, which is considerably faster than any relaxation rate of the composite.

To summarise the NDR cannot be a thermally induced effect as the Joule heating is substantially below that required to force the composite through the glass transition temperature.

4.4.2 Applications

The NDR region of the GSC can be used in much the same way as TD are used in creating oscillators and amplifiers [93]. Biasing a sample into the NDR region within an LC circuit will allow for AC oscillations to be generated and sustained as we show in chapter 6.4.1.

The soft malleable nature of the composite gives potential to fabricate flexible NDR devices which would allow the oscillations to be controlled using bend and strain, which we explore in chapter 6.4.2.

The greatest problem to overcome is the absence of NDR at room temperature. We create a paradoxical situation that the composite has to be below the glass transition temperature for the NDR to be observed and yet we try to create flexible devices. However this could be overcome by using a different matrix. The matrix would need a glass transition temperature above 300 K and have a work function that creates a higher tunneling barrier of around 250 meV. It may be possible to chemically alter the current silicone polymer used for this purpose or otherwise an epoxy or a high density polyethylene may be well suited.

4.4.3 Summary of NDR Mechanism

This chapter has presented the experimental and theoretical evidence for understanding the origins of the NDR region. We now briefly summarise our understanding of the mechanism we believe causes the NDR with the aid of figure 4-17. The schematic depicts a conduction line containing one particle, labelled X, that is orientated such that the conduction is across a bilayer. At zero bias the barrier is simply rectangular and current flows equally in both directions. As the bias increases from, V_1 to V_2, the potential is mostly dropped over the high resistance silicone tunneling barriers. The barriers become more and more sloped as the bias is increased causing them to become more *transparent* with the barrier resistance decreasing. At V_3 the barrier has become transparent with its resistance close to that of the graphite nanoparticles. The bias now starts be dropped across the graphite.

For particle X the bias is dropped across the bilayer and induces an opening of a *partial band-gap*. This increases the resistance of the particle. Thus at V_4 a sharp transition takes place whereby the resistance of the bilayer particle increases. A local electric field domain is created around this particle causing the potential elsewhere in the composite to decrease. This particle now controls the current through the conduction line. Further increasing the bias causes a greater opening of the band-gap and the current to decrease further, therefore giving rise to the observed NDR region.

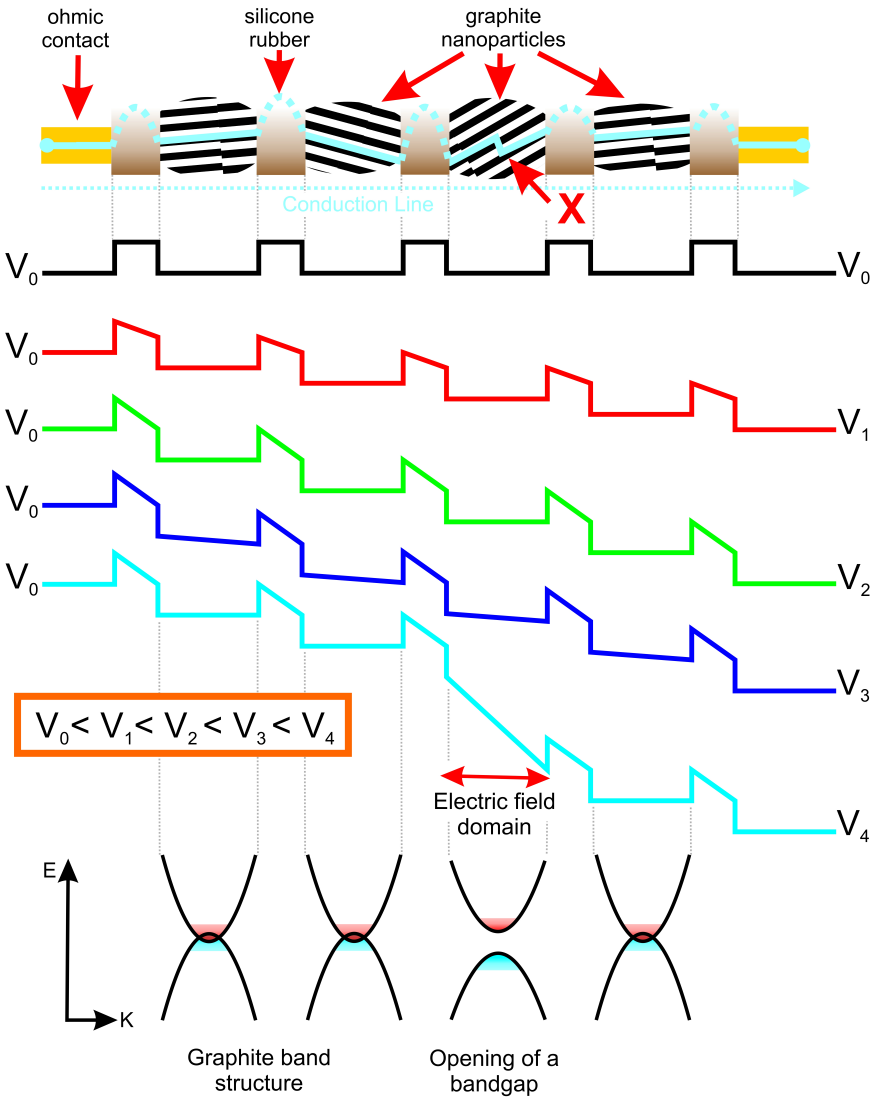

Figure 4-17: Schematic showing the potential variation across the graphite particles and silicone barriers as the bias is increased from V_0 to V_4. For particle X the bias is dropped across a bilayer and a partial band-gap is opened, leading to the formation of electric field domains with the particle becoming highly resistive.

4.5 Conclusion

In this chapter we have shown that there is a *robust* NDR region in the $I-V$ characteristics of a GSC below the glass transition temperature and above a threshold voltage. We have presented experimental results varying the graphite filling fraction, graphite structure, the probe separation distance and temperature. These results lead us to understand the NDR phenomenon to be due to a semi-metal to insulator transition of *embedded* graphene bilayers within the graphite nanoparticles. The transition is brought about by a transverse bias across specifically orientated particles opening a *partial energy gap* at the Fermi level of the bilayer. This causes the nucleation of highly resistive domain boundaries and the current to decrease.

We support the experimental evidence with theoretical calculations for the LDOS of the conduction band across the bilayer with a locally applied potential. We have calculated the current density across a single graphite-silicone-graphite barrier with the emitter graphite assumed to be orientated for bilayer conduction. We used this single barrier system to model the $I-V$ characteristics, varying the parameters of barrier width and barrier height. Through relating the experimental and theoretical results we extract a barrier width of $b \approx 100$ nm, that depends on the filling fraction, and a barrier height of $\psi = 165$ meV.

Chapter 5

Electromechanical Properties and Sensing

This chapter is an investigation of the electromechanical properties of the GSC with a view to potential devices and applications. We explore the room temperature conduction processes under bending and differential pressure; gaining an insight into the transient piezoresistive response and opening up avenues for potential further work.

Conductive composites are widely studied due to their potential as flexible skins and while the effect of uni-axial pressure on the piezoresistance has been previously reported [94, 95, 96], we were curious as to the effect of *bend induced strain* on the composite as the bend simultaneously induces longitudinal and transverse strains. We report a complex time dependent response due to the *viscoelastic* nature of the composite. Bending also allows precisely controlled strain increments and we are able to extract intrinsic properties of the composite arising from the *stress attenuation* in different planes.

One of our most exciting developments is the utilization of *conduction line destruction* that arises from abrupt changes to the tunneling percolation network and viscoelasticity of the matrix which makes the composite sensitive to sudden changes in pressure. We demonstrate this technique is sensitive enough to detect acoustic ultrasound pressures of 48 Pa. Further we have been able to utilize this sensitive behavior in building a differential pressure sensor array based on *resistance spiking*; detecting pressures of < 3.8 kPa.

This technique would help advance current research on flexible electronic skins that combine conductive rubbers with flexible transistors, as it offers an increased sensitivity and quick recovery time [13, 15, 97].

5.1 Introduction

Composites of conductive particles in flexible insulating materials have been extensively studied for over 30 years due to the potential applications of their piezoresistive properties [98, 99]. The insulating matrix allows the composite to be soft and flexible and at the same time provides protection for tough environmental conditions while the relatively low cost of the materials means that they are well suited to large scale monitoring [100]. Applications are numerous and include detection of deformations and vibrations of vehicle parts [95]; strain fatigue monitoring in parachute deployment [101]; robotic skins [102]; surgical instruments [99] and detection of turbulence across aeroplane wings [103].

Piezoresistive composite rubbers are commercially available and used in applications such as conductive rubber keypads or mechanical pressure switches [104]. Typically the conductive rubbers are fabricated to be close to the percolation threshold with the conductive filler volume fraction set such that the composite is just on the point of conducting, i.e with a very high resistance. When a pressure is applied the composite volume is reduced pushing the conductive particles closer to one another. The composite moves through the percolation threshold and the resistance decreases by an order of magnitude. The composite is therefore highly sensitive to pressure. Many of the reported cutting edge applications utilize the composite as an on/off switch, rather than as an accurate, calibrated pressure gauge due to the time dependent effects [15, 100, 102].

Current research is working towards creating the conductive rubbers into large area flexible devices, with the ability to detect local pressure changes simultaneously across the entire area, i.e fabricating a soft robotic skin that has the sensitivity and resolution of human skin. The difficulties that arise are from attaining the high resolutions that depends on the number, and proximity, of tactile sensing elements that are able to measure local changes in resistance of the composite. If a single continuous sheet of composite is used then spatial resolution issues are encountered due to cross talking between the tactile sensing elements, [99, 102, 105]. This is driving solutions that combine individual sensing elements and in situ transistors that allow each sensing element to be uniquely addressed in turn [2, 13].

One of the most important functions of any stress-strain sensor is the consistent measurement of the piezoresistive response with time and over many strain cycles. The more widespread use of conductive composite is held back due to two characteristics. Firstly, the viscoelasticity of the insulating phase causes

stress-strain relaxation leading to the resistance being strongly time dependent [10, 75, 96, 106, 107]. Secondly the tendency of the conductive phase to agglomerate leads to a large hysteresis over stress/strain cycles as agglomerates break apart leading to stress-softening of the composite, known as the Mullins effect [95, 108, 109, 110, 111]. These issues can be worked on by careful selection of the matrix and improving the particle dispersions.

The piezoresistance of the composite arises from two mechanisms that are interrelated and occur concurrently. The conduction takes place through the formation of conduction lines that penetrate through the composite; and simply the more conduction lines there are, the lower the resistance of the composite. Each conduction line is formed of closely spaced highly conductive particles. The particles themselves have a very low resistance and it is the tunneling resistance between the particles that determines the resistance of the conduction lines and thus the resistance of the composite.

As discussed in section 2.4 the tunneling resistance is exponentially dependent on the separation distance between the particles while the insulating matrix binds the particles in place through an encapsulation. The elasticity of the matrix allows some restricted movement of the conductive particles. When two particles move closer together there is a decrease in the tunneling resistance and when they are forced apart the resistance increases disproportionately. This creates a high resistance junction between the two particles that breaks the entire conduction line as depicted in figure 5-1(a).

The elasticity of the encapsulation forces the particles to return back to their original positions after having been perturbed; restoring conduction along the conduction line and hence the resistance to decrease back to its original value. The entire system can be pictured as a line of particles connected by springs that are damped, figure 5-1(b). When the line is perturbed the particles move relative to one another, some move closer and some further apart while the mean separation distance remains constant. However overall this creates a resistance spike that decays with time. The composite resistance is therefore highly sensitive to any perturbation such as the application of pressure, elongation or bend that cause stresses or strains inside the matrix.

In this chapter we explore both the *steady state* and *transient* piezoresistive response. We relate the viscoelastic response to changes in tensile and compressive strain along different axis through extracting the stress attenuation times from a Maxwell's model.

Next we study the AC impedance to examine the frequency range of the

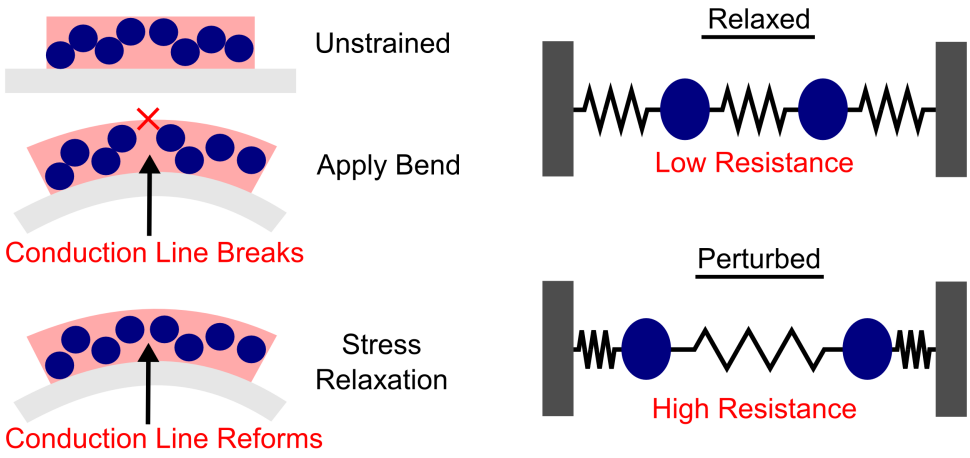

Figure 5-1: (a) Applying a bend causes the breaking of conduction lines by increasing the separation distance of the particles. Over time the composite relaxes and the conduction lines are able to reform. However the mean separation distance is now increased. (b) When the particle separation is equal the resistance is at a minimum. When the system is perturbed some particles will move. Those that are then separated by a large distance will have a high resistance and cause the destruction of the conduction line. Over time the system relaxes and the resistance decreases again.

composite and explore how the cut-off frequency varies with strain which we discuss in relation to the capacitance between particles in the conduction network.

Next utilizing the sensitivity of the composite to differential pressure we demonstrate the detection of underwater pressure waves. The ultrasound detection is shown to be dependent on the power output of the transducer and the composite has a pressure detection threshold of 48 Pa. There is a commensurability between the ultrasound wave length and composite width; which we explore through rotating the composite to incident waves; and discuss in relation to Bragg's law and the formation of standing waves.

Finally, we present the testing of a DPA of 64 individual composite elements, whose fabrication was detailed in section 3.6. Rather than measure the change in steady state resistance; the DPA elements utilizes the resistance spiking to detect pressures of < 3.8 kPa at a resolution of 10 dpi.

5.2 The Maxwell Model of Viscoelasticity

Viscoelasticity is where a material exhibits both viscous and elastic characteristics under deformation leading to a time dependent stress-strain relationship. There are two different scenarios, either a constant stress can be applied and the time dependent strain is measured which is referred to as creep. Or a constant strain can be applied and the time dependent stress measured, the *stress relaxation*.

In order to model the viscoelasticity we first start from a simple model that combines a spring and dash pot in a linear or parallel combination. The springs have perfectly elastic behaviour with elastic modulus E while the dash pots have perfect viscoelastic behaviour with viscosity η. The simplest of these models is the Maxwell model with a single spring in series with a single dash pot, shown in figure 5-2. The viscoelasticity in the Maxwell model means the material acts like an elastic body over a short time and a viscous fluid over a long time [112].

In the Maxwell model shown in figure 5-2 the total strain, ϵ must be the sum of the elastic component, ϵ_e, and viscous component, ϵ_v, such that,

$$\epsilon = \epsilon_e + \epsilon_v \,. \tag{5.1}$$

Considering the rate at which the strain changes with time we differentiate to find,

$$\frac{\mathrm{d}\epsilon}{\mathrm{d}t} = \frac{\mathrm{d}\epsilon_e}{\mathrm{d}t} + \frac{\mathrm{d}\epsilon_v}{\mathrm{d}t} \,. \tag{5.2}$$

We then use Hooke's law and assuming the spring to be elastic, $\sigma = E\epsilon_e$ where E is the elastic modulus, we can write,

$$\frac{\mathrm{d}\epsilon_e}{\mathrm{d}t} = \frac{1}{E}\frac{\mathrm{d}\sigma}{\mathrm{d}t} \,, \tag{5.3}$$

and the dash pot, which is a purely viscous damper with viscosity η, is given by [113],

$$\frac{\mathrm{d}\epsilon_v}{\mathrm{d}t} = \frac{\sigma}{\eta} \,, \tag{5.4}$$

Combining equations 5.2, 5.3 and 5.4 we find that,

$$\frac{\mathrm{d}\epsilon}{\mathrm{d}t} = \frac{1}{E}\frac{\mathrm{d}\sigma}{\mathrm{d}t} + \frac{\sigma}{\eta} \,. \tag{5.5}$$

To apply this for stress relaxation, where the strain is held constant in time, we

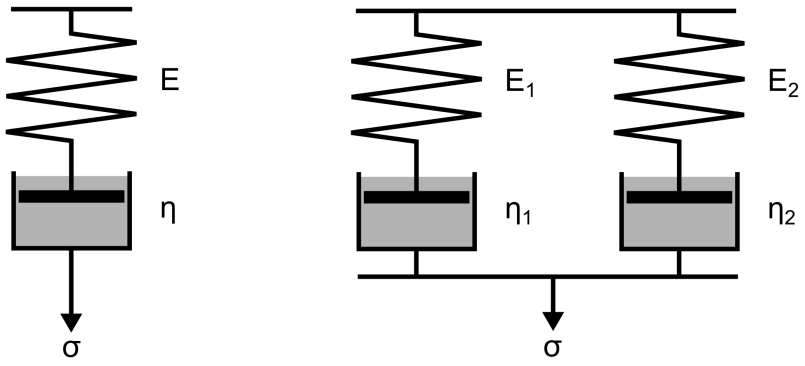

(a) (b)

Figure 5-2: (a) The Maxwell model consists of a spring with elastic modulus, E, in series with a dash pot of viscosity, η. The viscoelasticity in the Maxwell model means the material acts like an elastic body over a short time and a viscous fluid over a long time. (b) The generalised Maxwell model is for n spring dash pot systems in parallel. We consider the generalised Maxwell model for $n = 2$ systems.

simplify as $\dfrac{\mathrm{d}\epsilon}{\mathrm{d}t} = 0$ and equation 5.5 becomes,

$$\sigma + \frac{\eta}{E}\frac{\mathrm{d}\sigma}{\mathrm{d}t} = 0\,. \tag{5.6}$$

This is the differential equation for describing the Maxwell model for stress relaxation and which has the solution,

$$\sigma(t) = \sigma_0 \, \exp\left(-t/\tau\right) \,, \tag{5.7}$$

where σ_0 is the initial stress and $\sigma(t)$ is the time varying stress that relaxes according to the relaxation time $\tau = \dfrac{\eta}{E}$. If a sudden deformation is applied and the strain remains constant the stress will decay according to the time constant $\tau = \dfrac{\eta}{E}$ where η and E are fundamental intrinsic characteristics of the material.

The Maxwell model considers a single spring and dash pot in series. However for a solution that better resembles real materials we consider many of these spring and dash pot systems placed in parallel with each other. The parallel arrangement of n systems can be solved by making the assumption that stress affects arising from contributions, imposed over different times, overlay without interfering, referred to as the Boltzmann superposition principle [112]. We therefore arrive at the generalized Maxwell model for an arbitrary number of Maxwell

models (spring and dash-pot) connected in parallel,

$$\sigma(t) = \sum_{i=1}^{n} \sigma_n \exp(-t/\tau_n)\,, \tag{5.8}$$

where $\tau_n = \dfrac{\eta_n}{E_n}$ and σ_n the initial stress in system n. In a macroscopic composite there will be a large number of polymers and composite particles all interacting. However it is unnecessary to consider each polymer chain as its own spring and dash pot as similar polymer chains will all have the same intrinsic characteristics and therefore can be combined together as a single spring dash pot. Instead the n systems in parallel represents n different mechanisms that simultaneously take place. We make the assumption that we have two mechanisms at work in our GSC composite. Using figure 5-2(b) and equation 5.8, we write,

$$\sigma(t) = \sigma_1 \exp(-t/\tau_1) + \sigma_2 \exp(-t/\tau_2) \tag{5.9}$$

with $\tau_1 = \dfrac{\eta_1}{E_1}$ and $\tau_2 = \dfrac{\eta_2}{E_2}$ representing two different stress attenuation speeds of two distinct mechanisms that arise from the high aspect ratio of the composite with differences in the transverse and longitudinal planes.

We do not measure the direct stress attenuation of the composite; instead we measure the electrical resistance of the composite over time for a constant strain. It has been clearly shown in numerous studies that the change in conduction through the network, i.e the resistance, is directly related to changes in stress within the composite, [10, 94, 114, 115, 116]. Therefore we can rewrite equation 5.9 in terms of the resistance,

$$R(t) = R(\infty) + A_1 \exp(-t/\tau_1) + A_2 \exp(-t/\tau_2), \tag{5.10}$$

where A_1 and A_2 are constants relating to the resistance peaks. We also add the term $R(\infty)$ as the resistance of the composite does not tend to 0 after an infinite time after the stress has relaxed. Finally to apply the equation without having to wait for an infinite time for R to settle we subtract $R(t_c)$ for constant time, $t_c = 295$, and define the change in resistance δR as,

$$\delta R = A_1 \left(\exp\left(-t/\tau_1\right) - \exp\left(-t_c/\tau_1\right)\right) + A_2 \left(\exp\left(-t/\tau_2\right) - \exp\left(-t_c/\tau_2\right)\right)\,. \tag{5.11}$$

This equation is the four parameter model for relating the resistance relaxation in a conductive polymer composite due to two distinct stress attenuation speeds.

5.3 Methods

5.3.1 Precision Bending to Induce Bilayer Strain

Strain was applied to the composite through bending. The strain could be chosen to be either compressive or tensile strain through putting the composite, mounted onto a flexible substrate, on the inside or outside of the bend. Bending such that the composite is on the outside of the bend corresponds to a tensile strain, $+\epsilon$, and an inside bend a compressive strain, $-\epsilon$. Using the apparatus described in section 3.5, accurate adjustment of the bend radius, and hence the strain, is achieved through altering the bend radius via a horizontal displacement of two clamps that hold the sample in place and force it to bend outwards or inwards.

The induced bilayer strain is calculated from the bend radius which is a trigonometric relation to the horizontal displacement. These equations are derived in section 3.5. To have complete control over the strain and to be able to reproduce consistent strains within the composite we employ a stepper motor to produce the horizontal displacements.

The stepper motor was programmed to produced steps in the horizontal displacement of either 20 μm or 200 μm . The time between the steps was controlled using a LabView program and was varied from 60 s to 4,800 s. The bend radius and the bilayer strain was calculated, using the equations derived in section 3.5, directly from the total horizontal displacement, l, measured with respect to the flat length, l_0.

The change in resistance, ΔR, is the percentage change of resistance with $\Delta R = (R_t - R_0)/R_0$ where R_0 is the initial starting resistance at $t = 0$ and R_t is the resistance after time t. When comparing the resistance due to strain increment n, the resistance, R_F^n is the lowest resistance reached after strain increment n but before the next strain increment. The percentage change in R_F^n is then given by $\Delta R_F = (R_F^n - R_F^0)/R_F^0$ where n is the n^{th} strain increment and R_F^0 is the settled resistance for the composite under no strain (flat). This gives the steady state resistance change due to strain. As the resistance decays exponentially after the strain is applied, the time between strain increments was set such that R_F^n would effectively represent a settled steady state resistance. In the transient analysis δR is used to compare the exponential decay of resistance for different strain increments where $\delta R = R_t^n - R_F^n$.

To minimise environmental disturbances the apparatus was placed on an inch thick foam board to dampen vibrations; enclosed within a tight fitting box to stop air drafts; and the temperature was monitored.

5.3.2 AC Impedance Measurements

To measure the change in the bandwidth of the composite due to strain; the frequency was swept and the impedance measured for increasing strain in both compression and extension. The frequency measurements were automated using a 33120A Agilent function generator sweeping the frequency from 10 Hz to 1 MHz with 100 steps per logarithm with an amplitude of 1 V. The impedance was measured in a voltage divider circuit with a 100 kΩ resistor in series. The voltage over the composite, v_{out}, was measured with an Agilent DSO6014A oscilloscope. The average amplitude was recorded over 32 oscillations for each frequency. The strain was increased after each sweep with a 200 μm displacement step. The resistance was allowed to settle for 600 s before the next frequency sweep was initiated. The gain was calculated according to,

$$G = 20 \log \left(\frac{v_{out}}{v_{in}} \right) \tag{5.12}$$

and the cut-off frequency defined as $f_C = -3$ dB. The capacitance of the composite was estimated for each strain, n, according to,

$$C = \frac{1}{R_0^n \omega_C} \tag{5.13}$$

where R_0^n is the DC resistance for the n^{th} strain.

5.3.3 Ultrasound Pressure Measurements in Water

We were interested in finding the pressure detection threshold of the composite. We used ultrasound to apply an acoustic pressure that causes the composite resistance to increase due to conduction line destruction. We incidentally find commensurability between the width of the composite film and the ultrasound wavelength with resonances which we probe by rotating the sample relative to the direction of incident waves. This is discussed in relation to Bragg's law and the creation of standing waves.

The 4T resistance of the composite was measured in response to the acoustic pressure created through a short ultrasonic burst from an A380-SU transducer placed in a large water tank. The composite sample was positioned 8.5 cm away from the transducer and carefully aligned in the x and y direction to the center of the transducer face, the angle of the composite face to the transducer could be altered using a rotating platform, as shown in figure 5-3.

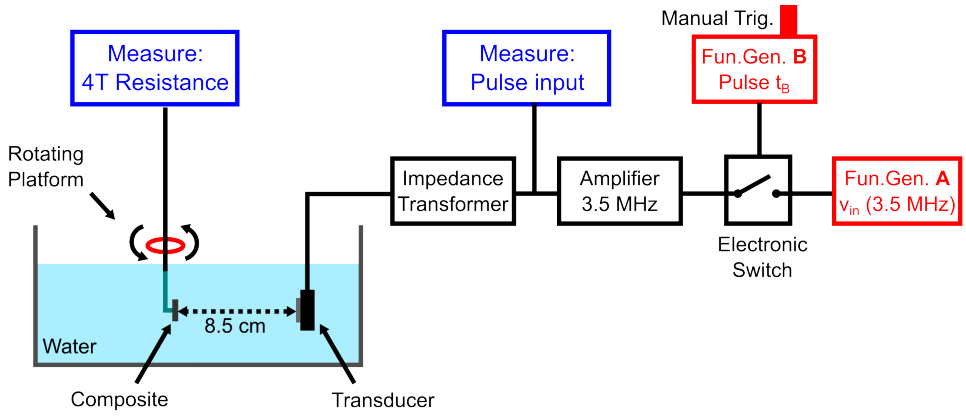

Figure 5-3: Experimental set-up for the ultrasound acoustic pressure measurements. Function generator **A** produces a continuous square wave of frequency 3.5 MHz and amplitude v_{in} that is varied between 10 mV and 110 mV. Function generator **B** produces a single cycle burst square waveform when manually triggered. The ON burst lasts for the programmed burst length t_B that is varied between 0.1 s and 10 s. The electronic switch closes during t_B; so the 3.5 MHz signal is fed to the amplifier; onto the impedance matching transformers; and into the transducer. The composite is 8.5 cm from the transducer and the angle it makes to the transducer is altered using a rotating platform. The 4T resistance of the composite is continually measured.

The transducer was controlled through two function generators and an electronic switch that enabled 3.5 MHz bursts to be applied to the transducer with a precisely controlled burst length, t_B. Function generator **A** was used to continuously produce a 3.5 MHz square wave with amplitude, v_{in}, between 10 mV and 110 mV. The signal was then turned on and off using an electronic switch that was switched through function generator **B**. Function generator **B** could be manually triggered to create a single TTL pulse of pre-programmed burst length t_B. The switch output was fed through an amplifier with a gain of 300 to create pulse inputs of up to $V_{PP} = 30$ V and then into an impedance matching transformer connected using a low impedance cable to the transducer. The 4T resistance of the composite was measured in time along with the amplitude and length of the pulse input.

The power into the transducer was varied by increasing v_{in} from 10 mV to 100 mV. The burst length, t_B, was varied from 0.1 s up to 10 s and the angle, θ, between the composite face and transducer face was altered between 0° and 90°. Each burst was repeated four times, with 60 seconds resistance recovery time, to enable an average response to be found. The change in resistance, δR, is defined as $\delta R = R_t - R_0$. The peak response, δR_B due to the burst is defined

as $\delta R_B = R_H - R_L$ where R_H is the maximum resistance of the composite at the end of the burst and R_L the resistance at the onset of the burst.

The acoustic pressure applied to the composite is calculated by first considering the input power, Γ_{in}, into the transducer,

$$\Gamma_{in} = \frac{V_{in}^2}{R} = \frac{V_{pp}^2}{2\, n_t^2\, R}\,, \tag{5.14}$$

where $R = 1.35$ MΩ is the impedance of the transducer and $n_t = 2.7$, the turn ratio on the impedance matching transformer. We then use the conversion efficiency of electrical power to mechanical power given by k_c^2 where $k_c = 0.55$ [117] and find the ultrasound intensity, I_T, output of the transducer, with radius $r = 12.5$ mm, to be,

$$I_T = \Gamma_{in} \frac{k_c^2}{\pi r^2}\,. \tag{5.15}$$

Typically I_T varied between 1 mW up to a maximum of 28 mW. The transducer produces a 3.5 MHz signal that is transmitted into the distilled water with a velocity $c_w = 1,480$ ms^{-1} and corresponding wavelength $\lambda = 420$ μm [118]. As the sample is 8.5 cm away from the transducer it is inside the near field distance, calculated as $N = \dfrac{r^2}{\lambda} < 0.085$, which means we can assume the attenuation is negligible [119, 120]. The acoustic pressure, P_a, is found from the relation between intensity and pressure [121],

$$I_T = \frac{P_a^2}{\rho_w c_w}\,, \tag{5.16}$$

where ρ_w is the density of water. Combining equations 5.14, 5.15 and 5.16 we therefore find the expression for the acoustic pressure at the composite as a function of input voltage,

$$P_a = V_{pp} \frac{k_c}{n_t\, r} \sqrt{\frac{c_w \rho_w}{2\pi\, R}}\,. \tag{5.17}$$

The maximum V_{pp} of 30 V equates to an acoustic pressure of 200 Pa incident on the composite. This is an estimate of the acoustic pressure carried in the water to the composite. Inside the near field distance there are local variations in the pressure which have not been accounted for [119]. Further we have not considered the velocity change as the wave passes into the composite. However as c_w is close to that of the velocity in silicone rubber [122], equation 5.17 provides a suitable first approximation for the acoustic pressure.

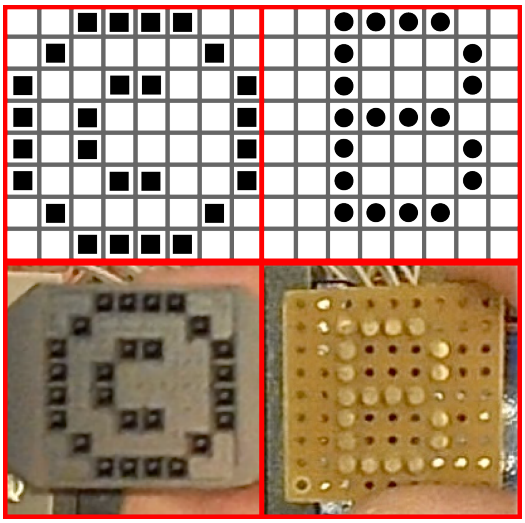

Figure 5-4: The C-stamp and B-stamp were used to exert pressure on specific composite pixels. The C-stamp was machined so that every protrusion was exactly the same height and includes holes for the guiding bars allowing it be dropped from a 1 cm height onto the composite. The B-stamp was not machined and thus some pixels were of an uneven height. With no guiding bars the B-stamp required careful alignment over the composite pixels.

5.3.4 Differential Pressure Array Test Procedure

The design and fabrication of the DPA is discussed in detail in chapter 3.6. Here the tests to measure its performance are explained. To initially test the sensitivity of the device individual elements were perturbed through applying a quick light touch with a pen nib. The resistance with time was recorded and the spike and decay times were used to set the sensitivity settings for the pressure mapping LabViewprogram.

Two stamps were used to test the device, a C-stamp and a B-stamp as shown in figure 5-4. The C-stamp comprises of 26 ON pixels and 38 OFF pixels. The stamp was machined so that the protruded ON pixels were domed shaped with the peaks aligned on a 2.54 mm lattice spacing. Guiding bars of the top face on the device align the C-stamp so that the stamps protruded pixels apply pressure to the centers of the composite pixels.

The B-stamp has 20 protruded ON pixels and 44 recessed OFF pixels. It is also on a 2.54 mm lattice. The pixels are cylindrical with the end face centered on the lattice with a diameter of 2 mm. There is no guiding system for the B-Stamp so the stamp is carefully aligned by placing it on the array such that the centers of each circular protrusion exactly sit on the center of a composite pixel.

A 100 μm thick plastic layer was placed over the composite array to protect

the soft pixels from damage. It also provided an electrically insulating layer to ensure there was no short circuiting between the stamp and the composite pixels. As the layer is very thin and flexible, it doesn't influence the application of pressure to the pixels.

The device was connected to the measurement circuit and the LabView program was used to monitor and display the perturbation response of each stamp. The C-stamp was tested through the addition of a 32 g weight on the back of the stamp, giving a total weight of 40 g. It was then dropped, using the guiding bars, from a height of 1 cm onto the composite array. The stamp was left on the composite for one minute before it was lifted off.

The B-stamp was tested through placing it on the composite with care taken to align the composite pixel centers with the centers of the circular protrusions. After one minute the B-stamp was gently rocked forward and backwards. After another minute the B-stamp was gently tapped. Finally one minute later the stamp was removed.

For all the tests the graphical display on the LabView program was recorded as well as the data for the resistance of each composite for every sweep. The entire measurement process was filmed to demonstrate the real time application of the DPA and can be found at [123].

5.4 Results

5.4.1 Steady State Piezoresistance with Bilayer Strain

We are interested in how the steady state resistance of the composite varies under *bilayer strain*. A typical change in resistance, ΔR, with time for three decreasing strains is shown in figure 5-5. The sample has an initial strain of $\epsilon = 16\%$. The resistance before the first strain decrement is steady and after 800 s the strain is decreased by releasing the sample bend in an automated 200 μm horizontal displacement step lasting 3 s. This creates a *resistance spike* with the initial resistance increasing by 3%, from 161.8 kΩ to 166.7 kΩ. The resistance then decays exponentially to reach a steady state resistance $\Delta R_F^1 = 0.77\%$ after 3,000 s.

The second strain decrement occurs at 5,600 s. The resistance again spikes from $\Delta R = 0.9\%$ to $\Delta R = 5.1\%$. The resistance spike is even greater than that of the previous spike. The resistance then decreases again and settles to a higher steady state resistance of $\Delta R_F^2 = 2.8\%$. The trend continues for the third strain

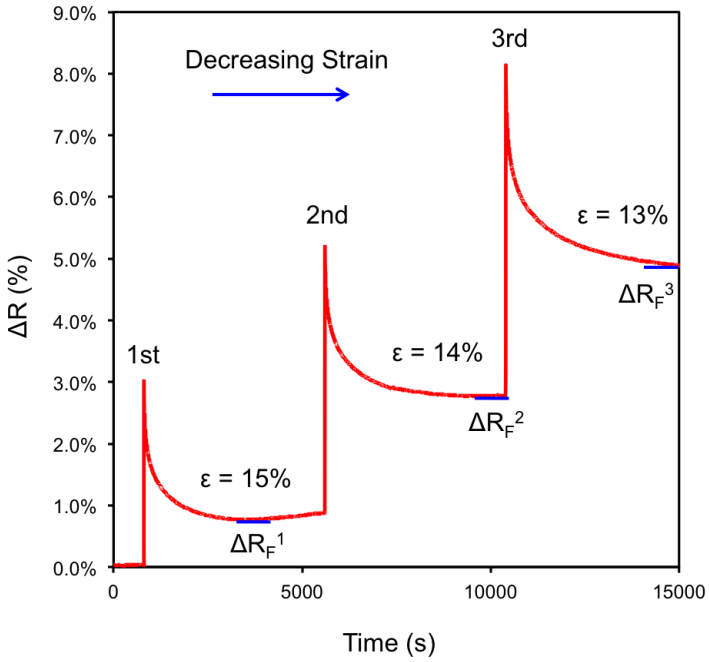

Figure 5-5: The piezoresistive response of a composite for three decreasing strains. The change in resistance, $\Delta R = (R_t - R_0)/R_0$ decays exponentially with time and eventually settles after $\approx 4,000$ s. The minimum resistance reached is a complex function of the strain that depends on whether more or less conduction lines have formed and whether the mean separation distance of particles in the conduction lines has increased or decreased.

decrement, the resistance spikes and then settles with time to a higher steady state value $\Delta R_F^3 = 4.8\%$.

The steady state resistance is a complex function of the strain that depends on whether more or less conduction lines have formed and whether the mean separation distance of particles in the conduction lines has increased or decreased. The focus of the following work is on understanding the changes in steady state resistance in relation to tensile and compressive strain; with the discussion of the exponential decay of resistance in section 5.4.2.

We examine the effect of strain on resistance more closely as we bend the composite in extension from flat to high strain in ten, 200 μm horizontal displacement steps, allowing 300 s between each bend increment for the resistance to decay. The bend is then decreased in a further ten, 200 μm steps so that the composite returns to being flat. This is repeated for two samples, A and B, as shown by the red and blue lines in figure 5-6, with both samples A and B showing similar resistance traces. Initially, for the first two steps, as the strain is increased the resistance R_F^n increases. After the third step the resistance then decreases as the strain is further increased with the resistance for the maximum bend, at 3,000 s and after the tenth step, being less than the initial starting resistance.

As the strain is then decreased a similar dependence is observed. The resistance increases again up to a maximum and then for the final two steps it decreases. This creates the *M-shaped* curve. To understand this complex dependence we need to consider that the composite is three dimensional and that it is mounted to an acetate layer, so that the application of bend creates a *bilayer strain*.

When bending in extension the composite lies on the outside of the bend. Due to the difference in Young's moduli between the acetate and silicone, more than two order of magnitude given in chapter 3.5.3, during bending the neutral axis of zero strain will always be in the acetate. Therefore this creates a *longitudinal* stretch along the length of the composite, a *tensile* strain. This tensile strain causes the mean separation distances of the particles in the longitudinal conduction lines to increase. This in turn creates an *increase* in tunneling resistance and thus the resistance of the composite increases.

However as with applying a stretch to any soft material continuing to increase the tensile strain will also cause a transverse *compressive* strain, figure 5-7. As the matrix itself is soft and the conductive particles are incompressible, the transverse compression causes the conductive particles to become closer to those above and below, in the transverse direction. This allows new conduction lines to form

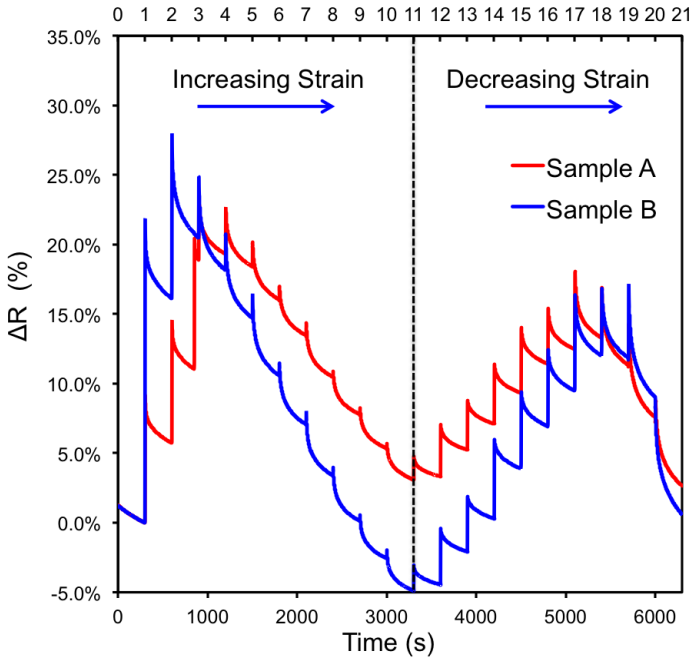

Figure 5-6: The composite is bent in extension to produce a tensile strain. The bend is increased through ten 200 μm horizontal displacement steps. The composite bend is then decreased again in a further ten steps returning it to flat. The composite is given 300 s between bends for the resistance to relax. This is repeated for two samples, A and B, shown as red and blue.

and therefore the resistance will decrease as the bend, in extension, is further increased.

To study this complex dependence more closely we apply smaller strain increments through 20 μm horizontal displacements up to $\epsilon = 6.3\%$ and then in 200 μm up to $\epsilon = 16.5\%$. The resistance, ΔR_F, is measured 60 s after the strain increment, with $\Delta R_F = (R_F^n - R_F^0)/R_F^0$, where R_F^0 is the resistance of the unstrained composite. The change in ΔR_F with tensile strain is shown in figure 5-8.

The resistance increase at low strains is now clear. The resistance increases rapidly up to $\epsilon = 7.5\%$. At which point there is a sharp turning point and the resistance then decreases with further increasing strain. This decrease appears to be almost linear with strain. We interpret this as the competition between the two mechanisms. The strain simultaneously causes both an extension in the longitudinal direction, that causes an increase in the tunneling distance between particles and consequently a rapid increase in resistance, and a compression in the transverse direction leading to the formation of a greater number of conduction lines and hence a decrease in resistance.

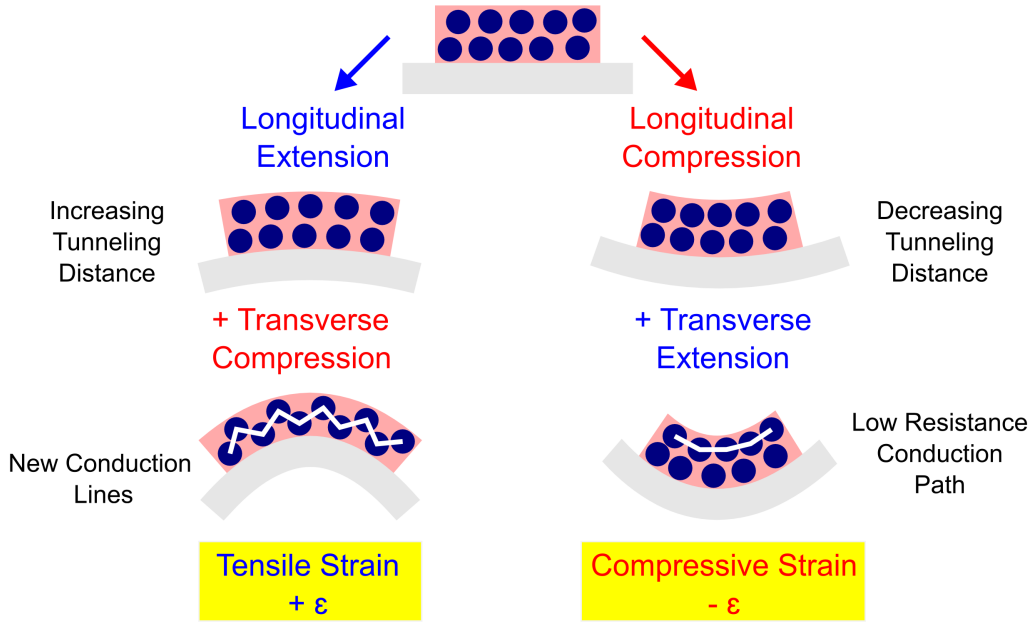

Figure 5-7: Bending in extension, tensile strain, causes a longitudinal stretch in the composite and a transverse compression. These two opposing mechanisms can increase or decrease the overall electrical resistance of the composite. Bending inwards causes a longitudinal compression in the composite and a transverse extension. On the inside of the bend the particles have small separation distances forming a low resistance path.

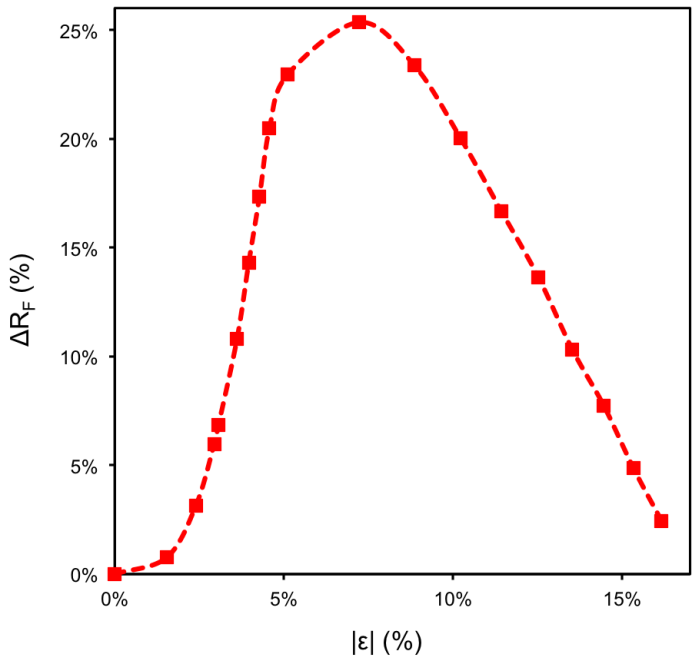

Figure 5-8: The change in resistance, ΔR_F, with strain as the sample is bent in extension. The step size is 20 μm up to $\epsilon = 6.3\%$ and then 200 μm thereafter with 60 s recovery time between increments. The transition between ΔR_F increasing with strain and decreasing with strain occurs at $\epsilon = 7.5\%$. The decrease in resistance for $\epsilon > 7.5\%$ is almost linear with strain.

To assess this reasoning we now apply a compressive strain by bending the composite inwards, with $\epsilon < 0$. The composite is bent in compression in twelve 200 μm steps and given 500 s to relax between steps. To enable a direct comparison the same sample is bent with the same strain sequence but in extension, $\epsilon > 0$. The results of ΔR_F with $|\epsilon|$ are shown in figure 5-9.

Straining in compression causes a 33% decrease in resistance for $\epsilon = -16\%$. The compressive strain produces only a decrease in resistance. This is because the compressive bilayer strain creates a longitudinal compression causing the mean separation distance of the particles to decrease. There is also a transverse extension, which would be expected to increase the resistance, however the resistance is defined by the lowest possible conduction path, which is found at the inside of the bend, figure 5-7 and thus no resistance increase is seen.

The results so far presented have been carried out on new, previously unstrained, samples. We now examine the resistance strain behaviour for a sample that has undergone many strain cycles, figure 5-10. It can be seen that bending at low strains in extension no longer produces the decrease in resistance, instead the resistance now remains almost constant up to $\epsilon = 7.5\%$ after which

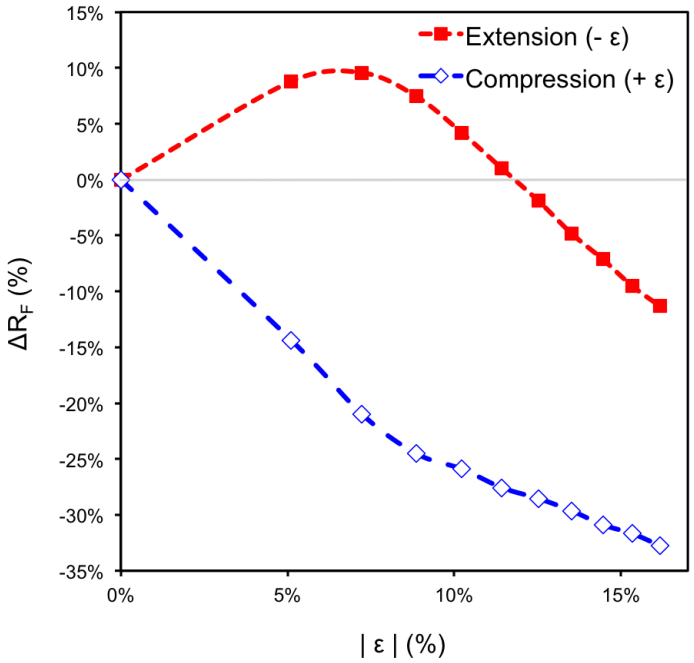

Figure 5-9: The difference between bending in compression and extension. In compression the ΔR_F monotonically decreases while in extensions ΔR_F increases and then decreases with the turning point around $\epsilon = 7.5\%$ The strain increments are in 200 μm steps every 500 seconds.

it decreases linearly with strain. When the extension is then decreased the resistance increases again along the same path with little hysteresis. Below $\epsilon < 10\%$ the resistance tends to a slightly reduced resistance of -5% as the sample has undergone *stress-softening*.

Initially bending in extension causes the particles to move apart and when the extension is relaxed the particles move back. However due to the *Mullins effect* [110, 111], the stress-strain curve depends on the previous maximum loading and when the load increases beyond its all time previous maximum the rubber is *softened* and after which requires a greater strain to produce the same stress. The particles on further bends are not moved apart by so much and so the resistance increase is suppressed.

The Mullins effect of stress-softening occurs due to the breaking up of agglomerates of conductive particles. This is an irreversible rearrangement and causes the observed hysteresis. The *stress-softening* effect is always more pronounced for high filling fractions of filler, like we have in these samples [110]. This is because creating homogeneous filler dispersion becomes more difficult for high filling fractions. Leading to the formation of agglomerates, which then break apart irreversible when strained.

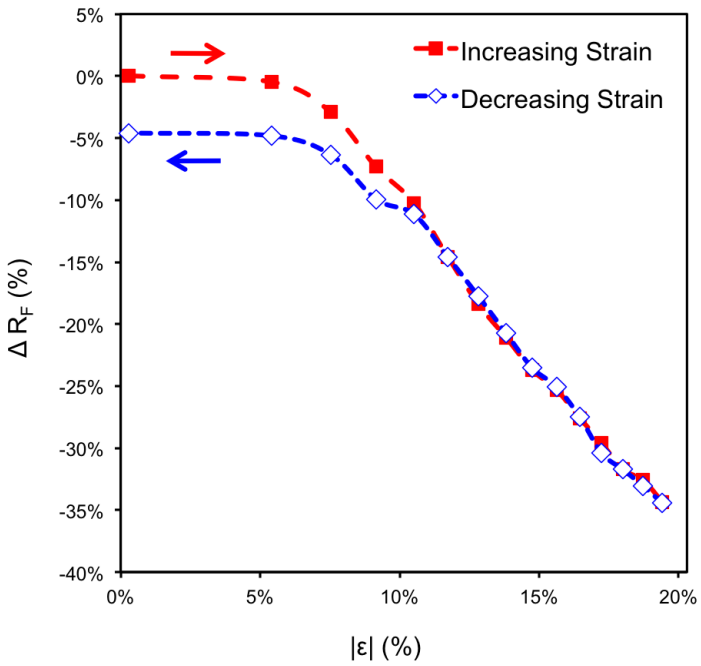

Figure 5-10: A sample that has already undergone many strain cycles is strained up to $\epsilon = 19\%$ (red squares) and then returned to flat (blue diamonds) in 200 μm steps with 600 s between steps. The resistance no longer shows a significant increases when $\epsilon < 7.5\%$. For $\epsilon > 7.5\%$ the decrease in ΔR_F is almost linear with strain and returns along the same path during relaxation with less than a 5% change in the unstrained resistance.

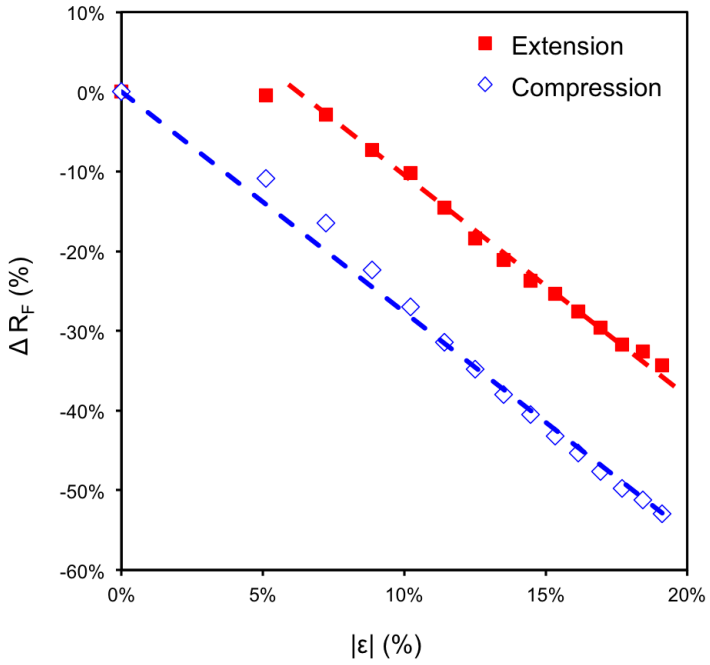

Figure 5-11: Comparing ΔR_F with strain for bending in compression and extension in 200 μm steps every 600 s. In compression ΔR_F decreases linearly with strain from $\epsilon = 0$ to $\epsilon = 19.1\%$ with a gradient $\Delta R/|\epsilon| = 2.77$. In extension the gradient of the linear region $\Delta R/|\epsilon| = 2.70$. The similarity in the linear response in both extension and compression makes the composite well suited as a flexible skin device.

The Mullins effect means that over strain cycles a greater strain will be required to produced the same stress, and so a hysteresis is observed. When bending in extension we have these two different mechanism simultaneously competing in different planes, longitudinal extension and transverse compression. The Mullins effect only applies for tensile stretching of the composite [111]. Thus in figure 5-10 we see the suppression of the increasing resistance for $\epsilon < 7.5\%$ while the compression, $\epsilon > 7.5\%$, remains much the same. When the strain is relaxed the resistance follows exactly the same resistance-strain path back up to $\epsilon = 10\%$, below which a slight decrease of resistance is observed of around 5%. With further strain cycles, while not exceeding the maximum strain, we would expect the hysteresis to be further reduced [108].

When we compare the effect of ΔR_F with strain for compression and extension after strain cycling we see that the compression now follows an almost linear fit of $|\epsilon|$ to ΔR_F and that the rate of change in resistance with strain is almost equal to that of the extension for $\epsilon > 7.5\%$, figure 5-9. In compression $\dfrac{\Delta R_F}{|\epsilon|} = 2.77$

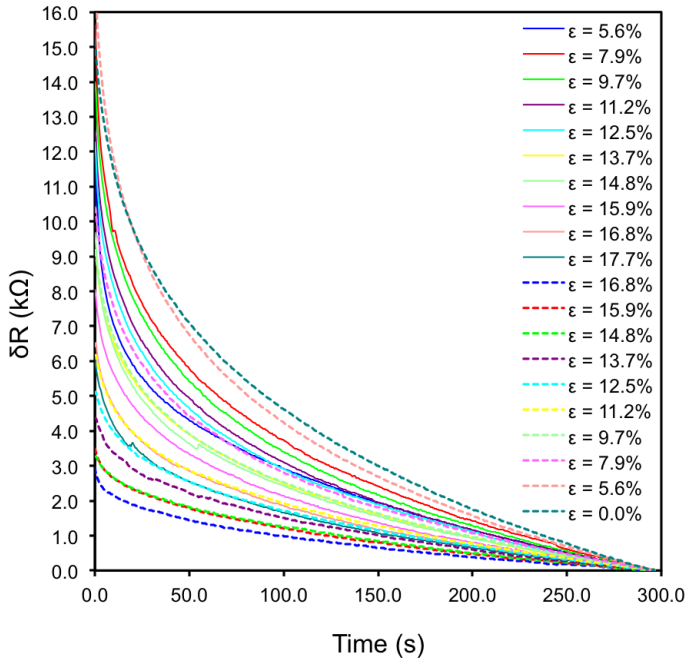

Figure 5-12: The change in resistance $\delta R = R_t^n - R_F^n$ from figure 5-6 for each strain n. The maximum δR at $t = 0$ varies as a function of the strain. However the decay is shown through equation 5.11 to be governed through time constants τ_1 and τ_2 that are independent of ϵ.

for $\epsilon = 0$ to $\epsilon = 19.1\%$. In extension $\dfrac{\Delta R_F}{|\epsilon|} = 2.70$ for $\epsilon = 7.5\%$ to $\epsilon = 19.1\%$. Therefore bending in tensile and compressive strain, $\pm\epsilon$ leads to similar change in ΔR_F once the composite has undergone stress softening.

As the response for bending in both compression and extension yields a linear fit to strain it means that the composite is well suited to the design of a sensor, such as a piezoresistive flexible skin. The main drawback though is the time dependent relaxation of the resistance which we shall now examine.

5.4.2 Transient Piezoresistance due to Viscoelasticity

Next we turn our attention to the resistance decay between strain increments which occurs due to the viscoelastic nature of the composite. We take each step shown in figure 5-6 and find the change in resistance, δR, between strain increments, and decrements, where $\delta R = R_T^n - R_F^n$ with R_T^n the resistance immediately after strain increment, n, and R_F^n the resistance just before the next strain increment. Thus δR is the change in resistance from $t = 0$ to $t = 295$ s for each strain, as shown in figure 5-12.

The maximum δR for each strain is always immediately after the strain in-

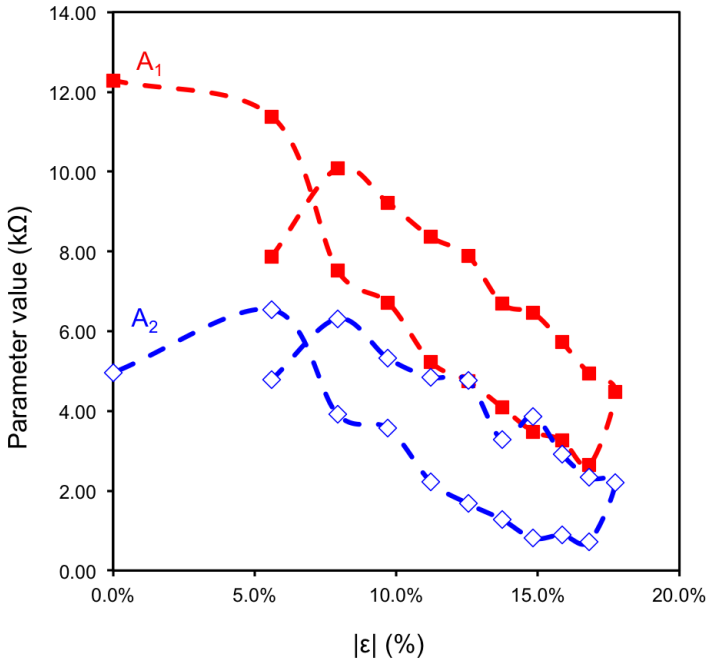

Figure 5-13: Fitting parameters A_1 and A_2 from equation 5.11. Both A_1 and A_2 are a function of strain, with A_1 showing the largest decrease from 12.3 kΩ at $\epsilon = 0$ to 2.7 kΩ at $\epsilon = 16.8\%$. A_2 has a smaller response and initially increases for low strains before decreasing.

crement at $t = 0$. It can be seen that this maximum δR is greatest for the lowest strains and decreases as strain is increased. It then increases again when strain is decreased. This is because the change in strain is greatest for the same horizontal displacement at low strain; at high strain the same horizontal displacement produces only a small strain increment. Therefore at low strain the same horizontal displacement causes the greatest disruption to the conduction network.

The four parameter model, derived in section 5.11, is fitted to the transient data of figure 5-12 using data fitting software. The change in the fitting parameters A_1 and A_2 with ϵ are shown in figure 5-13. Both A_1 and A_2 are a function of strain, with A_1 showing a significant decrease from 11.7 kΩ to 3 kΩ while A_2 initially increases slightly to a maximum of 5 kΩ and decreases to almost zero at maximum strain.

The fitting of the data finds that τ_1 and τ_2 remain constant with strain with $\tau_1 = 193.3$ s and $\tau_2 = 12.9$ s as shown in figure 5-14. This is what we would expect as they are intrinsic properties of the composite relating to viscosity and Young's modulus, which are not a function of strain. The two time constants have different orders of magnitude and correspond to different stress attention speeds in the composite. The mechanism for $n = 2$ is much faster and has a

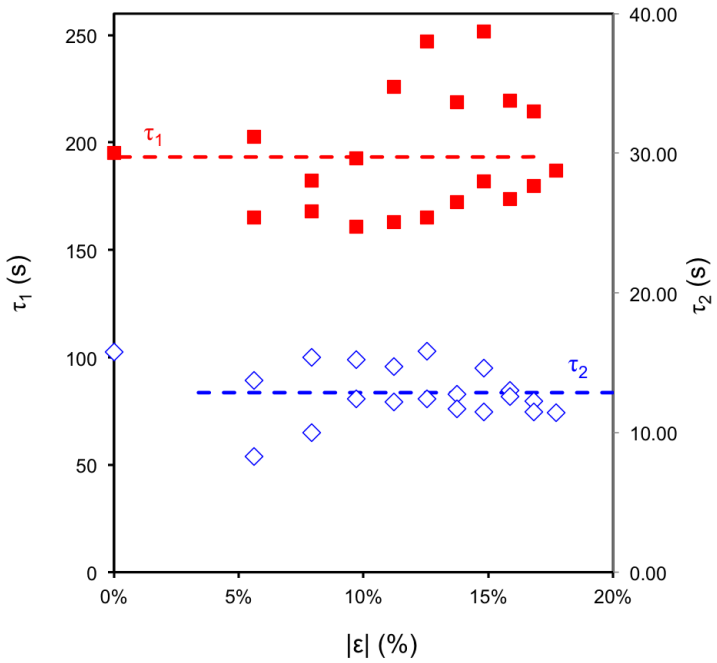

Figure 5-14: Fitting parameters τ_1 and τ_2 extracted from applying the four parameter model derived for viscoelasticity in equation 5.11. The time constants do not vary with strain with $\tau_1 = 193.3$ s and $\tau_2 = 12.9$ s and correspond to two different stress attenuation speeds in the composite.

smaller comparative influence at low strains than for $n = 1$.

We repeat the experiment for another sample of the same dimensions and filling fraction. Applying the four parameter model yields a similar strain dependence of A_1 and A_2 and values of $\tau_1 = 195.1$ s and $\tau_2 = 4.9$ s. These values are similar to those extracted for the first sample with τ_1 varying by less than 1%, and the values for τ_2 being within 8 s of each other. This provides evidence that τ_1 and τ_2 are intrinsic to the composite as they are consistent between similar samples.

Finally to satisfy ourselves that there are indeed two distinct stress attenuation speeds we plot $\ln(\delta R)$ against time, figure 5-15. Two clear slopes are observed that correspond to τ_1 and τ_2. The slopes run parallel for different strains which shows the that τ_1 and τ_2 remain constant with strain again showing that τ_1 and τ_2 are intrinsic properties of the composite.

The two distinct stress attenuation speeds arise due to two concurrent mechanism in the composite. We believe that they relate to differences between the stress relaxation in the transverse and longitudinal planes. As discussed for the changes in steady state resistance there is both a tensile strain in the longitudinal plane and a compressive strain in the transverse plane. It is feasible that the

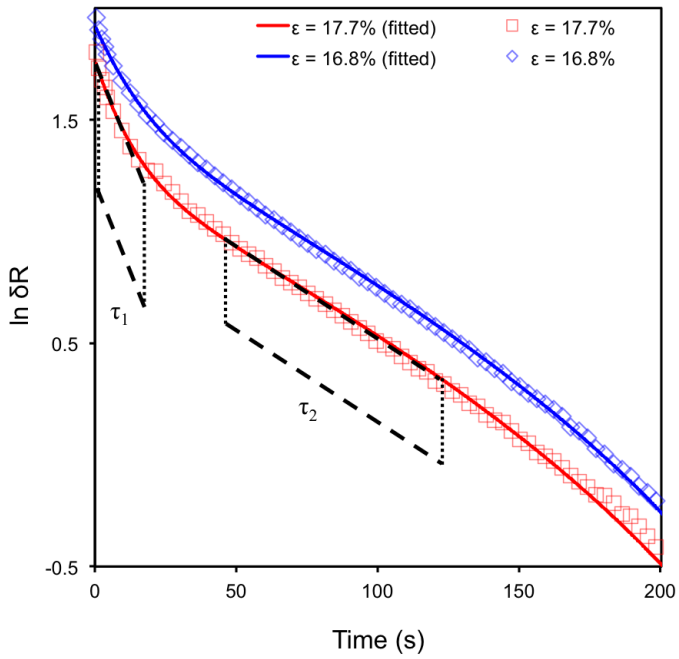

Figure 5-15: The two slopes correspond to different time constant values τ_1 and τ_2. The four parameter fit of the data follows the experimental data closely. The red line corresponds to S_1 at 17.7% strain while the blue S_2 at 16.8%. The time constants are independent of strain and vary little between similar samples.

stresses from these two strains will relax on different time scales. The influence of the conductive particles within the silicone rubber could lead to different values of the Young's moduli in strain and compression. According to the spring dash pot model the stress attenuation speed is equal to the ratio of viscosity to Young's modulus and assuming the viscosity of the composite remains constant then the Young's modulus between the longitudinal and transverse strain will vary by around a factor of 15.

To summarize we measure the stress relaxation speeds of the composite indirectly via the resistance decay between strain increments. We have applied a four parameter viscoelastic model to show that there are two stress attenuation speeds. The stress attenuation speeds remain invariant under strain. As the values are an order of magnitude different, we suggest they relate to two distinct mechanisms related to the bilayer strain that causes both longitudinal extension and transverse compression within the composite.

5.4.3 Bandwidth and Capacitance with Strain

Next we investigate the band width of the composite with strain. The input frequency was swept from 10 Hz to 500 kHz (63 rad s^{-1} to 3.14 Mrad s^{-1}) at a

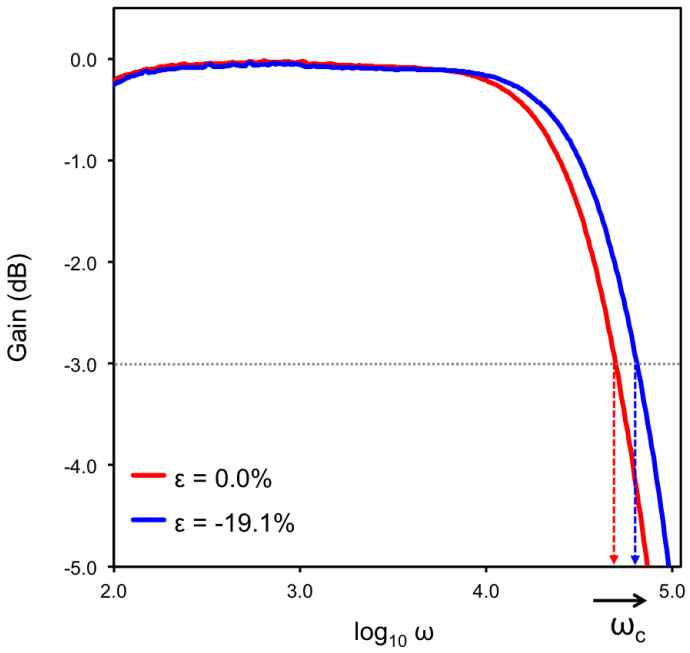

Figure 5-16: A bode plot showing the shift in cut-off frequency caused through straining the composite in compression. At $\epsilon = 0\%$ $\omega_C = 48,468$ rad s^{-1} and at $\epsilon = 19.1\%$ $\omega_C = 63,001$ rad s^{-1}. This is a shift in ω_C of 30%.

constant amplitude $V_{in} = 1$ V. The output voltage across the composite, V_{out}, was recorded with a 100 kΩ resistor in series. The frequency sweeps were repeated as the composite strain was increased from $\epsilon = 0\%$ to $\epsilon = 19.1\%$ in fourteen, 200 μm horizontal displacement steps. The composite was allowed to relax for 600 s between the strain increment and then commencing the frequency sweep.

The gain, G, calculated from equation 5.12 is shown as a function of angular frequency in figure 5-16 for the sample unstrained, $\epsilon = 0$ (red) and the sample under maximum compressive strain $\epsilon = -19.1\%$ (blue). Increasing the compressive strain increase the cut-off frequency. At $\epsilon = 0\%$ $\omega_C = 48,470$ rad s^{-1} while at $\epsilon = -19.1\%$ $\omega_C = 63,000$ rad s^{-1}. A shift in ω_C of 30%.

The incremental increase of ω_C with $|\epsilon|$ for both compressive and tensile strains is shown in figure 5-17 where the cut-off frequency increases monotonically for both. The shift due to tensile strain is not by as much for the compressive strain, with an increase in ω_C from 49,750 rad s^{-1} to 57,170 rad s^{-1}, at $\epsilon = 19.1\%$, an increase of 15%. To examine this further we take the DC resistance, R_0^n, for each strain and use equation 5.13 to estimate the capacitance of the composite for each strain, n, in both compressive and tensile strain. Plotting the variation of the composite capacitance with strain in figure 5-18 shows that the capacitance of the composite increases with increasing strain. The increase is greatest

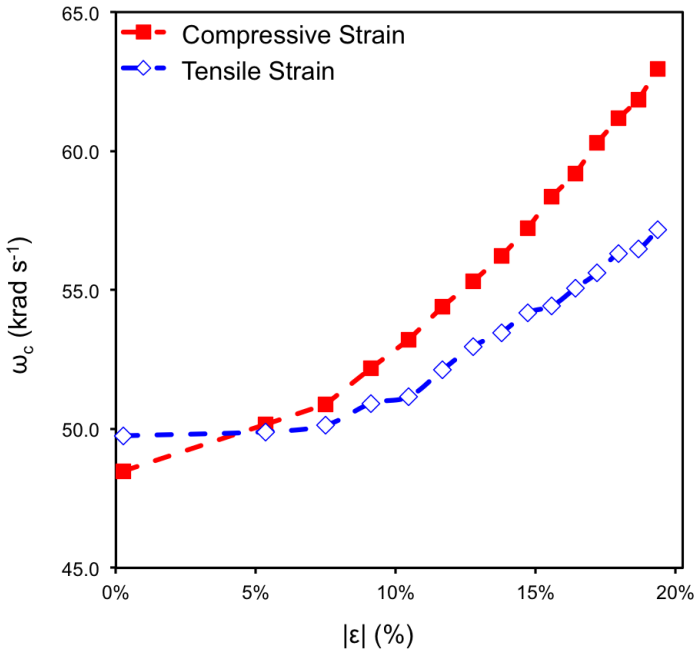

Figure 5-17: The cut-off frequency with $|\epsilon|$ for compressive and tensile strains up to $|\epsilon| = 19.1\%$. The cut-off frequency increases monotonically for both compressive and tensile strains. The increase is greatest when bending the composite to induce a compressive strain. The shift is as much as 30% at $|\epsilon| = 19.2\%$.

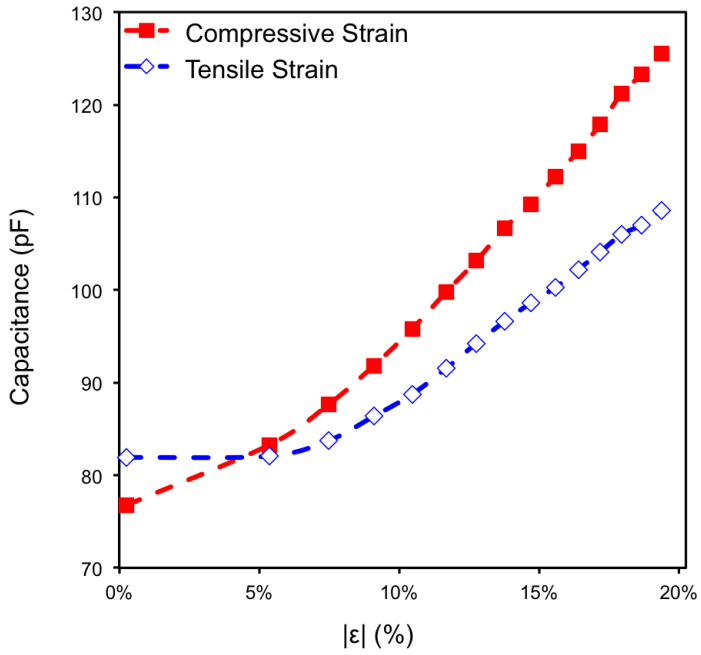

Figure 5-18: Increasing the strain increases the capacitance of the composite both in compressive and tensile strain. The increase is greatest for strain in compression where the capacitance increases from 77 pF to 125 pF.

for compressive strain with the composite capacitance increasing from 77 pF to 125 pF. There is also an increase under tensile strain from 82 pF to 109 pF.

It is interesting to note that with the cut-off frequency increasing it would be expected that the capacitance should then decrease with increasing strain. However we see the opposite with the capacitance increasing for both tensile and compressive strain. This is because the change in DC resistance is significant enough to overcome the increase in ω_C. The capacitance should be dependent on the separation distance between the conductive particles with particles, that are not in touching contact, forming micro-capacitors with surrounding particles. If the separation distance decreases with bend then the capacitance between particles would increase.

We can approximately relate the macroscopic bulk capacitance to the micro-capacitance between individual particles, using the laws for combining capacitors, as the particles can be considered to form lines of capacitors in both parallel and series. Taking the dimensions of the composite we find that there are around 1,000 particles in series along a conduction line and 1,000,000 of these conduction lines in parallel. Therefore the bulk capacitance $C \approx 1000 C_P$ where C_P is the capacitance between two particles. Assuming that the particles form parallel plate capacitors,

$$C_p = \frac{\epsilon_d \epsilon_0 A}{d}\,, \tag{5.18}$$

where d is the separation distance, A is the particle area, 400 nm $\times$ 400 nm, $\epsilon_0 = 8.85 \times 10^{-12}$ Fm^{-1} is the permittivity of free space and that the dielectric constant $\epsilon_d \approx 5 \times 10^3$ (based on similar high filling conductive composites [124, 125, 116]).

Using equation 5.18 and the bulk capacitance values from figure 5-18 we can calculate that the particle separation changes with compressive strain: At $|\epsilon| = 0\%$ $d = 92$ nm and at $|\epsilon| = 19.1\%$ $d = 57$ nm. The separation distance for the unstrained composite, $d = 92$ nm, is consistent with the value extracted when we considered the barrier width in chapter 4.3. The decrease in mean particle separation distance of 35 nm on straining is large and could explain why we see such a large resistance decrease in the samples under strain.

In summary we have shown that the composite has a bandwidth of 7.7 kHz. Straining the composite in compression yields an increase in bandwidth of 30%, to 10 kHz. We relate this to changes in the capacitance between graphite particles that is caused through a decrease in separation distance of 35 nm when the composite is strained.

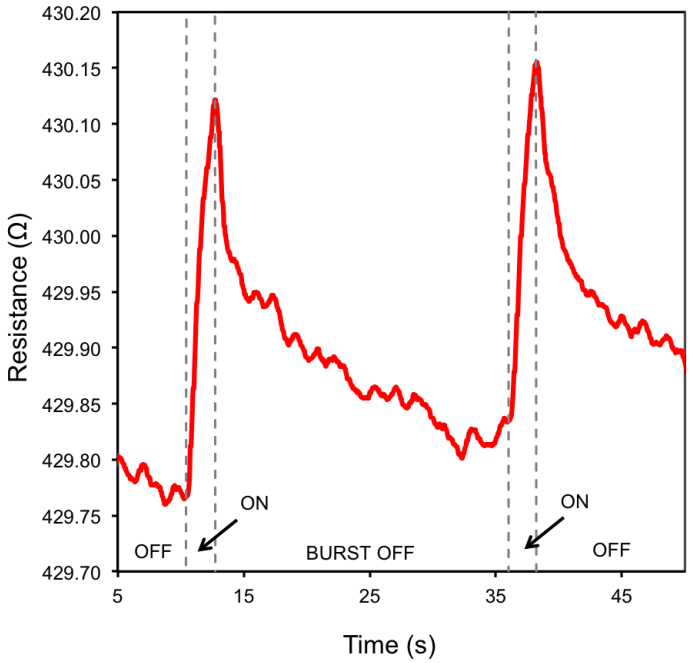

Figure 5-19: The 4T resistance with time for two 2 s bursts of ultrasound. The resistance changes are of the order 0.3 Ω and the background noise is ±50 mΩ. At the onset of the burst the resistance is low, R_L, and increases while the burst is applied. At the end of the burst the resistance peaks at its highest value, R_H, and then decays.

5.4.4 Detection of Acoustic Pressure from Ultrasound

We demonstrate the sensitivity of the GSC by applying an acoustic pressure via ultrasonic waves transmitted through water. The intensity, and hence pressure, of the ultrasound can be controlled by altering the voltage applied across the transducer. The composite can be rotated at an angle to the incident waves.

During a two second burst of ultrasound the 4T resistance, R, can be seen to increase, figure 5-19. As soon as the burst ends the resistance begins to decay back to close to the initial starting resistance. The decay is fast with a decay time of the order of just 10 s. There is some noise in the resistance, around ±50 mΩ, due to the sample being immersed in water making it sensitive to any waves or disturbances in the water tank. The resistance of the composite sample is $\simeq$ 430 Ω and the maximum change in resistance is 0.3 Ω.

Applying the ultrasound burst creates a response similar to that seen when strain or direct pressure is applied. The resistance spikes. This is because the *acoustic pressure* of the longitudinal sound waves causes *movement* of the conductive particles within the composite leading to the *breaking of conduction lines* and hence an increase in resistance.

We first consider three successive bursts, of $t_B = 10$ s and of constant power. To enable comparison between the bursts we superimpose one over another by setting the start of each burst as $t = 0$, shown in figure 5-20. All three resistance traces show the same behaviour, highlighting the reproducibility of the measurement technique. The maximum resistance increase is 1 Ω at the end of the burst at $t = 10$ s. When the burst is switched off the resistance decays immediately and at a similar rate for all three bursts. The resistance decays back to close to the initial starting resistance within 15 s of the burst ending.

Whilst the burst in ON δR increases with time. This is because the composite integrates the power transferred to it over the time interval of the burst [121]. The total energy transferred to the composite will therefore increase as the burst continues. The incident waves cause small movements of the conductive particles, causing the tunneling distances to change, and the resistance to increase. Medical ultrasound uses this movement of particles to create localised heating in the body [120].

Clearly δR_B is not a direct measurement of the energy absorbed. The increase in δR_B is not linear with t_B and instead follows approximately a square-root dependence. There must be an increasing energy requirement for the same resistance increase as the burst becomes longer. Possibly this is because it becomes more difficult to vibrate the molecules further from their equilibrium position.

We next examine the effect of increasing acoustic pressure, P_a, as a function of $\delta R_B = R_H - R_L$ for a fixed burst duration $t_B = 5$ s shown in figure 5-21. The pressure is varied by the input voltage, V_{pp}, and then calculated using equation 5.17. Increasing P_a from 51 Pa to 130 Pa causes a linear increase in δR_B from 0.01 Ω to 0.15 Ω. The error bars show the maximum and minimum δR_B from the four pulses. Extrapolating the linear fit to $\delta R_B = 0$ we find a pressure detection threshold of 48 Pa.

The effect of increasing the acoustic pressure is to create a greater disruption to the conduction network. The pressure calculated in equation 5.17 is the peak acoustic pressure. We can picture the ultrasound longitudinal wave passing through the composite creating local maximum and minimum pressures with a wavelength, $\lambda = 420$ μm. The greater the pressure gradient the greater the movement of the conduction particles in the matrix. Each particle will only be subject to a very small displacement as they are encapsulated by the matrix, however the macroscopic effect, of all the very small particle displacements from equilibrium, is to cause the resistance to increase.

Below the pressure detection threshold of 48 Pa there is no longer a detectable

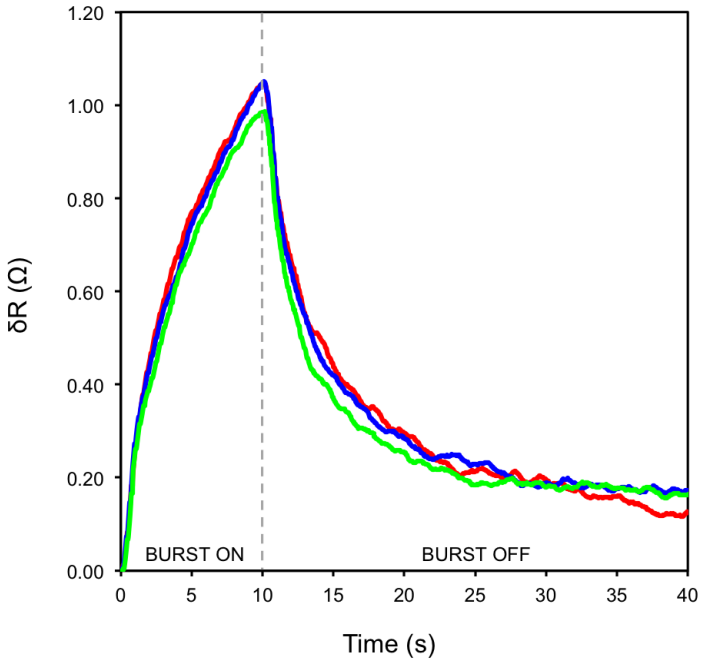

Figure 5-20: Comparing three successive bursts of ultrasound at a constant power and $t_B = 10$ s. All three bursts show a similar increase in resistance, δR during the burst and decay at the same rate once the burst is switched off.

change in resistance. What is not clear is whether this is due to the change in resistance being too small to be measurable or, if there is a certain minimum pressure required before it begins to influence the conduction network i.e a minimum pressure may be required before the particles are able to move relative to one another. This has similarities to what we observed in figure 5-10 where initially the increasing strain does not cause any sizable change in resistance and then for $\epsilon > 7.5\%$ the resistance begins to decrease linearly with strain. However there are differences between the two situations as in figure 5-10 the resistance is decreasing due to the formation of a greater number of conduction lines while in figure 5-21 the resistance increases as the ultrasound pressure causes particle movement in the conduction lines leading to conduction line destruction. For the utilization of the composite in sensory applications it will be important to understand if there is a minimum pressure, or strain, required before a change of resistance is detectable as this will always be the fundamental limit of the sensor.

Lastly we consider the angular dependence of the composite to the incident ultrasound waves. Initially this test was performed to confirm that the changes in composite resistance were due to the incident acoustic pressure. This is because altering the angle of the composite controls the power incident as the function $\cos\theta$. When $\theta = 90°$, due to the high aspect ratio of the composite, there is

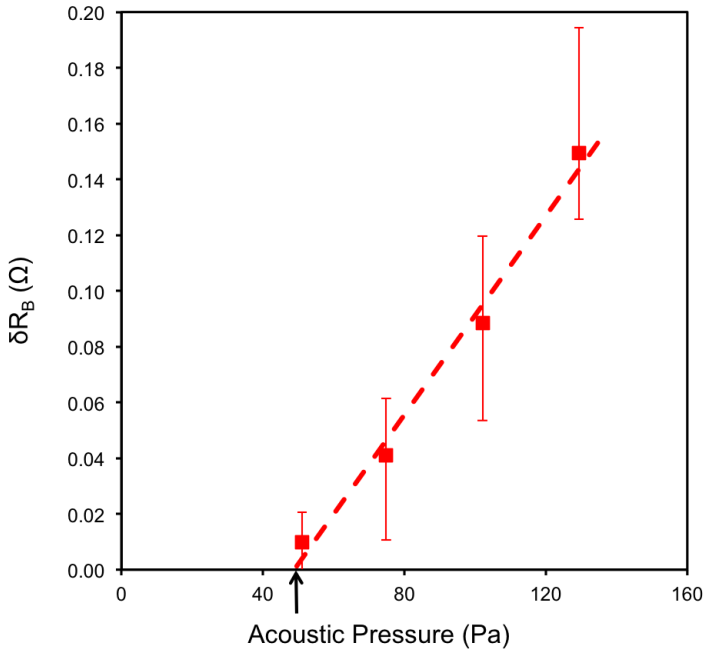

Figure 5-21: Increasing the acoustic pressure causes δR_B to increase for bursts of the same t_B. A greater acoustic pressure causes more disruption to the conduction network and hence a greater δR_B. The minimum pressure to cause a disruption to the conductive network, extrapolated from the linear fit to $\delta R_B = 0$, is 48 Pa (indicated by the black arrow).

effectively no ultrasound power that will be incident on the composite. The change in δR_B as the composite is rotated away from the incident waves by angle θ is shown in figure 5-22.

Firstly we note that $\delta R_B \simeq 0$ at $\theta = 90°$ confirming that the resistance changes we observe are certainly due to the incident ultrasound waves and not from a spurious electrical effect. However the maximum δR_B does not occur at $\theta = 0°$, as one might expect as this is when the greatest power is incident on the composite.

In fact we observe a complex response that contains three peaks in δR_B at $10°, 35°$ and $50°$. With the greatest increase in δR_B occurring at $35°$. To understand this we need to consider the dimensions of the high aspect ratio composite with height, $h = 90$ μm, and width, $w = 1.33$ mm. The height of the composite is shorter than the ultrasound wavelength, $\lambda = 420$ μm. However when the composite is rotated multiple wave fronts can exist across the *width* of the composite. The effective length of the composite in the plane of the direction of wave propagation varies as a function of $\sin\theta$. At certain angles the effective length becomes equal to an integer number of wavelengths, n, and similarly to

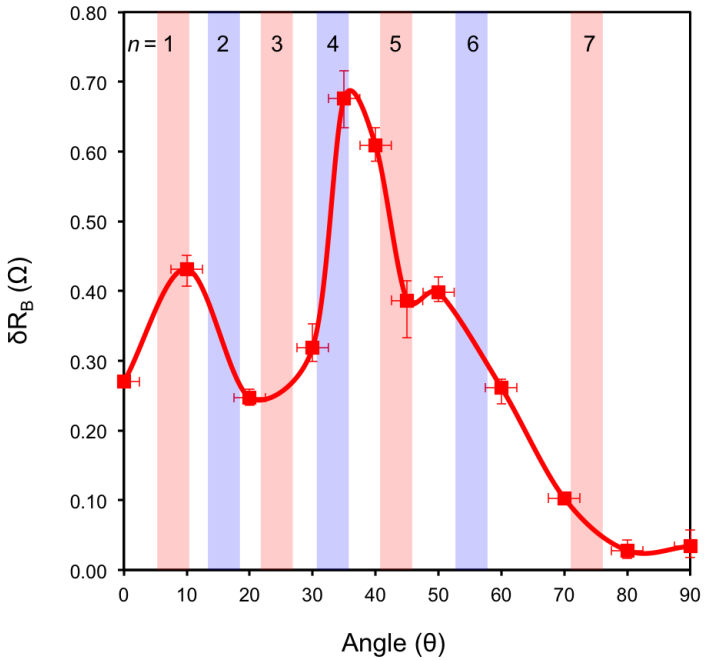

Figure 5-22: Rotating the composite at an angle θ to the incident wave causes a complex response of δR_B. We observe three peaks at $10°, 35°$ and $50°$. There are also minima at $20°$ and $45°$. The shaded red and blue lines indicate the calculated angles for destructive and constructive interference in the composite.

Bragg's law, these angles are found using,

$$n\lambda = 2w \sin\theta \,. \tag{5.19}$$

It is likely that at integer values of n standing waves are created within the composite, shown in figure 5-23. As the waves are longitudinal *odd* values of n will create *destructive* interference within the composite and *even* values of n will lead to *constructive* interference. Where there is destructive interference the acoustic pressure in the composite will be at a minimum and where there is constructive interference the acoustic pressure will be greatest and δR_B will be greatest. We calculate θ using equation 5.19 with $d = 1.33\ mm$ and $\lambda = 318\ \mu$m, instead of $\lambda = 420\ \mu$m, as we take account of the reduced sound velocity in the composite, $c_c = 1275\ \text{ms}^{-1}$ [122]. The calculated values of θ for $n = 1$ to 7 are shown in table 5.1 along with the observed maxima and minima.

The close fit between the calculated and observed values are remarkable considering the uncertainly in measuring the rotation angle is $\pm 5°$ and the incremental step size between rotations is large.

If we also consider that the incident power reduces as $\cos\theta$, shown as the

n	Calculated θ	Observed θ	Type
1	7.9	0 ± 5	*destructive*
2	15.9	10 ± 5	*constructive*
3	24.3	20 ± 5	*destructive*
4	33.2	35 ± 5	*constructive*
5	43.3	45 ± 5	*destructive*
6	55.3	50 ± 5	*constructive*
7	73.6	80 ± 5	*destructive*

Table 5.1: Comparing the calculated values of θ from equation 5.19 and the observed maxima and minima in $\delta R_B$of figure 5-22. Odd values of n correspond to destructive interference and mimima in δR_B and even values of n to peaks in δR_B.

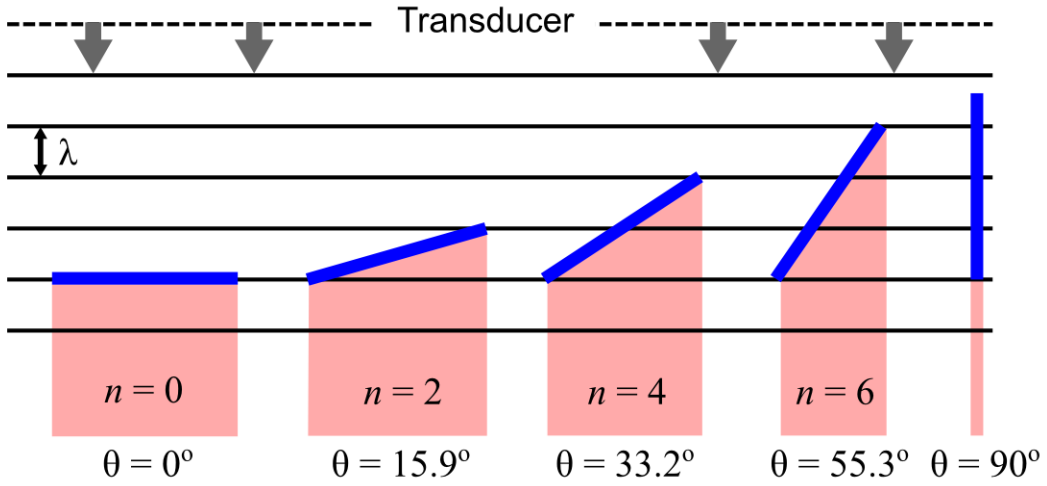

Figure 5-23: At even values of $n = 2, 4$ and 6 a standing wave is created along the composite width that constructively interferes to create a greater acoustic pressure and hence a larger increase in δR_B. As the composite is rotated the power incident on the surface reduces as $\cos\theta$, shown graphically by the red shaded areas reducing in width as θ is increased.

red shaded areas in figure 5-23, we begin to understand the complex angular dependence observed: The greatest δR_B occurs at $\theta = 35°$ due to the balance between the total incident power decreasing and the greatest disruption to the conduction lines along the plane of the composite.

In summary we have shown unequivocally that the composite is able to detect ultrasound waves. We have shown that increasing the total energy absorbed by the composite, by increasing the burst length, increases the resistance peak. We have also shown that a greater resistance peak is obtained by increasing the acoustic pressure. The pressure detection threshold is found to be 48 Pa. Finally we observe commensurability between the ultrasound wavelength and the composite width. We explain this as the creation of standing waves across the width of the composite that constructively or destructively interfere to create greater or less acoustic pressure to disrupt the conduction network.

5.4.5 Differential Pressure Array Imaging

The DPA was built to demonstrate the sensitivity and a potential application for the resistance spiking phenomena. An array of 64 composites were used to create images with each composite forming a single pixel.

The individual elements of the array were first tested through directly applying a small perturbation to individual composite pixels with singular taps with a pen nib. The small perturbation causes a large resistance spike in the pixel. Only the resistance of the perturbed pixel changes while the resistance of the other pixels remains constant. The resistance with time plots of three taps to the same pixel with two minutes between taps is shown in figure 5-24.

The tap causes the resistance to increase from 4.5 kΩ to over 6.5 kΩ. The tap is sharp and the resistance quickly decays back to close to the initial resistance. The resistance spike response is much greater than that seen in the bend-induced strain or ultrasound measurements. This is because the pressure applied is larger with the force directly applied to a small area. Also the geometry of the pixel means that the pressure applied is along the same axis as the direction of conduction. All the conduction lines will therefore be equally perturbed causing a greater resistance spike. The fast decay of the resistance could be attributed to the high filling fraction of the composite, $\rho = 34.8\%$. Further the NDI-Si molecules were included in the composite which act to better bind the composite in the silicone and possibly lead to a faster stress attenuation. It is not likely that the resistance spikes are caused by changes in contact resistance as the compres-

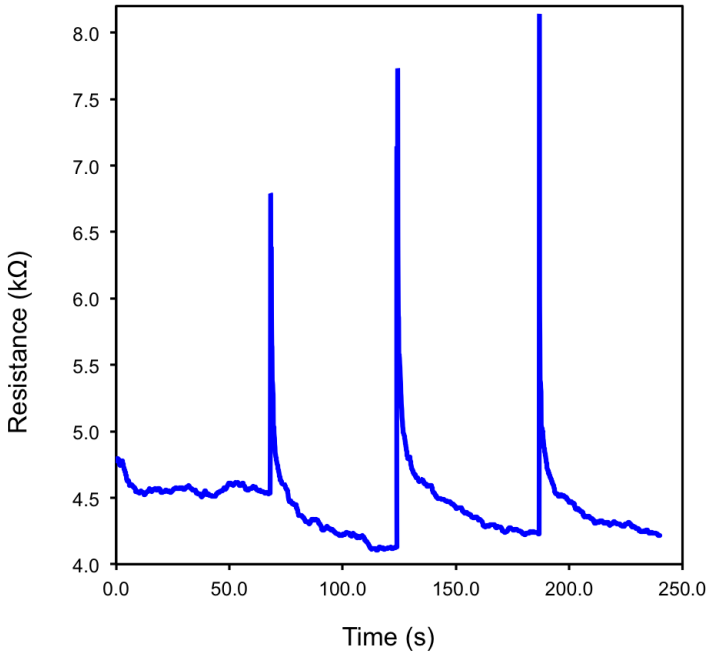

Figure 5-24: Applying a gentle perturbation to a composite in the array with a pen nib causes a spike in resistance. For the third perturbation there is a 92% increase in resistance.

sion is more likely to causes a decrease in the resistance as it acts to compress the composite onto both the contacts.

Now we examine the third perturbation more closely, figure 5-25, where the percentage change, $\Delta R = (R_0 - R)/R_0$, is shown with time. The resistance, having increased, falls from 92% to 25% in just 0.5 s. While after 10 seconds the resistance has fallen to $\Delta R < 10\%$. The four parameter model of viscoelasticity, equation 5.11, can be applied to find that $A_1 = 931, A_2 = 655, \tau_1 = 0.48$ s and $\tau_2 = 7.68$ s. Confirming that the decay times are significantly faster than seen previously. With $\tau_1 < 0.5$ s, and A_1 being the greater factor, the pixel could detect seperate pertubations with a frequency of up to 2 Hz.

The decay times and maximum resistance change were used to determine the sensitivity and time delay settings for the LabView program that monitors all the sensing elements. The sensitivity was set close to 15 %, i.e requiring a resistance change greater of $\Delta R > 15\%$, while the sweep frequency was set to 4 Hz, with each pixel addressed every 0.25 s so that the resistance spike could be captured for all 64 pixel array elements. A time delay of 10 s was used to enable the resistance to settle before continuing with the monitoring of the triggered pixel.

Screen shots for the graphic representation of the array from the C and B stamps are shown in figure 5-26(a) and (b). All pixels that were ON, i.e had a

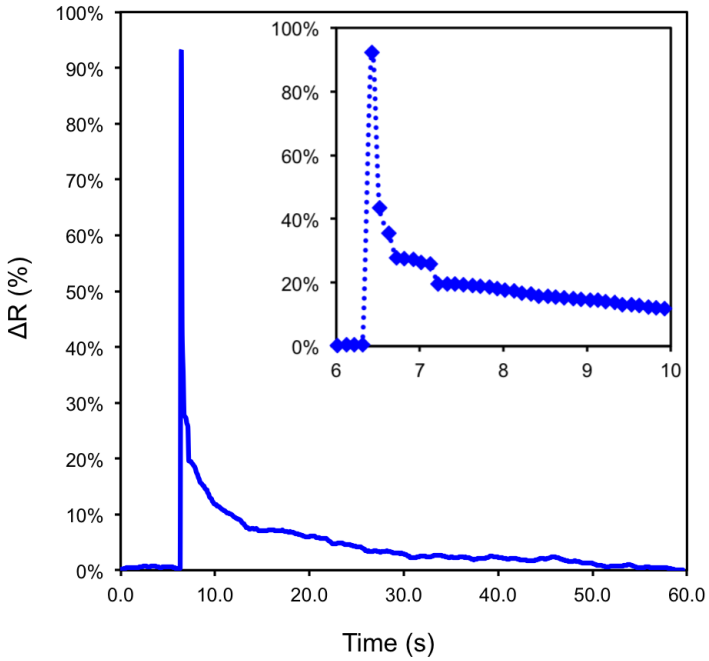

Figure 5-25: The resistance decays at a fast rate, returning to its starting value in under 60 s. (inset) Close inspection shows that the resistance change falls from 92% to 25% in 0.5 s and to under 10% within 10 s.

pressure applied, were found to correctly respond for both stamps. The C-stamp was imaged through dropping the stamp of weight 40 g from a height of 1 cm. All the ON pixels lit up within one sweep of the array after the stamp impacting the array. No OFF pixels were lit showing that the pixels are both electrically and mechanically isolated from one another.

The B-stamp responded well to rocking, with the rock forwards causing the top half of the array's ON pixels to trigger while the rock backwards did the same for the bottom half. With no guide bars for the B-stamp care was taken to keep the protrusions aligned over the center of the pixels.

A gentle tap to the B-stamp did not always cause all the ON pixels to trigger. This is because the force is spread over 20 pixels and with the area 20 times larger, the pressure is 20 times smaller. Further not all the protrusions of the B-stamp were of the exact same height which would cause a greater pressure to be exerted on some pixels than others. Likewise removing the B-stamp did not consistently cause all the pixels to trigger. Whereas removing the C-stamp, which was specifically machined such that all the protrusions were exactly the same height to ± 10 μm, did cause all the correct pixels to trigger. Removing the stamp causes a similar resistance spike with a similar breaking of conduction lines.

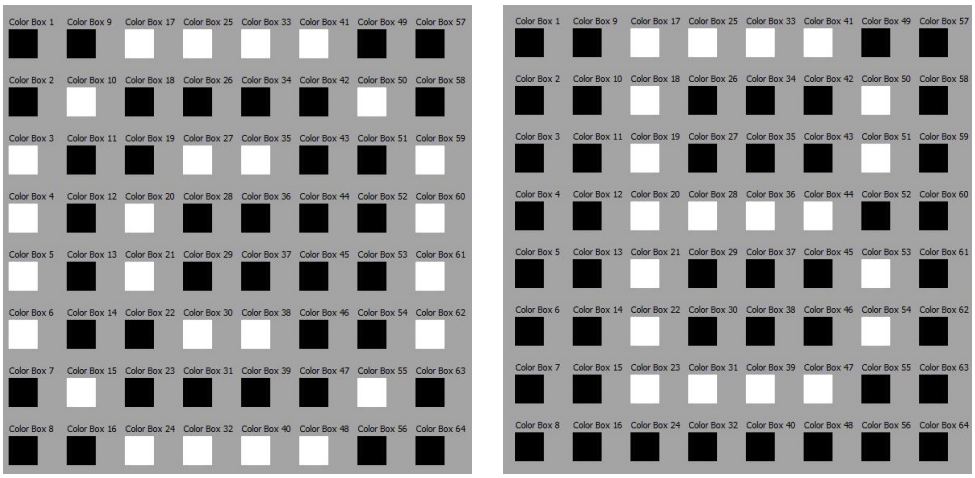

Figure 5-26: (a) The computer image of the array immediately after the C-stamp impacts on the pixel array. The white pixel squares correspond to the pixels in the array that have undergone a resistance change of $\Delta R > 15\%$. (b) The computer image for the B-stamp with same sensitivity setting. A video of the real time imaging can be found at [123]

The differential pressure, P, detected by the C-stamp can be estimated by taking the mass of the stamp, 40 g, and the area each pixel, $A = 4$ mm^2, so that the pressure per pixel is given by,

$$P = \frac{F}{26A} = 3.8 \text{ kPa}\,. \tag{5.20}$$

The composite is able to detect pressures less than 3.8 kPa as the sensitivity was set such that a 15% spike in resistance was required to trigger a pixel. Reducing the mass of the stamp to just 8 g and the sensitivity to 8%, triggered all but a few pixels. It is possible that these were pixels where the composite height was slightly reduced and so the full pressure wasn't exerted. However this would correspond to a detection of just 0.75 kPa per pixel.

In summary the DPA has been shown to reliably detect changes in pressure of less than 3.8 kPa caused by resistance spikes from the destruction of conduction lines. This is a sensitive imaging technique for measuring the differential pressure changes. The recovery time of the resistance is of the order of just a few seconds.

5.5 Summary

This chapter has discussed some of the electromechanical properties of GSC at room temperature. The changes in resistance due to bilayer strain, stress relaxation, AC impedance, acoustic pressure and differential pressure have been presented.

The bend induced bilayer strain is an accurate technique for altering the strain within the composite. We have shown that induced changes of the steady state resistance, after stress relaxation, is complex due to the differences in tensile and compressive strains created in the transverse and longitudinal directions. However once the composite has undergone stress softening the composite exhibits a reproducible linear change in resistance for both bending in compression and extension. The composite is well suited as a sensor such as a flexible skin. Except, that the viscoelasticity of the composite means that the resistance can take up to 300 seconds to settle. We analyse the resistance decay through the four parameter viscoelastic equation derived from a Maxwell spring dash pot model. We have shown that there are two time constants, that are invariant under strain, which we interpret as differences between elastic moduli in the longitudinal and transverse planes.

We have shown that the bandwidth of the composite is increased by as much as 30% with strain due to changes in the capacitance of the composite. We extract the capacitance from the cut-off frequency and relate this to the capacitance between individual particles to show that the particle separation distance decrease under strain.

The use of GSC to detect ultrasound via conduction line destruction is novel and we have used it to highlight how sensitive the percolation network is to perturbations. The pressure detection threshold was shown to be 48 Pa. We also observed a commensurability between the composite width and the ultrasound wavelength. We show that this can be interpreted in terms of the creation of standing waves inside the composite and that the maxima and minima follow Bragg's law.

Finally the composite is used in the DPA to consistently detect differential pressures of < 3.5 kPa. This is better than the piezoresistance of conductive rubbers and is a novel method of detection [126]. There is potential for creating one of these arrays on a flexible substate and using flexible transistors, such as pentacene transistors, an entirely flexible skin could be fabricated. Using the resistance spikes caused by conduction destruction allows a better sensitivity

than the pieozoresistance. Further through consideration of the pixel geometry and using NDI molecules the viscoelastic could possibly be reduced to under a second allowing for dynamic measurements to be made. For a large array, say 64 by 64, a high frequency input signal will be required to allow the change in impedance to be detected. However due to the intrinsic capacitance and cut-off frequency, 8 kHz, the maximum address frequency is just 2 Hz for a 4,096 pixel array.

Chapter 6

Electronic Amplification in the NDR Region

The aim of this chapter is to demonstrate that the GSC is capable of functioning as an *active* device, by sustaining oscillations in an inductor-capacitor (LC) circuit when biased in the NDR region. We first explain how this is possible by demonstrating a lambda diode as an oscillator and amplifier. In the process we derive and confirm equations for the oscillation frequency, the cut-off frequency and the gain of the amplifier.

We then show that the NDR region of the GSC can sustain oscillations, at the LC tank frequency, up to 12.5 kHz. We confirm that the oscillations are only present when the composite is biased in the NDR region.

The second aim of this chapter is to explore how the oscillations vary when a strain is induced in the composite. We strain the sample through bending and show that this shifts the NDR region. We show this can be used to vary the amplitude of the driven oscillations.

We also report the unexpected discovery of intrinsic oscillations, independent of the LC frequency, that can be tuned with strain. We show the intrinsic oscillation frequency increasing by as much as 84 Hz / % strain. Demonstrating a *flexible oscillator* with the strain encoded as frequency and showing the potential of the GSC as a flexible active device.

Finally we create a flexible strain-tuned amplifier. Using the NDR we are able to amplify a signal, at the intrinsic frequency, with a gain that can be tuned between 1 and 4.5.

6.1 Introduction

This chapter demonstrates the use of the NDR, exhibited in the GSC at low temperatures, as an active region to create oscillator and amplifier circuits. We show that straining the composite through bend induces changes to the oscillations. By utilizing the active region and combining this with the flexible nature of the composite we demonstrate a flexible and active *electronic skin*. Through encoding the strain as a frequency signal, i.e bending the sample and detecting a change in frequency, the composite mimics the behaviour of mechanoreceptor neurons in the human skin that provide the sense of touch. Mechanoreceptor neurons, such as Merkel receptors that lie just under the skin, respond to physical displacements such as bending. The bend applies a pressure to the cell membrane that causes sodium ions to enter the cell and generate an action potential. The greater the pressure, the more sodium ions are able to enter and the greater the number of action potentials, which increases the response frequency. The pressure is therefore encoded as a frequency: Whereby the greater the pressure, the higher the frequency [127]. It is this behaviour we attempt to mimic in the GSC.

The composite's physical characteristics, with its soft flexible and durable silicone matrix, make it well suited to applications in robotic skins. A few years ago one of the leaders in the field of flexible electronics stated that, *electronics of the future will be soft and rubbery* [11]. However the creation of flexible soft active devices has been difficult to achieve as they require new materials that are very different to current technology, based on silicon electronics, that is not suitable. Using an intrinsic NDR in a flexible material is one such path with which flexible electronics could progress and has not before been demonstrated.

Two of the most published research groups on flexible electronic skins use a conductive rubber to sense pressure as a passive element and develop flexible transistor arrays to interpret the signal [2, 13]. The focus for these groups has been the creation of large flexible transistor arrays that enable switching between individual pixels of the conductive rubber. One approach of Javey's group, in Berkeley California, has been to make the transistors from semiconducting nanowires, where the nanowires are small enough to remain robust to pressure changes [16, 128]. Recently they have also demonstrated this with semiconducting carbon nanotubes in place of the nanowires [12].

The approach of Someya's group, at the University of Tokyo, is to create flexible organic pentacene transistors that are flexible and then measure the resistance change in a graphite based conductive rubber [2, 14, 15, 97, 126]. The pentacene

transistors are built on a net, like a chain linked fence, with transistors positioned on each link. In this way the overall material is flexible and stretchable while the transistors remain unstrained. Javey's later publications also adapt this method through laser cutting a honeycomb mesh around the transistors [12].

Another group have also created thin film carbon nanotube transistors. The transistors are flexible and have an impressive mobility. While the devices they show are not for pressure detection they have been able to combine arrays of the transistors to create a ring oscillator [25].

These groups represent the state of the art, with many of the cited references here having been published in major journals within the last few years, and are highlights of the current intense research into flexible electronics. The flexibility of the devices mentioned arise from the combination of very thin films, and a conductive rubber as the pressure sensitive element. What we are able to demonstrate however, is the use of the composite as an *intrinsically active* component, via the NDR region, with strain tunable oscillations.

This chapter proceeds by initially explaining how NDR based oscillators and amplifiers operate, starting with the basics of oscillations in a LC circuit. The analysis for the incorporation of a NDR device in an LC circuit follows that of books by Chow and Chang which were originally written in regard to TD devices. However, the analysis is readily adapted to any device with NDR characteristics [93, 129]. Due to TDs no longer being widely available we construct a lambda circuit, from combining an n-channel and p-channel junction field effect transistor (JFET). The lambda circuit is shown to have a wide NDR region which is utilised in demonstrating oscillator and amplifier circuits. The results of the tuned amplifier circuit are analysed and compared to equations derived for the gain and phase shift.

Next we incorporate the GSC in an oscillator circuit and the NDR is clearly demonstrated to be capable of sustaining oscillations. A strain is applied through bend and the changes in oscillation frequency and amplitude are examined. An unexpected *intrinsic* frequency is discovered which can be tuned through strain. We attempt to explain the physical origins of the intrinsic frequencies by a positive feedback amplification mechanism caused by transient charge accumulations.

A resonant effect is found to occur when the LC tank frequency is set to the intrinsic frequency with a sharp increase in amplitude and stability of the oscillations. This resonance effect is taken advantage of in a tuned amplifier circuit where the composite is utilized in creating a *strain-tuned* amplifier, with a tunable gain between 1 and 4.5.

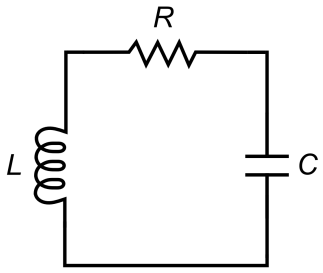

Figure 6-1: In the LCR circuit there is a continual exchange of energy between the inductor and capacitor that occurs at a frequency dictated by the inductance, L, and capacitance, C. The oscillations decay due to resistance, R, in the circuit.

6.2 Oscillator Circuit Theory

The parallel combination of an inductor and capacitor creates an LC circuit that is an electronic resonator, shown in figure 6-1. The behaviour of this circuit can be analysed starting from Kirchhoff's law and from the characteristic equations for the components, to arrive at a following differential equation to describe the time varying current $i(t)$ through the circuit as,

$$V_R + V_L + V_C = 0\,, \tag{6.1}$$

where,

$$V_R = R\,i(t) \qquad V_L = L\,\frac{\mathrm{d}i(t)}{\mathrm{d}t} \qquad V_C = \frac{1}{C}\int i(t)\,\mathrm{d}t\,. \tag{6.2}$$

Through combining equation 6.1 and 6.2 and differentiating by t we arrive at,

$$\frac{\mathrm{d}^2 i(t)}{\mathrm{d}t^2} + \frac{R}{L}\,\frac{\mathrm{d}i(t)}{\mathrm{d}t} + \omega_{LC}^2\,i(t) = 0 \tag{6.3}$$

where $\omega_{LC} = \sqrt{\dfrac{1}{LC}}$. The solution to the second order differential equation is an oscillating current, i(t), at a frequency ω_{LC} and with an amplitude that decays exponentially at $\exp\left(\frac{-R}{2L}t\right)$. For example the solution for $R = 5\ \Omega$, $L = 1$ mH, $C = 1\ \mu$F and initial current $i(0) = 1$ A is shown in figure 6-2. The red line shows the oscillations that occur at a constant frequency $f_{LC} = 5,033$ Hz, while the blue dotted line shows the exponential decay.

The exponential decay of the oscillations is due to the energy lost in the resistance R. However, if the resistance were negative then the oscillations would not decay; instead they would grow, indefinitely supplying energy to the circuit. Obviously negative resistance is not possible but a differential negative resistance,

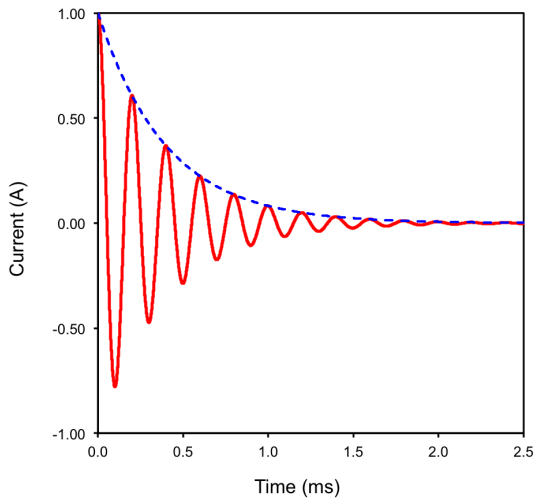

Figure 6-2: The time varying current from the solution of equation 6.3. The oscillations are at a constant frequency $f_{LC} = 5,033$ Hz with an exponentially decaying amplitude.

as we have in our composite, is enough to sustain oscillations and overcome the damping of the resistance in the circuit. The NDR requires that $\frac{\Delta I}{\Delta V} < 0$ and thus we can define a *negative conductance* $-|g|$ that will be used to sustain oscillations with the 'negative resistance' equal to $-\frac{1}{|g|}$.

Creating oscillators and amplifiers from NDR devices caused a lot of excitement in the late 1950's with the discovery of the tunneling diode in 1958 by Leo Esaki [130]. The Esaki diode, or TD, combines highly doped p and n regions that have a very small depletion region, $\simeq 5\ nm$, that form a tunneling barrier. When a small bias is applied electrons are able to tunnel across from the conduction band of the n region to the valence band of the p region and a current can flow. However as the bias is increased the number of empty states available for the electrons to tunnel into starts to decrease and the current decreases leading to a NDR region.

In TD the NDR allows oscillations to be sustained, and the tunnel barrier being small means the characteristic tunneling times are extremely fast, allowing for high frequency applications. These devices were therefore very successful as microwave oscillators and amplifiers. However they were overtaken in time by more conventional semiconducting devices that were easier to integrate into circuits. As it is difficult to get hold of TD devices we reproduce their $I - V$ characteristics through the combination of two JFET transistors arranged as a lambda circuit.

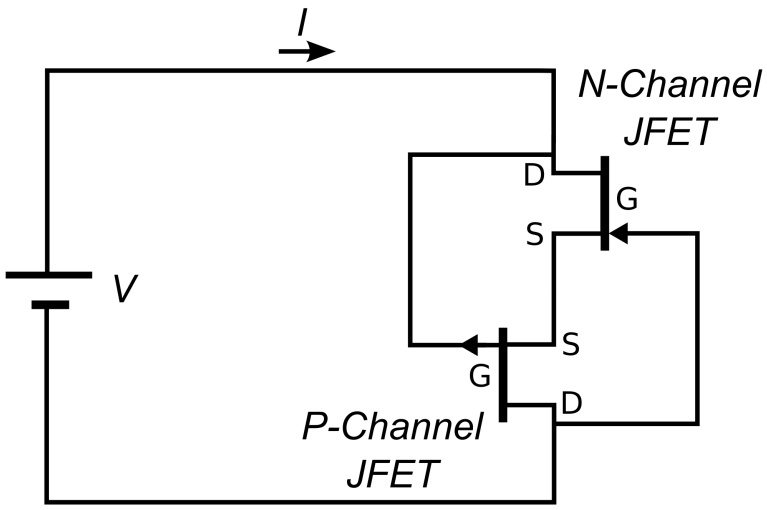

Figure 6-3: The lambda circuit combines an MPF102 n-channel JFET and a 2N3820 p-channel JFET. The sources of the two JFETs are connected together and the gates of each are connected to the drain of the other. This creates a two terminal NDR device.

6.3 Lambda Diode Example

The lambda circuit, or lambda diode, combines an n-channel JFET and p-channel JFET to create an NDR device. The sources of the two JFETs are connected together and the gates of each are connected to the drain of the other as in figure 6-3. An MPF102 is used for the n-channel JFET and a 2N3820 for the p-channel JFET to create a two terminal NDR device. To understand how the lambda diode creates the NDR region we must first understand the basic characteristics of the JFET. The n-channel JFET allows a large current to flow from drain to source when the gate - source voltage is zero, $V_{GS} = 0$, when a negative gate-source voltage is applied the depletion region extends across the channel and the current drop quickly to zero. For a p-channel JFET a current flows from source to drain when $V_{GS} = 0$ and when a positive V_{GS} is applied the depletion region extends across the p-channel and the current is pinched off.

The combination of the n-channel and p-channel JFET as shown in figure 6-3 leads to an NDR region as follows. Initially as a small voltage, V, is applied current, I, is able to flow. However as the current flows, due to the resistance of the JFET a positive potential is applied to the gate of the p-channel and a negative potential to the gate of the n-channel. This causes the resistance of the channels to increase. Further increasing V causes the channels to become further pinched and the current to decrease, creating a NDR region that extends up until

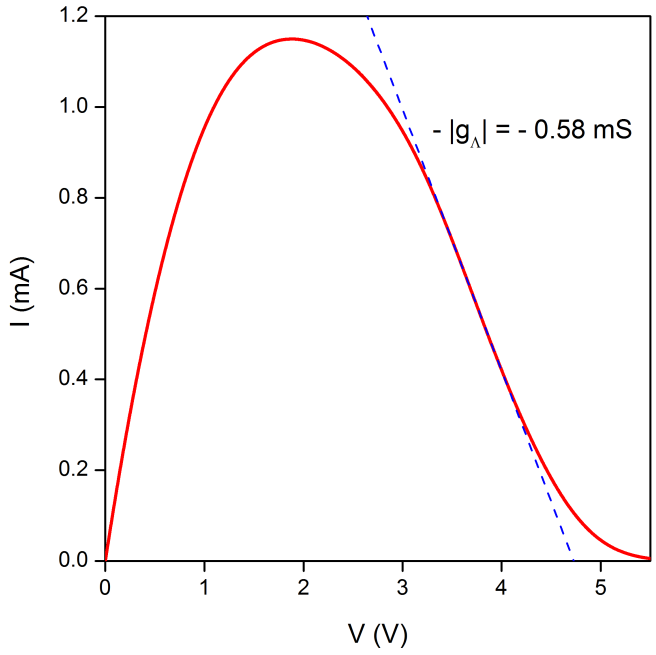

Figure 6-4: The $I-V$ characteristics of the lambda diode exhibit a linear NDR region between 3 V and 4 V with $\frac{\Delta I}{\Delta V} = |g_\Lambda| = 0.58$ mS corresponding to a negative resistance of $-\frac{1}{|g_\Lambda|} = -1,720\ \Omega$.

no current can flow, with the voltage completely switching off conduction.

The $I-V$ characteristics of the lambda diode are shown in figure 6-4. The onset of the NDR region in the lambda diode is at $V_P = 2$ V and $I_P = 1.15$ mA. The current is pinched at 5.5 V and does not increase again, which leads to a wide NDR region that supports oscillations. The slope of the curve in the NDR region is linear between 3 V and 4 V where,

$$\frac{\Delta I}{\Delta V} = |g_\Lambda| = 0.58 \text{ mS}, \tag{6.4}$$

which corresponds to a negative resistance of $-\frac{1}{|g_\Lambda|} = -1,720\ \Omega$. This allows for the lambda diode to support regular stable oscillations with amplitudes of up to 1 V.

6.3.1 Lambda Diode Oscillator

To create an oscillator the lambda diode is placed in parallel with an LC circuit and biased into the NDR region through a DC source. The lambda circuit of

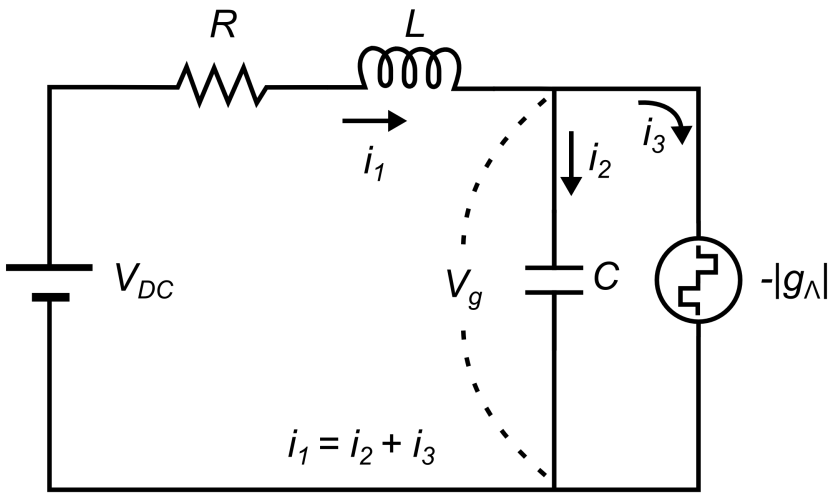

Figure 6-5: To create a simple oscillator the lambda diode, with negative conductance $-|g_\Lambda|$, is place in parallel with an LC circuit. A DC voltage source V_{DC} is used to bias the lambda diode into the NDR region.

figure 6-3 in now considered as a single 2T device with conductance $|g_\Lambda|$. The resistance R represents the internal resistances of the circuit, which mostly arises from the inductor. The complete oscillator circuit is shown in figure 6-5.

To understand how the oscillator circuit functions we follow the analysis of Chow [93]. Originally this was specifically for TD devices however the results are generic for any NDR devices including the lambda circuit and our GSC device. The only difference is that we assume that the internal inductance and capacitance are negligible in comparison to the external L and C.

We start the circuit analysis by considering the small signal impedance of the oscillator circuit, Z_T, shown in figure 6-5, when biased into the NDR region with,

$$Z_T = Z_R + Z_L + \frac{1}{\dfrac{1}{Z_C} + \dfrac{1}{Z_\Lambda}} \,. \tag{6.5}$$

Including the characteristic impedance of the resistive, capacitive and inductive elements at oscillation frequency ω,

$$Z_T = R + j\omega L + \frac{1}{j\omega C - |g_\Lambda|} \,, \tag{6.6}$$

and then separating the real and imaginary parts,

$$Z_T = R - \frac{|g_\Lambda|}{|g_\Lambda|^2 + \omega^2 C^2} + j\omega \left(L - \frac{C}{|g_\Lambda|^2 + \omega^2 C^2} \right) \,. \tag{6.7}$$

For the circuit to initially start oscillating Z_T must be negative at $\omega = 0$ which leads to one of the most important conditions for NDR based oscillators that,

$$|g_\Lambda|R < 1\,. \tag{6.8}$$

This means that the absolute of the negative differential resistance must always be greater than the resistance in the circuit such that the overall resistance of the circuit is negative and oscillations can grow.

Next, for the oscillations to be sustained with AC power generated by the oscillator, $\Re(Z_T) < 0$, i.e the overall circuit resistance must remain negative. The real part of equation 6.7 is a monotonically increasing function of ω that starts off negative when $|g_\Lambda|R < 1$ but at some frequency it will no longer be negative and above this frequency oscillations cannot be sustained. At this cross over we define the cut-off frequency f_{CO} at $\Re(Z_T) = 0$ such that,

$$f_{CO} = \frac{|g_\Lambda|}{2\pi C}\sqrt{\frac{1}{R|g_\Lambda|} - 1}\,. \tag{6.9}$$

Above f_{CO} the oscillating circuit is no longer considered as active as oscillations cannot be sustained due to the resistance of the circuit now being positive and the AC power is absorbed.

Next we determine the frequency at which the circuit will oscillate, f_0, assuming the source is purely DC, through equating the imaginary part of equation 6.7 to zero,

$$\omega_0 L - \frac{\omega_0 L}{|g_\Lambda|^2 + \omega_0^2 C^2} = 0\,, \tag{6.10}$$

Rearranging and inserting f_0 we find the oscillation frequency,

$$f_0 = \frac{1}{2\pi}\sqrt{\frac{1}{LC} - \frac{|g_\Lambda|^2}{C^2}}\,, \tag{6.11}$$

This is a variation on the frequency of oscillation in the resistor-inductor-capacitor (RLC) circuit where we found,

$$f_{LC} = \frac{1}{2\pi}\sqrt{\frac{1}{LC}}\,, \tag{6.12}$$

however when $|g_\Lambda|$ or L is small f_0 will tend towards f_{LC}. Usually we assume $f_0 = f_{LC}$, however in some cases we will require the full expression for f_0.

In order to analyze the stability of the oscillator circuit and describe transient

behaviour, we construct a general second order differential equation for the time varying current. Applying Kirchhoff's circuit laws we equate,

$$V_{DC} = V_R + V_L + V_g \,, \tag{6.13}$$

where $V_R = R\, i_1(t)$, $V_L = L\,\dfrac{\mathrm{d}i_1(t)}{\mathrm{d}t}$, and,

$$V_g = V_C = \frac{1}{C}\int i_2(t)\,\mathrm{d}t = \frac{1}{C}\int i_3(t) - i_1(t)\,\mathrm{d}t \,, \tag{6.14}$$

We assume that the NDR region is a linear slope with gradient $|g_\Lambda|$ around point V_0, I_0 such that,

$$V_g = \frac{I_0 - i_3(t) + V_0|g_\Lambda|}{|g_\Lambda|} \,. \tag{6.15}$$

We differentiate equation 6.13 to find an expression for $\dfrac{\mathrm{d}V_g}{\mathrm{d}t}$,

$$\frac{\mathrm{d}V_g}{\mathrm{d}t} = -R\,\frac{\mathrm{d}i_1(t)}{\mathrm{d}t} - L\,\frac{\mathrm{d}^2 i_1(t)}{\mathrm{d}t^2}. \tag{6.16}$$

and then differentiate equation 6.14 to find $i_3(t)$,

$$i_3(t) = i_1(t) - C\,\frac{\mathrm{d}V_g}{\mathrm{d}t} \,, \tag{6.17}$$

Using equation 6.13 we combine equations 6.15 and 6.16 to arrive at the second order differential equation,

$$L\frac{\mathrm{d}^2 i_1(t)}{\mathrm{d}t^2} + \left(R - \frac{L|g_\Lambda|}{C}\right)\frac{\mathrm{d}i_1(t)}{\mathrm{d}t} + \left(1 - \frac{R|g_\Lambda|}{C}\right) i_1(t) = \frac{I_0 + |g_\Lambda|(V_0 - V_{DC})}{C} \,. \tag{6.18}$$

The general solution of this second order differential equation is,

$$i_1(t) = A_1 \exp(\lambda_1 t) + A_2 \exp(\lambda_2 t) + \frac{I_0 + |g_\Lambda|(V_0 - V_{DC})}{C} \,, \tag{6.19}$$

where A_1 and A_2 are constants that can be found from the initial starting conditions and λ_1 and λ_2 are,

$$\lambda_1, \lambda_2 = \frac{1}{2}\left(\frac{|g_\Lambda|}{C} - \frac{R}{L}\right) \pm \sqrt{\frac{1}{4}\left(\frac{R}{L} - \frac{|g_\Lambda|}{C}\right)^2 - \frac{1 - R|g_\Lambda|}{LC}} \,. \tag{6.20}$$

The stability of the oscillator circuit can be considered through the four potential

regions of solutions for equation 6.20 that can be positive or negative; real or imaginary. A detailed stability analysis can be found in Chow [93] which we summarize as,

Region 1 Solutions that are positive and real will have no oscillations. The current will grows exponentially, which is unstable.

Region 2 Solutions that are negative and real will have no oscillations and the current will decay exponentially.

Region 3 Solutions that are negative and complex will produce sinusoidal oscillations that decay exponentially.

Region 4 Solutions that are positive and complex will provide sinusoidal oscillations that grow exponentially.

Wherever the solutions are complex, i.e in regions 3 and 4, the solutions to equation 6.19 will be sinusoidal. The oscillations will exponentially decay if $\frac{L|g_\Lambda|}{C} > R$, or exponentially grow if $\frac{L|g_\Lambda|}{C} < R$. If we take the special case where the oscillations neither decay or grow,

$$\frac{|g_\Lambda|}{C} - \frac{R}{L} = 0\,, \tag{6.21}$$

we find,

$$\lambda_1, \lambda_2 = 0 \pm j\sqrt{\frac{1}{LC} - \frac{|g_\Lambda|^2}{C^2}}\,. \tag{6.22}$$

This has the same form found for the oscillation frequency, ω_0 in equation 6.11. The solution for $i_1(t)$ thus becomes

$$\begin{aligned} i_1(t) &= \exp(j\omega_0 t) + \exp(-j\omega_0 t) + \frac{I_0 + |g_\Lambda|(V_0 - V_{DC})}{C} \\ &= 2\cos(\omega_0 t) + \frac{I_0 + |g_\Lambda|(V_0 - V_{DC})}{C}\,. \end{aligned} \tag{6.23}$$

The oscillations are steady and are sustained with the NDR exactly overcoming the resistive losses in the circuit.

As an interesting extension to equation 6.19 we can introduce a time varying $|g_\Lambda|$ to represent any instabilities in the NDR region. This might not necessarily apply to the well behaved lambda circuit but is very relevant for the GSC, as here there are significant instabilities in the NDR region. We set reasonable values of $L = 0.1$ mH, $C = 1$ mF and $R = \frac{LG}{C}$ and then define $|g_\Lambda|$ to be slowly time varying where $|g_\Lambda| = 0.58 \times 10^{-4}\,|\sin\omega_1\, t|$ with $\omega_1 << w_{LC}$.

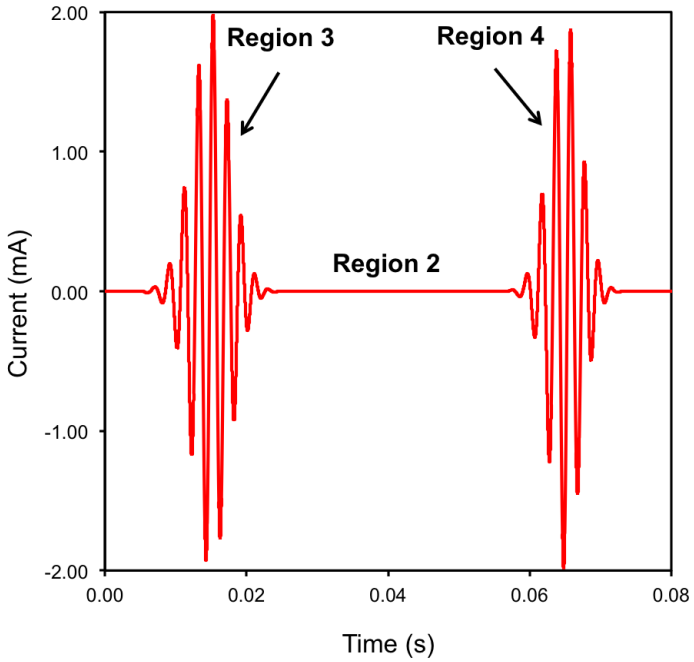

Figure 6-6: Modelling equation 6.19 with a time varying $|g_\Lambda|$ yields a *bursting behaviour*. The oscillations within the bursts have a slowly varying frequency which creates a broader FFT spectrum.

The simulated results show that the oscillations now occur in bursts in the form of wave packets, figure 6-6. The *bursting* occurs because the solutions cycle between **Region 3**, **Region 2** and then **Region 4**. with the oscillations only possible when the solutions are complex and $|g_\Lambda|R < 1$.

As the frequency of oscillation is given by equation 6.11 and $|g_\Lambda|$ is time varying we find the frequency varies slightly within the bursts. This yields a broader distribution of the oscillation frequency and if the FFT were to be plotted a broader peak would be observed. This simple model will help explain some of the transient effects observed for the GSC oscillator.

The analysis described above is based on that done by Chow [93]. We have seen how the lambda diode is able to be combined in an LC circuit to create an oscillator. Circuit analysis yields two important results, firstly for oscillations to be sustained $|g_\Lambda|R < 1$. Secondly, the frequency of oscillations has the additional term that includes the slope of the NDR, equation 6.11.

6.3.2 Lambda Diode Amplifier

One of our objectives was to create a flexible amplifier using the NDR region of the GSC. To explore how amplifier circuits function and to be able to arrive at a

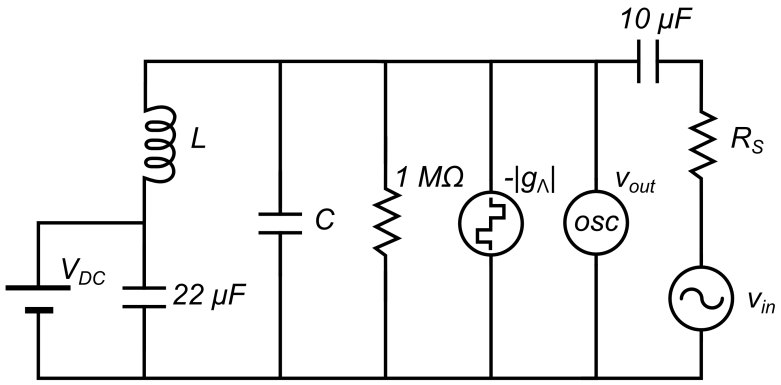

Figure 6-7: The tuned amplifier circuit. The lambda diode is in parallel with the LC circuit that sets the tank frequency, f_{LC}, and is biased into the NDR region using DC source, V_{DC}. The signal to be amplified comes from the AC source, v_{in}. The output voltage, v_{out}, is measured using an oscilloscope. The gain $A_v = \dfrac{v_{out}}{v_{in}}$ is tuned through varying resistance, R_S.

circuit design suitable for the GSC we first used the lambda diode as the active device.

We identified the *tuned* amplifier circuit, shown in figure 6-7, as most suited for our application due to its simplicity and close relation to that of the oscillator circuit. This type of circuit could be used in the volume control of a radio, as varying the resistance, R_S, controls the gain, A_v, at the frequency set by the LC tank.

If we consider the AC equivalent circuit in figure 6-8(a) and arrange it in the form of a potential divider, figure 6-8(b), we can form a set of equations to find A_v. Usually in a potential divider circuit v_{out} would not exceed v_{in} as both Z_1 and Z_2 would be positive values. However due to the the negative conductance $-|g_\Lambda|$ in some situations $Z_2 < 0$ and thus can yield $A_v > 1$. This is the amplifying response. The additional energy required for the amplification is supplied by the DC source, that is biasing the device into the NDR region.

In a potential divider the gain is given by,

$$A_v = \frac{v_{out}}{v_{in}} = \frac{1}{\dfrac{Z_1}{Z_2} + 1}\,, \tag{6.24}$$

where Z_2, shown in the red box in figure 6-8(a), is given by

$$\frac{1}{Z_2} = \frac{1}{j\omega_d L} + j\omega_d C - |g_\Lambda| + \frac{1}{R_L}\,, \tag{6.25}$$

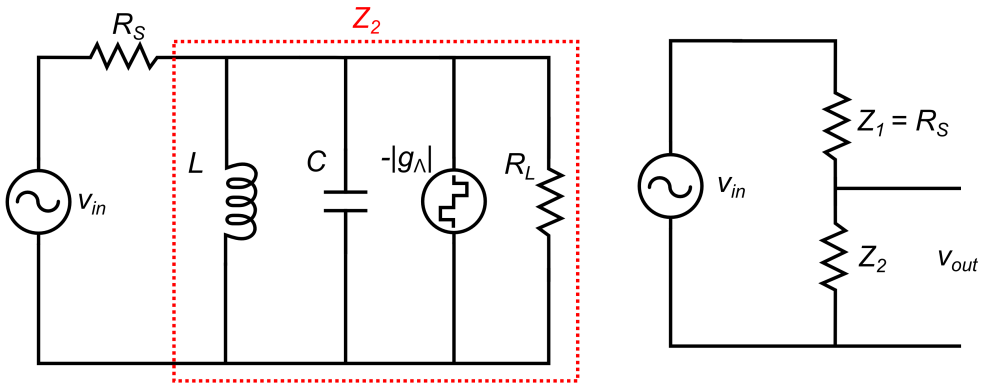

(a) (b)

Figure 6-8: (a) The AC equivalent circuit of the tuned amplifier. The boxed region Z_2 resembles the oscillator circuit, with an LC tank, but with an additional load resistance R_L. (b) Combining the components enclosed in the box as a single impedance Z_2 allows us to visualise a simple voltage divider circuit. In a passive device both Z_1 and Z_2 would be positive values and thus v_{out} would always be less than v_{in} however due to the negative conductance $-|g_\Lambda|$ in some situations Z_2 is negative and thus $v_{out} > v_{in}$ producing a gain $A_v > 1$.

and combining equations 6.24 and 6.25 we find,

$$A_v = \frac{1}{1 + R_S\left(\dfrac{1}{j\omega_d L} + j\omega_d C - |g_\Lambda| + \dfrac{1}{R_L}\right)}. \tag{6.26}$$

Rearranging to separate the real and imaginary components,

$$\begin{aligned} A_v = &\frac{\omega_d^2 L^2\left(1 - R_S|g_\Lambda| + \dfrac{R_S}{R_L}\right)}{R_S^2\left(1 - LC\omega_d^2\right)^2 + \omega_d^2 L^2\left(1 - R|g_\Lambda| + \dfrac{R_S}{R_L}\right)^2} \\ &+ j\frac{\omega_d L R_S\left(1 - LC\omega_d^2\right)}{R_S^2\left(1 - LC\omega_d^2\right)^2 + \omega_d^2 L^2\left(1 - R_S|g_\Lambda| + \dfrac{R_S}{R_L}\right)^2}. \end{aligned} \tag{6.27}$$

The absolute gain, $|A_v|$ is,

$$|A_v| = \frac{\omega_d L}{\sqrt{R_S^2\left(1 - LC\omega_d^2\right)^2 + \omega_d^2 L^2\left(1 - R_S|g_\Lambda| + \dfrac{R_S}{R_L}\right)^2}}, \tag{6.28}$$

and the phase shift, ϕ, is given by,

$$\phi = \arctan\left(\frac{R_S(1 - LC\omega_d^2)}{\omega_d L\left(1 - R_S|g_\Lambda| + \dfrac{R_S}{R_L}\right)}\right), \tag{6.29}$$

while these equations appear complex, if v_{in} is set such that it equals the tank frequency, $f_d = f_{LC} = \dfrac{1}{\sqrt{LC}}$ and taking $R_L << R_S$ the imaginary component becomes, $\Im(A) = 0$ and equation 6.27 simplifies too,

$$A_v = \frac{1}{1 - R_S|g_\Lambda|}\,. \tag{6.30}$$

The gain increases dramatically when $\dfrac{1}{|g_\Lambda|} \approx R_S$. Any deviation from $f_d = f_{LC}$ will cause the gain to decrease and for a phase shift to occur. If $f_d << f_{LC}$ or $f_d >> f_{LC}$ the phase will be shifted to either $+90°$ or $-90°$ respectively.

We tested the tuned amplifier circuit of figure 6-7 and compared the measured gain and phase shift to that described by equations 6.28 and 6.29. This was repeated for both a low LC tank frequency, $f_{LC} = 1.5$ kHz and a higher LC tank frequency $f_{LC} = 30.3$ kHz. The results over a range of drive frequencies, f_d, of v_{in} are shown in figure 6-9, where panels (a) and (c) correspond to the lower tank frequency; and (b) and (d) to the higher tank frequency.

At low tank frequency the calculated maximum gain cannot be attained by the circuit, 6-9(a). This is because the resistance of the inductor, which is not included in equations 6.28, is significant at 68 Ω. This additional series resistance absorbs some of the power, increasing the overall resistance of the circuit, and thus reducing the gain. Also at low tank frequency the measured phase shift is lower than that expected, due to the coupling capacitors having a sizable reactance at low frequencies.

For the higher tank frequency the measured gain and phase shift follow closely the calculated values. The inductance is smaller and has a negligible resistance while the coupling capacitors have a much smaller reactance at the higher drive frequencies.

Finally we show the maximum gain of the tuned amplifier circuit at the tank frequency, $f_{LC} = 30.3$ kHz. We set the drive frequency equal to the tank frequency, $f_d = f_{LC}$ and then increased the resistance, R_S from 0 Ω to 1,800 Ω and recorded the gain, figure 6-10.

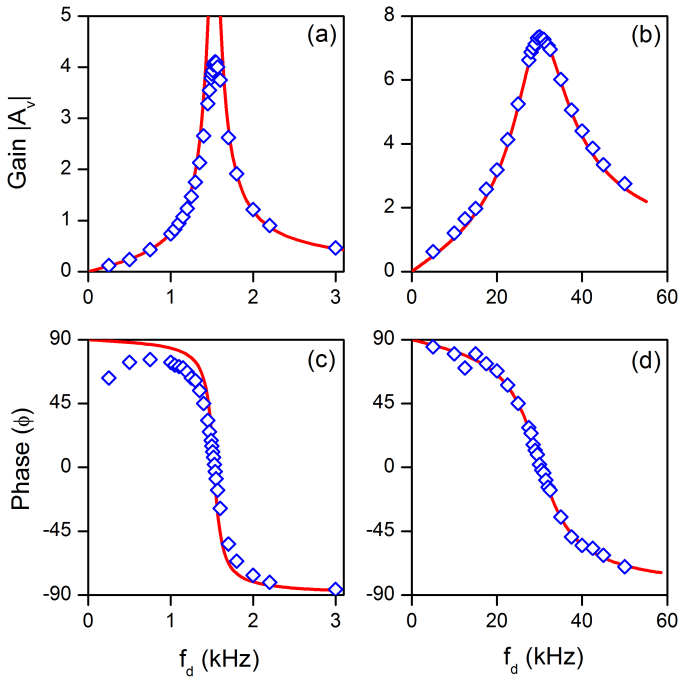

Figure 6-9: The experimental values of the gain, $|A_v|$, and phase shift, ϕ, of the tuned amplifier circuit for two values of tank frequency, f_{LC}. Panels (a) and (c) show $|A_v|$ and ϕ for $f_{LC} = 1.5$ kHz. Panels (b) and (d) the $|A_v|$ and ϕ for $f_{LC} = 30.29$ kHz. The calculated values of $|A_v|$ and ϕ from equations 6.28 and 6.29, red lines, follow closely that of the measured values at the higher tank frequency.

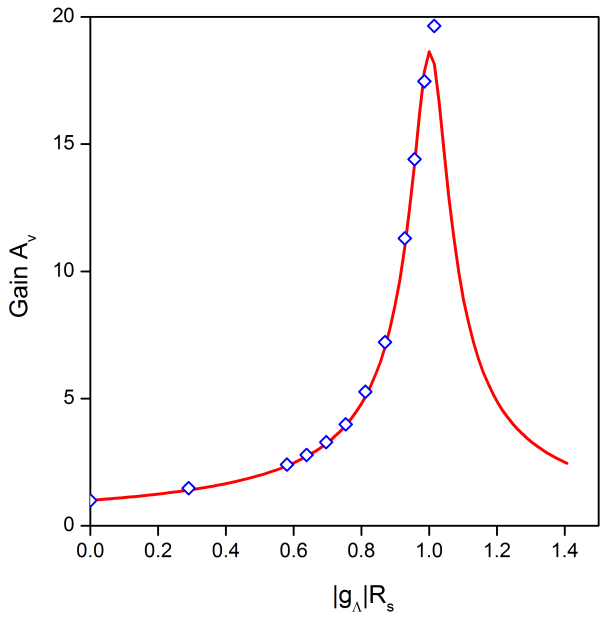

Figure 6-10: The tuned amplifier showing that the gain A_v increase as $|g_\Lambda|R_S$ tends to unity. A stable gain of 17.5 is observed for $R_S = 1,700\ \Omega$ where $|g_\Lambda|R_S = 0.99$, above this the gain becomes unstable and v_{out} is no longer sinusoidal. This is because v_{out} exceeds 1 V which is outside the linear region of the $I - V$ curve of the lambda diode. The red line shows the theoretical gain modelled using equation 6.27.

The x-axis is shown as $|g_\Lambda|R_S$ so that the gain should be maximum when $|g_\Lambda|R_S = 1$. The blue diamonds mark the measured gain and the red line the theoretical fit. The gain increases as expected up to $|g_\Lambda|R_S = 0.99$ where $A_v = 17.5$. The final data point at $|g_\Lambda|R_S = 1.015$ exceeds the theoretical maximum gain. This is because the amplitude is greater than the width of the linear region in the NDR and so the oscillations are no longer sinusoidal.

6.3.3 Summary of the Lambda Diode

In summary the lambda diode has been used to discuss and explain oscillator and amplifier circuits based on NDR devices. Equations to describe both the frequency of oscillations and the cut-off frequency have been derived. A model is shown that can be used to demonstrate bursting behaviour when the negative conductance is time variant.

The tuned amplifier circuit was found to be correctly described by the circuit equations. Only small discrepancies arise due to the resistance of the inductor and reactance of the coupling capacitors. A similar tuned amplifier circuit will be used for the GSC device.

6.4 Active Response of the GSC in the NDR region

6.4.1 Sustaining Oscillations in the NDR Region

The primary goal of this chapter was to establish whether the NDR region found in the GSC was capable of sustaining oscillations, in a similar manner to the lambda diode described in the previous section. Therefore the composite was placed in an oscillator circuit, replacing the lambda diode of figure 6-5. The LC tank frequency was set to $f_{LC} = 4.1$ kHz with $L = 10.1$ mH and $C = 149$ nF and the composite was biased into the NDR region.

Oscillations were immediately apparent with an amplitude varying between 5 and 20 mV, shown in the time series of figure 6-11(a). To confirm that the oscillations varied with the LC tank frequency the capacitance was decreased to $C = 49$ nF and the composite biased to the same point in the NDR region. Oscillations were again observed at the LC tank frequency and are shown in figure 6-11(b). The amplitude of the oscillations exhibits some transient bursting behaviour. Between bursts the oscillation amplitude decreases, < 1 mV, and is noisy with frequent phase shifts in time. In the oscillation bursts the amplitude grows to 6 mV with the frequency and phase remaining almost constant during the burst, which lasts for around 14 cycles.

To determine the oscillation frequency the FFT of the time series was calculated. The FFT amplitude with frequency, f_{out} is shown for both capacitance values 149 nF in red and 49 nF in blue in figure 6-11. Clear peaks can be seen for both. For $C = 149$ nF the peak is sharpest, with a peak of 2.8 mV at $f_p = 4.16$ kHz, while for $C = 49$ nF the peak of 1.2 mV is at $f_p = 7.18$ kHz. This confirms that the oscillations are indeed set by the LC tank frequency and generated by the NDR region of the composite. As previously discussed the oscillation frequency can be calculated as,

$$f_0 = \frac{1}{2\pi}\sqrt{\frac{1}{LC} - \frac{|g_c|^2}{C^2}}\,, \tag{6.31}$$

where $|g_c|$ is the negative conductance of the composite which can be readily extracted from the $I - V$ curves. For this sample the slope of the $I - V$ curve was found to vary between $0.23 < |g_c| < 0.55$ mS. Inserting these values into equation 6.31 for the high value capacitance, 149 nF, yields $4.07 < f_0 < 4.12$ kHz while for the 49 nF capacitor yields $6.96 < f_0 < 7.14$ kHz. The measured

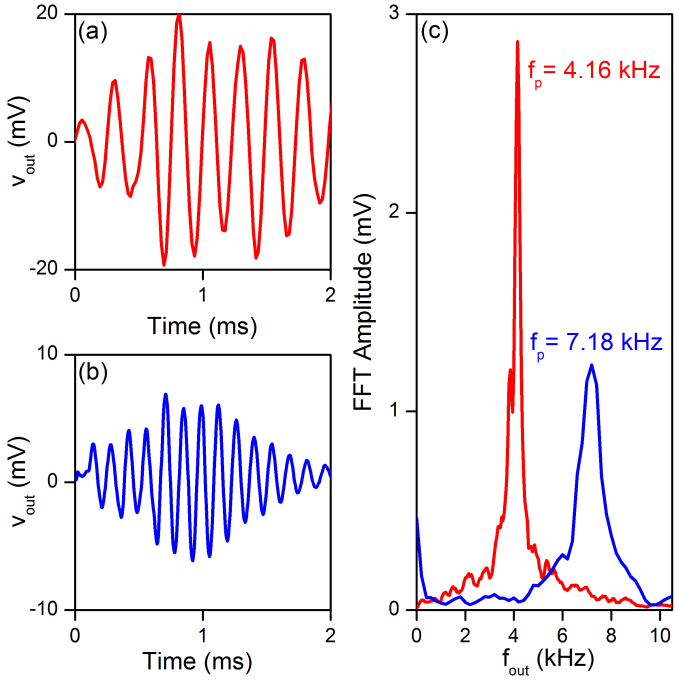

Figure 6-11: (a) The composite oscillations when biased in the NDR region in an oscillator circuit with $L = 10.1$ mH and $C = 149$ nF. (b) Decreasing the capacitance to $C = 49$ nF leads to transient bursting with the oscillations appearing to occur in wave packets. The bursting is due to time variations of $|g_c|$ from instabilities in the NDR region. (c) The FFT spectrum is computed for each time series. The higher capacitance produces a sharper and more pronounced peak at 4.16 kHz, red curve, while the lower capacitance has a broader spectrum centered on 7.18 kHz.

FFT peaks of figure 6-11 are very close to these calculated values. The smaller capacitance makes the second term in equation 6.31 more significant. Thus the same variation in $|g_c|$ produces a more significant variation in frequency and is why the FFT peak is broader.

The bursting behaviour also arises from the time variance of $|g_c|$. This leads to the oscillation amplitude changing with time and the creation of wave packets of oscillations. This effect was earlier modelled and shown in figure 6-6.

Next, to determine the oscillation behaviour over a range of frequencies the capacitance was varied between $C = 149$ nF and $C = 2.66$ nF for a fixed inductance of $L = 10.1$ mH. The time series of 35 cycles for different C values is shown in red, and for two cycles in blue, in figure 6-12(a-i). The oscillations have the greatest stability and least noise for the higher values of capacitance, the lower frequencies with the transient bursting behaviour that changes as the capacitance decreases.

In panel (a) each burst can be seen to lead almost straight into the next with the bursts lasting over 20 cycles while for (c) and (e) there are time delays of the order 1 ms between bursts. The bursts only now lasting for around 10 cycles in (c) and 5 cycles in (e) The oscillations in (g) and (h) are noisier and less defined, as the bursting lasts just a few cycles. This arises from the time variations of $|g_\Lambda|$ having a much greater effect when C is small. The oscillation amplitude remains roughly the same over the entire range from $f_{LC} = 4.1$ kHz to 30.8 kHz with amplitudes of 20 mV in the bursts.

To establish that the oscillations arise due to the NDR region, the bias across the composite was increased in 0.5 V increments up to and beyond V_P, whilst in the oscillator circuit with $L = 43$ mH and $C = 100$ nF. At each voltage step a time series was recorded and the corresponding FFT calculated. The $I - V$ curve is shown by the solid red line in figure 6-13. The colour map is generated from a normalised amplitude of the FFT, at each bias, with red indicating the maximum amplitude.

Below $V_P = 25$ V the composite is quiet and the FFT is flat. Above V_P the composite begins to oscillate at a frequency that is independent of the bias. This unequivocally establishes the oscillations are due to NDR region of the GSC, confirming that the composite is behaving as an active 2T device with the negative conductance sustaining the continual generation of oscillations.

There are in fact two distinct oscillation frequencies in figure 6-13. One peak corresponds to the expected LC tank frequency indicated as $f_{LC} = 2.32$ kHz. A second peak can be seen at a slightly higher frequency indicated as X with

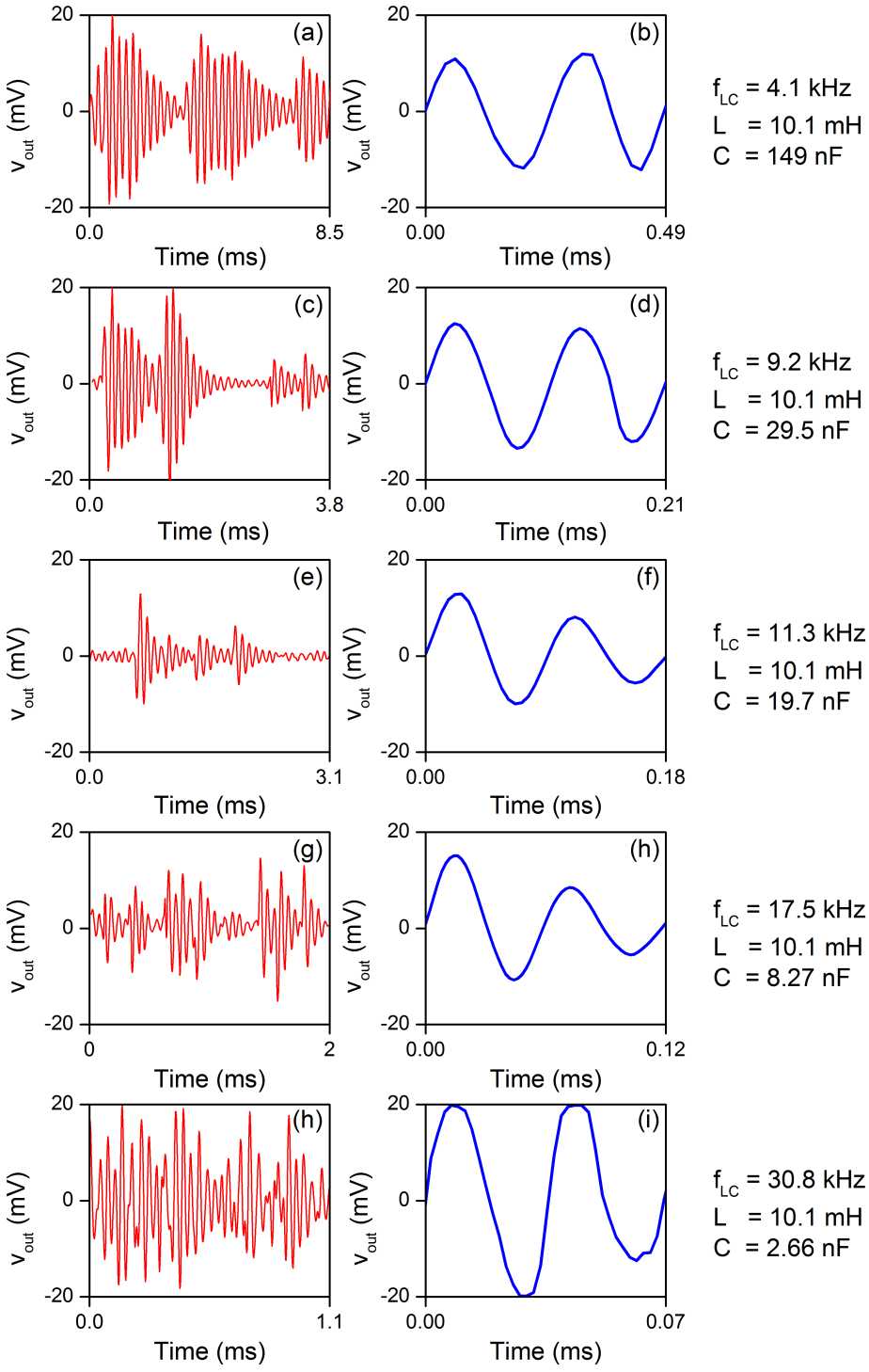

Figure 6-12: Time series for 35 oscillations (red) and 2 oscillations (blue) for a range of capacitor values spanning 149 nF to 2.66 nF and with the inductance held constant at 10.1 mH. Oscillations are clearest at the lower frequencies, (a) to (f) while for (g) to (i) the oscillations become noisy. This is due to the time variance of $|g_c|$ which at low C creates a broadening of the oscillation frequency.

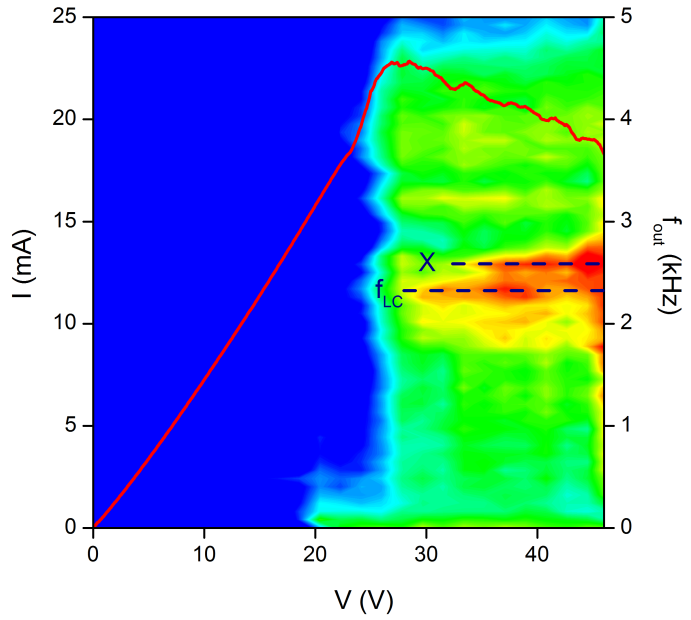

Figure 6-13: The $I-V$ characteristics of the composite are recorded whilst in the oscillator circuit. At 0.5 V increments a time series is collected and an FFT is performed. The oscillations are mapped across the $I-V$ curve. Oscillations are only present in the NDR region confirming that the composite is acting as the active element sustaining oscillations. Two distinct frequencies are observed one at the LC tank frequency, $f_{LC} = 2.32$ kHz, and the other indicated as X with $f_X = 2.58$ kHz.

$f_X = 2.58$ kHz.

We next explore the range of frequencies over which the composite is active as well as identify how this secondary oscillation frequency X varies with the tank frequency. The inductance was fixed at $L = 2.24$ mH and the capacitance varied in small increments such that the LC tank frequency could be varied from 1 kHz to 25 kHz in 0.5 kHz increments. A time series was recorded for each frequency and an FFT was performed. To enable a clean FFT spectrum a combination of electronic band pass filters and averaging was used, as described in chapter 3.4.4. The colour plot of f_{out} against f_{LC} is shown in figure 6-14. It is immediately apparent that there are two distinct behaviours with peaks extending in two different directions.

Firstly a line of peaks, (band of red), runs diagonally across the color map showing that the peak in the frequency spectrum, f_{out}, is proportional to the tank frequency, f_{LC}. The pink dashed line indicates f_0 from equation 6.31 and shows that the oscillation frequency of the composite is at the LC tank frequency. The

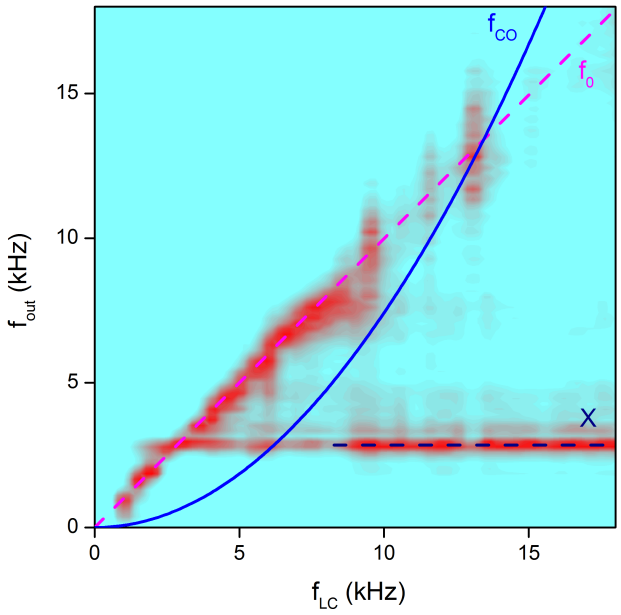

Figure 6-14: A 2D colour map to examine f_{out} as a function of f_{LC}. The pink dashed line indicates the theoretical oscillation frequency, f_0. The composite oscillates at f_0 up to where it intercepts the cut-off frequency, f_{CO}, indicated by the blue line, at 12.5 kHz. The intrinsic frequency shown as the dotted blue line marked X remains invariant with f_{LC}, at $f_X = 2.85$ kHz.

theoretical cut-off frequency, f_{CO}, shown by the solid blue line in figure 6-14, is calculated from equation 6.9 with $R_S = 12\ \Omega$ from the resistance of the inductor and $|g_c| = 0.34$ mS extracted from the $I-V$ curve. Above f_{CO} the composite no longer oscillates at the tank frequency, f_{LC}. The interception between f_{CO} and f_0 sets the maximum *LC driven* frequency at 12.5 kHz. The cut-off frequency, determined by the slope of NDR region, is where f_0 intercepts f_{CO}. Here the active region stops providing AC power and instead starts absorbing power, therefore no longer being able to sustain oscillations.

The second ridge of peaks can be seen to remain at a constant frequency at $f_{out} = 2.85$ kHz. The blue dashed line marked X remains invariant with f_{LC}. These oscillations appear above the theoretical cut-off frequency. They are therefore not related to the LC tank frequency of the oscillator circuit and must be an *intrinsic* frequency to the composite. This is interesting as an intrinsic frequency was not observed below V_P in figure 6-13 which means it arises from a process occurring in the NDR region.

Where $f_X = f_{LC}$ the oscillations become most stable and have the largest amplitude, and the sharpest peak in frequency domain. This is due to a resonance effect, with the amplitudes from the two different mechanisms constructively

combining .
A summary of the results for the composite in the LC oscillator circuit is as follows:

1. The composites NDR region is capable of sustaining oscillations up to the cut-off frequency.
2. No oscillations are present outside the NDR region.
3. The oscillation frequency is given by the LC tank frequency
4. A bursting behaviour arises due to the instabilities in the NDR region.
5. An intrinsic frequency is observed that is independent of the LC tank frequency, remaining constant over different LC values.
6. The intrinsic frequency is able to be resonant when $f_X = f_{LC}$.

So far we have not discussed the possible origins of intrinsic frequency however this will be addressed in the following sections as we study the effect of strain on the composite oscillations.

6.4.2 Strain Dependant Oscillations

We now consider the effect of applying a strain to the composite on both its low temperature $I - V$ characteristics and its ability to function as the active component in an oscillator. The motivation being that if the application of strain can switch the oscillations on or off, or tune the oscillation frequency, then we have a flexible oscillator that could be used as a flexible skin.

A bilayer strain was applied to the sample using the lead screw actuator arrangement as described in section 3-10. This allowed the composite to be placed in either compressive, $-\epsilon$, or tensile, $+\epsilon$, strain. The system was then cooled to 77 K and the $I - V$ characteristics and oscillations were recorded. In order to change the bend radius the composite was thermally cycled to room temperature. After an initial temperature and strain cycle the composite exhibited only minimal hysteresis over further cycling. The strain is calculated using the bilayer strain equation derived in section 3.8. The maximum bend before permanent deformation of the acetate corresponds to a bilayer strain of around 20%.

The influence of increasing strain on the composites $I - V$ characteristics is significant. There are changes to the low field resistance, onset of NDR and slope of the NDR region, all of which can be seen in figure 6-15 and figure 6-16 and are described as follow:

Low Field At low field, $V < V_P$, the resistance increases for both increasing compressive and tensile strain. This is as much as 585 Ω to 851 Ω for $\epsilon = 0$ to $\epsilon = -15\%$ and a 585 Ω to 799 Ω increase for $\epsilon = 0$ to $\epsilon = 13\%$. This response is different to the room temperature response of resistance to strain where both compressive and tensile strain decreased resistance and is due to the composite being below its glass transition temperature.

NDR Onset The voltage threshold, V_P, for the onset of the NDR region increases substantially. A 15 % compressive strain leads to a shift in V_P of 22.7 V to 26.4 V; a 16 % increase.

NDR Region The slope of the NDR region, $|g_c|$, reduces for increasing strain. This will affect both the oscillation frequency and cut-off frequency as they are both a function of $|g_c|$. A calculation for the change in cut-off frequency due to changes in $|g_c|$ can be found in appendix E.

To ascertain if any of these changes in the $I - V$ characteristics could then lead to a change in the oscillating behaviour, the composite was placed in an oscillator circuit with $L = 22.7$ mH and $C = 4.7$ μF. The composite was then

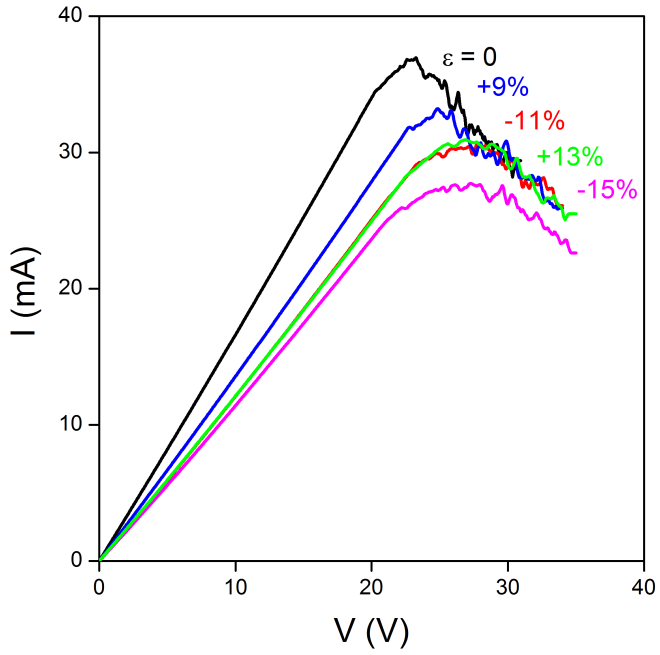

Figure 6-15: Straining the composite in compressive, $-\epsilon$, or tensile, $+\epsilon$, strain leads to a significant shift in the $I-V$ characteristics. The low field resistance increases by 45% for $\epsilon = 0$ to $\epsilon = -15\%$. While V_P shifts from 22.7 V to 26.4 V, a 16 % increase in V_P.

biased to two different voltages 15.0 V and 22.5 V that lie close to, and either side, of V_P. The $I-V$ characteristics for each strain and oscillations at each bias are shown in figure 6-16.

At $\epsilon = 0$ there are small, < 0.5 mV, but stable oscillations at 15 V as this is at the onset of the NDR region. While for $\epsilon = +11\%$ and $\epsilon = -13\%$ at 15 V there are no oscillations and instead there is just noise with amplitude < 0.2 mV. This is because the strain has caused V_P to increase and thus a 15 V bias is not sufficient for the composite to be in the NDR region and oscillations are therefore not sustained.

Biasing the composite at 22.5 V is sufficient to bring the composite into the NDR region for all strains. Oscillations can be observed at the tank frequency of 490 Hz for all strains. There is no measurable change in the oscillation frequency due to strain. This is because the change in $|g_c|$ is small. Which means, using equation 6.31, that the difference in oscillation frequency, f_0, compared to the LC tank frequency f_{LC} will be just 10 Hz even at the maximum strain.

The oscillations have the greatest stability and amplitude for $\epsilon = 0$, exceeding 3 mV. The oscillation amplitude decreases for both compressive and tensile strain by more than a factor of 5. This is due to the composite being furthest into the

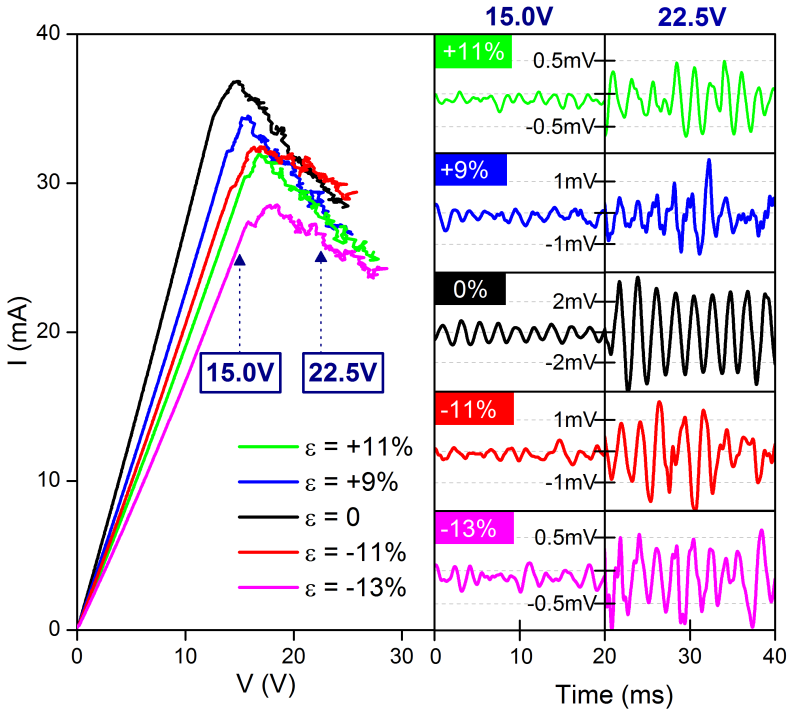

Figure 6-16: The composite is placed in an oscillator circuit with $L = 22.7$ mH and $C = 4.7$ μF and the $I-V$ characteristics recorded for tensile and compressive strain. At two voltages 15 V and 22.5 V the oscillations are recorded. At 15 V the composite is just in the NDR region for $\epsilon = 0$ and oscillations are observed, while for $\epsilon = -13\%$ there are no oscillations at 15 V. Demonstrating that the composite oscillator can be switched ON or OFF using strain to shift the $I - V$ curves. At 22.5 V all curves are in the NDR region and oscillations are observed for all strains. The oscillations exhibit the least noise and have the greatest amplitude for $\epsilon = 0$ as here the NDR is steepest and with the least fluctuations.

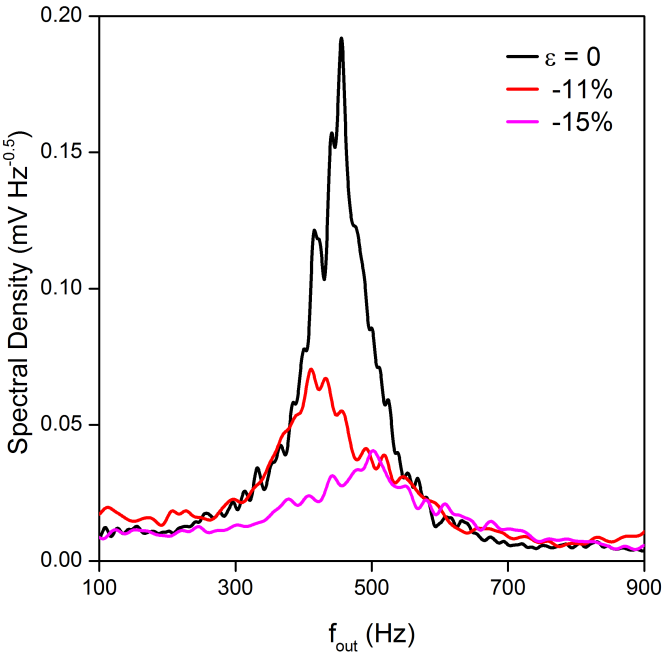

Figure 6-17: The spectral density FFT spectrum for a composite at the same bias in an LC circuit with $f_{LC} = 488$ Hz. Increasing the compressive strain decreases the peak output power significantly. From 0.19 mV Hz$^{-0.5}$ at $\epsilon = 0$ to 0.07 mV Hz$^{-0.5}$ for $\epsilon = -11\%$ to 0.04 mV Hz$^{-0.5}$ for $\epsilon = -15\%$.

NDR region for $\epsilon = 0$. This then provides a wider NDR region and thus larger oscillations are accessible. Further the slope of $|g_c|$ appears to become more stable, with fewer fluctuations, and thus the oscillations have a greater stability.

We have therefore demonstrated that the composite can be used as an oscillator that can be switched ON and OFF by using strain to shift the $I - V$ characteristics, for the same bias point, in and out of the NDR region. We have also shown that the oscillation amplitude is a function of strain, with an increasing strain causing a decrease the oscillation amplitude.

We now show this in the FFT spectrum for three different strains in figure 6-17. The LC tank frequency is 488 Hz and the peak frequencies of all three strains remains close to this. However the peak spectral density decreases from 0.19 mV Hz$^{-0.5}$ at $\epsilon = 0$; to 0.07 mV Hz$^{-0.5}$ for $\epsilon = -11\%$; to 0.04 mV Hz$^{-0.5}$ for $\epsilon = -15\%$. This shows another possible oscillator application whereby the oscillation amplitude is directly tunable via strain reducing by 79% with a 15% increase in composite strain.

Next we explore how the cut-off frequency changes with strain and how the intrinsic frequency responds to strain. The composite was placed in an oscillator circuit with $L = 43.3$ mH and biased into the NDR region. The capacitance was

then varied from 14.62 μF to 9.1 nF such that the LC tank frequency increases from 200 Hz to 4,000 Hz in 200 Hz steps. The FFT spectrum was measured for each step using the method described in section 3.4.4. This was repeated for a range of compressive strains, shown in figure 6-18 with (a) $\epsilon = 0$, (b) $\epsilon = -7.0\%$, (c) $\epsilon = -9.9\%$, (d) $\epsilon = -12.2\%$ and (e) $\epsilon = -14.1\%$. The yellow dashed line shows f_0 up to the yellow point, which is the calculated cut-off frequency, f_{CO}, for each strain. The calculation off_{CO} from the slope of the NDR region is described in appendix E.

Starting with $\epsilon = 0$, there are no clear oscillations that follow f_0. Instead the spectrum is dominated by two lines of oscillations at 314 Hz and 2.1 kHz both of which are independent of the LC tank frequency. As the strain is increased to $\epsilon = -7.0\%$ the composite now oscillates at the LC tank frequency. These oscillations continue up until the calculated f_{CO}.

As the strain is further increased the composite continues to oscillate at f_0 up to f_{CO}. The cut-off increases with increasing strain due to the reduced slope of $|g_c|$ and for each strain the calculated f_{CO} follows that of the maximum f_0 observed.

We turn our attention to the oscillations that are independent of f_{LC}, marked by the blue dashed line X. We have already mentioned the intrinsic oscillation frequency in the previous section figure 6-14. Here we see that f_X, while invariant under f_{LC}, increases with strain. As panel (f) of figure 6-18 shows f_X increases from 2.1 kHz at $\epsilon = 0$ to 3.3 kHz at $\epsilon = -14.1\%$. The increase is almost linear at a rate of 84 Hz / % increase in strain. The intrinsic frequency is more apparent above f_{CO}. This is because the oscillations at f_0, below f_{CO}, dominate the spectrum and thus mask f_X. We now consider the origins of these intrinsic frequencies in more detail.

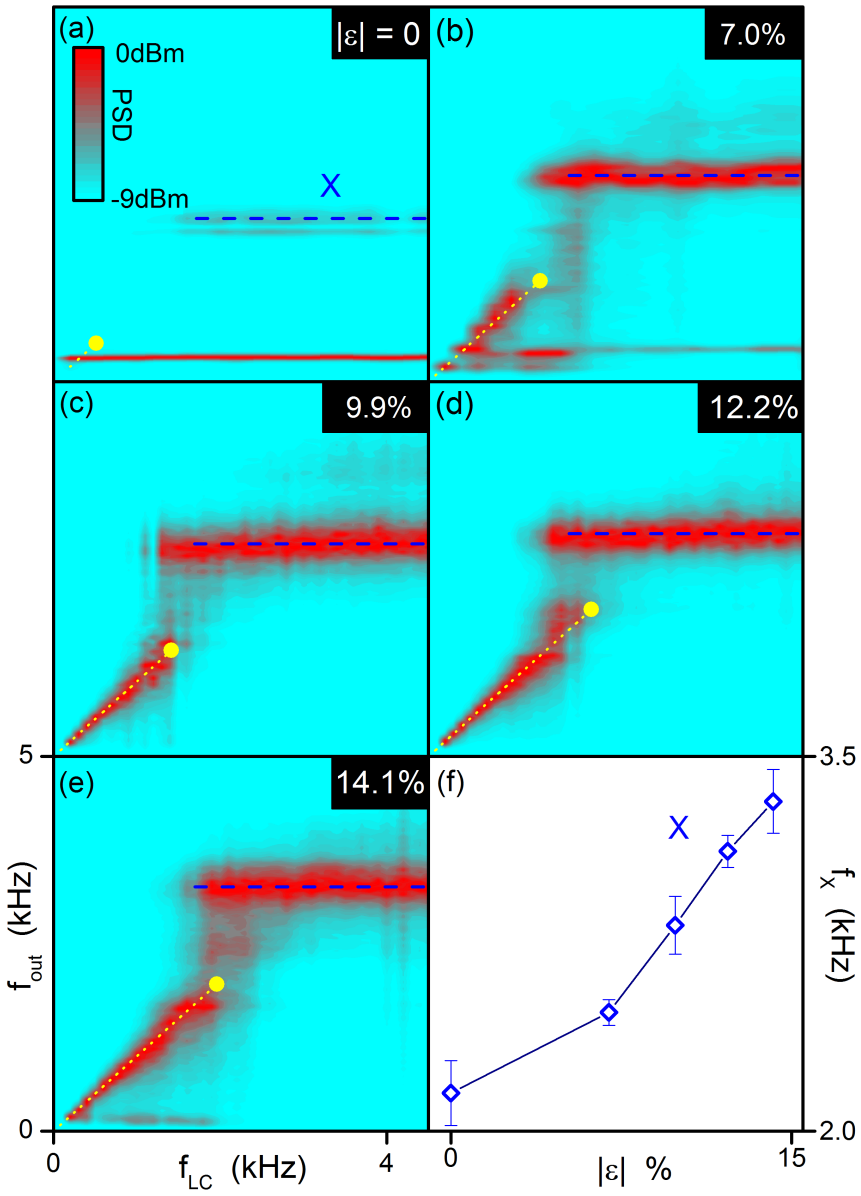

Figure 6-18: (a)-(e) The frequency response with increasing compressive strain, $-\epsilon$. The composite oscillates at the LC tank frequency up to the cut-off frequency f_{CO}. The yellow dashed line indicates the calculated f_{CO}, from appendix E, that increases with strain. The blue dashed line, labelled X is the intrinsic frequency that linearly increases with strain. (f) The shift in f_X is from 2.1 kHz at $\epsilon = 0$ to 3.3 kHz at $\epsilon = -14.1\%$ a significant increase of 84 Hz / % strain.

6.4.3 Strain Tunable Intrinsic Frequency Mode

The appearance of an intrinsic oscillation frequency was unexpected. Before attempting to explain the origins of this mode we first summarise the key observations:

1. The intrinsic frequency mode is independent of the LC tank, remaining invariant to changes in LC tank frequency, shown in figure 6-14

2. Oscillations at f_X only appear when the composite is biased into the NDR region, as shown in figure 6-13.

3. The intrinsic frequency mode is related to the strain applied to the composite with f_X having a linear relationship to ϵ. The increase is significant at 84 Hz / % strain, shown in figure 6-18(f).

4. If $f_{LC} = f_X$ then a resonance effect takes place with much larger oscillations that are stable with little phase shifting or bursting effect. We make use of the resonance effect in constructing a flexible amplifier.

5. The oscillations occur even after the LC circuit has been removed confirming that they are completely independent of the LC tank frequency.

It is reasonable to speculate that the observed intrinsic frequencies are related to the *conduction processes* occurring within the composite when it is biased into the NDR region. This is for two reasons. Firstly, the oscillations *only* occur when the composite is biased in the NDR region and not before. Secondly, the intrinsic frequency shifts in response to *physical changes* of the composite, strain, but not to changes in the oscillator circuit.

As established in chapter 4, the NDR occurs due to highly resistive domains being formed from the breaking of the conduction band in individual graphite particles. It is possible that these resistive domains will cause charge to accumulate around the resistive particle creating a local potential across the domain cell. Transient charge accumulations across the cell could then cause oscillations in the following way:

Transient charge accumulation ($+\Delta Q$) in one particle will increase the capacitive bias in the adjacent silicone barrier ($+\Delta V$). As the cell is biased into the NDR region, the current decreases ($-\Delta I$). This in turn reduces the charge accumulation ($+\Delta Q$) and the local bias drops ($-\Delta V$). However the cell remains

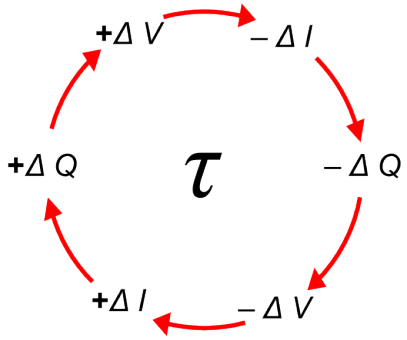

Figure 6-19: A possible mechanism by which the intrinsic oscillations occur is through transient charge accumulations across the highly resistive domains that materialize when the composite is biased into the NDR region. This leads to cyclic changes in the charge ΔQ, local bias ΔV and current ΔI that occur over a period τ.

biased in the NDR region and so this causes the current to increase ($+\Delta I$) and resume the transient charge accumulation. Leading to a cyclic feedback mechanism as shown in figure 6-19

A positive feedback loop of this kind instigated by the NDR could explain the intrinsic oscillations. The feedback loop will oscillate on a time scale, τ, which could then be related to the intrinsic frequency as $\tau = \dfrac{1}{f_X} = 0.46$ ms. If τ is due to a capacitive charging effect then it can be considered as an RC time constant with $\tau = \dfrac{C}{|g_c|}$. This yields a value of $C \approx 100\ nF$ that *decreases* with strain. It is not clear why the capacitance would decrease with strain but it is likely to be associated with the changes in particle separation distances due to the compression of the matrix. However this does not correlate well with the observed changes in capacitance in section 5.4. Clearly further work is required to better understand the origins of these intrinsic oscillation modes.

Despite not fully understanding the origins of the intrinsic frequencies we can still take advantage of them. We make use of the resonance effect when $f_{LC} = f_X$ to construct a flexible amplifier.

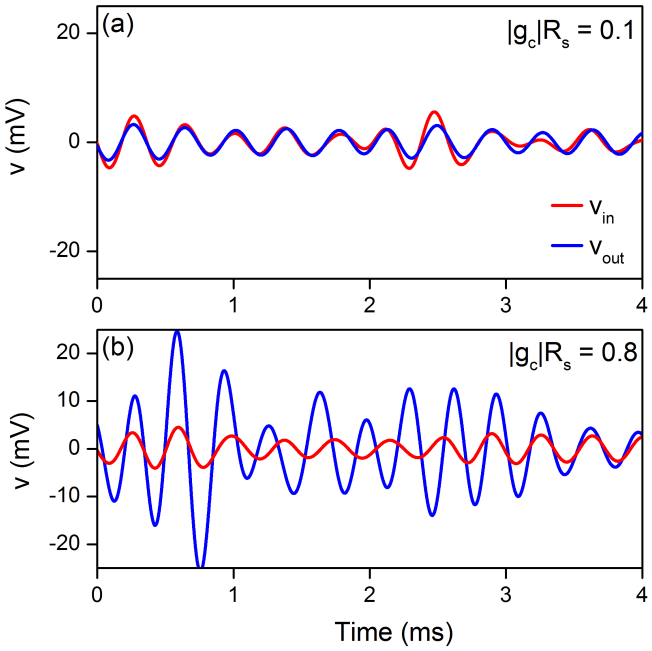

Figure 6-20: Time series comparing v_{in} and v_{out} for two different values of $|g_c|R_S$. (a) For $|g_c|R_S = 0.1$ the gain is just 1.05 with v_{out} just exceeding the input signal, v_{in}. (b) When $|g_c|R_S = 0.8$ there is now a substantial gain of 4.5. The amplitude and phase fluctuate due to changes in $|g_c|$.

6.4.4 Strain-Tuned Flexible Amplifier Via NDR

Having demonstrated that the composite functions as an oscillator when biased into the NDR region we next include it as the active component in a tuned amplifier circuit. We use the same tuned amplifier circuit as for the Lambda diode amplifier in figure 6-7 but with the active component replaced as the GSC device. Based on the observed resonance effect, the input frequency to be amplified was chosen as the composites intrinsic frequency, f_X, with the LC tank frequency set such that, $f_D = f_X = f_{LC}$. This generates the greatest possible amplification and stability. The key parameter in the tuned amplifier is the resistance, R_S, and its relation to the negative conductance $|g_c|$. When $|g_c|R_S \to 0$ there is no amplification, and when $|g_c|R_S \to 1$ the gain is at a maximum.

The composite intrinsic frequency was found to be 2.75 kHz and thus the tank frequency was set to $L = 104$ mH and $C = 34.3$ nF and $f_D = 2.75$ kHz with amplitude, $v_{in} = 5$ mV. The $I - V$ curve was taken in order to extract the slope the negative conductance as $|g_c| = 1.3$ mS.

First we present two time series where $|g_c|R_S = 0.1$ and $|g_c|R_S = 0.8$, shown in figure 6-20 (a) and (b) respectively. For $|g_c|R_S = 0.1$ the oscillations are in

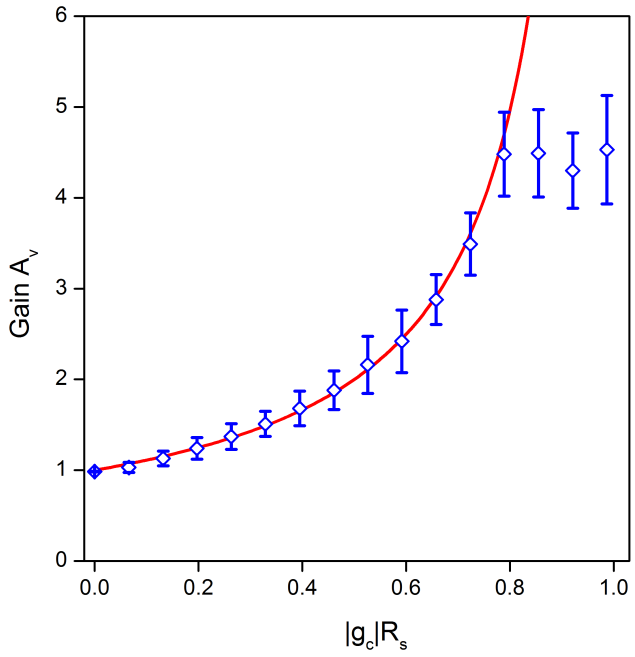

Figure 6-21: The gain of a tuned amplifier circuit with the composite as the active component. The averaged gain, blue diamonds, follows that of the theoretical gain, red line, closely up to a maximum $A_V = 4.5$. Above $|g_c|R_S = 0.8$ the gain remains constant due to the bursting behaviour caused by instabilities in $|g_c|$. The error bars are the standard error of the gain.

phase and v_{out} just exceeds that of the input, v_{in} such that $A_V = 1.05$. However the amplitude of v_{out} is not constant due to fluctuations in $|g_c|$.

For $|g_c|R_S = 0.8$ there is a substantial gain of 4.5. The gain is again variable due to fluctuations in $|g_c|$. There is also a phase shift that is not constant as f_d does not exactly equal f_{LC} and when $|g_c|$ fluctuates the phase shifts forward and back. However overall the composite is functioning as the active component of the tuned amplifier device.

Next we vary R_S in 50 Ω steps up to $|g_c|R_S = 1$. Calculation of the exact gain is difficult and a program was written that segmented 600 ms of data into 25 cycle length sections where the gain is steady. A bandpass filter of 1 kHz to 5 kHz was applied and the amplitude for each oscillation was calculated to find the gain $A_V = \dfrac{v_{out}}{v_{in}}$.

The gain as a function of $|g_c|R_S$ is shown in figure 6-21. The red line shows the theoretical gain calculated using equation 6.28 with $|g_c| = 1.3$ mS, $L = 104$ mH, $C = 34.3$ nF and $R_L = 1$ MΩ. The composite closely follows the theoretical gain up to $|g_c|R_S = 0.8$ where the gain reaches a maximum of $A_V = 4.5$.

As $|g_c|R_S$ is further increased the gain does not increase further. This is due

to a significant bursting effect with short bursts of high gain followed by a low gain. Single oscillations have amplitudes of over 40 mV, $A_V > 8$, however the oscillations quickly decay to only a small gain. Therefore the averaged gain does not continue to increase beyond $|g_c|R_S = 0.8$.

We have demonstrated a flexible amplifier where the gain can be tuned between 1 and 4.5 via a resistance. A gain greater than 4.5 could be achieved if the instabilities in $|g_c|$ could be eliminated. In order to amplify at a different signal the composite would need to be *strained* to induce a change in the intrinsic frequency. The LC tank must then be made equal to the intrinsic frequency. In this manner the composite is a *strain-tuned* amplifier capable of amplifying signals between 2.1 and 3.3 kHz.

6.5 Summary

The foremost aim of this chapter was to convince the reader of the GSCs ability to function as an active device; capable of generating and sustaining oscillations. It was unequivocally shown that the LC driven oscillations arise solely due to the NDR region through demonstrating that, outside the NDR region the composite is quiet and in the NDR region there are spontaneous oscillations at the LC frequency.

The second aim of this chapter was to explore how the oscillations varied with strain. Various dependence's were observed.

1. Increasing the strain shifted the onset of the NDR region to a greater value of V_P. This, with careful biasing, allows the oscillations to be switched on and off with strain.

2. The oscillation amplitudes vary with the bias position relative to the NDR region. Thus the oscillation amplitude is also a function of strain when the bias point lies close to V_P.

3. Intrinsic frequencies are observed that are independent of the LC tank frequency and increase with strain by approximately 84 Hz / % strain.

This third point is the most interesting as it is most similar to the behaviour of mechanoreceptor neurons in human skin, where the strain is recorded as a frequency. We believe that the intrinsic frequencies arise from transient charge accumulations across highly resistance domain boundaries when the composite is in the NDR region.

The composite was included as the active element of a tuned amplifier circuit and using the intrinsic frequency we were able to create a strain-tuned amplifier. The gain was then shown to be tunable between 1 and 4.5. The presence of bursting and an unsteady phase shift were due to the time variance of $|g_c|$.

The demonstration of a flexible amplifier is impressive as usually NDR based amplifiers are built from TD devices with a specifically engineered band structures. Yet, we are able to show a soft flexible material as an active amplifying device. Furthermore, we have been able to combine strain and the active properties of the GSC to encoding the strain as a frequency using the intrinsic frequency. This is an efficient method in which to measure the strain and would lend itself well to a flexible skin.

What this chapter does not address is that although the composite is described as a flexible oscillator, the NDR is only present at low temperatures, 77 K. This is below the glass transition temperature of the composite. The composite must be bent at room temperature to induce strain and then cooled to 77 K. The eventual goal is to raise the temperature at which the composite exhibits the NDR to room temperature. The various methods by which this could be achieved are discussed in the following chapter.

Another draw back that arises is from the time variance of $|g_c|$ for a fixed bias. The fluctuations appear random when the composite is biased in the NDR region. If $|g_c|$ remained constant the $I-V$ characteristics would allow for oscillations with amplitude of the order $\pm$ 5 V but instead we only observe $\pm$ 50 mV oscillations. The next stage of work is to identify where these instabilities arise from and then to attempt to stabilize the NDR.

Chapter 7

Conclusions and Future Work

This thesis has presented research regarding the electromechanical properties of a composite formed of graphite nanoparticles in a silicone rubber matrix. We have made the exciting discovery of a NDR region in the $I - V$ characteristics of the composite at low temperatures. We have conducted a detailed study on the effects of volume fraction, filler type, probe separation and temperature dependence; combined with theoretical modelling of the LDOS in graphite and the tunneling current across a single graphite-silicone barrier. From this evidence we arrived at the conclusion that the NDR occurs due to the composite breaking up into domains of constant electric field, separated by highly resistive *domain boundaries*. These are identified as individual graphite nanoparticles whose *orientation* in the electric field favour conduction across an embedded bilayer graphene. An electric field opens a partial *energy gap* at the Fermi level causing the current carrying bilayer to undergo a *semi-metal to insulator* transition. The current therefore decreases, causing the NDR.

Part of the significance of this discovery is that the NDR creates an *active* region in a *flexible* soft composite; usually NDR is only seen in silicon based technology which is not inherently flexible. The composite is therefore suitable as a flexible electronic skin and subsequent work was towards the realization of a flexible active device.

With this in mind, we explored the electromechanical properties of the composite. Through bending the composite on an acetate substrate we induced a *bilayer strain* and studied the piezoresistance. We found that this was dominated by resistance spiking, due to conduction line *destruction*. We discussed the *viscoelastic* properties of the composite that lead to the long resistance relaxation times. Rather than find ways to minimise the resistance spiking we instead embraced it as a mechanism that is extremely sensitive to perturbations.

We were able to utilize the composite in the detection of ultrasound waves and demonstrated a pressure detection threshold of 48 Pa. We also observed a commensurability between the composite width and ultrasound wave length due to the creation of standing waves along the composite width, in accordance with Bragg's law.

We also described in detail the fabrication of a DPA, designed for the detection of resistance spikes. We used the DPA device to image shapes and objects with pressures less than 3.8 kPa, with a raster scan frequency of 4 Hz over the 64 pixel array. Traditionally conductive rubbers are used for their piezoresistance but we believe that conduction line destruction offers a greater sensitivity. Possibly why we observed such large resistance spikes from small pressures is due to the high concentrations of graphite particles we achieved in our composite.

Having explored the strain dependence and pressure spiking we next utilized the active region to create a flexible oscillator and amplifier. We found that the composite was indeed capable of *sustaining oscillations* at the LC tank frequency. We were able to demonstrate the LC driven oscillations up to 12.5 kHz where the composite's NDR region reached its cut-off frequency. The amplitude of the oscillations was around 20 mV which is two orders of magnitude smaller than that implied by the width of the NDR region. The reduced amplitude as well, as the bursting behaviour we observed, is caused by inherent instabilities in the slope of the negative conductance. We understand this as the rerouting of conduction paths in the percolation network.

Despite the small oscillation amplitude and bursting behaviour we implemented our vision for a flexible active device through straining the composite whilst biased in the NDR and incorporated in an oscillator circuit. We observed changes in the oscillation amplitude but not significant changes in the LC driven frequency. However, we also discovered an unexpected *intrinsic* frequency of the composite that was found to be independent of the LC tank frequency whilst having a significant linear dependence on the induced strain, 84 Hz / % strain. We explain the intrinsic frequencies as arising from *transient charge accumulations* in the resistive regions of the conduction network. While we do not fully understand this yet, the intrinsic frequencies are well suited for creating a flexible active device as encoding the strain as a frequency mimics the response of *mechanoreceptor* neurons of the human skin. Further we were able to demonstrate the composite in an amplifying circuit with the NDR region shown to provide a gain that is tunable between 1 and 4.5. This was achieved by matching the LC tank frequency to the strain dependant intrinsic frequency.

Where we fall short of presenting a truly flexible active device is that the NDR region occurs only at low temperatures, from the requirement of the silicone matrix being below its glass transition temperature. Above the glass transition the matrix is able to expand under Joule heating such that the silicone barrier never becomes transparent enough for the semi-metal to insulator transition to be induced. Clearly the composite is therefore not actually flexible and a device requiring cooling to 77 K is of little practical use. However ideas for overcoming this problem and to bring the NDR up to a room temperature effect, are discussed in the future research section.

The DPA and ultrasound detection have shown good potential for developing a flexible skin, although not an active one, except that the viscoelasticity of the composite needs to be considered. The resistance is time dependant and the relaxation time sets an upper limit for the maximum frequency for recording separate perturbation incidents at around 2 Hz. Also describing the DPA as a fully flexible device is not quite accurate as only the composite pixels are soft and still require in situ silicon transistors for the read-write address procedure. Again this is a problem that can be overcome and is explained next.

7.1 Future Research

Two significant areas for future research into GSC are; the development of a room temperature NDR device; and the creation of a completely *flexible* high resolution DPA.

7.1.1 Towards Room Temperature NDR

It is highly desirable to be able to manipulate the tunneling conduction in the GSC so that it can exhibit room temperature NDR. There are two main problems that need to be overcome to achieve this:

1. The glass transition temperature of the composite needs to be increased to 300 K, or above, so that there is no thermal expansion of the composite as the current flows.

2. The height of the tunneling barrier needs to be increased from 165 meV to about 250 meV so that thermo-activated currents, that inhibit the NDR, are quenched [4].

Solutions to overcoming these two key problems reside around altering the structure and chemistry of both the graphite and polymer matrix and include:

- Finding a host polymer with a higher glass transition. We have identified epoxy, polyethylene and polystyrene all as being potentially well suited and with glass transition temperatures above 300 K. Some of these polymers may become saturated before enough graphite can be introduced. It may also be possible to chemically modify the current silicone polymer through changing the functional groups on the siloxanes. The difficulty though, is that in altering the matrix we still require a high volume fraction of graphite within it, for the narrow tunneling barriers.

- The graphite nanoparticles could be replaced by graphene nano-platelets. The nano-platelets consist of just a few graphite layers and have a high aspect ratio. Incorporating these and using an electric field to align the particles may allow suitable conduction lines for NDR to be formed at lower volume fractions.

- It is possible to increase the graphite miscibility in polymer. We have developed NDI based molecules, with Dr Dan Pantos, with aromatic cores that attach to the graphite planes. Appendages can be included that then directly polymerize with the surrounding silicone rubber, anchoring the particle into the matrix, and so increasing the miscibility. The preliminary studies, presented in chapter 3.3, show this is a promising line of enquiry. The next stage would be to use the presence of the NDI molecule to alter graphite's electronic properties through altering the aromatic ring to be either electron rich or electron deficient. Using this in conjunction with the nano-platelets should lead a controllable surface conductivity. Also covering the graphene nano-platelets with a resistive layer may assist in quenching the thermo-activated current, as well increasing miscibility.

In summary to progress towards room temperature NDR it is important that we are able to find ways to control the tunneling barrier and height while also the chemistry of the polymer. This should enable us to increase the glass transition temperature and quench thermo-activated currents over the barrier.

7.1.2 A High Resolution Flexible Skin

To create a flexible high resolution DPA that has a resolution better than that of human skin and that is suitable for cutting edge applications, such as flexible electronic skins, we envisage an array of 64 by 64 composite pixels, of size 100 μm in order to create a 1 cm^2 4,096 pixel array with a resolution exceeding 250 dpi.

To make the array truly flexible we would follow the method of Someya and fabricate organic flexible pentacene transistors, that have a mobility of 1.4 $cm^2V^{-1}s^{-1}$ and that can be switched with a 20 V gate voltage [15]. These can be readily made on the size of array discussed above using clean room fabrication techniques. Creating the gates and contacts can be achieved through thermal deposition of Au on to a flexible substrate. We have so far used acetate sheet as our flexible substrate but other similar flexible substrates may be better suited such as a polyethylene naphthalate film that has suitable stretching characteristics and a smooth surface.

The next stage would then be to combine the flexible transistors with the composite pixels. This could be achieved via the novel imprint lithography methods we developed in chapter 3.2.3. Finally, the electronic addressing and measurement system described for the DPA prototype in chapter 3.6, could be simply scaled up for the larger array.

The processes briefly described above could be used to create a truly flexible differential pressure sensitive array. The ultimate objective would be to then combine a room temperature NDR composite with the array described above to enable encoding the strain into frequency at a sensitivity and resolution that exceeds that of human skin.

7.2 Concluding Remarks

The work described in this thesis has demonstrated the potential for GSCs as a flexible electronic skin. We reported the discovery of a NDR region in the low temperature $I - V$ characteristics of the composite and have shown the NDR region to exhibit strain-tuned oscillations. We also demonstrated a sensitive method for differential pressure detection that advances the methods used in current research of flexible skins.

Appendix A

Publications

1. S. Littlejohn, A. Nogaret, and S. Crampin, "Tunneling negative differential resistance in a flexible active composite," *Advanced Materials*, vol. 23, no. 25, pp. 28152818, 2011.

2. S. Littlejohn, A. Nogaret, S. R. Davies, M. Henini, H. E. Beere and D. A. Ritchie, "Microwave power generation by magnetic superlattices," *Applied Physics Letters*, vol. 99, no. 24, pp. 242107-242107, 2011.

3. S. Littlejohn, A. Nogaret, J. Ihm and H. Cheong, "Negative differential resistance in graphite-silicone polymer composites," *AIP Conference Proceedings*, vol. 1399, no. 1, pp. 843-844, 2011.

4. S. Littlejohn and S. Crampin and A. Nogaret, "Negative differential resistance in a flexible graphite silicone composite," *Technical Proceedings of the* 2012 *NSTI Nanotechnology Conference*, vol. 1, pp. 165-168, 2012.

5. S. Littlejohn, A. Nogaret, G. M. Prentice, G. D. Pantos, "Pressure sensing and electronic amplification with functionalized graphite-silicone composite," *Advanced Functional Materials*, 2013. Submitted.

Appendix B

Procedure for Imprint Lithography Stamp

The procedure for the stamp fabrication was as follows:

1. Clean [100] silicon wafer with acetone and IPA
2. Spin photoresist S1813 for 30 s at 5000 rpm
3. Bake for 15 minutes at 90°C
4. Soak in chlorobenzene for 5 minutes
5. Bake for a further 15 minutes at 90°C
6. Expose, using Hall bar mask, for 8.5 s (bulb power dependant)
7. Develop in 351 developer (10:35 Di water to 351) for 30 s
8. Deposit 300 nm of chromium in 60 nm stages, allowing cooling between runs
9. Lift off in warm acetone to leave silicon Hall bar exposed
10. Use ICP-RIE to etch according to recipe in appendix C.
11. Measure depth of etch ($\approx$ 110 μm with rate 475 nm/minute)

Appendix C

ICP-RIE Recipe for Deep Silicon Etch

The ICP-RIE recipe used for etching was run for 5 minutes followed by a period of 10 minutes cooling. This was repeated 48 times for an etch of over 100 μm. The parameters on the Oxford Instruments Plasmalab System 80 were:

- 12 sccm SF_6 and 10.5 sccm O_2
- 240 V DC Bias
- 300 mW/cm^2 RF
- 99.6 mT
- Graphite plate
- 14°C water

The ICP-RIE recipe was developed through a process of trial and error. The advantage of the recipe used was that it allowed a fast etch rate of 475 nm/minute with minimal undercutting. The etch proceeds through a creation of a plasma containing SF_6 and O_2 which under the influence of the strong electric field generates free radicals of F^* and O^*. The fluorine radicals react with the exposed silicon and form SiF_4, the etching process, while the oxygen radicals passivate the silicone surface through forming SiO_xF_y (siliconooxyfluoride) inhibiting the etch. During the etching process there is clearly a competition between the competing mechanisms of etching and passivation. Through the correct balance of parameters of RF power, pressure, flow rates and temperature it is possible to optimised the competing mechanisms to attain high anisotropic etching and have complete

control of the shape of the side walls, (ideally vertical) [131]. The anisotropy is achieved due to a thick build up of the SiO_xF_y layer (which is proportional to O_2 content) on the side walls while at the trench bottom the layer is extremely thin because of the intense ion bombardment [132].

Appendix D

Synthesis of Silane Functionalized Naphthalenediimide

The reaction was performed on 0.744 mmol (200 mg) of 1,4,5,8 - naphthalene-tetracarboxylic dianhydride and 1.56 mmol (0.27 ml) of (3-aminopropyl)trimethoxysilane which were suspended in 6 ml dimethylformamide in a pressure tight microwave tube. The reaction mixture was then sonicated for 30 minutes at which point gelation occurs. The reaction mixture was heated under microwave irradiation for 10 minutes at $140 \pm 5°C$. The resulting solid was filtered from the mother liquor. The product was purified by sequential suspension for 1 hour and filtering of solid from water, 1M HCl(aq), acetone, dichloromethane and acetone, respectively. The product was dried under vacuo to yield a light brown solid (338 mg, 93%).

Appendix E

Calculation of Cut-Off Frequency

The theoretical cut-off frequency of the oscillations generated from the NDR region and LC tank is calculated as,

$$f_{CO} = \frac{|g_c|}{2\pi C}\sqrt{\frac{1}{R_S|g_c|} - 1}. \tag{E.1}$$

The cut-off frequency therefore depends on the series resistance in the circuit, R, and the negative conductance, $|g_c|$, of the composite. The value of $|g_c|$ can be extracted from the 4T $I-V$ characteristics of the composite. The slope of the NDR region for different values of strain are shown by the blue lines of figure E-1. The series resistance can be found by comparing the difference in the low field resistance between the 2T and 4T curves, shown as black and red respectively in figure E-1. This will be the sum of, the contact resistance of the sample, $\approx 120\ \Omega$; the internal resistance of the inductor, 32 Ω; and the resistance of the low pass filter on the voltage source, 150 Ω, which is then subtracted as this resistance does not impact on the AC equivalent circuit.

Having extract R and $|g_c|$ it is then possible to calculate f_{CO}. The increasing f_{CO} with strain is shown in table reftab:fcutoffValues. These values are used to compare the observed and calculated cut-off frequency in figure 6-18.

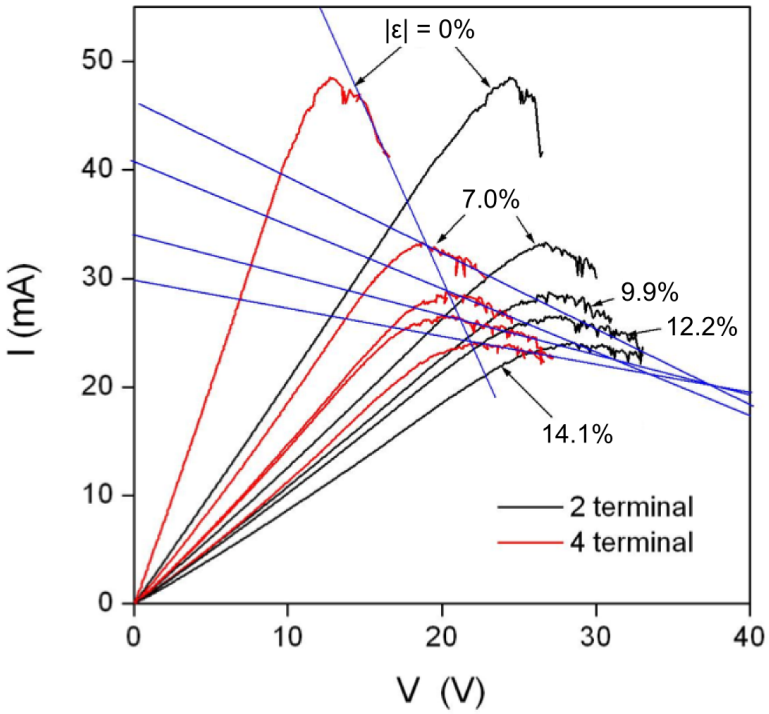

Figure E-1: The 4T and 2T (red and black) $I-V$ curves of the composite under increasing strain. The slope of $|g_c|$ and the series resistance, R, can be extracted in order to calculate f_{CO}.

$\|\epsilon\|$ (%)	R (Ω)	$\|g_c\|$ (mS)	f_{CO} (Hz)
0	108	3.125	512
7.0	121	0.7	1346
9.9	110	0.59	1414
12.2	129	0.364	1962
14.1	146	0.26	2480

Table E.1: The extracted values of the series resistance of the circuit, R, and the negative conductance $|g_c|$ are used to calculated the theoretical cut-off frequency, f_{CO}, of the oscillator under increasing bilayer strain, $|\epsilon|$.

Bibliography

[1] J. A. Rogers, "Toward paperlike displays," *Science*, vol. 291, no. 5508, pp. 1502–1503, 2001.

[2] T. Someya, Y. Kato, T. Sekitani, S. Iba, Y. Noguchi, Y. Murase, H. Kawaguchi, and T. Sakurai, "Conformable, flexible, large-area networks of pressure and thermal sensors with organic transistor active matrixes," *Proceedings of the National Academy of Sciences*, vol. 102, no. 35, pp. 12321–12325, 2005.

[3] M. I. Tiwana, S. J. Redmond, and N. H. Lovell, "A review of tactile sensing technologies with applications in biomedical engineering," *Sensors and Actuators A: Physical*, vol. 179, pp. 17–31, 2012.

[4] S. Littlejohn, A. Nogaret, and S. Crampin, "Tunneling negative differential resistance in a flexible active composite," *Advanced Materials*, vol. 23, no. 25, pp. 2815–2818, 2011.

[5] K. S. Novoselov, A. K. Geim, S. V. Morozov, D. Jiang, Y. Zhang, S. V. Dubonos, I. V. Grigorieva, and A. A. Firsov, "Electric field effect in atomically thin carbon films," *Science*, vol. 306, no. 5696, pp. 666–669, 2004.

[6] A. K. Geim and K. S. Novoselov, "The rise of graphene," *Nature Materials*, vol. 6, no. 3, pp. 183–191, 2007.

[7] E. V. Castro, K. S. Novoselov, S. V. Morozov, N. M. R. Peres, J. M. B. L. dos Santos, J. Nilsson, F. Guinea, A. K. Geim, and A. H. C. Neto, "Biased bilayer graphene: Semiconductor with a gap tunable by the electric field effect," *Physical Review B*, vol. 99, no. 21, p. 216802, 2007.

[8] Y. Zhang, T.-T. Tang, C. Girit, Z. Hao, M. C. Martin, A. Zettl, M. F. Crommie, Y. R. Shen, and F. Wang, "Direct observation of a widely tunable bandgap in bilayer graphene," *Nature*, vol. 459, no. 7248, pp. 820–823, 2009.

[9] X. W. Zhang, Y. Pan, Q. Zheng, and X.-S. Yi, "Time dependence of piezoresistance for the conductor-filled polymer composites," *Journal of Polymer Science Part B: Polymer Physics*, vol. 38, no. 21, pp. 2739–2749, 2000.

[10] L. Wang, T. Ding, and P. Wang, "Effects of instantaneous compression pressure on electrical resistance of carbon black filled silicone rubber composite during compressive stress relaxation," *Composites Science and Technology*, vol. 68, pp. 3448–3450, 2008.

[11] J. A. Rogers and Y. Huang, "A curvy, stretchy future for electronics," *Proceedings of the National Academy of Sciences*, vol. 106, no. 27, pp. 10875–10876, 2009.

[12] T. Takahashi, K. Takei, A. G. Gillies, R. S. Fearing, and A. Javey, "Carbon nanotube active-matrix backplanes for conformal electronics and sensors," *Nano Letters*, vol. 11, no. 12, pp. 5408–5413, 2011.

[13] K. Takei, T. Takahashi, J. C. Ho, H. Ko, A. G. Gillies, P. W. Leu, R. S. Fearing, and A. Javey, "Nanowire active-matrix circuitry for low-voltage macroscale artificial skin," *Nature Materials*, vol. 9, no. 10, pp. 821–826, 2010.

[14] T. Sekitani, U. Zschieschang, H. Klauk, and T. Someya, "Flexible organic transistors and circuits with extreme bending stability," *Nature Materials*, vol. 9, no. 12, pp. 1015–1022, 2010.

[15] T. Someya, T. Sekitani, S. Iba, Y. Kato, H. Kawaguchi, and T. Sakurai, "A large-area, flexible pressure sensor matrix with organic field-effect transistors for artificial skin applications," *Proceedings of the National Academy of Sciences*, vol. 101, no. 27, pp. 9966–9970, 2004.

[16] H. Ko, R. Kapadia, K. Takei, T. Takahashi, X. Zhang, and A. Javey, "Multifunctional, flexible electronic systems based on engineered nanostructured materials," *Nanotechnology*, vol. 23, no. 34, p. 344001, 2012.

[17] J. W. Morley, A. W. Goodwin, and I. Darian-Smith, "Tactile discrimination of gratings," *Experimental Brain Research*, vol. 49, no. 2, pp. 291–299, 1983.

[18] V. Maheshwari and R. Saraf, "Tactile devices to sense touch on a par with a human finger," *Angewandte Chemie International Edition*, vol. 47, no. 41, pp. 7808–7826, 2008.

[19] A. Sinitskii and J. Tour, "Graphene electronics, unzipped," *IEEE Spectrum*, vol. 47, no. 11, pp. 28–33, 2010.

[20] H. W. Kroto, J. R. Heath, S. C. O'Brien, R. F. Curl, and R. E. Smalley, "C60: Buckminsterfullerene," *Nature*, vol. 318, no. 6042, pp. 162–163, 1985.

[21] R. C. Haddon, L. E. Brus, and K. Raghavachari, "Rehybridization and π-orbital alignment: the key to the existence of spheroidal carbon clusters," *Chemical Physics Letters*, vol. 131, no. 3, pp. 165–169, 1986.

[22] R. Bakry, R. M. Vallant, M. Najam-ul Haq, M. Rainer, Z. Szabo, C. W. Huck, and G. K. Bonn, "Medicinal applications of fullerenes," *International Journal of Nanomedicine*, vol. 2, no. 4, pp. 639–649, 2007.

[23] X. Wang, Q. Li, J. Xie, Z. Jin, J. Wang, Y. Li, K. Jiang, and S. Fan, "Fabrication of ultralong and electrically uniform single walled carbon nanotubes on clean substrates," *Nano Letters*, vol. 9, no. 9, pp. 3137–3141, 2009.

[24] S. Aikawa, E. Einarsson, T. Thurakitseree, S. Chiashi, E. Nishikawa, and S. Maruyama, "Deformable transparent all carbon nanotube transistors," *Applied Physics Letters*, vol. 100, no. 6, p. 063502, 2012.

[25] D. Sun, M. Y. Timmermans, Y. Tian, A. G. Nasibulin, E. I. Kauppinen, S. Kishimoto, T. Mizutani, and Y. Ohno, "Flexible high-performance carbon nanotube integrated circuits," *Nature Nanotechnology*, vol. 6, no. 3, pp. 156–161, 2011.

[26] A. B. Dalton, S. Collins, E. Munoz, J. M. Razal, V. H. Ebron, J. P. Ferraris, J. N. Coleman, B. G. Kim, and R. H. Baughman, "Super-tough carbon-nanotube fibres," *Nature*, vol. 423, no. 6941, pp. 703–703, 2003.

[27] S. Iijima, "Helical microtubules of graphitic carbon," *Nature*, vol. 354, no. 6348, pp. 56–58, 1991.

[28] S. Iijima and T. Ichihashi, "Single-shell carbon nanotubes of 1-nm diameter," *Nature*, vol. 363, no. 6430, pp. 603–605, 1993.

[29] L. Landau and E. Lifshitz, *Statistical physics, Part 1.* Pergamon Press, 1980.

[30] Y. Lin, C. Dimitrakopoulos, K. A. Jenkins, D. B. Farmer, H.-Y. Chiu, A. Grill, and P. Avouris, "100-GHz transistors from wafer-scale epitaxial graphene," *Science*, vol. 327, no. 5966, p. 662, 2010.

[31] E. McCann, "Asymmetry gap in the electronic band structure of bilayer graphene," *Physical Review B*, vol. 74, no. 16, p. 161403, 2006.

[32] X. Bourrat, *Sciences of Carbon Materials*. Universidad de Alicante, 2000.

[33] D. D. L. Chung, "Review graphite," *Journal of Materials Science*, vol. 37, no. 8, pp. 1475–1489, 2002.

[34] A. Celzard, E. McRae, G. Furdin, and J. F. Mareche, "Conduction mechanisms in some graphite-polymer composites: the effect of a direct-current electric field," *Journal of Physics: Condensed Matter*, vol. 9, no. 10, p. 2225, 1997.

[35] M. S. Dresselhaus and G. Dresselhaus, "Intercalation compounds of graphite," *Advances in Physics*, vol. 52, no. 1, pp. 1–186, 2002.

[36] S. Krivit, J. Lehr, and T. Kingery, *Nuclear Energy Encyclopedia: Science, Technology, and Applications*. Wiley, 2011.

[37] B. Kelly, *Physics of Graphite*. Applied Science Publishers, 1981.

[38] K. S. Novoselov, A. K. Geim, S. V. Morozov, D. Jiang, M. I. Katsnelson, I. V. Grigorieva, S. V. Dubonos, and A. A. Firsov, "Two-dimensional gas of massless Dirac fermions in graphene," *Nature*, vol. 438, pp. 197–200, 2005.

[39] J. C. Slonczewski and P. R. Weiss, "Band structure of graphite," *Physical Review*, vol. 109, no. 2, pp. 272–279, 1958.

[40] J. W. McClure, "Band structure of graphite and de Haas-van Alphen effect," *Physical Review*, vol. 108, no. 3, pp. 612–618, 1957.

[41] P. R. Wallace, "The band theory of graphite," *Physical Review*, vol. 71, no. 9, pp. 622–634, 1947.

[42] R. C. Tatar and S. Rabii, "Electronic properties of graphite: A unified theoretical study," *Physical Review B*, vol. 25, no. 6, pp. 4126–4141, 1982.

[43] J. Charlier, X. Gonze, and J. Michenaud, "First-principles study of the electronic properties of graphite," *Physical Review B*, vol. 43, no. 6, pp. 4579–4589, 1991.

[44] S. Brandt, N.B. Chudinov, *Semimetals: Graphite and its compounds*. North Holland, 1988.

[45] M. Charlier and A. Charlier, "The electronic structure of graphite and its base origins," *Chemistry and Physics of Carbon*, vol. 20, p. 61, 1987.

[46] I. Spain, "The electronic properties of graphite," *Chemistry and Physics of Carbon*, vol. 8, pp. 1–143, 1973.

[47] Y. Hancock, "The 2010 nobel prize in physics–ground-breaking experiments on graphene," *Journal of Physics D: Applied Physics*, vol. 44, no. 47, p. 473001, 2011.

[48] G. W. Semenoff, "Condensed-matter simulation of a three-dimensional anomaly," *Physical Review Letters*, vol. 53, no. 26, pp. 2449–2452, 1984.

[49] N. D. Mermin, "Crystalline order in two dimensions," *Physical Review*, vol. 176, no. 1, pp. 250–254, 1968.

[50] H. Boehm, A. Clauss, G. Fischer, and U. Hofmann, "Surface properties of extremely thin graphite lamellae," *Proceedings of the Fifth Conference on Carbon*, 1962.

[51] L. M. Viculis, J. J. Mack, and R. B. Kaner, "A chemical route to carbon nanoscrolls," *Science*, vol. 299, no. 5611, p. 1361, 2003.

[52] A. H. Castro Neto, F. Guinea, N. M. R. Peres, K. S. Novoselov, and A. K. Geim, "The electronic properties of graphene," *Reviews of Modern Physics*, vol. 81, no. 1, pp. 109–162, 2009.

[53] K. S. Novoselov, E. McCann, S. V. Morozov, V. I. Fal'ko, M. I. Katsnelson, U. Zeitler, D. Jiang, F. Schedin, and A. K. Geim, "Unconventional quantum Hall effect and Berry's phase of 2π in bilayer graphene," *Nature Physics*, vol. 2, no. 3, pp. 177–180, 2006.

[54] E. McCann and V. I. Fal'ko, "Landau-level degeneracy and quantum Hall effect in a graphite bilayer," *Physical Review Letters*, vol. 96, no. 8, p. 086805, 2006.

[55] E. McCann, D. S. L. Abergel, and V. I. Fal'ko, "Electrons in bilayer graphene," *Solid State Communications*, vol. 143, no. 1, pp. 110–115, 2007.

[56] T. Ohta, A. Bostwick, T. Seyller, K. Horn, and E. Rotenberg, "Controlling the electronic structure of bilayer graphene," *Science*, vol. 313, no. 5789, pp. 951–954, 2006.

[57] J. B. Oostinga, H. B. Heersche, X. Liu, A. F. Morpurgo, and L. M. K. Vandersypen, "Gate-induced insulating state in bilayer graphene devices," *Nature Materials*, vol. 7, no. 2, pp. 151–157, 2008.

[58] B. E. Feldman, J. Martin, and A. Yacoby, "Broken-symmetry states and divergent resistance in suspended bilayer graphene," *Nature Physics*, vol. 5, no. 12, pp. 889–893, 2009.

[59] R. Donnet, J. Bansel and M. Wang, *Carbon Black: Science and Technology*. Marcel Dekker, 1993.

[60] C. Liu, Z. Yu, D. Neff, A. Zhamu, and B. Z. Jang, "Graphene-based supercapacitor with an ultrahigh energy density," *Nano Letters*, vol. 10, no. 12, pp. 4863–4868, 2010.

[61] B. Z. Jang, C. Liu, D. Neff, Z. Yu, M. C. Wang, W. Xiong, and A. Zhamu, "Graphene surface-enabled lithium ion-exchanging cells: Next-generation high-power energy storage devices," *Nano Letters*, vol. 11, no. 9, pp. 3785–3791, 2011.

[62] L. S. Schadler, X. Wang, J. Nelson, and H. Hillborg, *Dielectric Polymer Nanocomposites*. Springer New York, 2010.

[63] S. Dietrich and A. Amnon, *Introduction To Percolation Theory*. Taylor and Francis, 1985.

[64] S. R. Broadbent and J. M. Hammersley, "Percolation processes," *Mathematical Proceedings of the Cambridge Philosophical Society*, vol. 53, no. 3, pp. 629–641, 1957.

[65] S. Kirkpatrick, "Percolation and conduction," *Reviews of Modern Physics*, vol. 45, no. 4, pp. 574–588, 1973.

[66] F. Carmona, "Conducting filled polymers," *Physica A: Statistical Mechanics and its Applications*, vol. 157, no. 1, pp. 461–469, 1989.

[67] I. Balberg, "Tunneling and nonuniversal conductivity in composite materials," *Physical Review Letters*, vol. 59, no. 12, pp. 1305–1308, 1987.

[68] I. Balberg, "A comprehensive picture of the electrical phenomena in carbon black–polymer composites," *Carbon*, vol. 40, no. 2, pp. 139–143, 2002.

[69] F. Carmona, P. Prudhon, and F. Barreau, "Percolation in short fibres epoxy resin composites: Conductivity behavior and finite size effects near threshold," *Solid State Communications*, vol. 51, no. 4, pp. 255–257, 1984.

[70] J. I. Hong, L. S. Schadler, R. W. Siegel, and E. Martensson, "Rescaled electrical properties of ZnO/low density polyethylene nanocomposites," *Applied Physics Letters*, vol. 82, no. 12, pp. 1956–1958, 2003.

[71] D. K. Roy, *Quantum Mechanical Tunneling and Its Applications*. World Scientific, 1986.

[72] R. Tsu and L. Esaki, "Tunneling in a finite superlattice," *Applied Physics Letters*, vol. 22, no. 11, pp. 562–564, 1973.

[73] Alchemie Ltd, Warwick, UK, *Technical DataSheet RTV 139*, 2011.

[74] L. Lopez, A. Cosgrove, J. Hernandez-Ortiz, and T. Osswald, "Modeling the vulcanization reaction of silicone rubber," *Polymer engineering and science*, vol. 47, no. 5, pp. 675–683, 2007.

[75] T. Ding, L. Wang, and P. Wang, "Changes in electrical resistance of carbon-black-filled silicone rubber composite during compression," *Journal of Polymer Science Part B: Polymer Physics*, vol. 45, no. 19, pp. 2700–2706, 2007.

[76] J. Zhang, S. Zhang, S. Feng, and Z. Jiang, "The correlativity of positive temperature coefficient effects in conductive silicone rubber," *Polymer International*, vol. 54, no. 8, pp. 1175–1179, 2005.

[77] Nanostructured and Amorphous Materials, Clay Road, TX, USA, *Material Safety Data Sheet Graphite powder*, 2012.

[78] S. Banerjee, M. Sardar, N. Gayathri, A. K. Tyagi, and B. Raj, "Conductivity landscape of highly oriented pyrolytic graphite surfaces containing ribbons and edges," *Physical Review B*, vol. 72, no. 7, p. 075418, 2005.

[79] L. Kleiner-Shuhler, R. Brittain, M. R. Johnston, and K. W. Hipps, "Scanning tunneling microscopy and orbital-mediated tunneling spectroscopy of n,n-dioctyl-1,8:4,5-naphthalenediimide adsorbed on highly ordered pyrolytic graphite from various solvents and in different environments," *Journal of Physical Chemistry C: Nanomaterials and Interfaces*, vol. 112, no. 38, pp. 14907–14912, 2008.

[80] S. Timoshenko, "Analysis of bi-metal thermostats," *Journal of the Optical Society of America*, vol. 11, no. 3, pp. 233–255, 1925.

[81] W. Yoon, S. Chung, P. R. Berger, and S. M. Asar, "Room temperature negative differential resistance in polymer tunnel diodes using a thin oxide layer and demonstration of threshold logic," *Applied Physics Letters*, vol. 87, no. 20, p. 203506, 2005.

[82] A. Tang, S. Qu, Y. Hou, F. Teng, H. Tan, J. Liu, X. Zhang, Y. Wang, and Z. Wang, "Electrical bistability and negative differential resistance in diodes based on silver nanoparticle-poly(n-vinylcarbazole) composites," *Journal of Applied Physics*, vol. 108, no. 9, p. 094320, 2010.

[83] L. D. Bozano, B. W. Kean, V. R. Deline, J. R. Salem, and J. C. Scott, "Mechanism for bistability in organic memory elements," *Applied Physics Letters*, vol. 84, no. 4, pp. 607–609, 2004.

[84] J. Ouyang, "Application of nanomaterials in two-terminal resistive-switching memory devices," *Nano Reviews*, vol. 1, p. 5118, 2010.

[85] A. Ramesh, P. R. Berger, and R. Loo, "High 5.2 peak-to-valley current ratio in Si/SiGe resonant interband tunnel diodes grown by chemical vapor deposition," *Applied Physics Letters*, vol. 100, no. 9, p. 092104, 2012.

[86] J. Huang, "Carbon black filled conducting polymers and polymer blends," *Advances in Polymer Technology*, vol. 21, no. 4, pp. 299–313, 2002.

[87] K. Sugihara, K. Kawamuma, and T. Tsuzuku, "Temperature dependence of the average mobility in graphite," *Journal of the Physical Society of Japan*, vol. 47, no. 4, pp. 1210–1215, 1979.

[88] X. Wang, L. Zhi, and K. Mullen, "Transparent, conductive graphene electrodes for dye-sensitized solar cells," *Nano Letters*, vol. 8, no. 1, pp. 323–327, 2008.

[89] X. W. Zhang, Y. Pan, Q. Zheng, and X. S. Yi, "Piezoresistance of conductor filled insulator composites," *Polymer International*, vol. 50, no. 2, pp. 229–236, 2001.

[90] L. Zhou, J. Lin, H. Lin, and G. Chen, "Electrical-thermal switching effect in high-density polyethylene/graphite nanosheets conducting composites," *Journal of Materials Science*, vol. 43, no. 14, pp. 4886–4891, 2008.

[91] F. El-Tantawy, K. Kamada, and H. Ohnabe, "A novel way of enhancing the electrical and thermal stability of conductive epoxy resin-carbon black composites via the Joule heating effect for heating-element applications," *Journal of Applied Polymer Science*, vol. 87, no. 2, pp. 97–109, 2003.

[92] J. Zhang, S. Feng, and X. Wang, "DC current voltage characteristics of silicone rubber filled with conductive carbon black," *Journal of Applied Polymer Science*, vol. 94, no. 2, pp. 587–592, 2004.

[93] W. F. Chow, *Principles of tunnel diode circuits*. Wiley New York, 1964.

[94] W. Peng, X. Feng, D. Tianhuai, and Q. Yuanzhen, "Time dependence of electrical resistivity under uniaxial pressures for carbon black/polymer composites," *Journal of Materials Science*, vol. 39, no. 15, pp. 4937–4939, 2004.

[95] M. Knite, V. Teteris, A. Kiploka, and J. Kaupuzs, "Polyisoprene-carbon black nanocomposites as tensile strain and pressure sensor materials," *Sensors and Actuators A: Physical*, vol. 110, no. 1, pp. 142–149, 2004.

[96] L. Chen, G. H. Chen, and L. Lu, "Piezoresistive behavior study on finger-sensing silicone rubber/graphite nanosheet nanocomposites," *Advanced Functional Materials*, vol. 17, no. 6, pp. 898–904, 2007.

[97] J. A. Rogers, T. Someya, and Y. Huang, "Materials and mechanics for stretchable electronics," *Science*, vol. 327, no. 5973, pp. 1603–1607, 2010.

[98] W. E. Snyder and J. St. Clair, "Conductive elastomers as sensor for industrial parts handling equipment," *IEEE Transactions on Instrumentation and Measurement*, vol. 27, no. 1, pp. 94–99, 1978.

[99] S. Nambiar and J. T. W. Yeow, "Conductive polymer-based sensors for biomedical applications," *Biosensors and Bioelectronics*, vol. 26, no. 5, pp. 1825–1832, 2011.

[100] M. Hussain, Y.-H. Choa, and K. Niihara, "Conductive rubber materials for pressure sensors," *Journal of Materials Science Letters*, vol. 20, pp. 525–527, 2001.

[101] C. Cochrane, M. Lewandowski, and V. Koncar, "A flexible strain sensor based on a conductive polymer composite for in situ measurement of

parachute canopy deformation," *Sensors*, vol. 10, no. 9, pp. 8291–8303, 2010.

[102] M. Shimojo, A. Namiki, M. Ishikawa, R. Makino, and K. Mabuchi, "A tactile sensor sheet using pressure conductive rubber with electrical-wires stitched method," *IEEE Sensors Journal*, vol. 4, no. 5, pp. 589–596, 2004.

[103] M. Gad-el Hak, *The Taming of the Shrew: Why Is It so Difficult to Control Turbulence?*. Springer Berlin, 2007.

[104] "Example of commercially available piezoresistive rubbers: www.zoflex.com," September 2012.

[105] M. Cheng, C. Tsao, Y. Lai, and Y. Yang, "The development of a highly twistable tactile sensing array with stretchable helical electrodes," *Sensors and Actuators A: Physical*, vol. 166, no. 2, pp. 226–233, 2011.

[106] D. Beruto, M. Capurro, and G. Marro, "Piezoresistance behavior of silicone-graphite composites in the proximity of the electric percolation threshold," *Sensors and Actuators A: Physical*, vol. 117, no. 2, pp. 301–308, 2005.

[107] W. Luheng, D. Tianhuai, and W. Peng, "Research on stress and electrical resistance of skin-sensing silicone rubber/carbon black nanocomposite during decompressive stress relaxation," *Smart Materials and Structures*, vol. 18, no. 6, p. 065002, 2009.

[108] L. Wang, T. Ding, and P. Wang, "Effects of compression cycles and precompression pressure on the repeatability of piezoresistivity for carbon black-filled silicone rubber composite," *Journal of Polymer Science Part B: Polymer Physics*, vol. 46, no. 11, pp. 1050–1061, 2008.

[109] K. Yamaguchi, J. J. C. Busfield, and A. G. Thomas, "Electrical and mechanical behavior of filled elastomers. i.) the effect of strain," *Journal of Polymer Science Part B: Polymer Physics*, vol. 41, no. 17, pp. 2079–2089, 2003.

[110] L. Mullins, "Softening of rubber by deformation," *Rubber Chemistry and Technology*, vol. 42, no. 1, pp. 339–362, 1969.

[111] J. Diani, B. Fayolle, and P. Gilormini, "A review on the Mullins effect," *European Polymer Journal*, vol. 45, no. 3, pp. 601–612, 2009.

[112] T. Osswald and G. Menges, *Materials Science of Polymers for Engineers*. Hanser, 2003.

[113] M. Shaw and W. MacKnight, *Introduction to Polymer Viscoelasticity*. Wiley, 2005.

[114] W. Shouli, W. Peng, and D. Tianhuai, "Resistive viscoelasticity of silicone rubber/carbon black composite," *Polymer Composites*, vol. 32, no. 1, pp. 29–35, 2011.

[115] L. Flandin, A. Chang, S. Nazarenko, A. Hiltner, and E. Baer, "Effect of strain on the properties of an ethylene-octene elastomer with conductive carbon fillers," *Journal of Applied Polymer Science*, vol. 76, no. 6, pp. 894–905, 2000.

[116] J. K. M. Stübler, N. Fritzsche, "Mechanical and electrical analysis of carbon black networking in elastomers under strain," *Polymer Engineering and Science*, vol. 51, no. 6, pp. 1206–1217, 2011.

[117] G. Yaralioglu, A. Ergun, B. Bayram, E. Haeggstrom, and B. Khuri-Yakub, "Calculation and measurement of electromechanical coupling coefficient of capacitive micromachined ultrasonic transducers," *Ultrasonics, Ferroelectrics and Frequency Control*, vol. 50, no. 4, pp. 449–456, 2003.

[118] S. Bhargava, *Principles and Practice of Ultrasonography*. Jaypee Brothers, 2002.

[119] OlympusNDT, Waltham, MA, USA, *Technical Notes For Transducer A380-SU*, 2009.

[120] *Health Effects of Exposure to Ultrasound and Infrasound*. Health Protection Agency, Centre for Radiation, Chemical and Enviromental Hazards, 2010.

[121] W. L. Nyborg, "Heat generation by ultrasound in a relaxing medium," *The Journal of the Acoustical Society of America*, vol. 70, no. 2, pp. 310–312, 1981.

[122] D. L. Folds, "Speed of sound and transmission loss in silicone rubbers at ultrasonic frequencies," *The Journal of the Acoustical Society of America*, vol. 56, no. 4, pp. 1295–1296, 1974.

[123] "http://people.bath.ac.uk/pysarn/pressure_imaging.m4v," June 2012.

[124] F. He, S. Lau, H. L. Chan, and J. Fan, "High dielectric permittivity and low percolation threshold in nanocomposites based on poly(vinylidene fluoride) and exfoliated graphite nanoplates," *Advanced Materials*, vol. 21, no. 6, pp. 710–715, 2009.

[125] J. Xu, M. Wong, and C. Wong, "Super high dielectric constant carbon black-filled polymer composites as integral capacitor dielectrics," *54th Proceedings of the Electronic Components and Technology Conference*, vol. 1, pp. 536–541, 2004.

[126] T. Sekitani and T. Someya, "Stretchable, large-area organic electronics," *Advanced Materials*, vol. 22, no. 20, pp. 2228–2246, 2010.

[127] L. A. Freberg, *Discovering Biological Psychology*. Wadsworth USA, 2009.

[128] T. Takahashi, K. Takei, E. Adabi, Z. Fan, A. M. Niknejad, and A. Javey, "Parallel array InAs nanowire transistors for mechanically bendable, ultrahigh frequency electronics," *ACS Nano*, vol. 4, no. 10, pp. 5855–5860, 2010.

[129] N. Chang, K, *Parametric and Tunnel Diodes*. Prentice-Hall, 1964.

[130] L. Esaki, "Discovery of the tunnel diode," *IEEE Transactions on Electron Devices*, vol. 23, no. 7, pp. 644–647, 1976.

[131] H. Zou, "Anisotropic Si deep beam etching with profile control using SF_6/O_2 plasma," *Microsystem Technologies*, vol. 10, no. 8, pp. 603–607, 2004.

[132] R. Knizikevicius, "Simulations of Si and SiO_2 etching in SF_6+O_2 plasma," *Vacuum*, vol. 83, no. 6, pp. 953–957, 2009.